Deposit & Copying of Dissertation Declaration

UNIVERSITY OF CAMBRIDGE

Board of Graduate Studies

Please note that you will also need to bind a copy of this Declaration into your final, hardbound copy of thesis - this has to be the very first page of the hardbound thesis.

1 Surname (Family Name)	Forenames(s)	Title
Yu	Hiu Ming	Mr.

2 Title of Dissertation as approved by the Degree Committee

Resistance of Carbon Fibre Reinforced Composites to Quasi-static and Ballistic Perforation

In accordance with the University Regulations in *Statutes and Ordinances* for the PhD, MSc and MLitt Degrees, I agree to deposit one print copy of my dissertation entitled above and one print copy of the summary with the Secretary of the Board of Graduate Studies who shall deposit the dissertation and summary in the University Library under the following terms and conditions:

1. Dissertation Author Declaration

I am the author of this dissertation and hereby give the University the right to make my dissertation available in print form as described in 2. below.

My dissertation is my original work and a product of my own research endeavours and includes nothing which is the outcome of work done in collaboration with others except as declared in the Preface and specified in the text. I hereby assert my moral right to be identified as the author of the dissertation.

The deposit and dissemination of my dissertation by the University does not constitute a breach of any other agreement, publishing or otherwise, including any confidentiality or publication restriction provisions in sponsorship or collaboration agreements governing my research or work at the University or elsewhere.

2. Access to Dissertation

I understand that one print copy of my dissertation will be deposited in the University Library for archival and preservation purposes, and that, unless upon my application restricted access to my dissertation for a specified period of time has been granted by the Board of Graduate Studies prior to this deposit, the dissertation will be made available by the University Library for consultation by readers in accordance with University Library Regulations and copies of my dissertation may be provided to readers in accordance with applicable legislation.

3 Signature	Date
	11 January 2017

Corresponding Regulation

Before being admitted to a degree, a student shall deposit with the Secretary of the Board one copy of his or her hard-bound dissertation and one copy of the summary (bearing student's name and thesis title), both the dissertation and the summary in a form approved by the Board. The Secretary shall deposit the copy of the dissertation together with the copy of the summary in the University Library where, subject to restricted access to the dissertation for a specified period of time having been granted by the Board of Graduate Studies, they shall be made available for consultation by readers in accordance with University Library Regulations and copies of the dissertation provided to readers in accordance with applicable legislation.

Resistance of Carbon Fibre Reinforced Composites to Quasi-static and Ballistic Perforation

Hiu Ming Yu

Queens' College

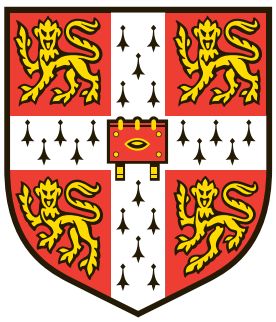

Submitted to the University of Cambridge

for the degree of Doctor of Philosophy

January 2017

Resistance of Carbon Fibre Reinforced Composites to Quasi-static and Ballistic Perforation

Hiu Ming Yu

Summary

The failure mechanisms, as well as the indentation and penetration resistance, of carbon fibre reinforced plastic (CFRP) cross-ply laminates were investigated under quasi-static and ballistic loading. In this thesis, the two most prominent failure modes were indirect tension and shear plugging. To characterise the indirect tension mechanism, CFRP cross-ply coupons with various matrix shear strengths were subjected to uniaxial out-of-plane compression between lubricated platens, while CFRP cross-ply beams were subjected to quasi-static indentation between a flat bottom indentor and a lubricated back support. The out-of-plane compressive strength was accurately predicted by finite element simulations and analytical models. To characterise the shear plugging mechanism, quasi-static cropping tests were performed on CFRP cross-ply beams. A beam configuration was selected to allow for ease of identifying the failure mechanisms.

The investigation was extended to consider the effect of matrix shear strength on the ballistic performance of simply supported CFRP cross-ply beams impacted by a flat projectile. Laminates with high matrix shear strength failed by shear plugging, and the penetration velocity increased with decreasing matrix shear strength. As the matrix shear strength decreased further, the failure mode switched to indirect tension and subsequently the penetration velocity remained elevated, independent of the matrix shear strength.

Having established that shear plugging is associated with low impact resistance, a new type of bilayer CFRP composite (comprising one low and one high matrix shear strength layer) was developed with the intent of suppressing this shear plugging mode. The ballistic penetration resistance of the bilayer beams was compared to that of the above monolithic CFRP beams using the same ballistic set-up. It was observed that the shear plugging mode in the high strength layer was suppressed when the layer was placed at the distal face; failure switched to a back face tensile mode, and the impact resistance was improved.

The investigation was extended to a more realistic impact environment: CFRP cross-ply laminates in a plate configuration were perforated by a steel ball. Specimens were tested under quasi-static and ballistic loading with either a back-supported condition (simulating a thick laminate) or an edge-clamped condition. The CFRP plates failed by indirect tension when back-supported but failed by shear plugging when edge-clamped. It was found that the addition of a protective aluminium alloy layer did not alter the failure mechanism of the CFRP, but did produce a load spreading effect that increased the penetration resistance.

Preface

This thesis is submitted for the degree of Doctor of Philosophy at the University of Cambridge. The research work herein was conducted in the Cambridge University Engineering Department between October 2012 and September 2016, under the supervision of Professor Norman A. Fleck. The research work was sponsored by the Office of Naval Research (ONR), U.S. (Prime Award No. N62909-14-1-N232). The studentship for the author was sponsored by the Croucher Foundation and the Cambridge Commonwealth, European & International Trust.

This dissertation is of my own work and contains nothing which is the outcome of work done in collaboration, except where reference is made in the text to the work of others. This document in whole or in part, has not been submitted for any other degree, diploma or qualification.

This thesis contains approximately 62,000 words, 86 figures, and 15 tables, in accordance with the specifications laid down by the Board of Graduate Studies.

Hiu Ming Yu

Cambridge, UK

January 2017

Acknowledgments

The author would like to express his sincere gratitude to Professor Norman Fleck for his supervision and advice. He taught me the meaning of academic rigour and has had a transformative influence on me, both as a researcher and on a personal level. I have a tremendous amount of respect for Professor Fleck's achievements and exceedingly high standards.

My advisor, Professor Vikram Deshpande, has been a constant source of mentorship and inspiration to me. I have benefited greatly from his advice, expertise, and insights.

My time at the University of Cambridge has been an unparalleled learning opportunity, and could not have been possible without the financial support of the Croucher Foundation and the Cambridge Commonwealth, European & International Trust. My research was facilitated by funding from the Office of Naval Research. Finally, the collaboration of Hexcel Ltd. was greatly appreciated, as it provided raw materials and assistance with the autoclave manufacturing process for the fibre composites analysed in this thesis.

I would also like to acknowledge the contribution of researchers whose previous research on similar topics was of great value to my thesis: Dr. Karthikeyan Kandan, Dr. Syed Khaderi, Dr. Julia Attwood, Dr. Benjamin Russell, and Dr. Mark O'Masta. They have generously taken the time to explain the subtleties of their methods and findings to me.

Many thanks to the members of the University of Cambridge, the Department of Engineering, and the Cambridge Centre for Micromechanics. I would particularly wish to highlight the professionalism and invaluable technical expertise of Alan Heaver, Simon Marshall, Len Howlett, Ann Bahnweg, Alistair Ross, and Alex Casabuena. It is also extremely likely that this thesis would not have been completed without the moral support and encouragement of Dr. Eral Bele, Dr. Julian Tan, Dr. Harika Tankasaka, Ashish Goel,

Erik Pickering, Kevin Maloney, Patryk Jedrasiak, Jack Tavener, Burigede Liu, Dr. Wolfram Bosbach, and Dr. Lizbeth Prieto. I would also like to congratulate my dear friends, Dr. Evangelos Avgoulas and Dr. Antonia Symeonidou, on their recently obtained degrees and well-deserved new titles. Thank you to all of my friends in Cambridge for countless happy memories and fascinating conversations.

I have also been honoured by the mentorship of Professor Glenn Hibbard, the supervisor during my Master's Degree. He instilled in me a true passion for science, motivated me throughout my studies, and has always been an exemplary role model. Equally significant in my life are my two best friends Leo Monaco and Khaled Abusamk. I have always been able to rely on their encouragement and support, and wish them the very best in their Ph.D. studies. A heartfelt thank you to my big sister, Virginia Yu, for all her love and support.

Finally, I cannot emphasise enough the contribution of my loving wife Alexandra Basevich, for her generosity in proof reading this originally incomprehensible dissertation. Since $t = 0$, Alexa had been nothing but patient, supportive, and a source of happiness. Thank you!

Summary

The failure mechanisms, as well as the indentation and penetration resistance, of carbon fibre reinforced plastic (CFRP) cross-ply laminates were investigated under quasi-static and ballistic loading. In this thesis, the two most prominent failure modes were indirect tension and shear plugging. To characterise the indirect tension mechanism, CFRP cross-ply coupons with various matrix shear strengths were subjected to uniaxial out-of-plane compression between lubricated platens, while CFRP cross-ply beams were subjected to quasi-static indentation between a flat bottom indenter and a lubricated back support. The out-of-plane compressive strength was accurately predicted by finite element simulations and analytical models. To characterise the shear plugging mechanism, quasi-static cropping tests were performed on CFRP cross-ply beams. A beam configuration was selected to allow for ease of identifying the failure mechanisms.

The investigation was extended to consider the effect of matrix shear strength on the ballistic performance of simply supported CFRP cross-ply beams impacted by a flat projectile. Laminates with high matrix shear strength failed by shear plugging, and the penetration velocity increased with decreasing matrix shear strength. As the matrix shear strength decreased further, the failure mode switched to indirect tension and subsequently the penetration velocity remained elevated, independent of the matrix shear strength.

Having established that shear plugging is associated with low impact resistance, a new type of bilayer CFRP composite (comprising one low and one high matrix shear strength layer) was developed with the intent of suppressing this shear plugging mode. The ballistic penetration resistance of the bilayer beams was compared to that of the above monolithic CFRP beams using the same ballistic set-up. It was observed that the shear plugging mode in the high strength layer was suppressed when the layer was placed at the distal

face; failure switched to a back face tensile mode, and the impact resistance was improved.

The investigation was extended to a more realistic impact environment: CFRP cross-ply laminates in a plate configuration were perforated by a steel ball. Specimens were tested under quasi-static and ballistic loading with either a back-supported condition (simulating a thick laminate) or an edge-clamped condition. The CFRP plates failed by indirect tension when back-supported but failed by shear plugging when edge-clamped. It was found that the addition of a protective aluminium alloy layer did not alter the failure mechanism of the CFRP, but did produce a load spreading effect that increased the penetration resistance.

Contents

1 Introduction and Thesis Outline **1**

1.1 Introduction 1

1.2 Thesis Outline 4

2 Literature Review **7**

2.1 Introduction 7

2.2 Failure Mechanisms of Fibre Composites under Quasi-static Out-of-plane Loading 8

2.2.1 Failure Mechanisms in Uniaxial Out-of-plane Compression 9

2.2.2 Failure Mechanism in Back-supported Indentation Tests 12

2.2.3 Perforation Mechanisms in Quasi-static Punch Tests . . . 16

2.3 Failure Mechanisms of Fibre Composites under Ballistic Loading 20

2.3.1 Classification of Impact Based on Impact Velocity 21

2.3.2 Shear Plugging Mechanism 22

2.3.3 Membrane Stretching Mechanism 27

2.3.4 Indirect Tension Mechanism 29

2.3.5 Summary of Ballistic Perforation Mechanisms 30

2.4 The Role of Fibre, Matrix, and Lamination on the Impact Resistance of Composite Laminates 31

2.4.1 The Role of Fibre 31

2.4.2 The Role of Matrix 36

2.4.3 Hybridisation with Different Fibres 40

2.4.4 Lamination with Metal Layers 43

2.5 Conclusions 47

3 The Effect of Matrix Shear Strength on the Measured Out-of-plane Compressive Strength of CFRP Cross-ply Laminates 48

3.1 Introduction . . . 50

3.2 Laminates Manufacture . . . 52

3.3 Test Methods . . . 54

3.3.1 Out-of-plane Compression Test . . . 54

3.3.2 Deformation Mechanics and Failure Mechanism . . . 55

3.4 Results . . . 56

3.4.1 Out-of-plane Compressive Response . . . 56

3.4.2 Compressive Strength versus Specimen Size . . . 58

3.4.3 Pressure Distribution of the Laminates during Compression . . . 60

3.4.4 Observed Deformation and Failure Mechanisms . . . 63

3.5 Discussion . . . 65

3.6 Conclusions . . . 67

4 Finite Element and Analytical Models of CFRP Cross-ply Laminates under Quasi-static Out-of-plane Compression 69

4.1 Introduction . . . 70

4.1.1 Strain Rate Sensitivity of Matrix Flow . . . 71

4.1.2 Pressure Dependence of the Matrix Shear Strength . . . 71

4.1.3 Pressure Dependence of Fibre Tensile Strength . . . 71

4.2 Finite Element Simulation for the Predictions of the Average Pressure at Compressive Failure . . . 72

4.2.1 Description of the Finite Element Method . . . 72

4.2.2 Constitutive Law for Each Composite Ply . . . 74

4.2.3 Failure Criterion for Each Composite Ply . . . 84

4.3 Analytical Models for the Out-of-plane Compressive Strength . 86

4.3.1 Elastic Laminate Plate Theory for the Out-of-plane Compressive Strength . . . 86

4.3.2 Elastic-plastic Analytical Model . . . 88

4.3.3 Elastic-viscoplastic Analytical Model 92
4.4 Accuracy of Predictions 97
4.4.1 Compressive Response 97
4.4.2 Pressure Distribution during Out-of-plane Compression 99
4.4.3 Compressive Strength versus Specimen Size 99
4.5 Conclusions 104

5 The Effect of Matrix Shear Strength on the Perforation Behaviour of CFRP Beams under Quasi-static and Ballistic Loading 105

5.1 Introduction 107
5.2 Specimen Manufacture 109
5.3 Test Methods 111
5.3.1 Quasi-static Indentation Test 111
5.3.2 Quasi-static Cropping test 111
5.3.3 Ballistic Impact Test 112
5.4 Results 115
5.4.1 Quasi-static Indentation Test 115
5.4.2 Quasi-static Cropping Test 116
5.4.3 Ballistic Test 121
5.5 Discussion 127
5.5.1 Failure Mechanisms in the Quasi-static Indentation and Cropping Tests 127
5.5.2 Failure Mechanisms in the Ballistic Test 128
5.5.3 Estimation of Penetration Velocity 129
5.5.4 The Effect of Perforation Mechanism on the Failure Time 131
5.6 Conclusions 134

6 Perforation of Bilayer CFRP Beams under Quasi-static and Ballistic Loading 135

6.1 Introduction 137
6.1.1 Scope of Study 138
6.2 Specimen Manufacture 139

6.3 Experimental Methods . . . 140
6.3.1 Quasi-static Indentation Test . . . 140
6.3.2 Quasi-static Cropping Test . . . 141
6.3.3 Ballistic Impact Test . . . 141
6.4 Results . . . 143
6.4.1 Quasi-static Indentation Test . . . 143
6.4.2 Quasi-static Cropping Test . . . 143
6.4.3 Ballistic Impact Test . . . 144
6.5 Discussion . . . 149
6.5.1 Failure Mechanisms . . . 149
6.5.2 Penetration Velocity . . . 149
6.6 Conclusions . . . 151

7 Perforation of Aluminium Alloy-CFRP Bilayer Plates under Quasi-static and Ballistic Loading 153

7.1 Introduction . . . 155
7.1.1 Scope of Study . . . 156
7.2 Specimen Manufacture . . . 157
7.3 Test Methods . . . 159
7.3.1 Ballistic Tests . . . 159
7.3.2 Quasi-static Indentation Tests . . . 160
7.3.3 Post-test Characterisation . . . 162
7.4 Results . . . 164
7.4.1 Failure Mechanisms . . . 164
7.4.2 Quasi-static Edge-clamped Indentation Response . . . 164
7.4.3 Quasi-static Back-supported Indentation Response . . . 169
7.4.4 Effect of Boundary Condition on the Average Indentation Pressure . . . 171
7.4.5 Effect of the Metal Layer on the Indentation Cut Fraction 172
7.4.6 Ballistic Impact Response . . . 174
7.5 Discussion . . . 176
7.5.1 Failure Mechanisms . . . 176

7.5.2 A Comparision of the Quasi-static and Ballistic Responses 177
7.5.3 Effect of Metal Layer Protection on the Specific Energy Dissipation . . . 179
7.6 Conclusions . . . 179

8 Conclusions and Future Work 181
8.1 Conclusions . . . 181
8.2 Suggestions for Future Work . . . 183
8.2.1 Numerical Methods to Predict the Ballistic Limit of Cross-ply Laminates Failing by Indirect Tension . . . 183
8.2.2 The Effect of Matrix Shear Strength on the Impact Tolerance of Cross-ply Laminates . . . 183
8.2.3 The Effect of the Metal Layer's Yield Strength on the Ballistic Resistance of Metal-CFRP Bilayers . . . 184

References 184

A Summary of the Partial Curing Process 199

B Measurements of Matrix Shear Strength of CFRP Laminates 202
B.1 ±45° Tensile Test . . . 204
B.2 Short Beam Shear Test . . . 208

C Analytical Models of the Stress State at the Centre of a Cross-ply Laminate under Out-of-Plane Compression 210
C.1 Elastic Laminate Plate Theory . . . 211
C.2 Elastic-plastic Model . . . 212
C.3 Elastic-viscoplastic Model . . . 214
C.4 Compressive Response at Specimen Centre . . . 216
C.4.1 Effect of Out-of-Plane Elastic Modulus . . . 217
C.4.2 Effect of Poisson's Ratio . . . 217
C.4.3 Effect of Matrix Shear Strength in the Elastic-plastic Model . . . 217
C.4.4 Effect of Strain Rate in the Elastic-viscoplastic Model . . . 217

D Preliminary Experiment: Effect of Matrix Shear Strength on the Ballistic Response of CFRP Plates **219**

D.1 Materials Manufacturing and Properties 219

D.2 Ballistic Impact Test 222

D.3 Results 223

E Preliminary Experiment: Effect of Adhesive on the Ballistic Response of an AA1050A-H6-CFRP Bilayer Plate **227**

Chapter 1

Introduction and Thesis Outline

1.1 Introduction

Carbon fibre composites are in high demand globally for use in diverse structural applications. In general, fibre reinforced plastic (FRP) laminates are a type of composite material consisting of a polymeric matrix bonded with a fibre reinforcement. They offer superior strength-to-weight and stiffness-to-weight ratios in comparison to traditional alloys. Currently, different types of FRP laminates are uniquely suited to different engineering applications. Ultra-high molecular weight polyethylene (UHMWPE) fibres and aramid fibres are polymer fibres made of organic molecular chains with high orientation. These fibres have high flexibility and are known to have one of the highest strength-to-weight ratios; therefore, they are currently used in manufacturing lightweight flexible body armour for blast and ballistic protection, as shown in Figure 1.1. However, these flexible fibres have low axial compressive strength and bending stiffness, limiting their use in structural applications. In contrast, carbon fibres have higher axial compressive strength and bending stiffness, and thus carbon fibre reinforced plastic (CFRP) laminates are widely used in structural applications in the aerospace, automotive, and sporting goods industries. The demand for CFRP is constantly growing. In a report on the composite market conducted by Carbon Composites e.V., it was stated that $\sim$ 53,000 tonnes of CFRP were manufactured in 2014 and this generated $\sim$ 2 billion US$ of revenue. This report also posited that global demand is expected to double by 2020,

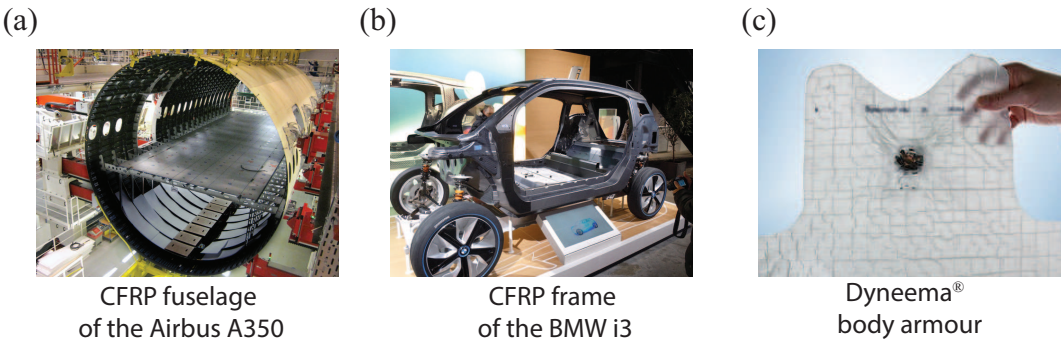

Figure 1.1: Examples of fibre composites used in structural applications, such as a) CFRP fuselage of the Airbus A350 (Airbus, 2011) and b) CFRP frame of the BMW i3 (Jessel, 2013), as well as ballistic applications, such as c) Dyneema® body armour (Textile World, 2009).

reaching 100,000 tonnes (Written et al., 2015). Recent developments in the aerospace and automotive industries also demonstrate a growing need for CFRP composites, with the fuselage of the Airbus A350 being manufactured with CFRP and the BMW i3 becoming the first mass-produced commercial vehicle featuring CFRP, as shown in Figure 1.1.

The major disadvantage of CFRP composites is that they have low impact resistance compared to other composites such as UHMWPE fibre-based Dyneema® and Kevlar® composites. This limits the application of CFRP in armour manufacturing and drastically increases the repair costs of structural applications utilising CFRP. For example, the outer frame of a commercial vehicle can be damaged from the low velocity impact of debris on the freeway.

When CFRP is impacted by a projectile at velocities from 20 to 50 m/s, they can be damaged through epoxy matrix cracking and ply delamination. This damage is usually at the sub-surface level and barely visible to the naked eye, and is therefore referred to as barely visible impact damage (BVID). BVIDs are difficult to detect and are detrimental to the post-impact structural performance of the composites. For instance, the in-plane compressive strength of CFRP can be reduced when BVID is formed, limiting the service life. At higher impact velocities, above 100 m/s, it appears that CFRP is usually penetrated through a localised shear plugging mechanism, first identified by Cantwell and Morton (1989a,b, 1990) in their drop weight experiments. They revealed that a plug is formed consisting of transverse matrix cracks, ply delamination, and fibre fracture when CFRP laminates are subjected to impact loading.

In contrast, Attwood et al. (2014); Karthikeyan et al. (2013b); O'Masta et al. (2015a) have recently demonstrated that the ballistic resistance of Dyneema® cross-ply composites is dictated by a local indentation-type mechanism involving the in-plane tensile failure of plies, referred to as the indirect tension mechanism. Attwood et al. (2014) revealed that indirect tension can arise in Dyneema® cross-ply composites through quasi-static uniaxial out-of-plane compression. The indirect tension mechanism requires a 0°/90° stacking of plies and anisotropy in Poisson expansion within the plane of each ply. In general, Dyneema® composites provide significantly higher energy dissipation in ballistic impact compared to CFRP composites.

If this superior performance is attributable to the indirect tension mechanism, it may be possible to stimulate indirect tension in CFRP and thus achieve higher levels of impact resistance.

Several studies have provided insights into the possibility of improving the impact resistance of CFRP composites. Preliminary experiments by Karthikeyan et al. (2013b) have suggested that matrix shear strength has a significant effect on the ballistic limit of CFRP composites. Furthermore, they observed shear plugging in autoclaved cross-ply laminates, whereas as-received prepregs exhibited progressive perforation. They noted that this latter mode involved tensile failure of the fibres, but they did not identify the mechanism as indirect tension. The investigations in the current thesis shall show that this mechanism of ballistic perforation is indeed indirect tension.

Data from Bieniaś et al. (2015); Peijs et al. (1990a); Peijs and Venderbosch (1991) suggested that there remains potential to protect CFRP against projectile threats through the use of composite hybridisation. Peijs et al. (1990a); Peijs and Venderbosch (1991) showed that hybrid composite layers consisting of alternating UHMWPE fibre-based Spectra® and CFRP layers have higher impact resistance than monolithic CFRP layers. Vlot (1991, 1993, 1996) have shown that the impact resistance of various fibre composites can be improved by bonding them with alternating metal layers into hybrid composites known as fibre metal laminates. These fibre metal laminates included armaid fibre reinforced aluminium laminates (ARALL®), glass reinforced aluminium laminates (GLARE®), and carbon fibre reinforced aluminium laminates (CARAL). Furthermore, Vlot (1991, 1993, 1996) demonstrated that GLARE® composites offer higher impact resistance than

both their monolithic composite precursors and monolithic aluminium alloys with the same thickness. More recently Bieniaś et al. (2015) demonstrated that composite sandwiches consisting of a CFRP core and two aluminium alloy face sheets have higher impact resistance than monolithic CFRP laminates of the same thickness. The reason for this improvement is not fully understood and shall be further investigated in the current thesis.

The above studies indicate that there remain the following uncertainties within the fields of composite science and ballistic research: (i) Is the indirect tension mechanism responsible for the superior ballistic performance of Dyneema® composites compared to CFRP composites? (ii) What is the role of matrix shear strength in the dynamic failure mechanism and its effect on the impact resistance of fibre composites? (iii) Is it possible to suppress the commonly observed shear plugging mechanism or alternatively to activate the indirect tension mechanism in CFRP composites and thus enhance their impact resistance? (iv) What are the other contributing factors in designing composites with high impact resistance?

1.2 Thesis Outline

This thesis provides a set of comprehensive quasi-static and ballistic experiments, as well as associated simulations, with the intent of improving the ballistic resistance of CFRP cross-ply laminates by suppressing the brittle shear plugging mechanism or activating the indirect tension mechanism. First, the literature review presented in Chapter 2 suggests that the dominant perforation mechanism of fibre composites under ballistic loading ranges from the indirect tension mechanism to a shear plugging mode.

The indirect tension and shear plugging mechanisms of CFRP cross-ply laminates were first characterised through various types of transverse indentation and compression experiments under quasi-static loading. The indirect tension mechanism was thoroughly characterised by subjecting CFRP cross-ply coupons with various matrix shear strengths to uniaxial out-of-plane compression between lubricated platens, with the experimental results summarised in Chapter 3. Finite element simulations and analytical models were developed to predict the laminates' out-of-plane compressive strength, and are presented in Chapter 4. To further study the indirect

tension mechanism under conditions representative of a ballistic impact, CFRP cross-ply beams were subjected to quasi-static indentation between a flat bottom indenter and a lubricated back support to promote indirect tension mechanism. To characterise the shear plugging mechanism, quasi-static cropping tests were performed on CFRP cross-ply beams. A composite beam configuration was selected to allow for ease of identifying the failure mechanisms. The results of the back-supported indentation and cropping tests of CFRP beams are reported in Chapter 5.

With this obtained knowledge, the study was extended in Chapter 5 to investigate the ballistic perforation mechanisms and penetration resistance of CFRP cross-ply beams with various matrix shear strengths, impacted by a flat projectile with a simply supported condition. It was found that the shear plugging mode commonly observed for CFRP laminates switched to the indirect tension mode for laminates with lower matrix shear strength.

With the intent of suppressing the shear plugging mode, a new type of bilayer composite was developed (consisting of a low matrix shear strength layer and a high matrix shear strength layer). The ballistic penetration resistance of these bilayer CFRP beams with different stacking configurations was compared to that of the above monolithic CFRP beams through the same ballistic test mentioned above (i.e. subject to a flat projectile with a simply supported condition), as reported in Chapter 6.

Chapter 7 extends the investigation to a more realistic impact environment. CFRP cross-ply laminates in a plate configuration were perforated normally by a steel ball. Specimens were tested under both quasi-static and ballistic loading with a back-supported condition (simulating a thick laminate) and under a more common edge-clamped boundary condition. The potential of suppressing the shear plugging mode was further explored by comparing the quasi-static and dynamic responses of the above monolithic CFRP plates to those protected by a layer of aluminium alloy. Table 1.1 guides the reader by summarising the chosen CFRP specimens and types of experimental set-up conducted in Chapters 3 to 7. Finally, the conclusions of the above studies are summarised in Chapter 8, and avenues for future research are proposed.

Table 1.1: Summary of tests conducted in Chapters 3 to 7.

Chapter	Specimen type	Loading condition	Boundary condition	Test
3 & 4	CFRP cross-ply coupons	quasi-static	rigid platens	out-of-plane compression
5	CFRP cross-ply beams	quasi-static	rigid back-supported	indentation with a flat indenter
			simply supported	cropping test with a flat punch
		ballistic	simply supported	ballistic test with a flat-bottom projectile
6	CFRP bilayer cross-ply beams	quasi-static	rigid back-supported	indentation with a flat indenter
			simply supported	cropping test with a flat punch
		ballistic	simply supported	ballistic test with a flat-bottom projectile
7	monolithic CFRP and aluminium alloy-CFRP bilayer plates	quasi-static	edge-clamped	indentation with a hemispherical indenter
			rigid back-supported	indentation with a hemispherical indenter
		ballistic	edge-clamped	ballistic test with a steel ball
			rigid back-supported	ballistic test with a steel ball

Chapter 2

Literature Review

2.1 Introduction

An extensive literature has been established on the impact resistance and perforation mechanisms of fibre composites since their invention in the 1940s. Notable reviews include Abrate (1991); Bibo and Hogg (1996); Cantwell and Morton (1991); Cheeseman and Bogetti (2003); Tabiei and Nilakantan (2008). The purpose of this chapter is to identify gaps in the existing knowledge and to suggest methods of improving the impact resistance of carbon fibre reinforced plastic (CFRP) through (i) the reduction of matrix shear strength, (ii) protection using laminates with low matrix shear strength, and (iii) protection using metal layers.

This literature review is divided into three sections. First, the failure mechanisms of fibre composite laminates under quasi-static out-of-plane loading are provided. Second, the failure mechanisms in ballistic loading conditions are discussed. The final section of this chapter reviews the influence of fibre, matrix, and composite lamination on impact resistance, with the aim of understanding what activates a particular failure mechanism.

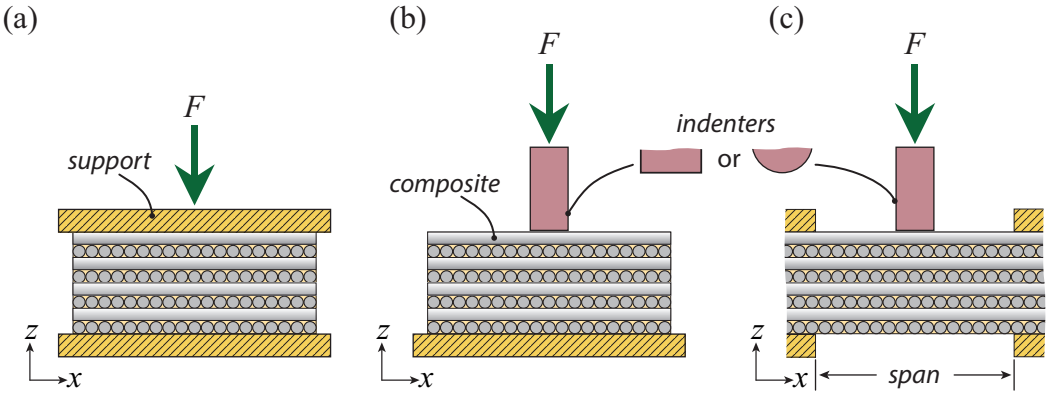

Figure 2.1: Schematic illustrations in profile view of a fibre composite subjected to a quasi-static a) uniaxial out-of-plane compression test, b) back-supported indentation test with a flat or hemispherical indenter, and c) punch test with a flat or hemispherical indenter.

2.2 Failure Mechanisms of Fibre Composites under Quasi-static Out-of-plane Loading

As a first step in understanding the impact resistance of fibre composites and their perforation mechanisms, many researchers have investigated fibre composites under quasi-static out-of-plane loading with the intent of obtaining results in a more controlled manner than in ballistic experiments. These quasi-static experiments can be classified into three types of tests: (i) uniaxial out-of-plane compression test, (ii) back-supported indentation test with a flat or hemispherical indenter, and (iii) quasi-static punch test with a back face opening using a flat or hemispherical indenter, as illustrated by the schematics in Figure 2.1. Various fibre composites have been investigated through these quasi-static experiments, primarily carbon fibre reinforced plastic (CFRP), glass fibre reinforced plastic (GFRP), aramid fibre composites (commonly known by their trade names of Kevlar® or Twaron®), and ultra high molecular weight polyethylene (UHMWPE) fibre comspoites (commonly known by their trade names of Spectra® or Dyneema®). The remainder of this section provides a detailed review of the failure mechanisms of these fibre composites reported in the above quasi-static experiments.

2.2.1 Failure Mechanisms in Uniaxial Out-of-plane Compression

Early investigations of fibre composites mainly focused on their in-plane structural performance, whereas their out-of-plane performance was largely ignored. There is only limited literature regarding the uniaxial out-of-plane compression of fibre composites. An early study by Henriksson (1990) compared the uniaxial out-of-plane compressive response (in terms of average pressure $\bar{p}$ and compressive strain $-\varepsilon_{zz}$) and compressive strength (in terms of average pressure at failure $\bar{p}_f$) of AS4/8552 CFRP unidirectional (UD) plies and $[0°/90°]$ cross-ply laminates. He observed that the UD plies failed at a compressive strength of $\sim$ 250 MPa with fibres remaining intact but matrix cracks propagating at $\sim 30°$ away from the loading axis (similar results were observed by Collings (1974)). In contrast, the cross-ply laminates failed at a much higher compressive strength ($\sim$ 1 GPa) and exhibited both fibre and matrix failure. To explain the difference in compressive strength, Henriksson (1990) conducted an additional experiment by compressing a UD laminate inside a lateral confinement that prevented Poisson expansion of the plies transverse to the fibre (referred to as constrained compression). The lateral confinement raised the compressive strength of the UD laminate to $\sim$ 2 GPa (higher than that of the cross-ply laminates), see Figure 2.2. He therefore proposed that the cross-ply lamination served as a partial constraint to the expansion of each ply, resulting in their high compressive strength compared to UD laminates. The underlying failure mechanism of the CFRP cross-ply laminates remained unclear. However, some insight may be obtained from a recent investigation by Attwood et al. (2014) into the compressive behaviour of a different type of fibre composite, Dyneema®.

Attwood et al. (2014) compared the uniaxial out-of-plane compressive response and failure strength of Dyneema® UD plies and cross-ply laminates with a range of specimen sizes with side length $L \times L$. They found that the compressive strength (in terms of average pressure at failure $\bar{p}_f$) of the cross-ply laminates ($\sim$ 1 GPa) was significantly higher than that of the UD plies ($\sim$ 20 MPa), see Figure 2.3. It was observed that, under compression, the cross-ply laminates failed in a catastrophic manner consisting of Poisson expansion of plies and ply tensile failure. They then proposed that the compressive failure of the cross-ply laminates was governed by an 'indirect tension mechanism'. The

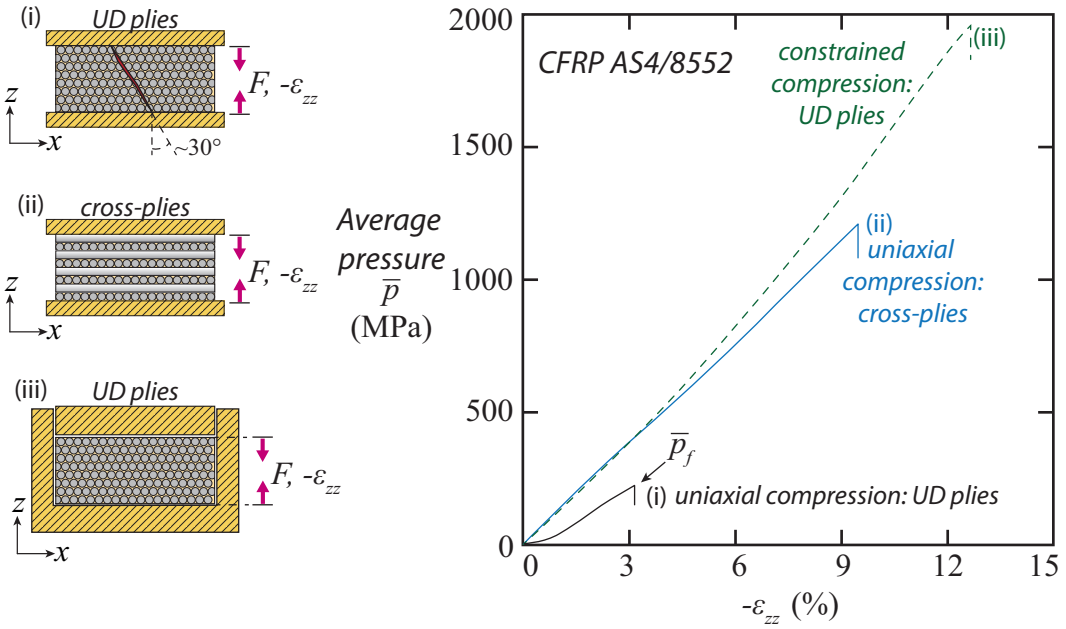

Figure 2.2: Plot of the uniaxial out-of-plane compressive response (in terms of average pressure $\bar{p}$ and compressive strain $-\varepsilon_{zz}$) of UD and cross-ply laminates of AS4/8552 CFRP composites, and the constrained compressive response of the UD plies. Image adapted from Henriksson (1990).

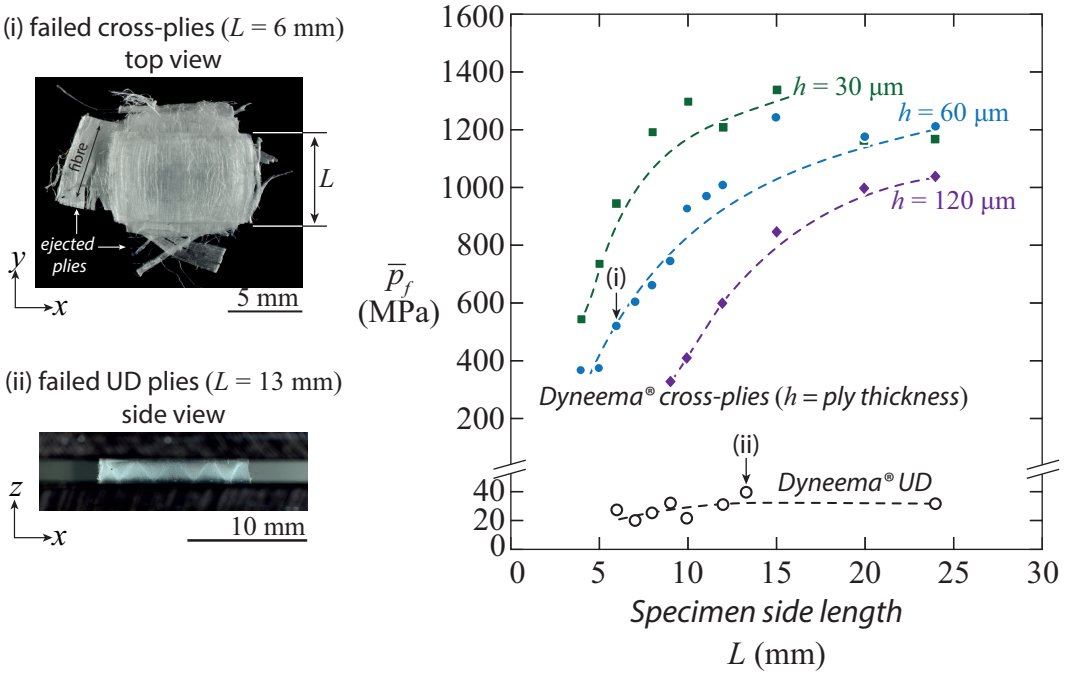

Figure 2.3: Plot of the uniaxial compressive strength (in terms of average pressure at failure $\bar{p}_f$) of Dyneema® UD plies and cross-ply laminates as functions of specimen size with side length $L \times L$. The figure also displays optical images after failure of the UD and cross-ply specimens, with their respective positions on the plot labelled as (i) and (ii). Image adapted from Attwood et al. (2014).

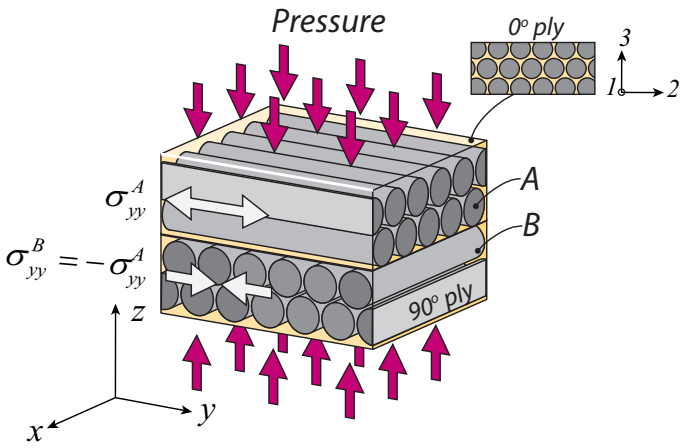

Figure 2.4: Illustration of the indirect tension mechanism in a pair of 0°/90° plies under out-of-plane pressure. Poisson lateral expansion in the 0° ply parallel to the fibre is normally much less than in the 90° ply transverse to the fibre. Under out-of-plane compression, this mismatch in Poisson lateral expansion causes tension strain in the 0° ply and compression in the 90° ply.

indirect tension mechanism arises as a result of (i) the anisotropy in Poisson expansion within the plane of each ply, and (ii) a 0°/90° stacking of plies, see Figure 2.4. A short explanation of indirect tension is given below.

Consider a stack of alternating 0° and 90° plies under out-of-plane compressive pressure p in the z-direction, and limit attention to the response of a unit cell comprising a single 0 ° ply (labelled A in the figure) adhered to an underlying 90° ply (labelled B). If the two plies were allowed to slide freely and without adhesion then, under the same out-of-plane compressive loading, ply B would undergo a much larger Poisson expansion in the y-direction than ply A, due to the orientation-dependent Poisson's ratio. Such relative deformation is disallowed by the adhesion of the two layers, and the two layers share the same strain in the y-direction; consequently, layer A is subjected to a tensile stress σ^A_{yy}, whereas layer B experiences a compressive stress $\sigma^B_{yy} = -\sigma^A_{yy}$ as there is no net force in the y-direction. By a symmetry argument, $\sigma^B_{xx} = \sigma^A_{yy}$ and $\sigma^A_{xx} = \sigma^B_{yy}$. Therefore, the out-of-plane compressive pressure p causes each ply to undergo tensile straining in the fibre direction.

Based on the above explanation, Attwood et al. (2014) developed finite element and analytical models that accurately predicted the compressive strength of the Dyneema® cross-ply laminates. Another recent study by O'Masta et al. (2015b) further characterised the influence of laminate defects, such as voids, on the compressive strength of Dyneema® cross-ply laminates.

Prior to the work in this thesis, indirect tension had only been reported in Dyneema® cross-ply laminates. Therefore, Chapters 3 and 4 extend the investigation to the quasi-static uniaxial out-of-plane compressive response of CFRP cross-ply laminates and reach the conclusion that CFRP cross-ply laminates also fail by the above indirect tension mechanism.

2.2.2 Failure Mechanism in Back-supported Indentation Tests

In a ballistic test, the out-of-plane deformation of the fibre composites is more complicated and the stress distribution is usually more localised than in the above uniaxial compression test. To extend the investigation to a more realistic ballistic environment in a controlled manner, many researchers have conducted back-supported quasi-static indentation tests on fibre composites, which can simulate the ballistic response of a thick laminate whose inertia causes local indentation damage. The indenters used in these experiments had either a flat bottom or a hemispherical shape, as illustrated in the schematics in Figure 2.1b.

An early investigation by Woodward et al. (1994) examined the response of different types of woven composite plates (GFRP, Kevlar®, Spectra®, and nylon composites) indented by a cylinder. Scott (2011) extended the work by Woodward et al. (1994) to include the indentation response of aramid and UHMWPE cross-ply laminates. Scott (2011) reported a 'saw tooth' shaped load-displacement response for the cross-ply laminates. This type of 'saw tooth' shape has also been reported in other studies (Attwood et al., 2016; Cain and Gaviola, 2015; O'Masta et al., 2016; Scott and Cheeseman, 2008). More recently, Attwood et al. (2016) conducted a set of indentation tests on the above Dyneema® UHMWPE cross-ply laminates in a beam configuration (with width $H = 12.4$ mm) using a flat indenter (with width $w = 3$ mm to 12.4 mm). They found that the average pressure $\bar{p} \equiv F/(bw)$ at the first failure was associated with ply tensile rupture. This average pressure at failure $\bar{p}_f$ was comparable to the out-of-plane compressive strength of the Dyneema® cross-ply laminates and was independent of the indenter width, see Figure 2.5. As a result, they concluded that these cross-ply composites failed by the same indirect tension mechanism as the those in the above uniaxial out-of-plane compression tests.

Other researchers have investigated the indentation response of fibre composites such as CFRP laminates using a hemispherical indenter. In these experiments, the researchers found that the load-displacement curves would closely follow the Hertzain contact law (Henriksson, 1990; Majeed et al., 2012; Suemasu et al., 1992). Although many studies have focused on the indentation response, only limited literature regarding the failure mechanism is available. In an investigation given by Jørgensen et al. (1998), it was observed that the first sign of damage in a cross-ply laminate was ply delamination near the edge of contact. Their finite element simulations revealed that this delamination was caused by the mismatch of Poisson's ratios in the alternating layers.

Another study given by Poe Jr. (1991) further characterised the failure mechanism of an off-angle helical CFRP laminate after fibre failure had occurred. The helical CFRP laminate had a $\left\{(\pm 56.5^\circ)_2 / 0^\circ / [(\pm \underline{56.5^\circ})_2 / 0^\circ]_3 / [(\pm 56.5^\circ)_2 / 0^\circ]_7 / (\pm 56.5^\circ)_2\right\}$ lay up and was bonded to a plain woven CFRP layer (in the lay up, note that the underlined helical layers were 1.6 times thicker than the other 56.5° layers). Poe Jr. (1991) performed a quasi-static indentation test on the above helical CFRP laminate using a hemispherical indenter (with a 25.4 mm radius) and supported by an aluminium platen with a small convex curvature (1.8 m radius), see Figure 2.6a. The indentation contact radius a and the average pressure $\bar{p}$ were calculated assuming Hertzian contact for a semi-infinite isotropic body (i.e. $\bar{p} = F/(\pi a^2) = (2/3)p_{max}$ where F is the indentation load and p_{max} is the peak pressure located at the centre line beneath the indenter). The locations of the failure in each ply were revealed using a de-ply process by burning off the resin at the ply-ply interfaces. When the indentation average pressure $\bar{p}$ exceeded $\sim$ 648 MPa (associated with a force F = 267 kN), fibre tensile cracks would initiate directly beneath the hemispherical indenter near the centre line where the contact pressure was at a maximum, see example optical images in Figure 2.6b. Poe Jr. (1991) also observed matrix crack formation next to the broken fibres and thus proposed that the failure of the matrix precipitated the fibre failure. However, it is worth noting that the optical evidence of the fibre failure mode in the above study is remarkably similar to what would be expected from the indirect tension mode.

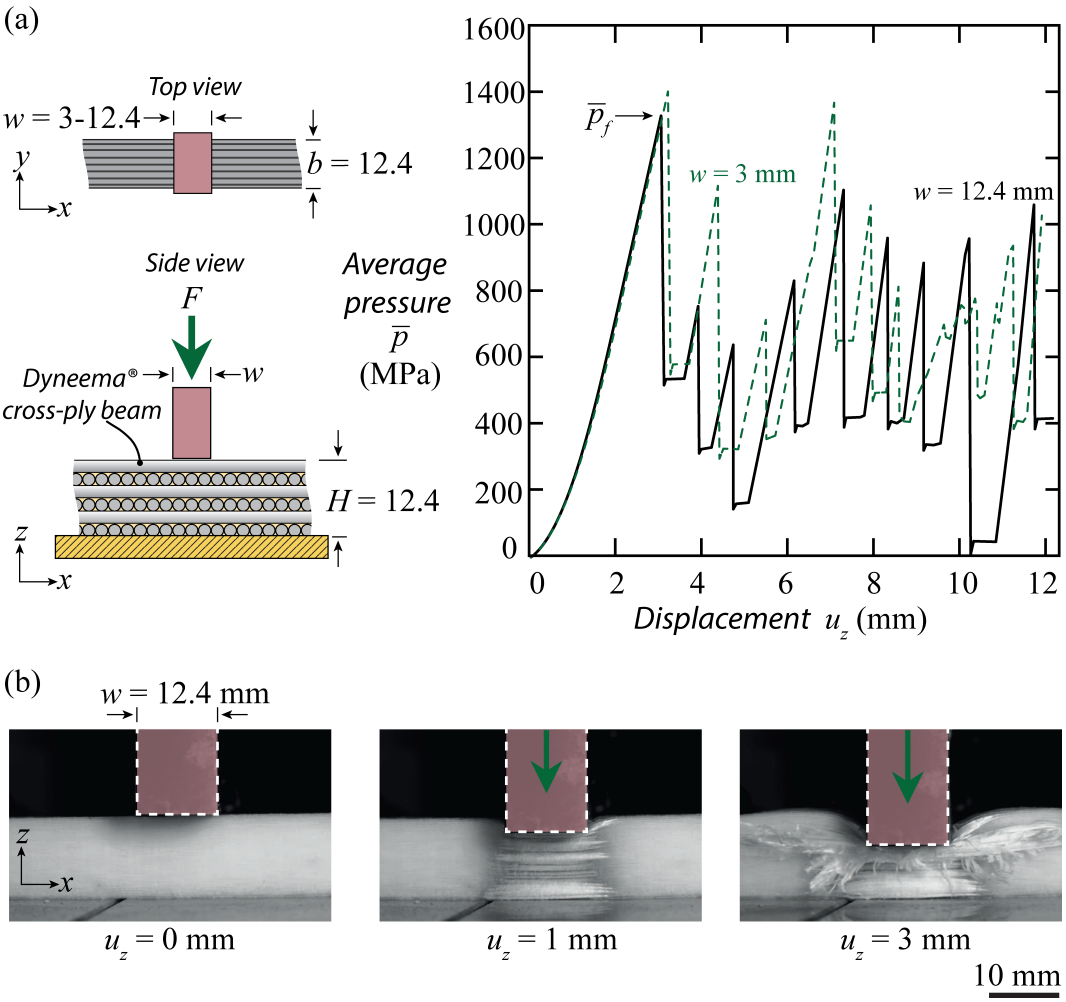

Figure 2.5: Summary of a) the back-supported indentation response (in terms of average pressure $\bar{p}$ and displacement u_z) of Dyneema® cross-ply beams using a flat indenter (with width $w = 3$ mm and 12.4 mm) and b) the optical images taken of the specimen with $w = 12.4$ mm during the indentation test. All dimensions in the schematic illustrations are in mm. Image adapted from Attwood et al. (2016).

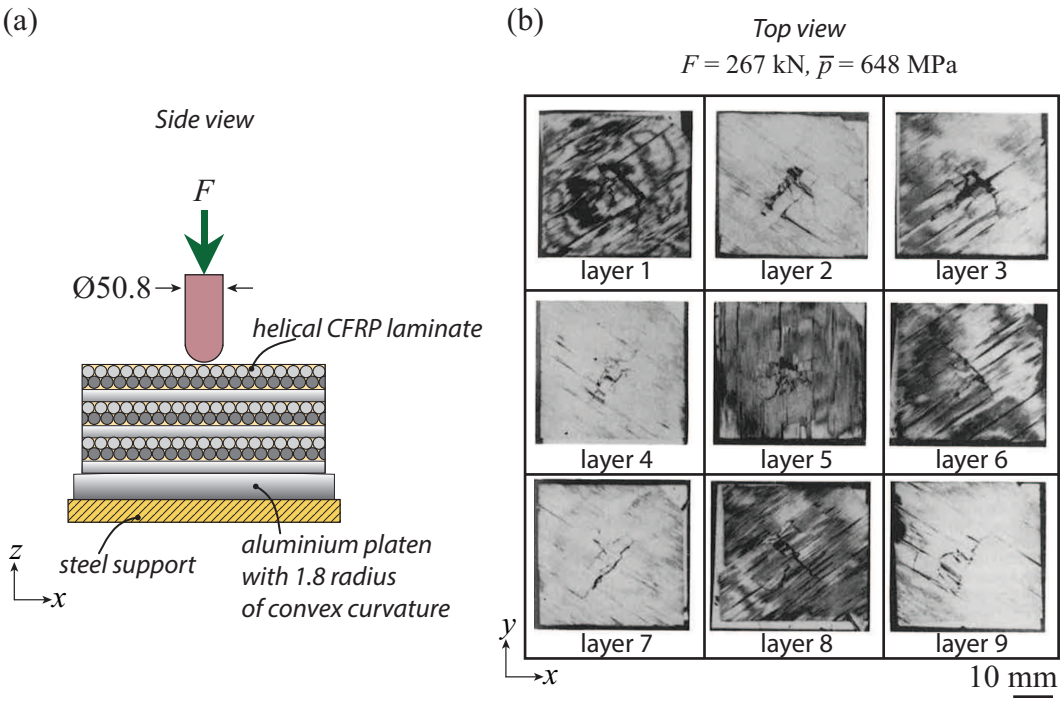

Figure 2.6: Summary of a) the indentation test set-up of a helical CFRP laminate using a hemispherical indenter (with a 25.4 mm radius) and b) the optical images of the top 9 plies after the laminate was indented to an average pressure $\bar{p} \sim 648$ MPa (associated with a force $F = 267$ kN). All dimensions in the schematic illustrations are in mm. Image adapted from Poe Jr. (1991).

2.2.3 Perforation Mechanisms in Quasi-static Punch Tests

In a ballistic test, the failure mode of a fibre composite varies depending on its bending stiffness and plate thickness. While the above back-supported indentation tests simulated the ballistic response of thick laminates, many researchers also focus on characterising the response of thinner composites for which back face deflection can affect the failure mode. To this end, they have conducted quasi-static punch tests on fibre composites where back face deflection is permitted. The indenters used in these experiments either had a flat bottom or had a hemispherical shape, as illustrated in the schematics of Figure 2.1c. In general, the perforation behaviour of structural composites, such as CFRP and GFRP, has been found to involve a form of the shear plugging mechanism. In contrast, the perforation behaviour of armour-grade composites, such as UHMWPE fibre composites, has been found to involve laminate slippage or membrane stretching.

2.2.3.1 Perforation Mechanism in Structural Composites

An early investigation given by Lee and Sun (1993) revealed that the load-displacement response of quasi-isotropic CFRP laminates (with a $[0°/90°/\pm 45°]_{2s}$ lay up and a thickness of ~ 2 mm) subjected to indentation by a flat punch (with a punch diameter $D_p = 14.5$ mm and a span diameter $D_s = 3D_p$) showed a 'double peak' shaped curve, see Figure 2.7a. The first peak load was associated with matrix shear crack formation at an angle of $\sim 45°$ and ply delamination (Liu et al., 1993), see Figure 2.7b. The matrix shear cracks were usually located beneath the edge of contact where the out-of-plane shear stress was at a maximum. A sequence of spikes followed this first peak and was associated with fibre fracture at the top face underneath the edge of contact, see Figure 2.7b. Finally, a secondary peak was observed, which marked the shear plug formation where the material underneath the indenter sheared out of the laminate and created a perforation. Similar results were also reported by Jørgensen (1994) and Zhou (1996) for a quasi-static punch test of CFRP cross-ply laminates and woven GFRP laminates with flat-bottom and hemispherical indenters, respectively.

A numerical study by Jørgensen and Horsewell (1997) further confirmed that

the matrix failure was caused by the local tensile stress generated by the out-of-plane shear deformation beneath the edge of contact. This type of failure mechanism is commonly referred to as shear plugging. It is worth noting that many researchers have also observed this shear plugging mechanism in the ballistic tests of structural composites such as CFRP and GFRP laminates. Since most research has been concerned with improving the impact resistance of these structural composites, more detailed characterisation of this shear plugging mode has been obtained through ballistic experiments. Therefore, a more detailed discussion on shear plugging will be given in the next section, which focuses on the ballistic failure mechanisms of fibre composites.

2.2.3.2 Perforation Mechanisms in Armour-grade Composites

Lee et al. (2001) conducted a quasi-static punch test on 5-ply-thick plain woven UHMWPE fibre based Specta® 900/polyurethane composite laminates using an indenter replicating a fragment-simulating projectile (see indenter dimensions in Figure 2.8a) under an edge-clamped boundary condition. They found that the woven armour-grade composites would slip out from the testing apparatus if the clamping force at the support was low (this slippage behaviour has not be reported in structural composites). When the clamping force exceeded a critical threshold, instead of slipping, the composite would deform by a stretching mode until fibre tensile rupture occurred, as illustrated in the schematic in Figure 2.8b. This type of perforation is commonly referred to as membrane stretching. Figure 2.8a shows the load-displacement response of a composite when the clamping force is sufficient to activate the membrane stretching mechanism. It is worth noting that a single peak load was observed in the punch response of the armour-grade composites (as opposed to the above-mentioned 'double peak' shaped curve for structural composites where shear plugging is the active mode). A recent study by Karthikeyan et al. (2013a) conducted a similar quasi-static stretch bend test on a different type of armour-grade composite (Dyneema®) in a cross-ply beam configuration using a cylindrical roller and under both bolted-end and wrapped-end conditions. The membrane stretching mechanism was also observed in these armour-grade cross-ply laminates.

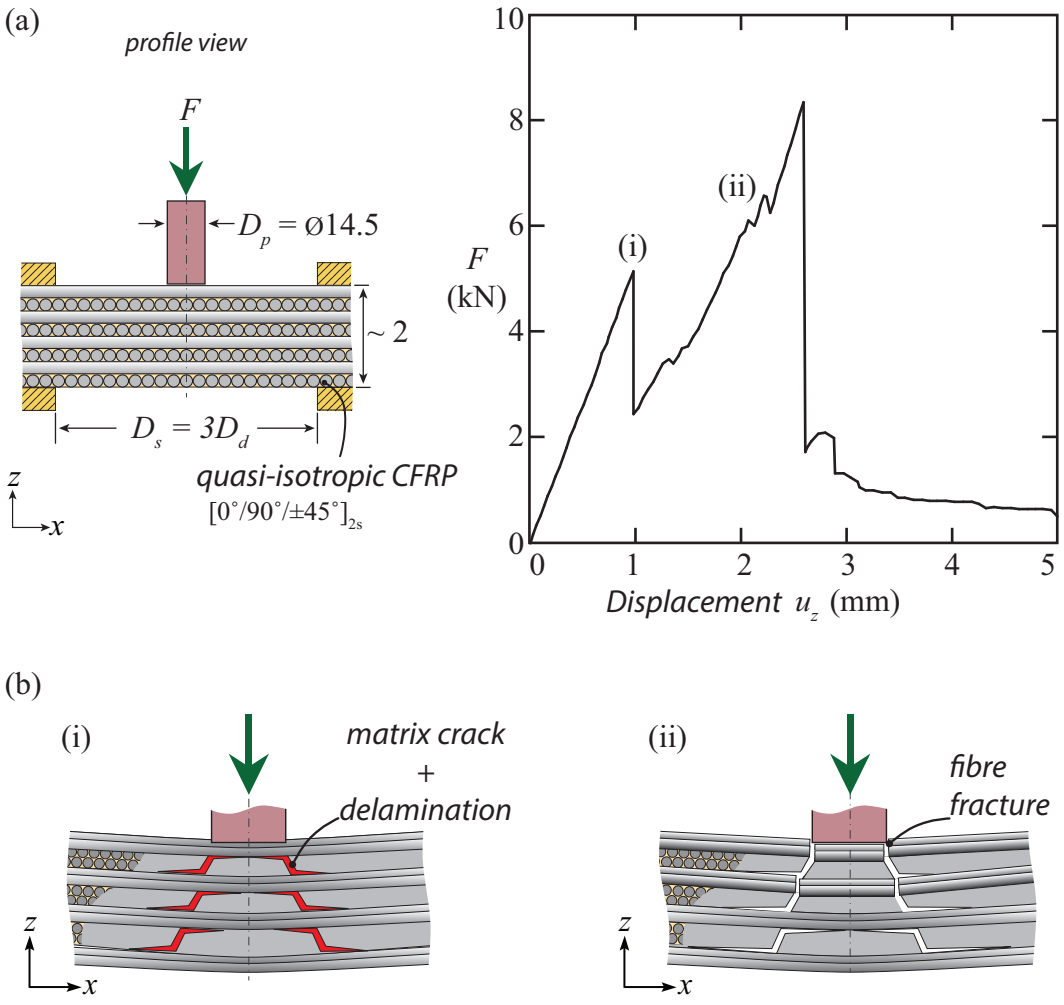

Figure 2.7: Summary of a) the quasi-static punch load-displacement response of a quasi-isotropic CFRP laminate (with a $[0°/90°/\pm 45°]_{2s}$ lay up and a thickness of ~ 2 mm) subjected to indentation by a flat punch (with a punch diameter D_p = 14.5 mm and a span diameter $D_s = 3D_p$) and b) the schematic illustrations of the onset of matrix shear crack formation and ply delamination at (i), as well as the fibre fracture at (ii) in the load-displacement curve. All dimensions in the schematic illustrations are in mm. Images adapted from Lee and Sun (1993).

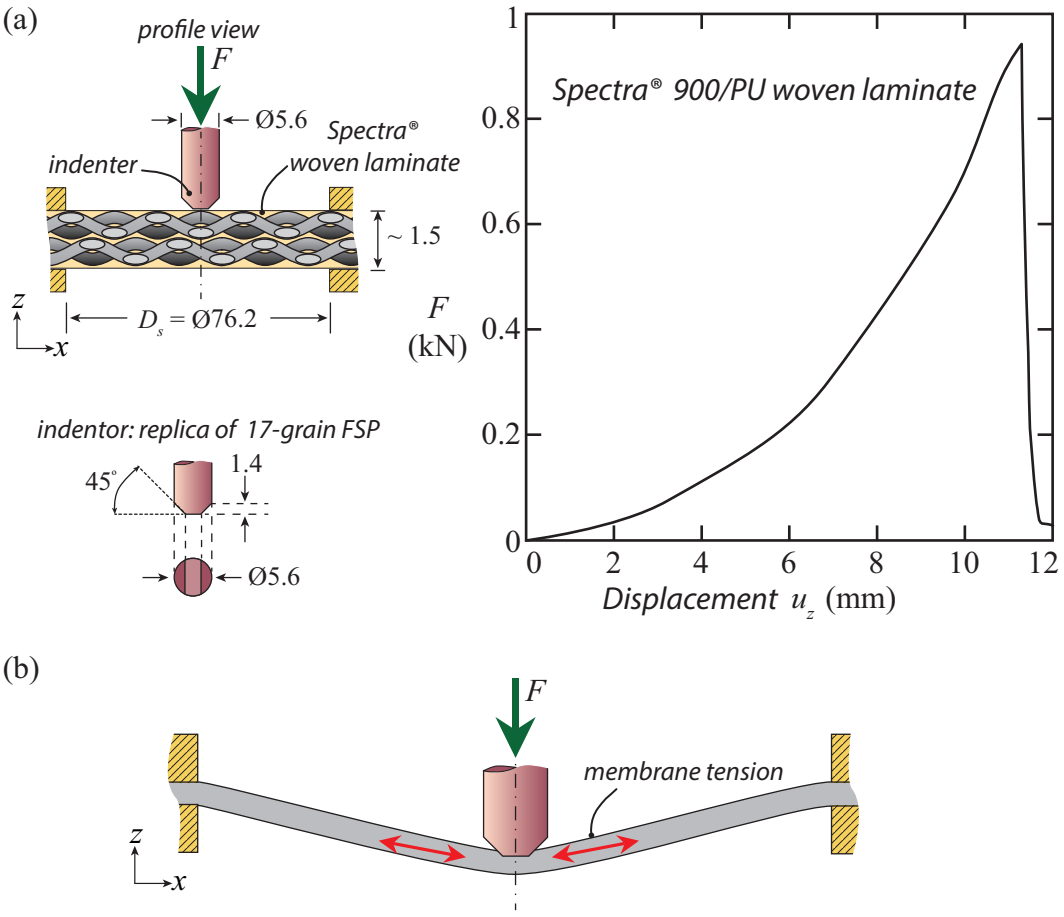

Figure 2.8: Summary of a) the quasi-static punch load-displacement response of a 5-ply-thick plain woven Specta® 900/polyurethane composite laminate (with a thickness of ~ 1.5 mm) perforated by an indenter replicating a 17-grain fragment-simulating projectile (FPS) and b) the schematic illustration of membrane tension in a laminate. All dimensions in the schematic illustrations are in mm. Images adapted from Lee et al. (2001).

2.3 Failure Mechanisms of Fibre Composites under Ballistic Loading

Under ballistic loading, the failure mechanisms of fibre composites can differ from their quasi-static behaviour due to wave propagation and the inertia of the composites after impact. This section provides a detailed literature review regarding the failure of fibre composites under ballistic loading. Richardson and Wisheart (1996) have provided a comprehensive review of the typical impact failure mechanisms in fibre composites subjected to low velocity impacts. This review focused primarily on structural composites consisting of carbon fibre or glass fibre reinforcements and high strength epoxy matrices. Structural composites are usually brittle upon impact and show evidence of damage/failure at relatively low impact velocities. The main contributing failure mechanism in structural composites is generally considered to be a form of the shear plugging mechanism.

Cheeseman and Bogetti (2003) provided a review of the impact performance of armour-grade composites (they also referred to these composites as compliant composites). Unlike traditional structural composites, armour-grade composites are usually composed of flexible fibres such as ultra high molecular weight polyethylene (UHMWPE) fibres (Spectra® and Dyneema®) and aramid fibres (Kevlar® and Twaron®). Armour-grade composites normally contain a $\sim$ 20% weight fraction of matrix material with low shear strength. These composites generally outperform structural composites under impact loading, and show signs of damage/failure only at intermediate to high velocities. Although early studies have proposed that the perforation of armour-grade composites is due to the shear failure of the fibre (Iremonger and Went, 1996; Scott, 1999), recent investigations by the Fleck and Deshpande group at the University of Cambridge revealed that the impact failure of armour-grade composites of various thicknesses is facilitated by fibre tensile failure (Attwood et al., 2014; Karthikeyan and Russell, 2014; O'Masta et al., 2015a). Their results, along with data from Cunniff (1992, 1999); Phoenix and Porwal (2003) indicate that armour-grade composites can fail in one of two mechanisms: membrane stretching or indirect tension. The following subsection will provide a classification of impact events based on impact velocity. The remainder of this section will provide a detailed review of the current understanding

and the latest research progress regarding the above-mentioned impact failure mechanisms in fibre composites: (i) shear plugging mechanism, (ii) membrane stretching mechanism, and (iii) indirect tension mechanism.

2.3.1 Classification of Impact Based on Impact Velocity

The impact velocity of the projectile v_0 will affect the magnitude of the stress waves that propagate through the composite target. At a high impact velocity, the magnitude of these stress waves may be sufficient to cause localised damage. At a lower impact velocity, the magnitude of these stress waves may be insufficient to cause damage, but failure could occur due to the deflection of the target. Consequently, for a given kinetic energy, the deformation and perforation mechanisms of a composite target impacted by a projectile will differ greatly depending on whether the projectile has low velocity and large mass (e.g. dropped tools) or high velocity and small mass (runway debris, small arms fire, etc.). It is also expected that the ballistic failure mechanism would be qualitatively similar to that in the quasi-static punch experiments at significantly low impact velocity but would deviate from quasi-static results as the impact velocity increases. As a result, impact tests are generally categorised into low and high velocity impacts.

There is currently no single definition of low versus high velocity that is generally accepted. For instance, Cantwell and Morton (1991) classified low velocity as $v_0 \leq 10$ m/s, whereas Abrate (1991) classified it as $v_0 \leq 100$ m/s. In a loose sense, low velocity impacts refer to events that can be treated as quasi-static or where boundary condition can affect the impact response of the target (Shivakumar et al., 1985; Sjoblom et al., 1988). In contrast, high velocity impacts refer to the impact responses that are dominated by stress wave propagation, in which boundary condition effects can be ignored. Robinson and Davies (1992) proposed a rule of thumb to determine transition from low velocity to high velocity. They defined a low-velocity impact as one in which the through-thickness stress wave plays no significant part in the stress distribution and determined that out-of-plane compressive strain $-\varepsilon_{zz}$ can be estimated from the impact velocity v_0 as $-\varepsilon_{zz} = v_0/c_T$. As the compressive stress wave is assumed to play no role in a low-velocity impact, the transition from low to high velocity can be characterised as the point at which

compressive strain results in failure. This transition point is therefore material dependent. Considering that the typical wave speed in the through thickness direction is approximately $c_T \sim 2000$ m/s for common epoxy composites and assuming that the out-of-plane compressive failure strain is $-\varepsilon_{zz} = 0.5$ - 1%, the transitional velocity can be estimated as ranging from 10 m/s to 20 m/s. Generally, the ballistic failure mechanism of shear plugging is reported in low velocity impacts, whereas mechanisms such as indirect tension and membrane stretching are reported in high velocity impacts.

2.3.2 Shear Plugging Mechanism

Structural composites such as carbon fibre reinforced plastic (CFRP) and glass fibre reinforced plastic (GFRP) that comprise a thermoset epoxy matrix normally show signs of damage at relatively low impact velocity ($v_0 < 30$ m/s) or at low impact energy ($W < 1$ J). Their failure events usually progress through three stages as impact velocity increases: (i) transverse matrix crack formation (also known as splits), (ii) delamination and micro crack formation, and (iii) fibre fracture and full penetration (Richardson and Wisheart, 1996). The combination of failure involving transverse matrix cracks and delamination are commonly referred to as barely visible impact damage (BVID), since both forms of damage are difficult to detect by the naked eye and can only be revealed by specimen sectioning, X-ray scanning, or ultra-sound scanning. At full penetration, this type of failure mechanism is usually referred to as shear plugging because the material underneath the projectile can shear out of the composite panel forming a plug. It is essential to fully characterise each of the above-mentioned stages and their interactions in order to understand the causes of shear plugging; the remainder of this section provides details on each of the stages.

2.3.2.1 Transverse Matrix Crack Formation

Takeda et al. (1982a) first identified the formation of transverse matrix cracks in glass fibre/epoxy cross-ply laminates when impacted by a rigid projectile in the out-of-plane direction. This type of matrix crack formation represents the first sign of damage and therefore the velocity at which matrix crack formation occurs can be considered as a damage threshold Choi et al. (1991a,b).

Figure 2.9a shows a schematic illustration of the transverse crack formation in a cross-ply laminate moments after impact by a spherical projectile. The matrix cracks typically arise in the *2-3* plane of a ply underneath the edge of the projectile and are inclined at $\sim 45°$ to the transverse plane (Boll et al., 1986; Joshi and Sun, 1985; Sjögren et al., 2001).

Takeda et al. (1981) also conducted a ballistic experiment to study wave propagation by embedding strain gauges in the composite target. Based on their data, Takeda et al. (1982a) proposed that the matrix crack formation resulted from the combined effects of in-plane tension and out-of-plane shear. A numerical study by Chang et al. (1990) reached a similar conclusion: the out-of-plane compressive strain σ_{33} is negligible and failure is therefore caused by a combination of tensile stress σ_{22} and shear stress σ_{23}, as illustrated in Figure 2.9a. Note that this type of matrix crack formation is similar to the failure mode observed in quasi-static punch tests and is understood to be caused by the through-thickness shear failure of the matrix (Jørgensen, 1994; Liu et al., 1993).

2.3.2.2 Delamination and Micro Crack Formation

Choi and Chang (1992); Choi et al. (1991a,b) have conducted in-depth investigations in the formation sequence of the matrix cracks and delamination. They found that if the aforementioned matrix cracks reach the interface between plies with different fibre orientations (referred to as critical matrix cracks), interply delamination would initiate from these cracks. They observed that two delamination cracks can form out of a single matrix crack and propagate along the ply-ply interface: the delamination along the upper interface of the 90° ply would propagate toward the centre line of the projectile, while the one located at the bottom interface would grow away from the projectile and toward the end support of the composite target, as illustrated in Figure 2.9b. Takeda et al. (1982b) observed similar behaviour, although they found that delaminations do not always propagate precisely along the interface, but can run slightly to either side. Finally, the finite element analyses given by Hou et al. (2001, 2000) also reached similar conclusions. Furthermore, they found that the delaminations propagating toward the centre line of the projectile were less severe than those propagating away from the projectile. They argued that the propagation of the delaminations beneath

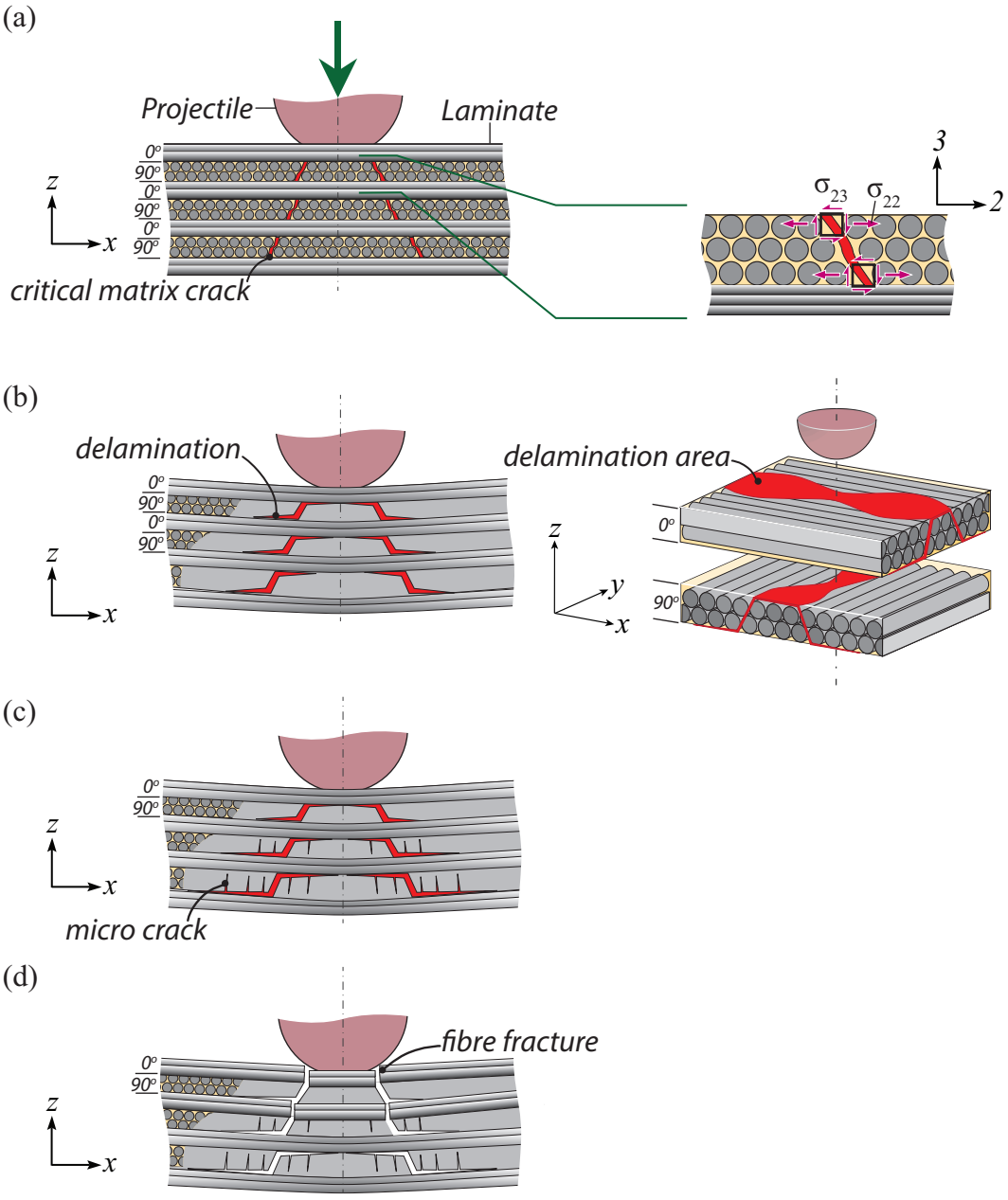

Figure 2.9: Schematic illustrations of the damage sequence in the shear plugging mechanism of a cross-ply composite laminate impacted by a spherical projectile. a) An illustration of the matrix crack formation caused by a combination of tensile stress σ_{22} and shear stress σ_{23}, adapted from Chang et al. (1990). b) An illustration of the propagation of delamination cracks and the observed peanut-shaped delamination area, adapted from Liu (1988); Liu and Malvern (1987). c) An illustration of the formation of micro cracks, adapted from Choi et al. (1991a,b). d) An illustration of the fibre fracture underneath the edge of contact, adapted from Cantwell and Morton (1989a,b, 1990); Shyr and Pan (2003).

the projectile were suppressed due to the out-of-plane compressive pressure, offering a crack-closure effect.

Liu (1988); Liu and Malvern (1987) revealed that the delamination area along the ply-ply interface closely resembles a peanut shape for cross-ply laminates. The major axis of this peanut shaped delamination area is oriented in the direction of fibres in the ply beneath the interface, as illustrated in Figure 2.9b. This feature of the delamination area was also widely reported by multiple researchers through X-ray CT-scan experiments (Chang et al., 1990; Choi and Chang, 1992; Guild et al., 1993; Joshi and Sun, 1985; Wu and Shyu, 1993; Wu and Springer, 1988). Furthermore, Liu proposed that delamination is a result of the anisotropic bending stiffness in each ply (where the bending stiffness is significantly higher in the fibre direction than in the direction transverse to the fibre) and the bending stiffness mismatch between adjacent plies. He observed that, under deflection, each ply would bend concave locally along the fibre direction and convex in the direction transverse to the fibres, and developed analysis that predicted the peanut shaped delamination area of the cross-ply laminates.

In addition to the delamination, Choi et al. (1991a,b) observed that multiple matrix cracks (referred to as micro cracks) may also form at higher impact velocities. Similar observations were reported by Liu and Malvern (1987); Wu and Springer (1988). These micro cracks form in the area near the back face of the laminate, as illustrated in Figure 2.9c. In contrast to the inclined critical matrix cracks that instigate delamination, these micro cracks are generally much finer and mostly oriented vertically. The formation of these micro cracks is due to tensile straining caused either by longitudinal tensile wave propagation or global deflection of the composite plate.

2.3.2.3 Fibre Fracture and Full Penetration

As the impact velocity or the impact energy increases further, the matrix crack formation and delamination is followed by fibre fracture. At this stage, failure progresses with more fibres rupturing as the impact velocity/energy increases, eventually leading to full penetration. Investigations by Cantwell and Morton (1989a,b, 1990); Cristescu et al. (1975); Zhou (1995) showed that when GFRP and CFRP laminates are impacted by a blunt impactor, fibres would first fracture at the top face underneath the edge of contact and the fractures

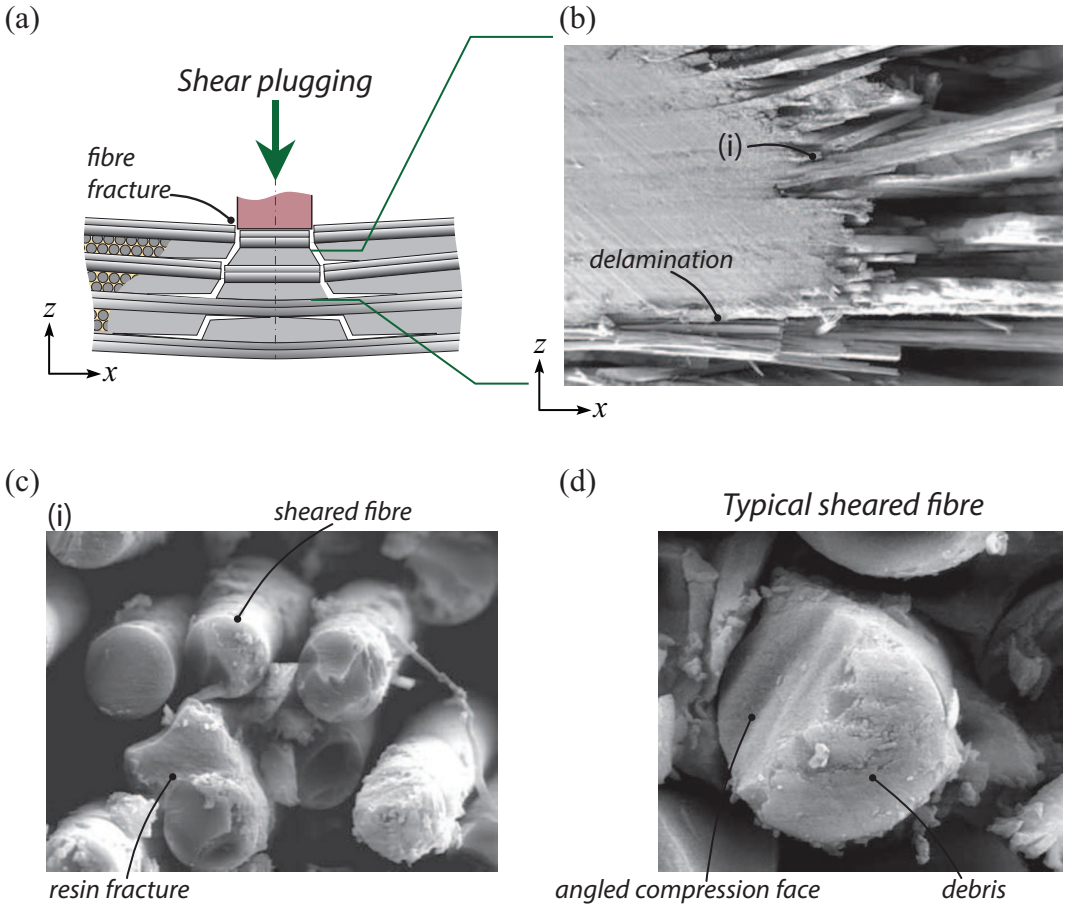

Figure 2.10: Summary of the SEM fractography analysis given by Greenhalgh (2009) on shear plugging. a) Schematic illustration of shear plugging. b) Failure profile view of shear plugging. c) Fracture surfaces of the fibres in the shear plugging mechanism. d) A typical fracture surface of a carbon fibre that failed by shear deformation.

would propagate to connect with the above-mentioned 'critical matrix cracks', as illustrated in Figure 2.9d. As the impact velocity/energy increases, these cracks would propagate further from the top face toward the back face in the area underneath the edge of the projectile. A SEM fractography analysis given by Greenhalgh (2009) suggested that the fracture of these fibres was due to shear deformation. In brief, Greenhalgh (2009) showed that the fracture surface of a carbon fibre failing by shear plugging (see Figures 2.10b and 2.10c) often exhibits an angled compression face that is remarkably similar to the fracture surface of a sheared carbon fibre (see Figure 2.10c).

Cantwell and Morton (1989a,b, 1990) identified that, at full penetration, the projectile would generally remove a conical-shaped shear plug from the composite target. An investigation by Shyr and Pan (2003) in which GFRP

laminates were impacted by a spherical projectile resulted in similar findings, with the additional observation that fibre tensile breakage may also occur near the back face due to beam deflection at full penetration.

Lee and Sun (1993) recognised that this shear plugging mechanism resembles the failure in the quasi-static punch test of the composite laminates. Consequently, they conducted a numerical simulation to predict the threshold of damage initiation and propagation in CFRP laminates punched through by a cylindrical indenter. They accurately predicted the threshold force that causes matrix failure using a maximum principle stress failure criterion in the *2-3* plane of a 90° ply, and predicted the shear plugging force based on the total strain energy release rate (defined as the sum of the mode I (G_I) and mode II (G_{II}) strain energy release rates). While the above studies represent a fundamental approach to determining the energy and force required to form a shear plug, modern methods of predicting penetration velocity v_p typically take a simplified approach by prescribing the shear plugging energy based on quasi-static punch tests Gama and Gillespie Jr. (2008, 2011); Mines et al. (1999).

2.3.3 Membrane Stretching Mechanism

The impact failure mechanism of thin armour-grade composites (i.e. composite laminates typically with low bending stiffness and panel thickness H less than 1 mm) usually fail by a membrane stretching mechanism. Notable insights were offered by Cunniff (1992, 1999); Lim et al. (2003, 2002). In brief, after a projectile has impacted a composite target, a longitudinal tensile wave would propagate at a speed $c_L \sim \sqrt{E_L/\rho}$ (where E_L is the in-plane modulus and ρ is the density of the target) from the impact area toward the end support. Regions ahead of this longitudinal wave front are essentially at rest, but regions behind the wave front are under longitudinal tensile strain ε_L, which can lead to fibre tensile failure. For thin laminates with low bending stiffness, a reverse pyramid can form below the projectile. The shear hinge of this reverse pyramid would then propagate in the same direction as the tensile wave but at a lower speed c_H, see Figure 2.11a.

Cunniff (1992, 1999) realised the importance of the material's tensile wave speed $c_L \sim \sqrt{E_L/\rho}$ and proposed that the penetration velocity v_p is correlated with the material properties of the composites through a parameter c^* with

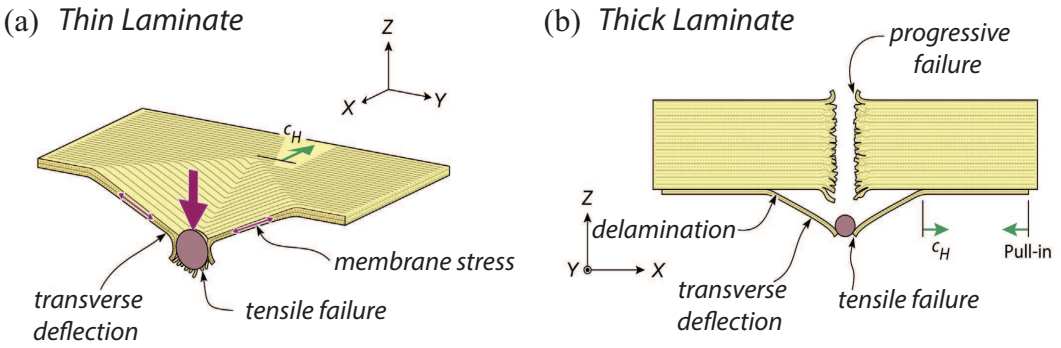

Figure 2.11: Schematic illustrations of membrane stretching mechanism in a) a thin composite laminate and b) the distal region of a thick composite laminate due to delamination. Images were taken from O'Masta et al. (2015a).

units of m/s. c^* is expressed as:

$$c^* = \left(\frac{\sigma_L \varepsilon_L}{2\rho} \sqrt{\frac{E_L}{\rho}} \right)^{1/3} \tag{2.1}$$

where σ_L is the longitudinal tensile strength, E_L is the longitudinal tensile modulus, ε_L is the longitudinal tensile failure strain, and ρ is the density (of the fibre or the laminates). Through experimental work and dimensional analysis, Cunniff found that the penetration velocities v_p of various woven composites with different plate thicknesses can be presented as a single trend when plotting the ratio of v_p/c^* as a function of $\rho_A A_p/m_p$ (where ρ_A is areal density of the target, A_p is the presented area of the projectile, and m_p is the projectile mass). Phoenix and Porwal (2003) then developed an analytical model assuming that (i) the tensile stress is uniform across the thickness of the composite, (ii) both the shear stress and hoop stress of the composite can be ignored for thin laminates, and (iii) ballistic perforation is governed by ply tensile failure. They were able to predict the penetration velocities v_p of various woven composites by calculating the longitudinal tensile wave induced strain and accounting for the momentum transfer between the projectile and the above-mentioned reverse pyramid. Their predictions were in good agreement with the data given by Cunniff (1992, 1999).

Although only thin laminates have been reported to exhibit full penetration through the membrane stretching mechanism, recent studies have shown that laminates with higher thickness often also show membrane stretching in last few plies near the back face for an impact velocity just below v_p (Karthikeyan

and Russell, 2014; O'Masta et al., 2015a). Karthikeyan and Russell (2014) proposed that membrane stretching in the distal region of a thicker laminate can be driven by delamination, see Figure 2.11b. Delamination often occurs in multi-ply laminates during ballistic events. For instance, Liu and Malvern (1987) proposed that delamination can take place as a result of the bending stiffness mismatch between adjacent plies. Iremonger and Went (1996) postulated that delamination could occur due to the following process: projectile impact gives rise to a compressive stress wave that propagates through the thickness of the laminate and reflects off the back face as a tensile wave, which triggers delamination. Karthikeyan and Russell (2014) estimated that the distal region of a thicker laminate can dissipate ~ 6.5 times more kinetic energy through membrane stretching than the rest of the material in the fibre composite panel.

2.3.4 Indirect Tension Mechanism

Recent investigations by Attwood et al. (2016); Karthikeyan and Russell (2014); O'Masta et al. (2015a) have revealed that UHMWPE fibre based Dyneema® cross-ply laminates with plate thickness of $H \geq 4$ mm fail by a local indentation-type mechanism involving the in-plane tensile failure of plies, see Figure 2.12a. This failure mechanism was first identified by Attwood et al. (2014) and referred to as indirect tension. Unlike the membrane stretching mode that was analysed by Phoenix and Porwal (2003) (i.e. ply tensile stress caused by the propagation of longitudinal tensile wave), the indirect tension mechanism is caused by the out-of-plane compressive straining of the cross-ply laminates.

Attwood et al. (2014) investigated the out-of-plane uniaxial compression of Dyneema® cross-ply composites under quasi-static loading. They found that fibre tensile stress can arise in cross-ply laminates under out-of-plane compressive loading due to (i) the anisotropy in Poisson expansion within the plane of each ply and (ii) a $0°/90°$ stacking of plies, as illustrated in Figure 2.12b. Under ballistic loading, a contact pressure is generated and can lead to indirect tension failure (analogous to how indirect tension arises as a result of quasi-static out-of-plane compression). Attwood et al. (2014) also found that the transverse compression strength of Dyneema® cross-ply laminates scales with the tensile strength of the fibres, and they demonstrated the existence

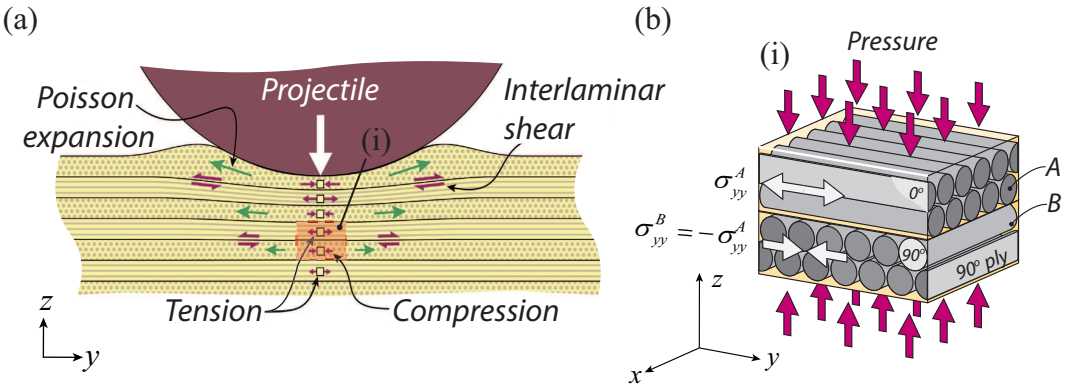

Figure 2.12: Schematic illustration of the indirect tension mechanism in a) a cross-ply laminate impacted by a spherical projectile (O'Masta et al., 2015a), and b) a close up illustration of region (i) where a pair of 0°/90° plies is under out-of-plane compression.

of the zone of shear lag around the periphery of the specimen. The combined studies of Attwood et al. (2014); Karthikeyan et al. (2013b) reveal that the ballistic resistance of Dyneema® cross-ply composites scales with the in-plane tensile strength. This has led DSM Dyneema, NL to develop a new range of Dyneema® composites with ultra-high tensile strength for ballistic applications such as SK99-t laminates, (Attwood, 2015).

2.3.5 Summary of Ballistic Perforation Mechanisms

In brief, structural composites such as CFRP and GFRP with epoxy matrices normally fail by a shear plugging mechanism and are usually brittle under impact loading, while armour-grade composites that consist of aramid fibres or UHMWPE fibres usually demonstrate better impact performance and fail by either membrane stretching or indirect tension (depending on the laminate thickness). For instance, when a 8.3×10^{-3} kg projectile impacts a 4 mm target, CFRP laminates are penetrated at $v_p \sim 100$ m/s and $W \sim 40$ J, whereas Dyneema® laminates are penetrated at $v_p \sim 500$ m/s and $W \sim 1000$ J (Karthikeyan et al., 2013b).

2.4 The Role of Fibre, Matrix, and Lamination on the Impact Resistance of Composite Laminates

Despite intensive research on the impact performance of various composites and their corresponding impact failure mechanisms, there is comparatively less knowledge of the governing parameters that cause a composite laminate to fail by one mechanism instead of another. Nevertheless, some insight can be gained by reviewing the current literature regarding which constituents of a composite laminate can influence its impact resistance. This section discusses the influence of fibre and matrix on the impact resistance of composite laminates, as well as the protective effect of hybridising structural composites with either armour-grade composites or metal layers. Other aspects such as the effects of stitching, z-pinning, weaving, and the usage of shear thickening fluids are also interesting, but are beyond the scope of this thesis. The reader may refer to reviews by Dransfield et al. (1994); Mouritz (2007); Srivastava et al. (2012); Tabiei and Nilakantan (2008) on these topics.

2.4.1 The Role of Fibre

Fibre reinforcements are the main load bearing components in composite laminates. They are therefore critical to the energy dissipation ability of the composites, particularly if fibre tensile failure is observed in the perforation stage of an impact event. The analysis from Cunniff (1992, 1999); Phoenix and Porwal (2003) showed that, if the laminate fails by a membrane stretching mechanism, the impact penetration velocity would increase monotonically with the so called Cunniff's velocity c^*. c^* can be viewed as the product of the specific tensile energy absorption $S_L^+\varepsilon_L^+/(2\rho)$ and the longitudinal tensile wave speed $c_L \sim \sqrt{E_L^+/\rho}$ of the fibre or the laminates, and it can be expressed as:

$$c^* = \left(\frac{S_L^+ \varepsilon_L^+}{2\rho} \sqrt{\frac{E_L^+}{\rho}} \right)^{1/3} \tag{2.2}$$

where S_L^+ is the longitudinal tensile strength, E_L^+ is the longitudinal tensile modulus, ε_L^+ is the longitudinal tensile failure strain, and ρ is the density

(of the fibre or the laminate). Figure 2.13 compares the range of c^* for various modern composite fibres and presents these data as a material properties chart. The fibre properties of the four commonly used fibres (glass fibres, carbon fibres, Kelvar® fibres, and Dyneema® fibres) are summarised in Table 2.1, data taken from Attwood et al. (2015); O'Masta (2014); Oya and Hamada (1998); Shinohara et al. (1993); Singletary (2000); Singletary et al. (2000). Both Figure 2.13 and Table 2.1 reveal that ultra-high molecular weight polyethylene (UHMWPE) Dyneema® fibres have the highest range of c^* among the four composite fibres. Many researchers have claimed that this is the primary reason for the high impact resistance of Dyneema® composites. While this explanation is sound, it should be noted that the ranges of c^* for glass fibres, carbon fibres, and Kevlar® fibres are all comparable, yet glass fibre and Kevlar® composites normally outperform carbon fibre composites.

Other researchers have claimed that composites made of fibres with higher axial tensile failure strain ε_L^+ would outperform other composites in an impact event (Beaumont et al., 1975; Enfedaque et al., 2010; Goldsmith et al., 1995; González et al., 2014). Note that Table 2.1 shows that the tensile failure strains ε_L^+ of aramid and UHMWPE fibres are about 2 to 3 times higher than that of carbon fibres ($\sim 3\%$ versus $\sim 1\%$).

The high ductility of aramid and UHMWPE fibres is closely related to the their microstructure in the sub-fibre level. Figure 2.14 compares the fibre microstructure of an UHMWPE fibre and a carbon fibre. UHMWPE fibres are made of highly crystallised chains of polyethylene (PE) molecules. Within the PE molecules, atoms are bonded by strong carbon-carbon covalent bonds. These long chains of PE molecules are then arranged into micro fibrils and macro fibrils parallel to the fibre axis (as illustrated in Figure 2.14a), with the fibrils bonded by a weaker van der Waals force (Kavesh and Prevorsek, 1995). In a tensile test, these micro fibrils and macro fibrils can be pulled-out from the fibre (while still bearing loads through shear lag), allowing the fibre to fail in a ductile manner with a large amount of local drawing and thus extending the axial tensile failure strain, see the SEM image in Figure 2.14a. In contrast, carbon fibres do not contain fibril microstructure. Instead, they are made of layers of graphene carbon atoms with strong carbon-carbon covalent bonds, which are stacked into a so called 'turbostratic graphite' structure. Each of these graphene sheets folds randomly on a cross section of the fibre but are mostly parallel to the fibre axis, as illustrated in Figure 2.14b.

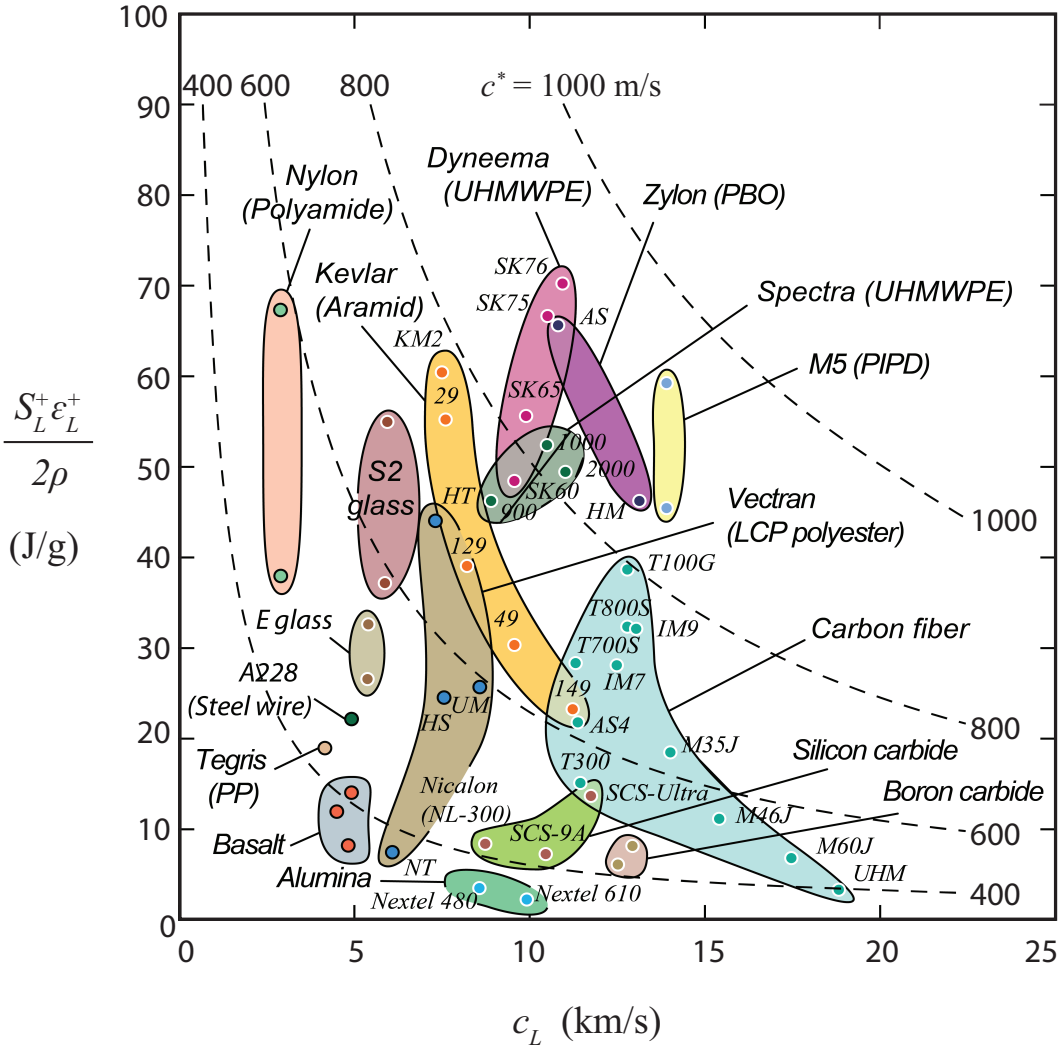

Figure 2.13: A material properties chart comparing the specific toughness and longitudinal wave speed of different composite fibres. Contours of the Cunniff velocity c^* are also plotted. Image adapted from O'Masta et al. (2015a).

Table 2.1: Summary of the mechanical properties of some common composite fibres.

		Glass fibre	Carbon fibre	Aramid (Kevlar®)	UHMWPE (Dyneema®)
Density [a]	ρ (Mg/m^3)	2.5	1.8 - 1.9	1.4 - 1.5	0.97
Axial tensile modulus [a]	E_L^+ (GPa)	69 - 87	231 - 436	71	89 - 116
Axial tensile strength [a]	S_L^+ (GPa)	3.4 - 4.8	4.4 - 6.4	2.9	2.7 - 3.6
Axial tensile failure strain [a]	ε_L^+ (%)	4 - 5.7	1.5 - 2.2	3.6	3.5 - 3.8
Axial compressive strength	S_L^- (GPa)	$\sim$ 1.5 [b]	$\sim$ 2.5 [c]	$\sim$ 0.26 [d]	$\sim$ 0.3 [e]
Transverse compressive Strength	S_T^- (GPa)	N/A	$\sim$ 0.6 [c]	$\sim$ 0.15 [d]	N/A
Cunniff's velocity [a]	c^* (m/s)	525 - 689	491 - 788	487 - 776	776 - 917

[a] Taken from O'Masta (2014)
[b] Taken from Oya and Hamada (1998)
[c] Taken from Shinohara et al. (1993)
[d] Taken from Singletary (2000); Singletary et al. (2000)
[e] Taken from Attwood et al. (2015)

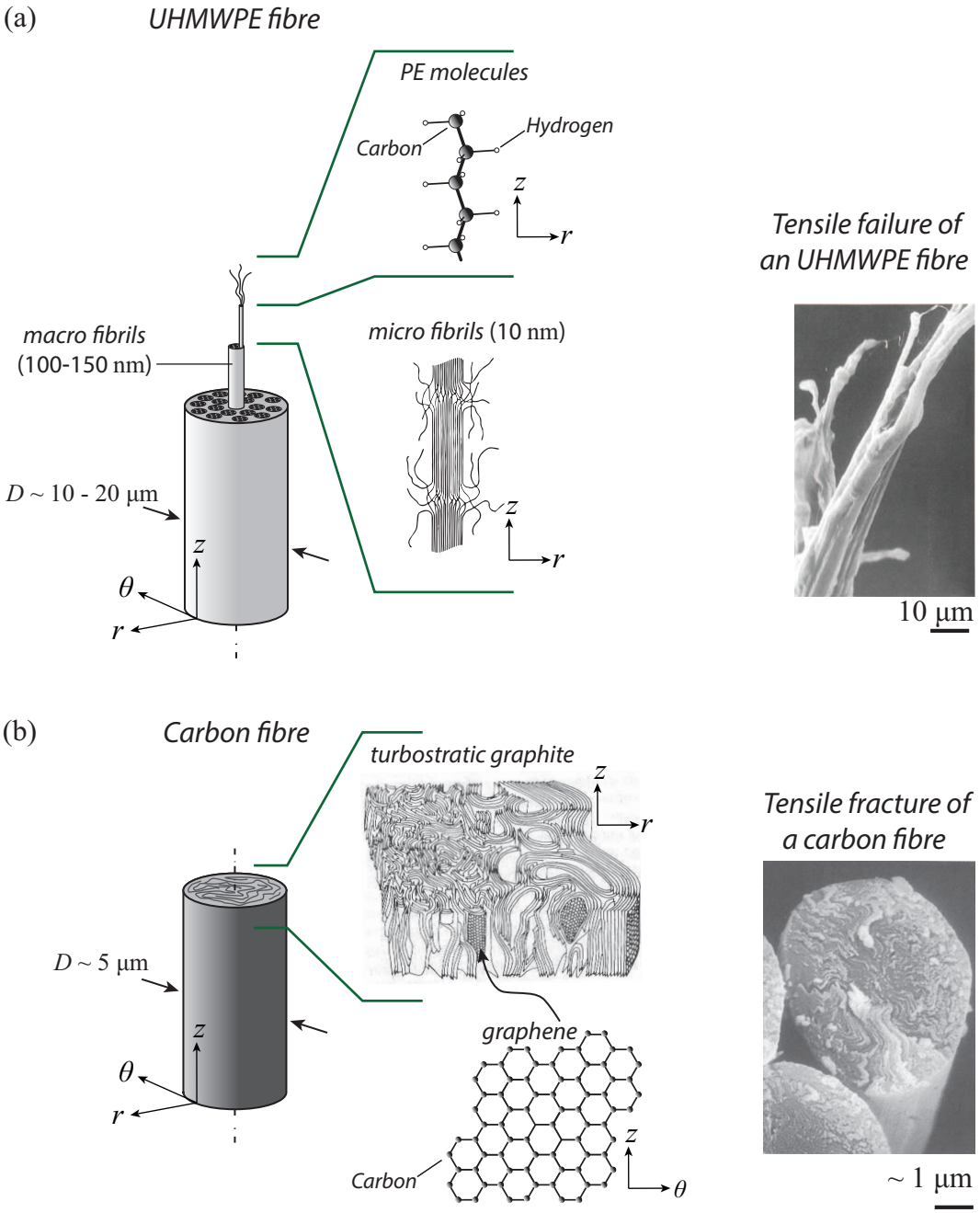

Figure 2.14: Schematic illustrations and SEM images of a) the microstructure of an UHMWPE fibre and its tensile failure morphology, and b) the microstructure of a carbon fibre and its tensile fracture surface. Images adapted from Hull (1981); Kavesh and Prevorsek (1995); Silverstein and Breuer (1993).

In a tensile test, carbon fibres fail in a brittle manner with negligible plastic deformation and a reduction of the cross-sectional area. While the above analysis provides some valuable insight on the relative energy dissipation abilities of various fibres, it assumes that fibre tensile failure is the dominant failure mode (i.e. failure due to membrane stretching or indirect tension). However, the analysis would not be applicable when fibres fail by shear, for instance in the shear plugging mode that is often observed for CFRP composites (e.g. by Cantwell and Morton (1990); Greenhalgh (2009)).

2.4.2 The Role of Matrix

Compared to the extensive research on composite fibres, less attention has been paid to understanding the role of matrix materials. An early investigation conducted by Williams and Rhodes (1982) compared the damage in 24 different CFRP laminates impacted by a spherical projectile at the same impact velocity, all with the same laminate thickness but with different thermoset epoxy matrices. They found that the delamination area in the laminates can be reduced by increasing the ductility of the matrix (represented by the tensile failure strain of the neat resin). A similar result was obtained by Hirschbuehler (1987), who found that the impact tolerance of CFRP composites (represented by the post-impact compressive strength) increases with matrix ductility (represented by the flexural failure strain). Unfortunately, these pioneering researchers mainly focused on improving the post-impact strength in structural composites and did not investigate the effect of matrix properties on penetration resistance.

Later studies have suggested that matrix properties play a role in determining the penetration resistance of composites. Hsieh et al. (1990) compared the penetration resistance of various fibre composites with matrices of unmodified epoxy versus toughened epoxy, for laminates made of carbon, Spectra®, and Kevlar® fibres. The laminates with toughened epoxy showed higher penetration resistance. This improvement was more pronounced for the CFRP laminates than the Spectra® and Kevlar® laminates.

Lee et al. (2001) compared the ballistic resistance of thin Spectra® laminates (with a thickness of $\sim$ 1.5 mm) between those constructed from (i) only dry fibres, (ii) fibres with a soft polyurethane matrix, and (iii) fibres with a stiffer vinylester matrix. The penetration velocity v_p increases in the following order:

dry fibres, laminates with polyurethane matrix, and laminates with vinylester matrix. Lee et al. (2001) proposed that a stiffer matrix can reduce the yarn mobility and allow more fibres to engage the projectile, thus increasing the overall impact energy dissipation. They cautioned that the opposite effect may be observed in thicker laminates since the increase in matrix stiffness may promote localised Hertzian failure along the periphery of the projectile.

Walker (2001) conducted a similar study by comparing the penetration resistance of Kevlar® laminates made of (i) only dry fibres and (ii) fibres with a polyvinyl butyral phenolic matrix. However, he obtained a contradictory result. Compared to the laminates with the matrix, the dry fibres showed a higher penetration velocity in the thin laminates, but a lower one in the thick laminates. He argued that, for thin laminates, increasing the resin content resulted in fewer fibres available for impact energy dissipation. Whereas for thick laminates, the increase in resin content improved the bending stiffness of the laminates and thus their resistance to perforation deformation.

Furthermore, de Ruijter et al. (2010) carried out an investigation of the effect of matrix modulus on the impact penetration velocity of woven armour-grade Twaron® composites. They found that, for a 10-ply-thick woven laminate ($\sim$ 3 mm thick), the penetration velocity v_p first rises as the matrix modulus increases from 10^{-4} GPa to 0.01 GPa, then remains constant at a maximum level while modulus ranges from 0.01 GPa to 1 GPa, and finally declines as modulus increases from 1 GPa to 10 GPa, as represented in Figure 2.15. They proposed that the observed changes in penetration resistance are related to the friction coefficient among the fibres. For low levels of matrix modulus (i.e. 10^{-4} to 0.01 GPa), the ballistic performance improves substantially due to increasing friction among the fibres. For intermediate levels of modulus (i.e. 0.01 GPa to 1 GPa), the impact performance is insensitive to the friction coefficient. However, for high levels of modulus (i.e. 1 GPa to 10 GPa), the increase in friction among the fibres may bring about a reduction in fibre mobility that can produce premature fibre breakage and localised damage. Unfortunately, the study did not investigate the failure mechanism(s) of the laminates and the above propositions have not yet been confirmed.

Karthikeyan et al. (2013b) recently conducted an investigation that focused on the effect of matrix shear strength on both the ballistic perforation mechanism and the penetration resistance of fibre composites. They demonstrated that a

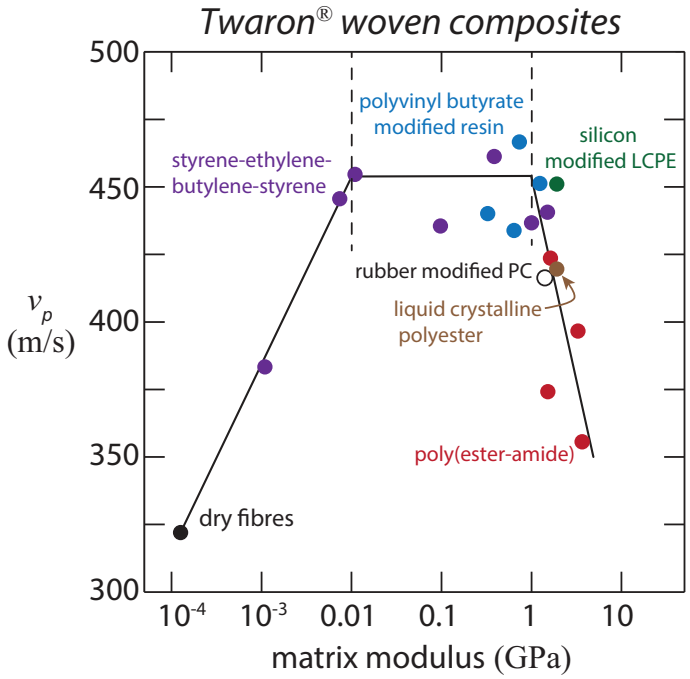

Figure 2.15: The measured ballistic penetration velocity v_p as a function of the matrix modulus for 10-ply-thick woven Twaron® fibre composites. Image adapted from de Ruijter et al. (2010).

reduction in matrix shear strength can improve the ballistic resistance of both Dyneema® and CFRP cross-ply laminates. In particular, they tested CFRP cross-ply plates of as-received uncured prepregs and autoclaved fully cured laminates, and found that the penetration velocity of a 4 mm thick CFRP cross-ply plate impacted by a 8.3×10^{-3} kg spherical projectile (as illustrated in Figure 2.16a) can be improved from 100 m/s to 300 m/s by reducing the matrix shear strength from 100 MPa to 0.1 MPa, see Figure 2.16b. Through X-ray computed tomography (CT scan), they observed that the cured CFRP laminates with a high shear strength matrix failed by a brittle cone-crack mode that resembles Hertzian failure and shear plugging failure, see Figure 2.16d. In contrast, the uncured prepregs behaved similarly to the Dyneema® composites and failed by a progressive perforation (i.e. number of failed plies increases with impact velocity) that involved the tensile failure of the fibres, see Figure 2.16c.

Overall, most of the above literature reveals that laminates with a matrix having low shear strength, low modulus, and high ductility offer superior ballistic resistance (e.g. thermoplastic PEEK versus thermoset epoxy matrix).

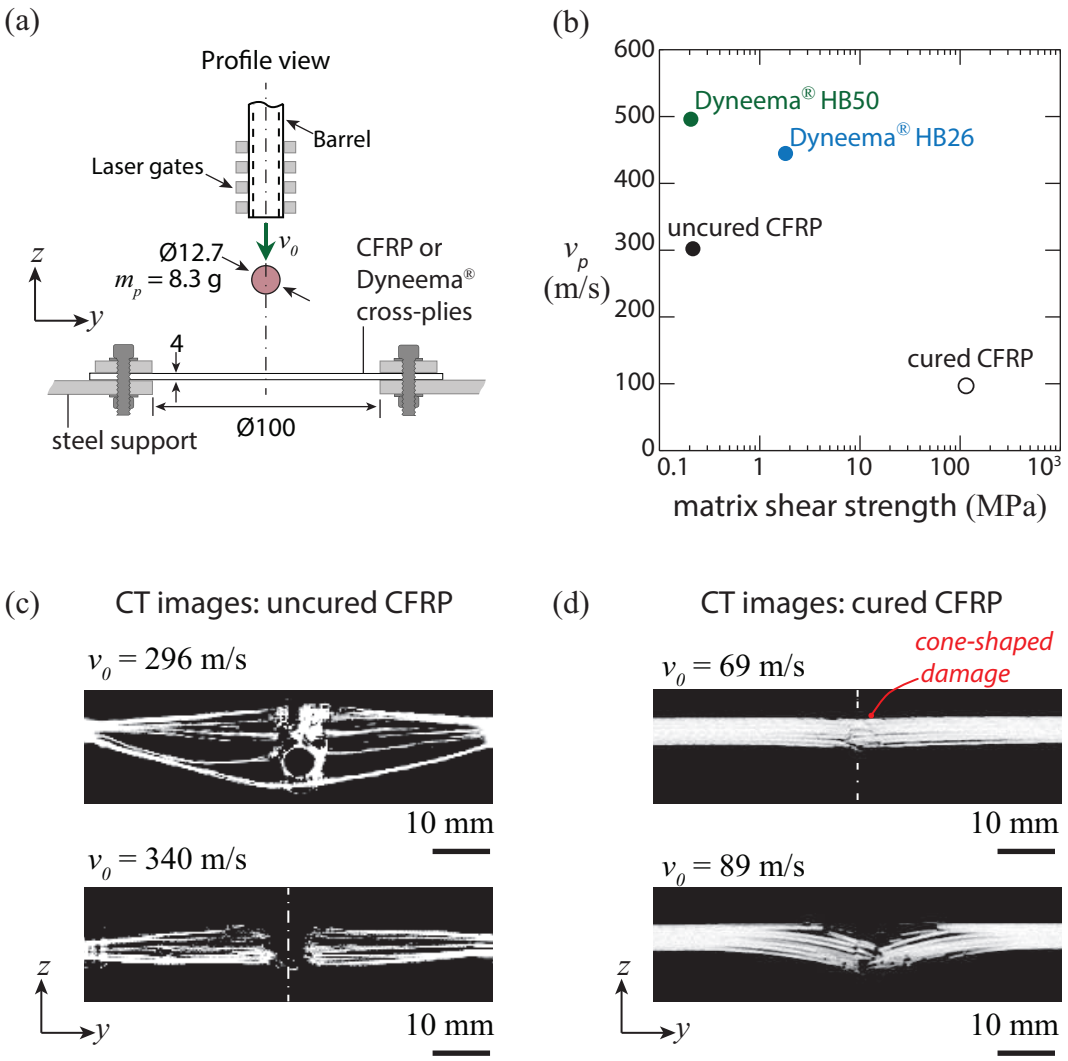

Figure 2.16: Summary of a ballistic experiment that demonstrated the effect of the matrix shear strength of composite laminates on their penetration velocity v_p. a) An illustration of the profile view of the ballistic test for a 4 mm thick composite plate; all dimensions are in mm. b) The measured ballistic penetration velocity v_p as a function of the matrix shear strength in CFRP and Dyneema® cross-ply laminates. CT scan images of c) uncured and d) cured CFRP cross-ply laminates tested at various impact velocities v_0. Images adapted from Karthikeyan et al. (2013b).

Although fibre failure is presumed to be responsible for the energy absorption during penetration, the matrix may have an indirect effect by constraining the mobility of the fibres and provoking a change in failure mechanism (Karthikeyan et al., 2013b; Lee et al., 2001). However, the precise effect of matrix properties on the prevailing failure mechanism is not understood. The results from Karthikeyan et al. (2013b) in particular motivated the current thesis to explore the following topics in Chapter 5: (i) to characterise the failure mechanism(s) of CFRP laminates as matrix shear strength decreases, (ii) to determine whether the newly characterised indirect tension mechanism can be activated in CFRP, and (iii) to assess the potential of creating structural composites with relatively high impact resistance.

2.4.3 Hybridisation with Different Fibres

As discussed in Section 2.4.1, for laminates with a given matrix material, composite fibres that have higher elongation to failure (i.e. glass fibres, aramid-based Kevlar® fibres, and UHMWPE-based Dyneema® fibres) show better impact performance than the less ductile carbon fibres. The drawback of these fibres with higher elongation to failure (referred to as HE fibres) is that they have lower in-plane compressive strength compared to their low elongation to failure counterparts (referred to as LE fibres). Consequently, multiple researchers since the 1970s have attempted to improve upon the impact resistance of composites with LE fibres or to enhance the in-plane compressive strength of composites with HE fibres, by combining them into 'fibre hybrid composites' (Beaumont et al., 1975; Harris and Bunsell, 1975; Mallick and Broutman, 1977; Perry and Adams, 1975). Swolfs et al. (2014) have provided a detailed review of the mechanical performance of fibre hybrid composites under quasi-static, fatigue, and ballistic loading. The following section focuses on the impact resistance of fibre hybrid composites.

Fibre hybrid composites comprise of at least two types of fibres bonded within a single matrix material (usually epoxy matrix). They are typically classified by levels of dispersion: (i) bilayer, (ii) alternating layer, and (iii) intermingled composites, as illustrated in Figure 2.17. The impact resistance of fibre hybrid composites varies significantly depending on the properties of the chosen fibre precursors, the matrix system, the degree of dispersion, as well as the relative position of the LE and HE layers.

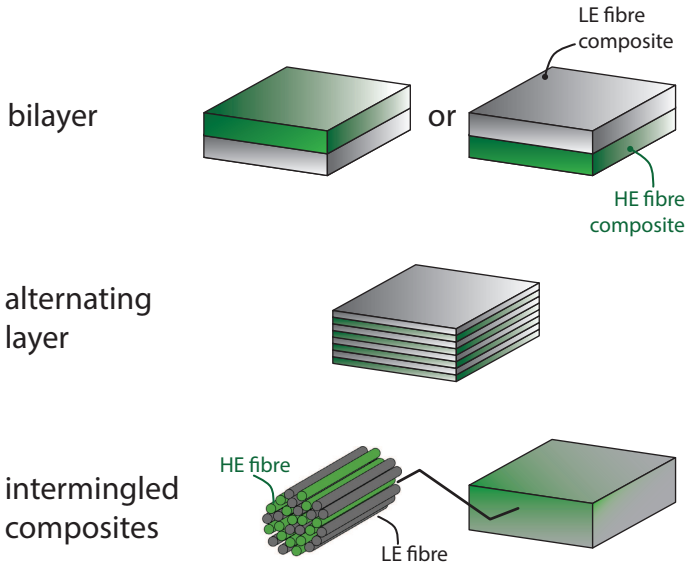

Figure 2.17: Schematic illustrations of the three typical classes of fibre hybrid composites. Image adapted from Swolfs et al. (2014).

Peijs and Venderbosch (1991) conducted a Charpy impact test on unidirectional hybrid beams comprising CFRP and UHMWPE fibres. They found a rather surprising result in which the total impact energy dissipation of hybrid beams can increase for beams with higher degrees of dispersion (i.e. higher number of alternating layers) and can even outperform the composite precursors; their data are presented in Figure 2.18. However, this benefit has not been observed for hybrid laminates tested under ballistic loading. In general, the ballistic resistance of fibre hybrids with a lower degree of dispersion (such as bilayer or trilayer composites) would usually lie between the impact resistances of their composite precursors on a equal-thickness basis, but could perform better or worse than the rule of mixtures (Jang et al., 1989; Mallick and Broutman, 1977; Sevkat et al., 2009). Figure 2.19 provides a visual explanation of positive and negative hybrid effects in relation to the rule of mixtures.

The perforation mechanisms of bilayer carbon fibre/UHMWPE fibre composites and multilayer carbon fibre/glass fibre composites have been investigated by Enfedaque et al. (2010); Peijs et al. (1990a,b). These studies reported that the failure mechanism of the CFRP layer was qualitatively similar to that of monolithic CFRP laminates, with failure consisting of transverse matrix cracks, ply delamination, and fibre fracture. Enfedaque et al. (2010) achieved similar results and argued that the presence of the HE layer helps the LE layer to sustain more deflection before fracture.

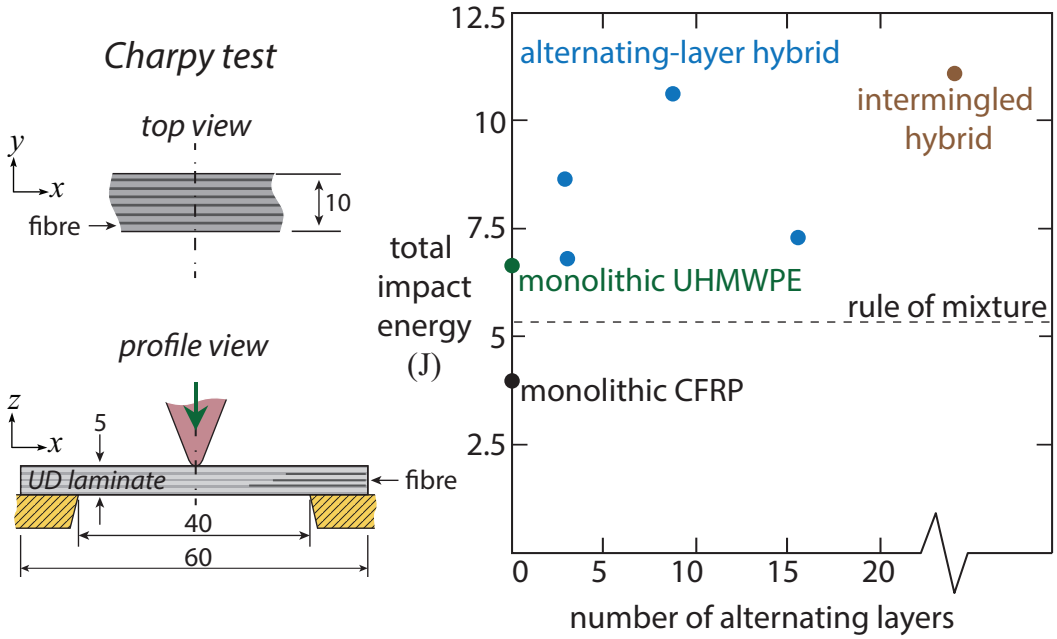

Figure 2.18: Plot of total impact energy as a function of number of alternating layers in the Charpy impact experiment of carbon fibre/UHWMPE fibre hybrid beams. Specimen dimensions in the figure are all in mm. Image adapted from Peijs and Venderbosch (1991).

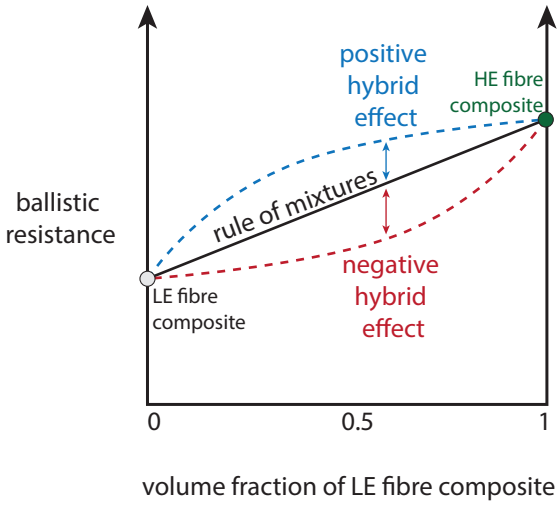

Figure 2.19: A visual explanation defining positive and negative hybrid effects in relation to the rule of mixtures. Image adapted from Swolfs et al. (2014).

Researchers have also been interested in determining the effect of layer position on the impact resistance of fibre hybrid composites. For a symmetric lay-up (i.e. laminates that have a mirror symmetry along the mid-plane), Enfedaque et al. (2010); Sevkat et al. (2009) showed that fibre hybrid composites have higher penetration resistance when the HE layers are placed at the outermost layers (i.e. the top and back faces with at least one other fibre layer in between). However, for an asymmetric bi-layer system, contradictory results have been reported. Park and Jang (2001); Sayer et al. (2010) showed that higher penetration resistance can be attained by placing the HE layer at the back, behind the LE layer. They argued that placing the HE layer at the tensile side allowed it to absorb more energy. In contrast, Jang et al. (1989) observed worse performance when placing the HE layer at the back and the LE layer on top. They suggested that when the LE layer was struck first, it perforated with a lesser degree of plastic deformation and thus offered inferior energy dissipation capability. To reconcile the above contradictory results, more research on bilayer composites is necessary.

Recently, Karthikeyan et al. (2013b) revealed that the impact resistance of monolithic CFRP composites with low matrix shear strength ($\sim$ 0.1 MPa) can be comparable to that of armour-grade Dyneema® composites and they exhibit a similar perforation mechanism. Their data suggests that it is possible to develop a new form of CFRP hybrids with an improved ballistic limit by alternating layers of CFRP with low and high matrix shear strength. As yet, no literature has investigated the impact response of hybrid composites constructed of the same fibre but with varying matrix properties. Therefore, Chapter 6 will investigate the ballistic response of bilayer CFRP laminates composed of CFRP layers with different matrix shear strengths ($\sim$ 0.1 MPa and $\sim$ 60 MPa).

2.4.4 Lamination with Metal Layers

Another type of hybrid composite can be formed by laminating fibre composites layers with metal layers, usually referred to as fibre metal laminates (FML). There are currently three types of FMLs: armaid fibre reinforced aluminium laminates (ARALL®), glass reinforced aluminium laminates (GLARE®), and carbon fibre reinforced aluminium laminates (CARAL). The concept of FML was originally introduced by Delft University of Technology

in the 1970s, where ARALL® composites were developed for their high fatigue strength. GLARE® composites were later introduced in the 1990s for their high impact resistance. Many researchers have investigated the quasi-static, dynamic, and fatigue responses of ARALL® and GLARE®, and detailed reviews have been compiled by Sadighi et al. (2012); Sinmazçelik et al. (2011). Figure 2.20a shows a schematic illustration of a typical fibre metal laminate. Commonly, FMLs such as ARALL®, GLARE®, and CARAL are constructed with 3 layers of aluminium alloy and 2 layers of fibre composites. The aluminium alloy layers are placed at the top, middle, and bottom, with the composite layers (either unidirectional or cross-ply) placed between them. The metal layers can be various grades of aluminium alloy (usually AA2024 or AA7475), while the fibres can be Kevlar® fibres, glass fibres, or carbon fibres, and the matrix in the composite layers is usually thermoset epoxy.

Pioneering work given by Vlot (1991, 1993, 1996) has compared the impact resistance among ARALL®, GLARE® and CARAL through a drop-weight experiment. He found that all types of FML show higher energy dissipation at impact penetration than their composite precursors. Notably, GLARE® composites show higher impact resistance even than monolithic aluminium alloy plates. An investigation given by Hoo Fatt et al. (2003) presented similar results, in which he found that the ballistic penetration velocity of s-glass epoxy-based GLARE® can be 13% higher than that of monolithic aluminium alloy plates with the same areal density. In general, the impact resistance of different FMLs can be ranked in the following order: (i) GLARE®, (ii) ARALL®, and (iii) CARAL. However, only a limited amount of literature is currently available regarding CARAL® and their impact performance is not fully understood (Bieniaś et al., 2015; Jaroslaw et al., 2016; Lawcock et al., 1998; Song et al., 2010; Vlot and Krull, 1997; Yu et al., 2015).

In his pioneering work, Vlot (1991, 1993, 1996) also investigated the cause of impact failure of various FML composites. He found that the relatively high elongation to failure ($\sim$ 5%) of glass fibres in GLARE® allow them to sustain a higher deflection before failure; thus, the first instance of failure in GLARE® was caused by shear fracture in the aluminium alloy (referred to as the 'aluminium critical' mode). In contrast, Kevlar® fibres and carbon fibres have lower elongations to failure ($\sim$ 1 - 3%), and thus the first failure in ARALL® and CARAL was caused by fibre failure (referred to as the 'fibre critical' mode). Vlot (1991, 1993, 1996) also found that GLARE® composites consisting of an

AA7475-T6 aluminium alloy, with high strength but low ductility, performed worse than composites consisting of an AA2024-T3 aluminium alloy, with low strength and high ductility. However, this yield strength effect was not observed for ARALL® composites, probably due to their 'fibre critical' mode. These observations were in agreement with studies by Jaroslaw et al. (2016); Liu (2010).

Caprino et al. (2004) investigated the perforation mechanism of GLARE® composites using CT-scanning. They revealed that transverse matrix crack formation and ply delamination within the GFRP layer can occur at low impact velocities, whereas high impact velocities are associated with the rupture of the aluminium alloy at the back face and fibre failure. A recent study by Bieniaś et al. (2015) investigated the damage mechanism of a composite sandwich consisting of a CFRP core and two aluminium alloy face sheets subjected to low-velocity impact. They observed that the CFRP layer in the sandwiches had fewer transverse matrix cracks and less delamination than in the monolithic CFRP plates, but the overall failure mechanism was similar, see Figures 2.20b and 2.20c. They proposed that the global deformation of the composite sandwiches may have dissipated the majority of the impact energy and mitigated the damage in the CFRP layer. However, their study did not investigate the penetration mechanism involving fibre failure at higher impact velocities. Consequently, Chapter 7 of this thesis will investigate the perforation mechanism(s) and the effect of the metal layer's yield strength on the ballistic resistance of aluminium alloy/CFRP bilayer plates.

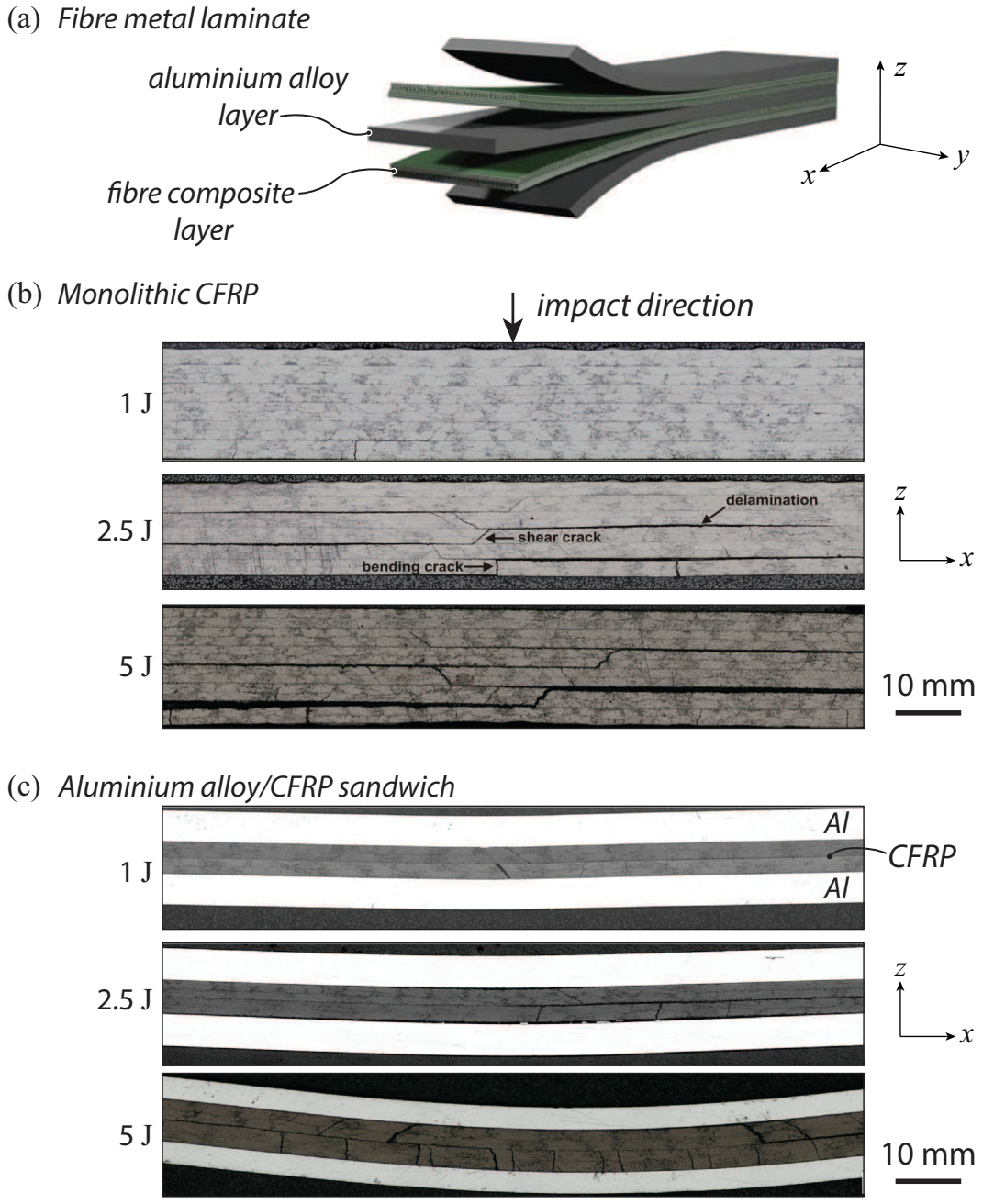

Figure 2.20: a) Schematic illustration of a typical fibre metal laminate that consists of alternating metal layers and fibre composite layers; image adapted from Sadighi et al. (2012). Optical images comparing the failure behaviours of b) a typical monolithic CFRP beam versus c) an aluminium alloy/CFRP composite sandwich; images adapted from Bieniaś et al. (2015).

2.5 Conclusions

The above literature review has established that there remain several critical uncertainties in the field of composite ballistic research.

(i) There are currently no generally accepted theories or criteria regarding the activation of the different perforation mechanisms (shear plugging, membrane stretching, and indirect tension) that are commonly observed in various fibre composites.

(ii) Recent data has suggested that the impact resistance of CFRP can be improved by a reduction of matrix shear strength that achieves a change in perforation mechanism. However, the precise effect of matrix properties on the prevailing failure mechanism is not understood.

(iii) It may be possible to achieve an improvement in ballistic limit by developing hybrid composites constructed with alternating layers of CFRP with low matrix shear strength and high matrix shear strength. The potential of this type of protection has not yet been investigated.

(iv) CFRP can be protected against projectile threats using metal layers; however, the reason for this improvement is unclear.

Consequently, this dissertation provides a set of comprehensive studies aimed at understanding the influence of matrix shear strength, composite hybridisation, and lamination with protective metal layers on the perforation mechanism(s) and resistance of CFRP laminates under quasi-static and ballistic loading.

Chapter 3

The Effect of Matrix Shear Strength on the Measured Out-of-plane Compressive Strength of CFRP Cross-ply Laminates

Summary

Recent studies have revealed that Dyneema® cross-ply laminates fail by an indirect tension mechanism when subjected to out-of-plane compression and impact loading (Attwood et al., 2014; Karthikeyan et al., 2013b; O'Masta et al., 2015a). The indirect tension mechanism has yet to be explored in carbon fibre/epoxy composite systems. This chapter investigates the failure mechanisms present in the quasi-static out-of-plane compressive response of carbon fibre/epoxy cross-ply laminates. Furthermore, the effect of matrix shear strength on the quasi-static compressive strength was characterised and the strain rate sensitivity of the laminates was measured in terms of compressive strength. For this study, CFRP [0°/90°] cross-ply laminates with five states of cure were obtained, varying from as-received uncured prepregs, to partially cured laminates, and finally to autoclaved fully cured laminates. The matrix shear strength increases along with degree of cure, from 0.1 MPa to 100 MPa.

Out-of-plane compression tests were conducted on the above laminates with various specimen side lengths $L \times L$ (with L in the range of 3 mm to 15 mm) and at various applied strain rates ($-\dot{\varepsilon}_{zz} = 8 \times 10^{-4} s^{-1}$, $8 \times 10^{-3} s^{-1}$, and $8 \times 10^{-2} s^{-1}$).

The strain rate sensitivity of the compressive response was pronounced for the uncured state, but quickly diminished as the specimens were partially cured. Measurements of the out-of-plane pressure distribution (i.e. normal compressive traction) during the compression tests were obtained using Fuji Prescale® films, and revealed the existence of a shear lag region where pressure builds up from the periphery of the specimens toward the centre. This results in a specimen size effect where the compressive strength (i.e. average pressure at failure) increases with specimen size. Pressure measurements also revealed that the length of the shear lag zone decreases as matrix shear strength of the specimens increases. As a result, for a given specimen size, the average pressure at failure increases with matrix shear strength. For the fully cured state, the shear lag length is significantly shorter than the specimen side length and the compressive response is insensitive to specimen size; the average pressure at failure is ~ 1.2 GPa.

Scanning Electron Microscopy (SEM) examination revealed that the laminates generally fail by an indirect tension mechanism: under compression, each ply expanded in the direction transverse to the fibre, stretching the adjacent plies in the fibre direction and causing fibre tensile failure. This tendency has one exception: laminates with the lowest state of cure (i.e. uncured prepregs) and small specimen size ($L < 5$ mm) that were tested at a low applied strain rate ($-\dot{\varepsilon}_{zz} = 8 \times 10^{-4} s^{-1}$) deformed by shear yielding.

3.1 Introduction

Recently, Attwood et al. (2016); O'Masta et al. (2015a) have demonstrated that the ballistic resistance of Dyneema® cross-ply composites is dictated by a local indentation-type mechanism involving the in-plane tensile failure of plies, referred to as indirect tension. This is a different mechanism from the membrane-stretching mode as analysed by Phoenix and Porwal (2003). The indirect tension mechanism was investigated by Attwood et al. (2014), who considered the out-of-plane uniaxial compression of Dyneema® cross-ply composites under quasi-static loading. Their results were in agreement with the early experiments reported by Henriksson (1990) on the quasi-static out-of-plane compresion of CFRP cross-ply laminates. However, Henriksson's study did not provide a failure analysis. The focus of the present study is to determine whether the indirect tension mechanism plays a role in the out-of-plane compressive response of CFRP cross-ply laminates.

The indirect tension mechanism can arise in cross-ply laminates under out-of-plane compressive loading by a pressure p, and is a result of (i) the anisotropy in Poisson expansion within the plane of each ply and (ii) a $0°/90°$ stacking of plies, see Figure 3.1. Consider a stack of alternating $0°$ and $90°$ plies under out-of-plane compression in the z-direction, and limit attention to the response of a unit cell comprising a single $0°$ ply (labelled A in the figure) adhered to an underlying $90°$ ply (labelled B). If the two plies were allowed to slide freely and without adhesion then, under the same out-of-plane compressive loading, ply B would undergo a much larger Poisson expansion in the y-direction than ply A, due to the orientation-dependent Poisson's ratio. Such relative deformation is disallowed by the adhesion of the two layers, and the two layers share the same strain in the y-direction; consequently, layer A is subjected to a tensile stress σ^A_{yy}, whereas layer B experiences a compressive stress $\sigma^B_{yy} = -\sigma^A_{yy}$ as there is no net force in the y-direction. By a symmetry argument $\sigma^B_{xx} = \sigma^A_{yy}$ and $\sigma^A_{xx} = \sigma^B_{yy}$. Consequently, the apply out-of-plane compressive pressure p generates axial tension in the fibre direction for each ply: hence the description 'indirect tension'.

In addition, edge effects can come into play: when a small sample is compressed between frictionless platens, the in-plane stresses must build up with increasing distance from the side face of a specimen in a shear lag manner. Such edge

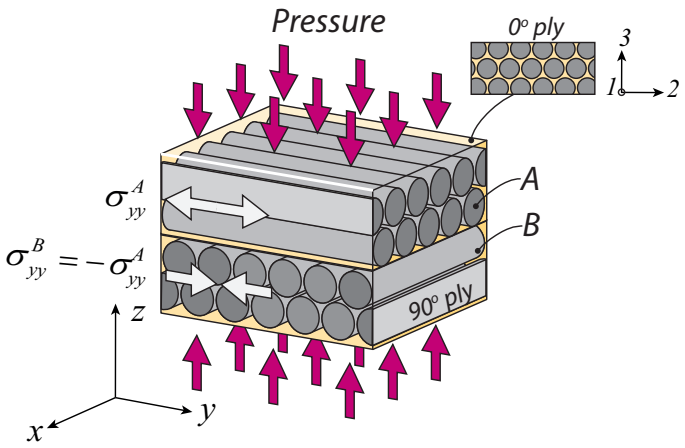

Figure 3.1: Schematic illustration of the indirect tension mechanism in a pair of 0°/90° plies under out-of-plane pressure. Poisson lateral expansion in the 0° ply parallel to the fibre is normally much less than in the 90° ply transverse to the fibre. Under out-of-plane compression, this mismatch in Poisson lateral expansion causes tension strain in the 0° ply and compression in the 90° ply.

effects lead to a reduction in the local pressure p. This has been explored by Attwood et al. (2014) for the case of an elastic-plastic composite response. Thus far, the out-of-plane compressive response of rate-dependent composites has not been characterised. This is a focus of the current study.

Preliminary experiments by Karthikeyan et al. (2013b) have suggested that matrix shear strength also has a significant effect on the ballistic resistance of carbon fibre reinforced plastic (CFRP). After testing cross-ply laminates of as-received prepregs and also autoclaved fully cured laminates, they observed shear plugging in the autoclaved materials and progressive perforation in the prepregs. Although they noted that the latter mode involved tensile failure of the fibres, they did not identify the mechanism to be one of indirect tension. A parallel study in Chapter 5 shall show that this mechanism of ballistic penetration is indeed indirect tension.

As it has been established that matrix shear strength has a significant effect on the failure mechanism of CFRP under dynamic loading, the present study seeks to determine the effect of matrix cure upon the quasi-static compressive response of CFRP cross-ply laminates. In particular, IM7/8552 carbon fibre/epoxy cross-ply composites with various specimen geometry (thickness-to-width ratio) were subjected to quasi-static out-of-plane compression. Furthermore, strain rate sensitivity of the matrix flow strength in composites is evident in tests employing a hot-wet environment or dynamic

loading (Daniel et al., 1981; Gates and Sun, 1991; Soutis and Turkmen, 1997; Staab and Gilat, 1995; Sun and Chen, 1989). Consequently, the effect of rate sensitivity of the matrix upon the out-of-plane strength is also investigated.

The outline of the current chapter is as follows. (i) The manufacturing process of CFRP cross-ply laminates is reported for various states of cure. (ii) Out-of-plane compression test results are reported. (iii) Results of additional interrupted test are reported, with pressure mapping used to reveal the distribution of contact pressure between the anvils and the specimens. (iv) The deformation behaviour and failure modes are examined by performing Scanning Electron Microscopy (SEM) on specimens from interrupted tests and failed specimens.

3.2 Laminates Manufacture

Cross-ply laminates $[0°/90°]_8$ were made from Hexply® 8552/35%/134/IM7 carbon fibre/epoxy prepregs (with ply thickness of 0.131 mm). Five states of cure were used, with the following labelling procedure employed throughout this chapter: (A) uncured, (B) partially cured at 100°C for 2 hours, (C) partially cured at 120°C for 2 hours, (D) partially cured at 180°C for 24 hours, and (E) autoclaved fully cured specimens. The uncured laminates (A) were laid-up by hand. Partially cured lay-ups of types (B) to (D) were prepared in a conventional air-oven using the above cure cycles and were compressed in-situ at 0.1 MPa in the through-thickness direction by spring-loaded platens (refer to Appendix A for the detailed drawing of the spring-loaded platens). The fully cured specimens (E) were autoclaved following the procedure recommended by Hexcel Ltd. (Hexcel Composites, 2013). Table 3.1 summarises the curing process specifications of laminate types (A) to (E). Prior to testing, materials (A) and (B) were cut to test dimensions using a knife, whereas materials (C) to (E) were cut using an abrasive cutting wheel. With the exception of the fully cured material (E), all laminates were stored at -15°C to avoid further curing and brought back to room temperature for 5 hours prior to testing.

The matrix shear strength of the laminates with five states of cure were measured using two ASTM-recommended shear test methods (ASTM Standard, 2013a,b). A $\pm 45°$ tensile test was used to measure the in-plane shear strength and a short beam shear test was used to measure the out-of-plane interlaminar shear strength of the laminates at various shear strain rates. The

Table 3.1: Curing process of CFRP laminates used in the quasi-static out-of-plane compression test.

Composite designation	Curing method	Curing temperature	Curing duration	Applied pressure
A	uncured	room temperature	–	–
B	oven cured	100°C	2 hours	out-of-plane 0.1 MPa
C	oven cured	120°C	2 hours	out-of-plane 0.1 MPa
D	oven cured	180°C	24 hours	out-of-plane 0.1 MPa
E	autoclaved	180°C	2 hours	hydrostatic 0.7 MPa

shear test set-ups and the detailed results are summarised in Appendix B. In general, the matrix shear strength increases with the state of cure. Laminates with low states of cure, such as materials (A) and (B), were shown to be strain rate sensitive. Their shear responses in the ±45° tensile test and short beam shear test were identical and can be characterised by a viscoplastic power-law:

$$\frac{\tau}{\tau_0} = \left(\frac{\dot{\gamma}}{\dot{\gamma}_0}\right)^m \tag{3.1}$$

where $\dot{\gamma}_0$ is a reference shear strain rate, τ_0 is a reference flow shear stress at a particular shear strain (chosen to be $\gamma = 5\%$), and m is an exponent (where $m > 0$) representing the strain rate sensitivity of the matrix flow stress. In contrast, laminates with high states of cure, such as materials (C) to (E), were found to be rate insensitive. Their shear yield strengths τ_y (defined to be τ at $\gamma = 5\%$) measured from the ±45° tensile test differed from their short beam shear strength. The shear parameters of materials (A) and (B) and the shear yield strength τ_y of materials (C) to (E) measured from the ±45° tensile test and short beam shear test are summarised in Table 3.2.

Table 3.2: Summary of shear test results measured from CFRP laminates with various states of cure.

Material	Reference strain rate $\dot{\gamma}_0(s^{-1})$	Reference shear stress τ_0 (MPa)	Strain rate sensitivity coefficient m	τ_y in $\pm 45°$ tensile test (MPa)	Short beam shear strength (MPa)
A	10^{-3}	0.11	0.45	–	–
B	10^{-3}	0.82	0.39	–	–
C	–	–	–	48 ± 2.3	22 ± 1.9
D	–	–	–	87 ± 8.2	61 ± 3.7
E	–	–	–	87 ± 0.85	99 ± 6.9

3.3 Test Methods

3.3.1 Out-of-plane Compression Test

For the five different states of cure, cross-ply specimens $[0°/90°]_8$ of thickness 2 mm (16 plies) and of side length $L \times L$ (with L in the range of 3 mm to 15 mm) were compressed in the out-of-plane direction between two hardened silver steel platens (700 Vickers), using a screw-driven test machine with a 150 kN load cell. The plates were lubricated with a low viscosity mineral oil, as illustrated in Figure 3.2. The compression tests were performed at three selected values of out-of-plane strain rate: $-\dot{\varepsilon}_{zz} = 8\times10^{-4}s^{-1}$, $8\times10^{-3}s^{-1}$, and $8\times10^{-2}s^{-1}$. For each state of cure, a minimum of 24 specimens were tested to failure at various specimen side lengths L and strain rates. The compressive load was recorded by the machine load cell and the displacement between the steel plates was measured using a laser extensometer. For selected samples, measurements were made of the pressure distribution (i.e. normal compressive traction) on the loaded face. To achieve this, pressure measurement films (Fuji Prescale®) were used to map out the pressure distribution of the specimens during the compression test. Fuji Prescale® films were chosen for their high resolving power ($\sim$ 0.2 mm) and large range of pressure measurement (up

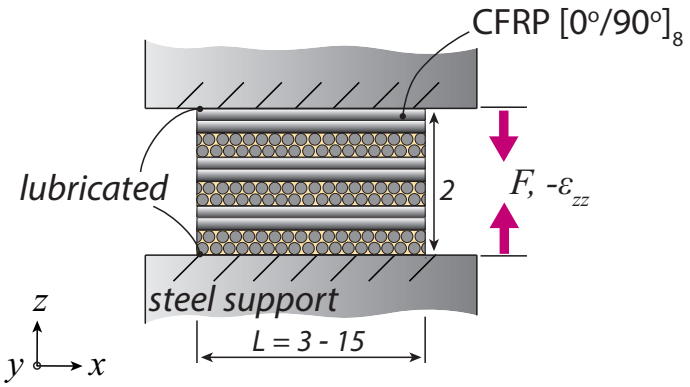

Figure 3.2: Schematic illustration of the quasi-static out-of-plane compression test set-up. F is the compressive force and u_z is the cross head displacement.

to 300 MPa). During the compression test, a stack of Fuji Prescale® films corresponding to different pressure ranges (i.e. one layer each of Prescale® MS film, HS film, and HHS film) was placed between the specimen and the steel plate. Each Fuji Prescale® film contains a colour-forming layer on top of a colour-developing layer. The colour-forming layer contains microcapsules with various sizes and wall strengths that are correlated with pressure. When pressure is applied, the microcapsules with various strengths would break at different pressures, creating a red coloured patch with varying intensity of colour depending on the local pressure. Calibrations had been conducted on the MS, HS, and HHS films by compressing them between two flat platens at incremental pressure levels, giving a calibrated pressure range of 35 MPa to 300 MPa. To ensure that a full pressure profile would be recorded for the CFRP laminates, specimens were unloaded before a peak pressure of 250 MPa was reached.

3.3.2 Deformation Mechanics and Failure Mechanism

Several additional specimens were subjected to out-of-plane compression and unloaded at a strain level either (i) before failure or (ii) immediately after failure, after which they were examined using Scanning Electron Microscopy (SEM):

(i) Unloading prior to failure allowed the deformation mechanics to be observed. Specimens used for this purpose were prepared in the following method prior to the test. One side of the specimens was polished and then gold coated. Vertical incisions with $\sim$ 0.5 mm spacing were then made by

using a knife to remove the gold coating. These incisions were used to visually demonstrate the deformation experienced by the plies.

(ii) The specimens that were compressed past failure were used to observe the failure mechanism. After the compression test, failed specimens were placed in a 425°C environment for 90 minutes to partially pyrolyse the resin in the laminate, following a de-ply technique developed by Freeman (1982) used to reveal the failure behaviour of the plies.

3.4 Results

3.4.1 Out-of-plane Compressive Response

Quasi-static out-of-plane compression tests were performed on cross-ply laminates $[0°/90°]_8$ with specimen side length L in the range of 3 mm to 15 mm with five different states of cure, (A) to (E). Examples of out-of-plane compressive response (expressed in terms of average pressure $\bar{p} = F/L^2$ versus compressive strain $-\varepsilon_{zz}$) at a strain rate of $-\dot{\varepsilon}_{zz} = 8 \times 10^{-4} s^{-1}$ are presented in Figure 3.3. The key observations derived from the figures are described below.

(i) It is apparent that the compressive response can be influenced by the specimen side length L. However, the relative significance of the size effect decreases as the laminate's state of cure increases. Consider material (A), which represents uncured prepregs. For $L = 3$ mm, compressive average pressure plateaus at 10 MPa due to shear yielding of the plies. As the specimen size increases, the compressive response switches from shear yielding to ply tensile failure as indicated by a sudden load drop (evidence that this is caused by the indirect tension mechanism will be presented in the next section). For instance, at $L = 7$ mm, material (A) experiences compressive failure at an average pressure of $\bar{p}_f = 175$ MPa (denoted with label $\times$ in Figure 3.3a), which represents a $\sim 170\%$ increase over the average pressure at failure for the $L = 3$ mm specimen. The specimen size effect is most pronounced in material (A) with lowest state of cure. As the matrix shear strength increases through the curing process, the specimen size effect becomes less significant. Once the fully cured state is reached, the failure average pressure of material (E) only increases $\sim 13\%$ from $\bar{p}_f = 1100$ MPa to 1250 MPa when L increases from 3 mm to 7 mm (see Figure 3.3e).

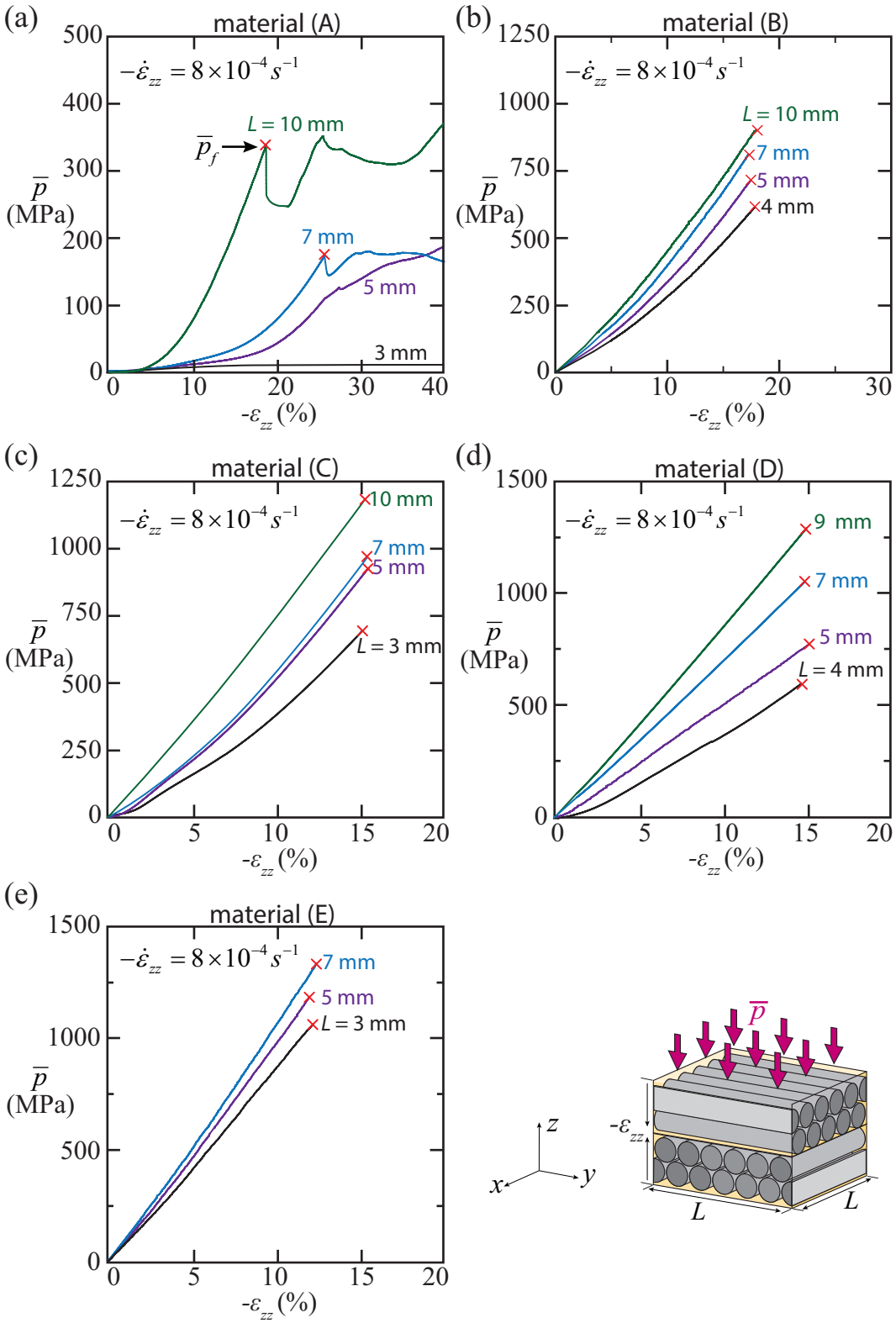

Figure 3.3: Plots of average pressure $\bar{p}$ as functions of compressive strain $-\varepsilon_{zz}$ of a) uncured material (A), b) partially cured material (B), c) partially cured material (C), d) partially cured material (D), and e) autoclaved material (E) at a strain rate of $-\dot{\varepsilon}_{zz} = 8 \times 10^{-4} s^{-1}$.

(ii) For a given specimen size, the average pressure at compressive failure $\bar{p}_f$ rises as matrix shear strength increases. For example, at $L = 7$ mm, $\bar{p}_f$ increases from 175 MPa to 1000 MPa to 1250 MPa as state of cure increase from material (A) to (C) and finally to (E).

(iii) There appears to be a stiffening effect in the compressive response of materials (A) and (C) at strain values prior to failure. This stiffening response has been reported for the transverse compression of unidirectional carbon fibre prepregs (Cai and Gutowski, 1992; Gutowski et al., 1987; Gutowski and Dillon, 1992; Hubert and Poursartip, 2001). It is understood that the stiffening response is caused by fibre rearrangement or fibres in contact with one another at large compressive strains. This fibre compaction response is most pronounced in the uncured state due to the high degree of viscoplastic strain, and gradually declines as matrix shear strength increases. At the fully cured state, material (E) with high matrix shear strength shows little plasticity and fibre compaction, which produces a linear compressive response.

3.4.2 Compressive Strength versus Specimen Size

Figures 3.4a to 3.4e show the measured the compressive strength (in terms of average pressure at compressive failure $\bar{p}_f$) versus specimen side length L at different states of cure and tested at various strain rates $\dot{\varepsilon}_{zz}$. Where compressive failure does not occur, plateau average pressure is used instead (i.e. material (A) at $L = 3$ mm and $-\dot{\varepsilon}_{zz} = 8 \times 10^{-4} s^{-1}$). These figures give rise to two key observations:

(i) It appears that the average pressure at failure $\bar{p}_f$ can be influenced by the compressive strain rate. This strain rate effect is most noticeable in material (A), which has the lowest state of cure. For instance, at $L = 7$ mm, $\bar{p}_f$ in material (A) rises from 150 MPa to 600 MPa as strain rate increases from $-\dot{\varepsilon}_{zz} = 8 \times 10^{-4} s^{-1}$ to $8 \times 10^{-2} s^{-1}$. This rate effect becomes undetectable in materials (B) to (E) due to the reduced strain rate sensitivity of the matrix after curing.

(ii) As was also illustrated in Figure 3.4, $\bar{p}_f$ is influenced by the specimen size. This size effect is most noticeable in material (A). For instance, at $-\dot{\varepsilon}_{zz} = 8 \times 10^{-4} s^{-1}$, $\bar{p}_f$ increases from 10 MPa to 350 MPa as L increases from 3 mm to 10 mm. The effect of specimen size gradually declines as matrix shear strength increases and thus becomes negligible in material (E).

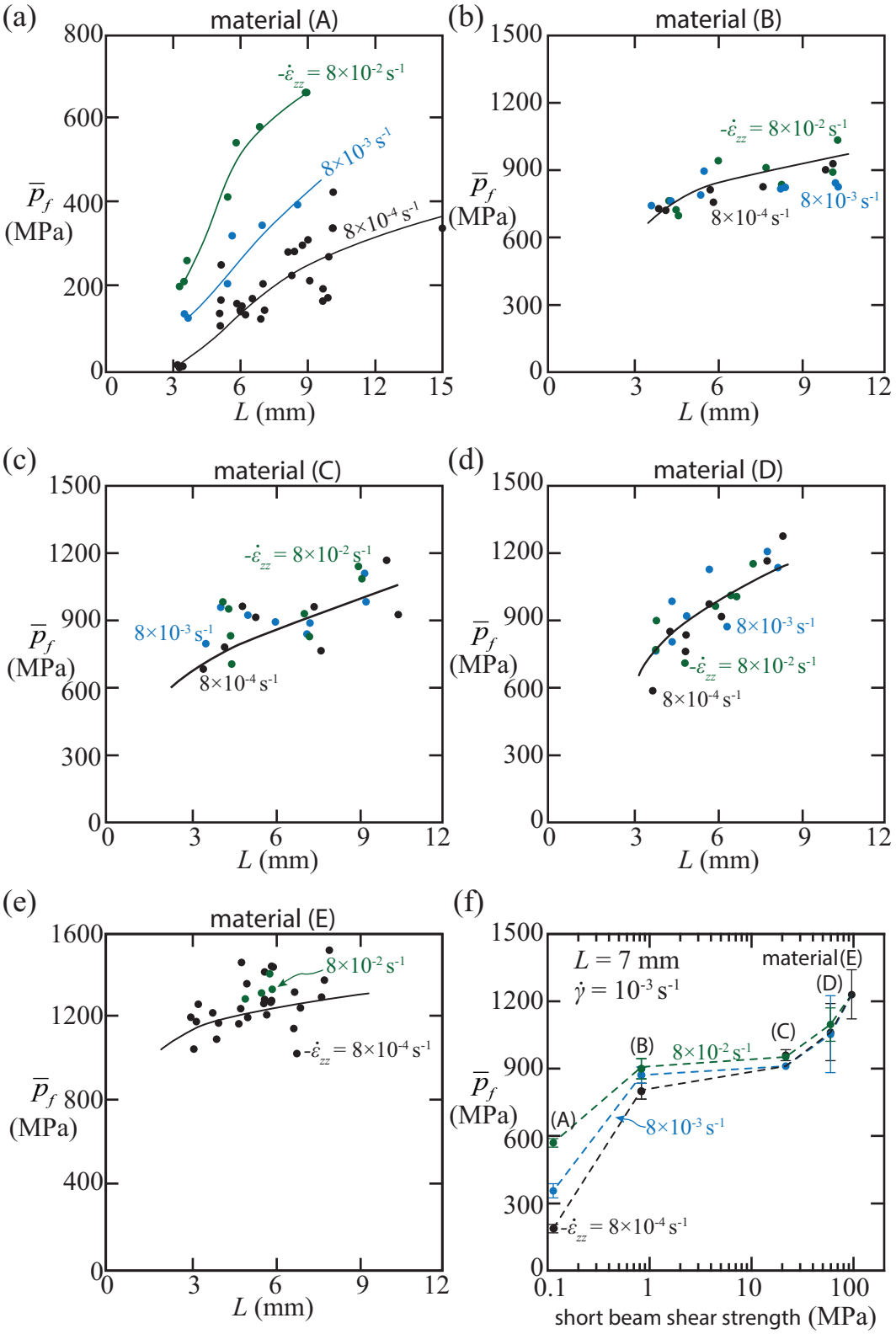

Figure 3.4: Plots of average pressure at failure $\bar{p}_f$ as functions of specimen side length L of a) material (A), b) material (B), c) material (C), d) material (D), and e) material (E) that were tested at various strain rates. f) Plot of $\bar{p}_f$ at a constant $L = 7$ mm as a function of material short beam shear strength that was tested at a shear strain rate of $\dot{\gamma} = 10^{-3}s^{-1}$. Lines are drawn to help reveal trends.

Figure 3.4f summarises the above data by displaying selected compression test results in terms of $\bar{p}_f$ (at test strain rates from $-\dot{\varepsilon}_{zz} = 8 \times 10^{-4} s^{-1}$ to $8 \times 10^{-2} s^{-1}$) versus the short beam shear strength of each material (tested at $\dot{\gamma} = 10^{-3} s^{-1}$) for a constant specimen size of $L = 7$ mm. Both the effects of matrix shear strength and the strain rate sensitivity are apparent here. In general, $\bar{p}_f$ scales along with matrix shear strength.

3.4.3 Pressure Distribution of the Laminates during Compression

Cross-ply laminate types (A), (B), (C), and (E) with specimen size of $L = 10$ mm were subjected to out-of-plane compression at a strain rate of $-\dot{\varepsilon}_{zz}$=$8 \times 10^{-4} s^{-1}$ at three pressure levels: $p_{max} = 100$ MPa, 200 MPa, and 250 MPa. p_{max} is defined to be the maximum pressure located at the centre of the specimen on the x-y plane in Figure 3.5 (i.e. $x = y = 0$). The out-of-plane pressure distribution of the laminates was recorded using Prescale® pressure measurement films. Examples of pressure distributions for materials (A), (B), (C), and (E) at compression pressure $p_{max} = 250$ MPa are reported in Figures 3.5a to 3.5d (due to the symmetry of the square specimens, only one quarter of the pressure profiles are presented). For all materials, pressures were at a minimum along the periphery of the specimens and would build up toward the centre of the specimens ($x = y = 0$), revealing the existence of shear lag zones. After the building pressures reached the ends of the shear lag zones, pressure remained uniform at a maximum of ~ 250 MPa. The existence of the shear lag zone is indicative of interlaminar shear plastic deformation, with the length of this zone λ correlating to the level of shear plastic deformation in the specimens.

Figure 3.6 summarises the pressure distribution of materials (A), (B), (C), and (E) at $p_{max} = 100$ MPa, 200 MPa, and 250 MPa by presenting only the pressure p along the centre line ($y = 0$) of the specimens. As matrix shear strength increases, interlaminar shear plastic deformation is suppressed, and thus λ gradually decreases. For example, at $p_{max} = 250$ MPa, λ as a function of matrix shear strength is as follows: ~ 2 mm for material (A), ~ 0.5 mm for material (B), ~ 0.3 mm for material (C), and ~ 0.2 mm for material (E).

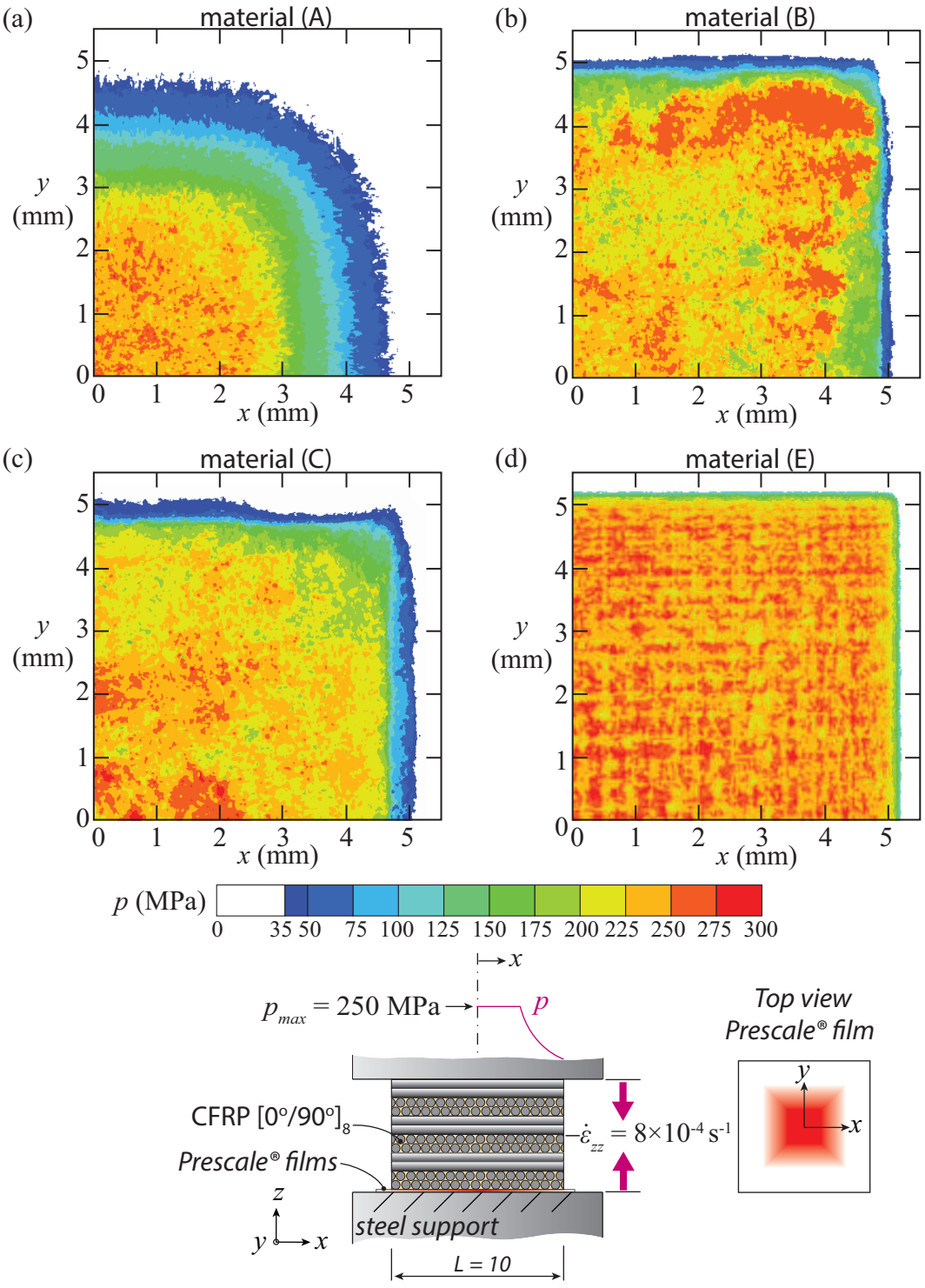

Figure 3.5: Out-of-plane pressure distributions measured from pressure sensitive films of cross-ply laminates a) material (A), b) material (B), c) material (C), and d) material (E) at different states of cure, all at a maximum pressure of $p_{max} = 250$ MPa (at $L = 10$ mm and $-\dot{\varepsilon}_{zz} = 8 \times 10^{-4} s^{-1}$).

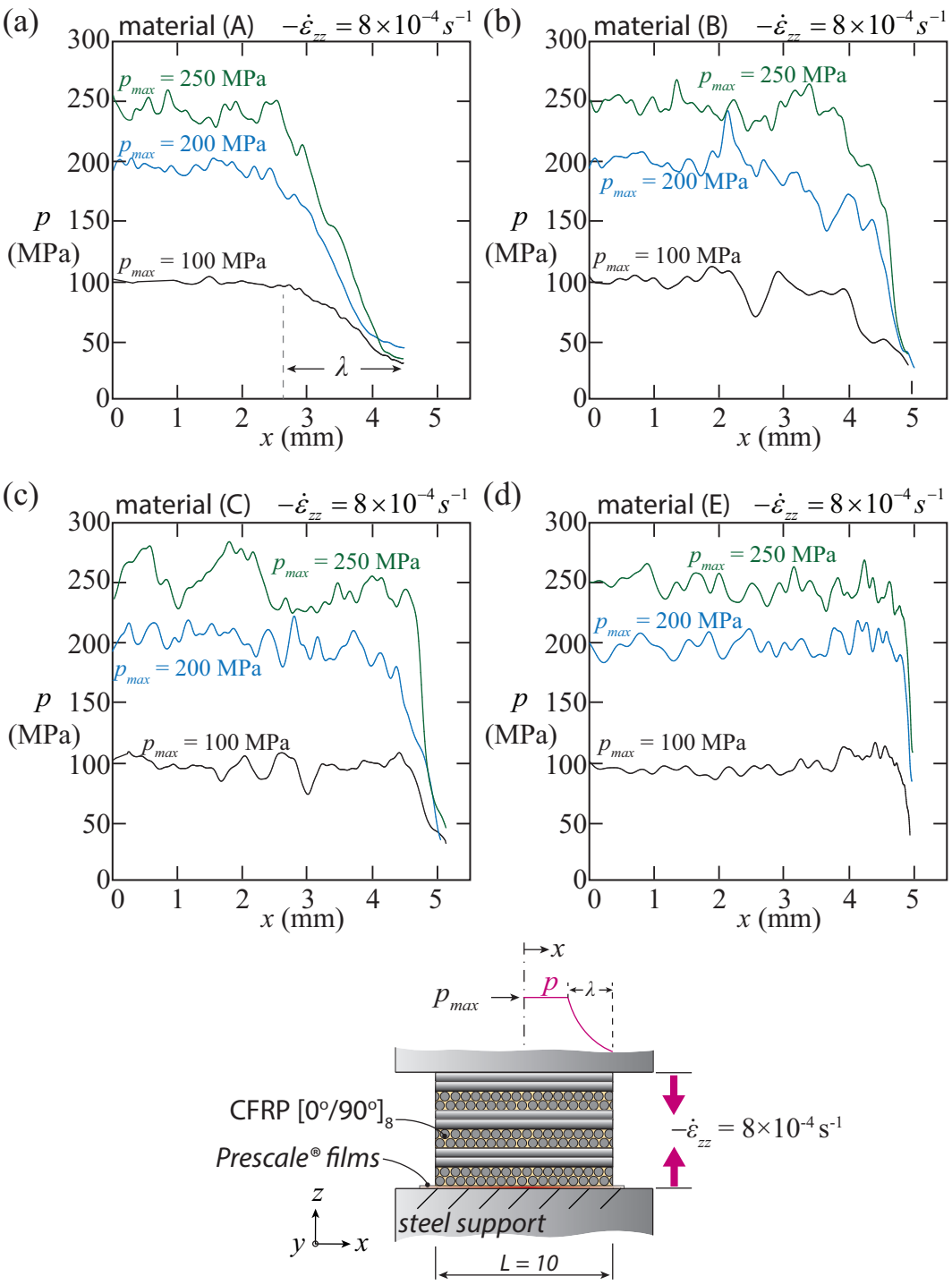

Figure 3.6: Plots of the pressure distribution along the centre line ($y = 0$) of a) material (A), b) material (B), c) material (C), and d) material (E) at different levels of p_{max} (at $L = 10$ mm and $-\dot{\varepsilon}_{zz} = 8 \times 10^{-4}s^{-1}$).

3.4.4 Observed Deformation and Failure Mechanisms

Cross-ply laminate types (A), (B), and (E) with specimen side length $L = 7$ mm were subjected to out-of-plane compression at a strain rate of $-\dot{\varepsilon}_{zz} = 8 \times 10^{-4} s^{-1}$ followed by unloading at (i) a strain level prior to failure (-ε_{zz}=12%) and (ii) immediately after failure. Prior to the compression tests, one side of the specimens was polished and then gold coated. Vertical incisions with ~ 0.5 mm spacing were then made by using a knife to remove the coatings. SEM side-views of specimens compressed to $-\varepsilon_{zz} = 12\%$ (before failure) revealed that the above incisions changed from vertical lines to a 'square wave' pattern accompanied by ply extrusions at the specimen edges, as shown in Figures 3.7a, 3.7c, and 3.7e. The above square wave pattern reveals that the deformation of the laminates was dictated by plastic Poisson expansion of the plies in the direction transverse to the fibres and by interlaminar shear at the interface between the alternating 0° and 90° plies. The plastic strains of the laminates can be compared qualitatively by examining the extent of the above Poisson expansion in the figures. The plastic strains in the specimens decrease as the state of matrix cure increases from materials (A) to (E), with Poisson expansion becoming almost undetectable in material (E). Specimens that were compressed past failure were de-plied and then examined using SEM. The middle plies of failed specimens (A), (B), and (E) are presented in Figures 3.7b, 3.7d, and 3.7f, respectively. Ply tensile failure is apparent in all the materials. Figure 3.7g illustrates the (i) Poisson expansion of plies and (ii) ply tensile failure in a cross-ply laminate. The above observations were consistent with the indirect tension failure of Dyneema® cross-ply laminates observed under out-of-plane compression (Attwood et al., 2014). Therefore, it is concluded that the CFRP cross-ply laminates in the current study also failed by the indirect tension mechanism.

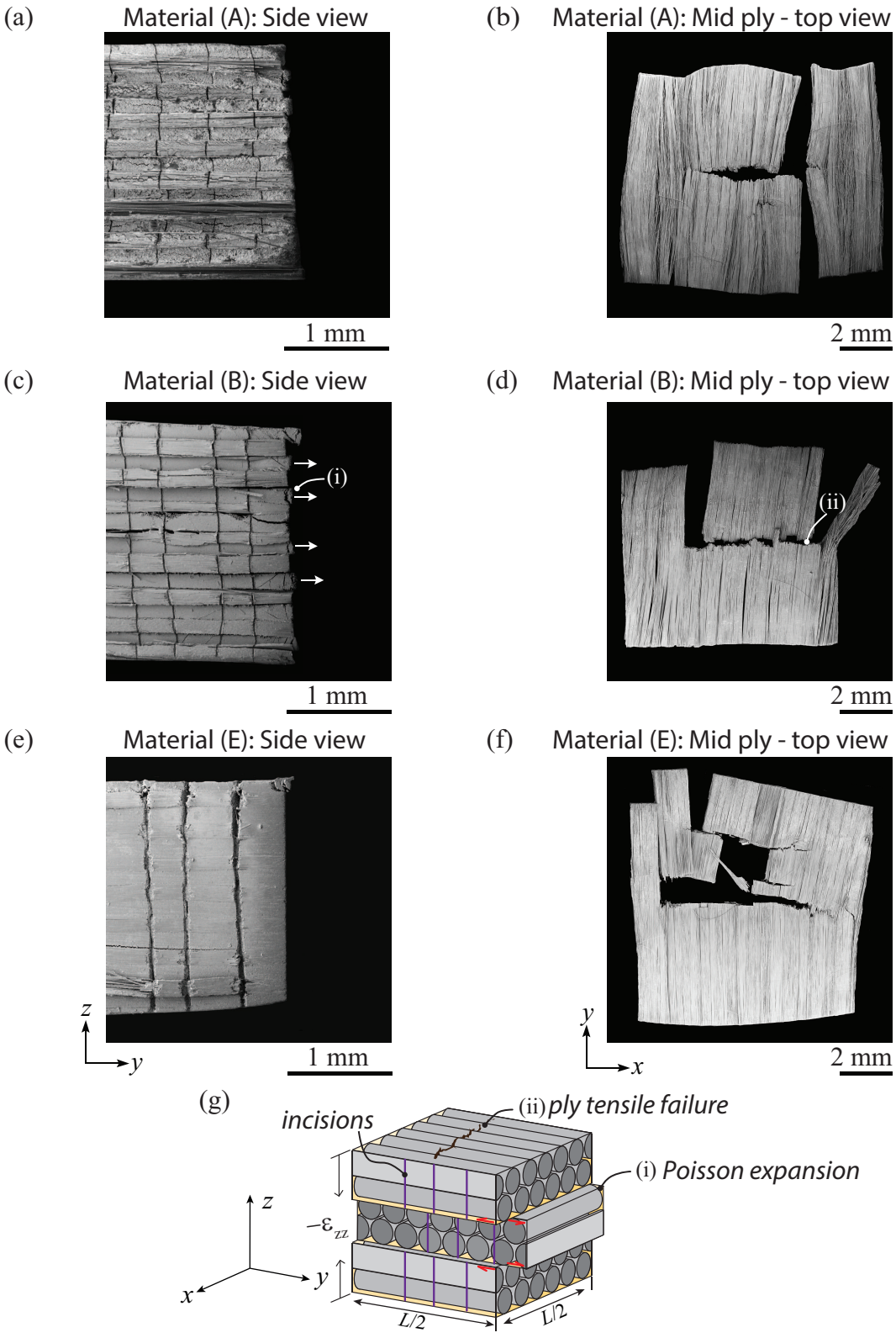

Figure 3.7: SEM side view images of $L = 7$ mm cross-ply specimens (with 0.5 mm vertical incisions) made of materials a) (A), d) (B), and e) (E) tested to a strain level prior to failure ($-\varepsilon_{zz} = 12\%$). SEM top view images of the mid-ply in materials b) (A), d) (B), and f) (E) after compression failure. g) A illustration of the (i) Poisson expansion of plies and (ii) ply tensile failure in the indirect tension mechanism.

3.5 Discussion

In the out-of-plane compression experiment, it was found that CFRP cross-ply laminates generally failed by an indirect tension mechanism, but uncured prepregs with small specimen size tested at a low applied strain rate experienced shear yielding. Consider a stack of alternating 0° and 90° plies (with size $L \times L$) under out-of-plane compression in the z-direction, and limit attention to the response of one quarter of the specimen (with size $L/2 \times L/2$) with a unit cell comprising a single 0° ply (labelled A) adhered to an underlying 90° ply (labelled B), as illustrated in Figure 3.8a.

The underlying causes of these failure mechanisms are summarised as follows.

(i) If the two plies are allowed to slide freely and without adhesion then, under the same out-of-plane compressive loading, ply B would undergo a much larger Poisson expansion in the x-direction than ply A, due to the orientation-dependent Poisson's ratio. However, at the centre of the specimen (defined as $x = y = 0$), such relative deformation is restricted by the adhesion of the two layers, and the two layers share the same strain in the x-direction. Consequently, layer A is subjected to an in-plane tensile stress σ_{xx}^{A} in the fibre direction, whereas layer B experiences an in-plane compressive stress $\sigma_{xx}^{B} = -\sigma_{xx}^{A}$ transverse to the fibre since there is no net force in the x-direction. By a symmetry argument, $\sigma_{yy}^{B} = \sigma_{xx}^{A}$ and $\sigma_{yy}^{A} = \sigma_{xx}^{B}$.

(ii) In the region near the periphery of the specimen, interlaminar shear occurs at the interface between the alternating 0° and 90° plies, introducing a shear lag effect. This creates a shear lag zone (with a length λ) where pressure p builds up from the periphery toward the centre, see profile view in Figure 3.8b.

(iii) For small specimens, the shear lag zone may cover the entire specimen (if the length of the shear lag zone λ is equal to half the specimen width $L/2$). In this case, the laminate would deform through shear yielding. This mechanism was only observed in uncured prepregs with specimen side length L less than 5 mm (with applied strain of $-\dot{\varepsilon}_{zz} = 8 \times 10^{-4} s^{-1}$).

(iv) For larger specimens, the pressure p remains constant at a maximum value of p_{max} in the area near the centre (i.e. outside of the shear lag zone). p_{max} increases as the compressive strain $-\varepsilon_{zz}$ rises and failure occurs due to ply tensile failure. This mechanism is referred to as indirect tension.

In addition to investigating the failure mechanisms, this study also evaluated

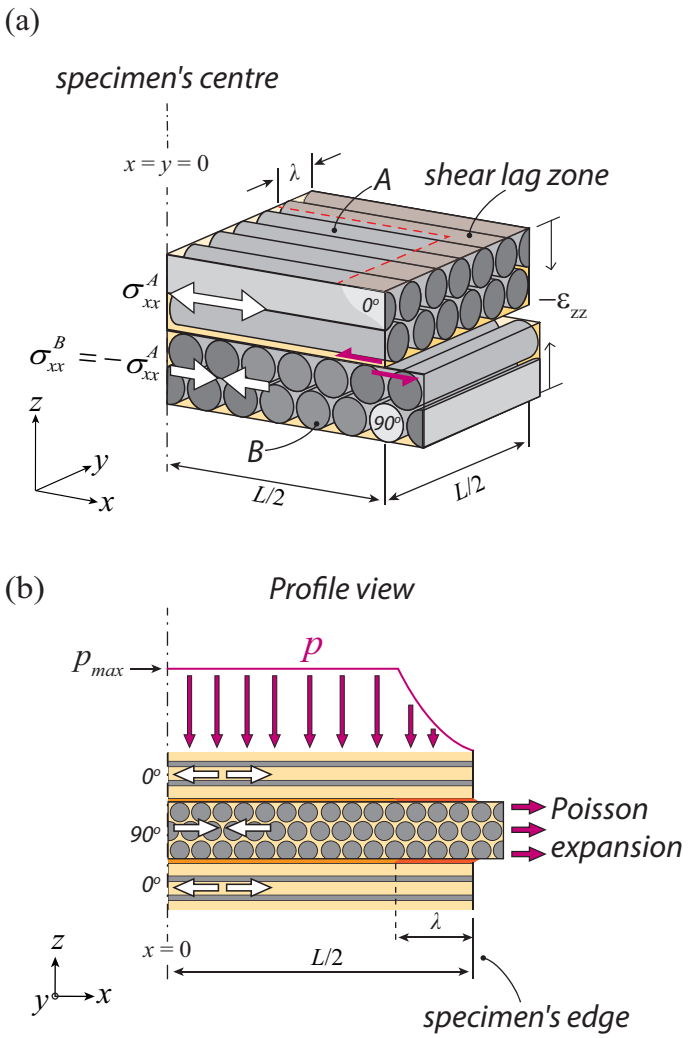

Figure 3.8: Schematic illustrations of a cross-ply laminate under out-of-plane compression with a unit cell equal to a quarter of a specimen (with size $L/2 \times L/2$) that comprises of a single 0° ply adhered to an underlying 90° ply. a) An illustration of the indirect tension mechanism arising as a result of the anisotropy in Poisson expansion within the plane of each ply. b) Its profile view showing the pressure p as it builds up from the periphery toward the centre of the specimen ($x = y = 0$) due to a shear lag effect.

the effects of applied compressive strain rate, laminate matrix shear strength, and specimen size on the compressive strength (i.e. average pressure at compressive failure $\bar{p}_f$). Laminates with the lowest state of cure deformed in a viscoplastic manner and demonstrated a pronounced strain rate sensitivity where $\bar{p}_f$ increases with the applied strain rate. This strain rate sensitivity quickly diminished as the laminates were partially cured. Pressure measurements also revealed that the above-mentioned shear lag length λ decreases as the matrix shear strength of the specimens increases. As a result, for a given specimen size, the $\bar{p}_f$ increases with the matrix shear strength. This shear lag effect also produces a specimen size effect where the $\bar{p}_f$ increases with specimen size. However, at the fully cured state, the shear lag length λ is significantly shorter than the specimen side length L and the compressive response is insensitive to specimen size, with $\bar{p}_f$ remaining constant at ~ 1.2 GPa.

3.6 Conclusions

The current study investigates the failure mechanisms of CFRP $[0°/90°]_8$ cross-ply laminates under quasi-static uniaxial out-of-plane compression, as well as the role of matrix shear strength. Cross-ply laminates with five states of cure were obtained, varying from as-received uncured prepregs, to partially cured laminates, and finally to autoclaved fully cured laminates. The matrix shear strength increased along with the degree of cure, from 0.1 MPa to 100 MPa. Out-of-plane compression tests were conducted on the above laminates with various specimen side lengths L and at various applied strain rates. Scanning Electron Microscopy (SEM) examination revealed that the laminates generally fail by an indirect tension mechanism: under compression, each ply expanded in the direction transverse to the fibre, stretching the adjacent plies in the fibre direction and causing fibre tensile failure. This tendency has one exception: laminates with the lowest state of cure (i.e. uncured prepregs) and small specimen size ($L < 5$ mm) that were tested at a low applied strain rate ($-\dot{\varepsilon}_{zz} = 8 \times 10^{-4} s^{-1}$) deformed by shear yielding.

In addition, the effects of matrix shear strength, specimen size, and applied strain rate on the compressive strength (i.e. the average pressure at

compressive failure) were also characterised. All else being equal, the compressive strength increased along with matrix shear strength. Similarly, the compressive strength also increased along with the tested specimen size and applied strain rate. However, the strain rate sensitivity quickly diminished as the laminates were partially cured.

Pressure measurements revealed that, during compression, pressure builds up from the periphery toward the centre of specimen in a shear lag manner. This shear lag effect was responsible for the above-mentioned specimen size effect. The size of the shear lag zone decreased as the matrix shear strength increased and eventually became a negligible proportion of the entire specimen. Thus, for autoclaved fully cured laminates, the compressive strength ($\sim$ 1.2 GPa) was insensitive to specimen size.

The above description of the indirect tension mechanism is in agreement with the findings of Attwood et al. (2014), who first observed this mechanism through a uniaxial out-of-plane compression test of Dyneema® cross-ply laminates. A recent study by O'Masta et al. (2015a) revealed that Dyneema® cross-ply plates fail by indirect tension under ballistic loading. Analogously, the indirect tension mechanism may be involved in the dynamic failure of CFRP cross-ply laminates. It is therefore important to develop a predictive method to explain the observations of the current chapter, which will be accomplished in Chapter 4.

Chapter 4

Finite Element and Analytical Models of CFRP Cross-ply Laminates under Quasi-static Out-of-plane Compression

Summary

The quasi-static out-of-plane compressive response and corresponding failure mechanisms of CFRP cross-ply laminates with various states of matrix cure were investigated experimentally, as discussed in Chapter 3. In the current chapter, finite element (FE) simulations and analytical models were developed to explain (i) the effect of matrix shear strength, (ii) the effect of specimen geometry, and (iii) the effect of applied strain rate on the laminates' compressive strength (i.e. the average pressure at compressive failure). These models were developed based on the elastic, elastic-plastic and elastic-viscoplastic behaviours of plies. Both the FE simulations and the analytical models were in good agreement with the experimental results and accurately predicted the compressive strength of the cross-ply laminates. The cross-ply laminates generally fail by indirect tension facilitated by ply tensile failure, with one exception: uncured laminates with small specimen size that were tested at a low applied strain rate, deformed by shear yielding.

4.1 Introduction

The goal of the current chapter is to develop predictive tools to explain the quasi-static out-of-plane compressive response of CFRP cross-ply laminates and their sensitivity to material and geometric parameters: matrix shear strength, specimen size, and applied strain rate. In particular, finite element (FE) simulations and analytical models will be developed and their predictive accuracy will be assessed through comparison with the experimental data obtained previously in Chapter 3.

The experiments described in Chapter 3 have revealed that, under uniaxial out-of-plane compression, CFRP cross-ply laminates generally fail by the indirect tension mechanism (except for uncured prepregs with small specimen size tested at a low applied strain rate, which deform by shear yielding). Indirect tension refers to a mechanism whereby out-of-plane compressive pressure generates axial tension in the fibre direction for each ply. The precise relationship between the in-plane stresses and the out-of-plane compressive pressure is dependent upon the choice of constitutive law for each ply, such as whether it behaves in an elastic, plastic, or viscous manner. In broad terms, the in-plane stresses are of the same order of magnitude as the out-of-plane compressive pressure p. Attwood et al. (2014) have investigated the indirect tension mechanism for the case of an elastic-plastic composite response. In the present study, a detailed analysis shall be developed for the response of a rate-dependent composite.

The current study adapted the FE and analytical models given by Attwood et al. (2014) to model the indirect tension (as well as shear yielding) in CFRP cross-ply laminate. Some modifications were made to the models in order to account for the strain rate sensitivity of the matrix flow. A literature review of the strain rate sensitivity of matrix flow is provided below. Furthermore, out-of-plane compression of the cross-ply laminates in the fully cured state leads to failure at a pressure in the order of 1 GPa. Such pressures are sufficiently high that the shear strength of the matrix and the fibre tensile strength are affected. The extent of this interaction is considered in detail in this study, but at this stage it is useful to review the literature on the effect of superimposed pressure upon the flow strength of the matrix and the tensile strength of fibres.

4.1.1 Strain Rate Sensitivity of Matrix Flow

Strain rate sensitivity of the matrix flow strength in composites is evident in tests employing a hot-wet environment or dynamic loading, as noted by inter alia Daniel et al. (1981); Gates and Sun (1991); Soutis and Turkmen (1997); Staab and Gilat (1995); Sun and Chen (1989). Generally, the rate sensitivity in the matrix yield strength is characterised by the viscoplastic power law (for more detail refer to Gates and Sun (1991); Weeks and Sun (1998)).

4.1.2 Pressure Dependence of the Matrix Shear Strength

It is generally recognised that the shear strength of the polymeric matrix in a fibre reinforced composite is pressure dependent. Collings (1974) observed that the transverse compressive strength of a 90° ply in CFRP is significantly higher than its corresponding tensile strength. He noted that compressive shear bands were formed at an angle of $\sim 30°$ from the loading axis instead of $\sim 45°$ as commonly seen in the shear yielding of metals. He proposed that the yield strength of the epoxy matrix is pressure dependent. Collings' work motivated a number of studies on the transverse compression of 90° plies with superimposed hydrostatic pressure, see for example (Hine et al., 2005, 1999; Pae and Phee, 1995; Zinoviev and Tsvetkov, 1998). In general, it was observed that the yield strength of the composites scales with the superimposed hydrostatic pressure. The underlying idea is that the fibres remain elastic, and slide past each other in the manner of a granular flow, with plastic deformation of the intervening polymeric matrix. A Mohr-Coulomb law is used to account for the pressure dependence of yield strength of the 90° ply, along with non-associated flow. For more detail, refer to (Argon et al., 1968; González and LLorca, 2007; Rabinowitz et al., 1970; Ward, 1971).

4.1.3 Pressure Dependence of Fibre Tensile Strength

Hine et al. (1999) showed that the tensile strength of dry carbon fibre tows decreases with an increase in superimposed hydrostatic pressure. Similarly, the tensile strength of carbon, glass and Kevlar® composites (in an epoxy matrix) decreases with increasing superimposed pressure, see for example (Hine et al.,

2005, 1999; Parry and Wronski, 1985, 1986; Sigley et al., 1991; Zinoviev and Tsvetkov, 1998). The precise reason for this weakening effect is unclear but the effect is widely recognised.

4.2 Finite Element Simulation for the Predictions of the Average Pressure at Compressive Failure

4.2.1 Description of the Finite Element Method

This section describes the finite element (FE) method used to simulate the out-of-plane compressive response of a cross-ply laminate with a specimen side length $L \times L$ consisting of a stack of alternating 0° and 90° plies. The description of the FE method in the current study is adapted from the analysis given by Attwood et al. (2014). A summary is given below.

Figure 4.1a illustrates a unit cell equal to a quarter of a pair of 0° and 90° plies (with size $L/2 \times L/2$) that comprises a single 0° ply adhered to an underlying 90° ply and subject to compression in the z-direction. The global coordinate system of the cross-ply laminates is defined such that directions x and y are orthogonal to each other, each parallel to one of the edges of the laminate, while z represents the out-of-plane direction. Periodic boundary conditions were enforced at the top and bottom surfaces in the stack of 0° and 90° plies. The displacements at these surfaces were constrained to be:

$$u_x^{(A)} = u_x^{(B)} \tag{4.1a}$$

$$u_y^{(A)} = u_y^{(B)} \tag{4.1b}$$

$$u_z^{(A)} = u_z^{(B)} - 2(H + 2h)\varepsilon_{zz} \tag{4.1c}$$

where $(H + 2h)$ represents the ply thickness and the subscripts (A) and (B) refer to the top and bottom surfaces of the stack, respectively. Meanwhile, quarter symmetry was enforced along the centre lines (i.e. $u_x = 0$ along $x = 0$

and $u_y = 0$ along $y = 0$), see Figure 4.1b, and displacement continuity was assumed along the interface between the two plies. Finite element simulations were performed using a dynamic implicit version of the commercial FE package ABAQUS (version 6.12), where the constitutive laws of each ply were implemented as a user material subroutine (UMAT). The next section provides a detailed description of the prescribed constitutive laws. The stress increments were calculated using a forward Euler method for the rate independent model and a rate tangent modulus method developed by Peirce et al. (1984) for the rate dependent model. The FE simulation is exited when the failure criterion for the ply is met.

To model the slip at the interfaces, each of the above 0° and 90° plies is constructed such that it consists of one core layer (with a height H) sandwiched between two interface layers (with a height h), as illustrated in Figure 4.1c. The material coordinate system of each unidirectional (UD) ply is defined such that the *1*-direction is parallel to the fibre, the *2*-direction is the in-plane direction transverse to the fibre, and the *3*-direction is the out-of-plane direction of the ply (parallel to z-direction in the global coordinate system). Unless otherwise specified, the above global and local coordinate systems are used throughout the remainder of the current study. The deformation behaviours of the core layer and interface layers differ only in two respects:

(i) It is assumed that slip can only occur in interface layers and is prohibited in the core layer. Therefore, in the core layer, the plastic shear strain rates $\dot{\varepsilon}^{pl}_{23}$ and $\dot{\varepsilon}^{pl}_{13}$ are restricted to be zero (i.e. $\dot{\varepsilon}^{pl}_{23} = \dot{\varepsilon}^{pl}_{13} = 0$).

(ii) The interface layers represent resin rich regions between alternating plies. Since they comprise mainly of resin, the in-plane moduli of the interface (E_{11} and E_{22}) should not differ. Therefore, the elastic modulus in the interface layers is set to be equivalent to the transverse modulus (i.e. $E_{11} = E_{22}$).

Each interface layer has an element height of h and each core layer has an element height of H. Since the interface layer mainly comprises resin, its thickness should be significantly lower than the ply thickness and can be lower than the diameter of the fibres (~ 5 μm in the current case). h was assumed to be 1 μm throughout the analysis and H was set to be 129 μm (i.e. the reported ply thickness 131 μm less $2h$), as summarised in Table 4.1. Each of the core layers and interface layers was discretised using eight-noded linear brick elements with reduced integration (C3D8R in the ABAQUS notation).

Each of these layers had square dimensions in the x-y plane with a side length of $L/2$ consisting of 22,500 cuboidal elements, and with element width of $L/300$ (with L ranging from 1 mm to 15 mm).

4.2.2 Constitutive Law for Each Composite Ply

The current study adapted the finite element model given by Attwood et al. (2014) to analyse the compressive response of the CFRP cross-ply laminates. Some modifications were made to account for: (i) the strain rate sensitivity of the matrix flow and (ii) the pressure dependency of the tensile failure criterion in the carbon fibre system. In Chapter 3, cross-ply laminates with five states of cure, denoted as materials (A) to (E), were tested under uniaxial out-of-plane compression. In these experiments, laminates with low states of cure were found to be strain-rate sensitive, whereas laminates with higher states of cure were less sensitive. Therefore, the current study developed three models to account for laminates that deformed in elastic, elastic-plastic, and elastic-viscoplastic manners. The elastic model, denoted by EL, was used as a benchmark to determine the upper limit of the compressive strength of the CFRP cross-ply laminates. The elastic-plastic model, denoted by EP, was used to predict the average pressure at failure $\bar{p}_f$ of laminate types (C) to (E) that have low rate sensitivity. Finally, the elastic-viscoplastic model, denoted by EVP, was used to predict the average pressure at failure $\bar{p}_f$ of rate sensitive laminate types (A) and (B).

The remainder of this section describes the constitutive laws used in these models. Note that these constitutive laws apply to both the core layers and the interface layers in the FE simulations. However, as mentioned in the previous section, the plastic shear strain rates in the core layer were enforced to be zero (i.e. $\dot{\varepsilon}_{23}^{pl} = \dot{\varepsilon}_{23}^{pl} = 0$) and the elastic modulus E_{11} in the interface layers was enforced to be $E_{11} = E_{22}$. The input parameters utilised in the FE simulations are summarised in Table 4.1.

4.2.2.1 Elastic Constitutive Law

Consider a pair of 0° and 90° plies under out-of-plane compression in the z-direction (refer to Figure 4.1c for local coordinate system) where each ply is deforming in an elastic transverse isotropic manner. The elastic strain rate

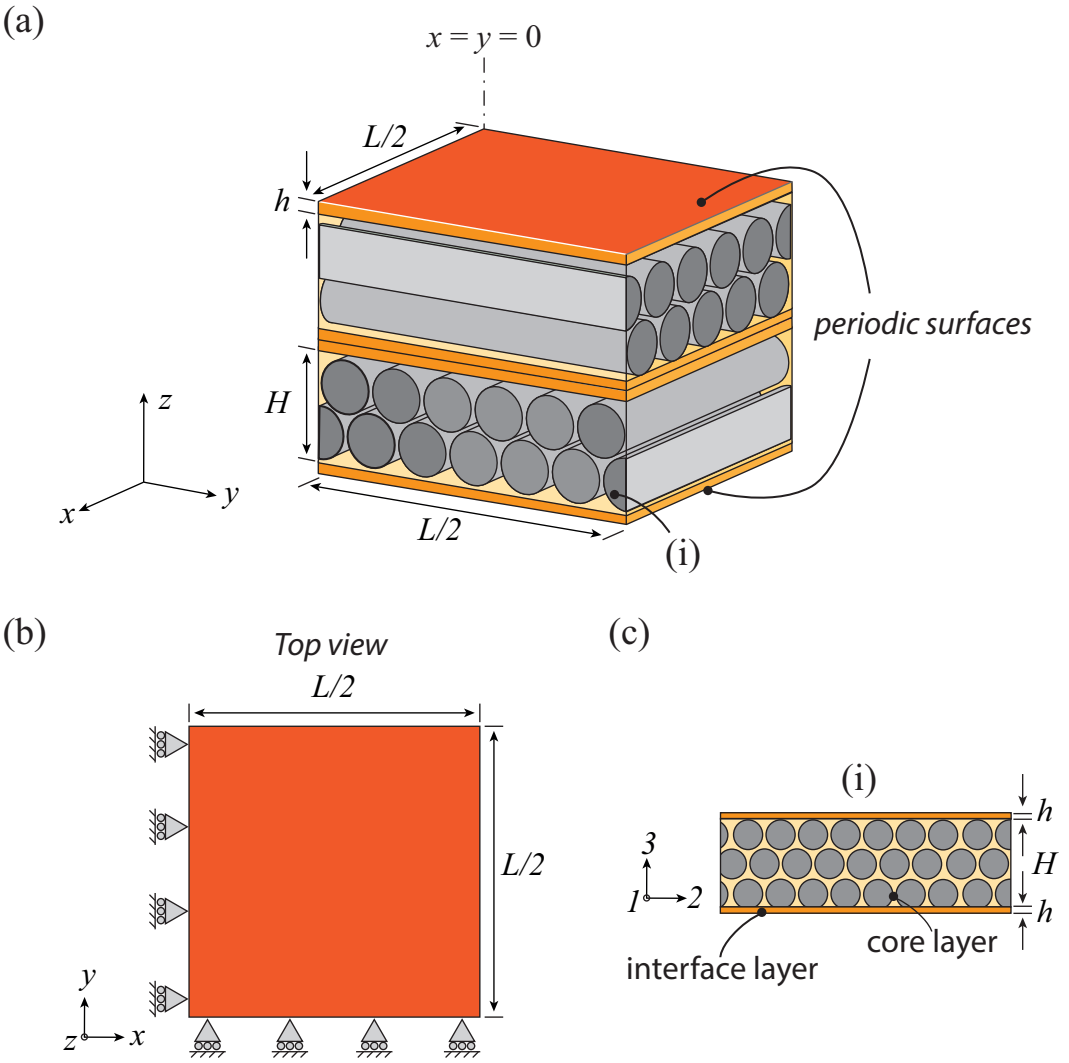

Figure 4.1: Schematic illustrations of the finite element model. a) An illustration of a unit cell equal to a quarter of a specimen (with size $L/2 \times L/2$) that comprises a single 0° ply adhered to an underlying 90° ply with global coordinates x, y, and z. Periodic boundary conditions were enforced at the top and bottom surfaces in the stack of 0° and 90° plies. b) An illustration of the plan view of the FE model with quarter symmetry enforced along the centre lines. c) An illustration of a single ply consisting of one core layer (with a height H) sandwiched between two interface layers (with a height h) with local coordinates *1*, *2*, and *3*.

Table 4.1: The geometrical parameters and material properties used in the FE and analytical models of the out-of-plane compressive responses of the CFRP cross-ply laminates.

Materials	A	B	C	D	E	–
Model types	EVP	EVP	EP	EP	EP	EL
Thickness of core layer H (μm)	129	129	129	129	129	129
Thickness of interface layer h (μm)	1	1	1	1	1	1
Reference stress σ_0 (MPa)	0.22	1.64	–	–	–	–
Reference strain rate $\dot{\varepsilon}_0$ (s^{-1})	5×10^{-4}	5×10^{-4}	–	–	–	–
Strain rate dependency m	0.45	0.39	–	–	–	–
Core layer shear yield strength τ_c (MPa)	–	–	48	87	87	–
Interfacial shear yield strength τ_i (MPa)	–	–	22	61	99	–
Matrix flow strength pressure dependency μ	0.05	0.2	0.2	0.2	0.2	–
In-plane modulus E_{11}(GPa) [a]	164	164	164	164	164	164
Transverse modulus E_{33}(GPa) [a]	10	10	10	10	10	10
Shear modulus G_{12}(GPa) [b]	5	5	5	5	5	5
Poisson's ratio ν_{23} [b]	0.43	0.43	0.43	0.43	0.43	0.43
Poisson's ratio ν_{21} [b]	0.02	0.02	0.02	0.02	0.02	0.02
Ply tensile strength S_L^+(GPa) [b]	2.7	2.7	2.7	2.7	2.7	2.7
Tensile strength pressure dependency α	2	2	2	2	2	2

[a] Data obtained from Hexcel Composites (2013).
[b] Data obtained from Marlett (2011).

components $\dot{\varepsilon}_{ij}^{el}$ inside each ply can be expressed in terms of the stress rate $\dot{\sigma}_{ij}$:

$$\begin{bmatrix} \dot{\varepsilon}_{11}^{el} \\ \dot{\varepsilon}_{22}^{el} \\ \dot{\varepsilon}_{33}^{el} \\ \dot{\varepsilon}_{23}^{el} \\ \dot{\varepsilon}_{13}^{el} \\ \dot{\varepsilon}_{12}^{el} \end{bmatrix} = \begin{bmatrix} 1/E_{11} & -\nu_{12}/E_{11} & -\nu_{12}/E_{11} & 0 & 0 & 0 \\ -\nu_{12}/E_{11} & 1/E_{33} & -\nu_{23}/E_{33} & 0 & 0 & 0 \\ -\nu_{12}/E_{11} & -\nu_{23}/E_{33} & 1/E_{33} & 0 & 0 & 0 \\ 0 & 0 & 0 & (1+\nu_{23})/E_{33} & 0 & 0 \\ 0 & 0 & 0 & 0 & 1/2G_{12} & 0 \\ 0 & 0 & 0 & 0 & 0 & 1/2G_{12} \end{bmatrix} \begin{bmatrix} \dot{\sigma}_{11} \\ \dot{\sigma}_{22} \\ \dot{\sigma}_{33} \\ \dot{\sigma}_{23} \\ \dot{\sigma}_{13} \\ \dot{\sigma}_{12} \end{bmatrix} \tag{4.2}$$

where E_{11} and E_{33} are the in-plane and out-of-plane elastic moduli of the ply, respectively, while ν_{12} and ν_{23} are the Poisson's ratios in the *1-2* and *2-3* planes, respectively. G_{12} is the shear modulus in the *1-2* plane. In the elastic model, these properties were taken from the measurements of fully cured Hexply® 8552/IM7 plies (Hexcel Composites, 2013; Marlett, 2011), as summarised in Table 4.1.

4.2.2.2 Elastic-Plastic Constitutive Law in Materials (C) to (E)

If the above ply deforms in an elastic-plastic manner, the total strain rate components $\dot{\varepsilon}_{ij}^{tot}$ are the sum of the elastic and plastic strain rates:

$$\dot{\varepsilon}_{ij}^{tot} = \dot{\varepsilon}_{ij}^{el} + \dot{\varepsilon}_{ij}^{pl} \tag{4.3}$$

The elastic strain rates $\dot{\varepsilon}_{ij}^{el}$ are expressed the same way as in Eq. (4.2).

Note that the elastic properties of material (E) in Eq. (4.2) were taken from the measurements of autoclaved cured Hexply® 8552/IM7 plies (Hexcel Composites, 2013; Marlett, 2011), as summarised in Table 4.1. The in-plane modulus E_{11} in materials (C) to (D) is expected to be dominated by the fibre and therefore set to be equal to the measurements for the fully cured material (E). The out-of-plane elastic modulus E_{33}, Poisson's ratios ν_{21} and ν_{23}, and shear modulus G_{12} have not been measured for materials (C) to (D),

but were deduced from the following arguments. (i) An analysis given in Appendix C calculates the stress state at the centre of the cross-ply specimen (i.e. ignoring shear lag effects) and reveals that the E_{33}, ν_{21}, and ν_{23} used in the elastic-plastic model only affect the predictions of compressive failure strain ε_f, but do not affect the predictions of average pressure at compressive failure $\bar{p}_f$. (ii) In the out-of-plane compression experiment of materials (C) to (D), described in Chapter 3, a stiffening response was observed prior to compressive failure $-\varepsilon_{zz} > 12\%$. This stiffening response is due to fibre compaction where fibres contact one another (Cai and Gutowski, 1992; Gutowski et al., 1987; Gutowski and Dillon, 1992; Hubert and Poursartip, 2001), which should cause the transverse modulus E_{33} of a ply to approach the transverse modulus of the fibre (i.e. $\sim$ 10 GPa for PAN-based carbon fibre (Ji et al., 2015), which is similar to the transverse modulus of a ply at the fully cured state). Since the models in this study focus on the failure of the laminates (after stiffening has occurred), it is assumed that E_{33} for all materials is equal to the modulus at the compacted state, i.e. 10 GPa. Therefore, the current study assumes that all the elastic properties in materials (C) to (D) are the same as those measured in material (E), as summarised in Table 4.1.

The plastic strain rate components $\dot{\varepsilon}_{ij}^{pl}$ can be calculated based on the chosen yield surface of a single ply. Attwood et al. (2014) have proposed that a yield surface F of a single unidirectional Dyneema® ply is comprised of four facets (f_1, f_2, f_3, and f_4). This yield surface F is adopted for the CFRP UD plies and is presented below.

$$f_1 \equiv \frac{|\sigma_{22} - \sigma_{33}|}{2} + \mu\sigma_h \tag{4.4a}$$

$$f_2 \equiv |\sigma_{12}| + \mu\sigma_h \tag{4.4b}$$

$$f_3 \equiv |\sigma_{23}| + \mu\sigma_h \tag{4.4c}$$

$$f_4 \equiv |\sigma_{13}| + \mu\sigma_h \tag{4.4d}$$

where $\sigma_h \equiv (\sigma_{22} + \sigma_{33})/2$ is the in-plane hydrostatic stress in the *2-3* plane and μ is a coefficient representing the pressure dependency of the matrix shear

strength.

Yielding occurs when the yield criterion is satisfied:

$$F \equiv max(f_1, f_2, f_3, f_4) - \tau_y = 0 \tag{4.5}$$

where τ_y is matrix shear yield strength at zero hydrostatic stress, $\sigma_h = 0$.

Note that the current FE models treat the core layer and the interface layers in a ply as separate materials. Depending on the particular laminate system and the selected manufacturing process, the matrix shear yield strength τ_y in the core layer (denoted τ_c) can differ from that in the interface layer (denoted τ_i). τ_c represents the in-plane matrix shear strength within a ply, whereas τ_i represents the interlaminar shear strength between the alternating plies. The shear yield strengths τ_c and τ_i of materials (C) to (E) were independently measured through a $\pm 45°$ tensile test and a short beam shear test, respectively. In brief, the shear response of materials (C) to (E) was insensitive to the applied strain rate in the range of $10^{-4}s^{-1}$ to $10^{-1}s^{-1}$. Also, the shear yield strengths (defined to be the τ at $\gamma = 5\%$) measured from $\pm 45°$ tensile test (i.e. τ_c) were different from those in the short beam shear test (i.e. τ_i). The values of τ_c and τ_i in the FE simulation were taken from these measurements, which are summarised in Table 4.1.

The other key material property in Eq. (4.4a) is the pressure dependence coefficient μ of the CFRP plies. For the current CFRP system, μ has not yet been measured and is thus treated as a fitting parameter. A short analysis using available data from the literature suggests that $\mu \sim 0.2$ for the cured CFRP plies in the current system, as demonstrated below.

Multiple research groups have conducted out-of-plane compression tests on 90° plies of carbon fibre/epoxy and glass fibre/epoxy composites with superimposed hydrostatic pressure, see (Hine et al., 2005, 1999; Pae and Phee, 1995; Parry and Wronski, 1990). In these studies, 90° plies were first loaded to a constant hydrostatic pressure with a magnitude P in a triaxial pressure cell. 90° plies were then compressed in the *3*-direction illustrated in Figure 4.2. The stress states during the test were $\sigma_{11} = \sigma_{22} = -P$ and $\sigma_{33} = -P + \sigma_a$, where σ_a is the applied compressive stress. In general, these researchers observed that both the compressive yield strength and the failure strength scale proportionally with the superimposed hydrostatic pressure. Figure 4.2 presents these data in terms of the normalised stress components σ_{22}/τ_y and

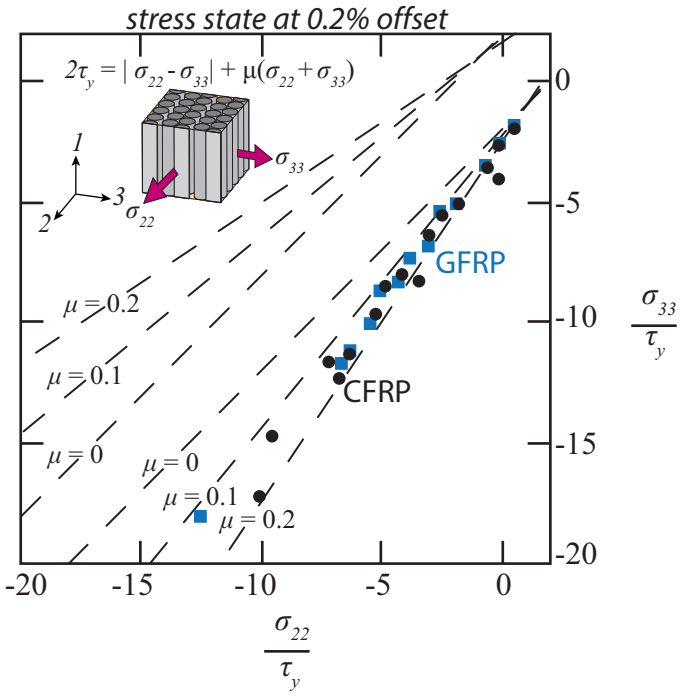

Figure 4.2: Plot of normalised stress components σ_{22}/τ_y and σ_{33}/τ_y at 0.2% offset strength in the σ_{33} versus ε_{33} stress-strain responses of CFRP UD plies and GFRP UD plies subjected to out-of-plane compression with superimposed hydrostatic pressure. Data of CFRP were obtained from Hine et al. (1999); Pae and Phee (1995). Data of GFRP were obtained from Hine et al. (2005); Parry and Wronski (1990).

σ_{33}/τ_y at yield. The yield point was defined to be the 0.2% offset strength in the σ_{33} versus ε_{33} stress-strain response.

These data are then compared to the currently proposed yielding criterion of a ply in the *2-3* plane ($\tau_y = f_1$) i.e.:

$$2\tau_y = |\sigma_{22} - \sigma_{33}| + \mu\,(\sigma_{22} + \sigma_{33}) \tag{4.6}$$

τ_y in the figure were obtained from the uniaxial out-of-plane compression of a UD ply when $\sigma_{22} = 0$ (i.e. $\tau_y = \sigma_{33}\,(\mu - 1)\,/2$), where σ_{33} is the 0.2% offset compression yield strength in the σ_{33} versus ε_{33} response. The data reveals that both carbon fibre/epoxy and glass fibre/epoxy composites are pressure dependent with a coefficient μ at ~ 0.2 and ~ 0.1, respectively. Preliminary FE simulation trials also showed that $\mu = 0.2$ is appropriate to predict the compressive response of materials (C) to (E) in the current study. Thus $\mu = 0.2$ is employed in further FE modelling, as shown in Table 4.1.

The plastic strain rate in the FE model is derived from the following

non-associated flow rule. For each of the yielding facets f_1, f_2, f_3, and f_4 in Eq. (4.5), the corresponding flow potentials g_1, g_2, g_3, and g_4 are:

$$g_1 \equiv \frac{|\sigma_{22} - \sigma_{33}|}{2} \tag{4.7a}$$

$$g_2 \equiv |\sigma_{12}| \tag{4.7b}$$

$$g_3 \equiv |\sigma_{23}| \tag{4.7c}$$

$$g_4 \equiv |\sigma_{13}| \tag{4.7d}$$

Assuming plastic flow with no strain hardening, the plastic strain rate components are written as:

$$\dot{\varepsilon}_{ij}^{pl} \equiv \dot{\lambda}_k \frac{\partial g_k}{\partial \sigma_{ij}} = \dot{\lambda}_1 \frac{\partial g_1}{\partial \sigma_{ij}} + \dot{\lambda}_2 \frac{\partial g_2}{\partial \sigma_{ij}} + \dot{\lambda}_3 \frac{\partial g_3}{\partial \sigma_{ij}} + \dot{\lambda}_4 \frac{\partial g_4}{\partial \sigma_{ij}} \tag{4.8}$$

where $\dot{\lambda}_k$ are non-negative plastic multipliers associated with each of the flow potentials g_k, and k is the summation index. Each of the $\dot{\lambda}_k$ can be individually calculated by stating:

$$\frac{\partial f_k}{\partial \sigma_{ij}} d\sigma_{ij} = \frac{\partial f_k}{\partial \sigma_{ij}} \left(C_{ijmn} \dot{\varepsilon}_{mn} - \dot{\lambda}_l C_{ijmn} \frac{\partial g_l}{\partial \sigma_{ij}} \right) = 0 \tag{4.9}$$

C_{ijmn} is the elastic modulus, and l is the summation index.

4.2.2.3 Elastic-viscoplastic Constitutive Law in Materials (A) and (B)

If the ply deforms in an elastic-viscoplastic manner, the total strain rate components $\dot{\varepsilon}_{ij}^{tot}$ are the sum of the elastic and viscoplastic strain rates:

$$\dot{\varepsilon}_{ij}^{tot} = \dot{\varepsilon}_{ij}^{el} + \dot{\varepsilon}_{ij}^{pl} \tag{4.10}$$

The elastic strain rate components $\dot{\varepsilon}_{ij}^{el}$ are expressed in the same manner as in Eq. (4.2). In the elastic-viscoplastic model, in-plane modulus E_{11} in Eq. (4.2) for materials (A) and (B) is expected to be dominated by the in-plane

modulus of the fibre and therefore set to equal the measurement for the fully cured material (E). The out-of-plane elastic modulus E_{33}, Poisson's ratios ν_{21} and ν_{23}, and shear modulus G_{12} have not been measured for materials (A) and (B), but are assumed to be equal to the measurements made for fully cured material (E) as per the arguments presented in Section 4.2.2.2. The values are summarised in Table 4.1.

Analogous to section 4.2.2.2, a non-associated viscoplastic flow law that consists of four facets is proposed such that the viscoplastic strain rate components $\dot{\varepsilon}_{ij}^{pl}$ are derived from the equivalent viscoplastic strain rate $\dot{\varepsilon}_e^{(k)}$ and the viscoplastic flow potentials Φ_k:

$$\dot{\varepsilon}_{ij}^{pl} = \dot{\varepsilon}_e^{(k)} \frac{\partial \Phi_k}{\partial \sigma_{ij}} = \dot{\varepsilon}_e^{(1)} \frac{\partial \Phi_1}{\partial \sigma_{ij}} + \dot{\varepsilon}_e^{(2)} \frac{\partial \Phi_2}{\partial \sigma_{ij}} + \dot{\varepsilon}_e^{(3)} \frac{\partial \Phi_3}{\partial \sigma_{ij}} + \dot{\varepsilon}_e^{(4)} \frac{\partial \Phi_4}{\partial \sigma_{ij}} \tag{4.11}$$

where k is the summation index. The equivalent viscoplastic strain rates $\dot{\varepsilon}_e^{(k)}$ in Eq. (4.11) are proposed to follow a viscoplastic power law:

$$\dot{\varepsilon}_e^{(k)} = \begin{cases} \dot{\varepsilon}_0 \left(\frac{\hat{\sigma}_k}{\sigma_0} \right)^{1/m} & for\ \hat{\sigma}_k > 0 \\ 0 & for\ \hat{\sigma}_k \leq 0 \end{cases}, \ k = 1, 2, 3, 4 \tag{4.12}$$

where σ_0 is the reference stress, $\dot{\varepsilon}_0$ is the reference strain rate, m is the strain rate sensitivity exponent, and $\hat{\sigma}_k$ are the proposed over stresses that govern the magnitude of $\dot{\varepsilon}_e^{(k)}$ in each of the four facets.

Recall that the current FE models treat the core layer and the interface layers in a ply as separate materials. Depending on the particular laminate system and the selected manufacturing process, the flow parameters σ_0, $\dot{\varepsilon}_0$, and m in the core layer can differ from those in the interface layer. The flow parameters σ_0, $\dot{\varepsilon}_0$, and m in the core layer and the interface layer can be determined based on their shear responses in a $\pm 45°$ tensile test and a short beam shear test, respectively. In brief, the shear responses of materials (A) and (B) were both sensitive to the applied shear strain rate $\dot{\gamma}$. Also, the shear flow parameters measured from the $\pm 45°$ tensile test were the same as those from the short beam shear test, including the reference shear stress τ_0 (defined to be the τ at shear strain of $\gamma = 5\%$ and tested at a reference shear strain rate $\dot{\gamma} = \dot{\gamma}_0$), reference shear strain rate $\dot{\gamma}_0$, and strain rate sensitivity exponent m. As a result, in the current FE models of materials (A) and (B), the flow parameters σ_0, $\dot{\varepsilon}_0$, and m used in the core layer and in the interface layers were set to be

equal: with the reference stress set as $\sigma_0 = 2\tau_0$ and the reference strain rate set as $\dot{\varepsilon}_0 = \dot{\gamma}_0/2$. These parameters are summarised in Table 4.1.

The over stresses $\hat{\sigma}_k$ in Eq. (4.12) are proposed to be:

$$\hat{\sigma}_1 \equiv |\sigma_{22} - \sigma_{33}| + 2\mu\sigma_h \tag{4.13a}$$

$$\hat{\sigma}_2 \equiv |\sigma_{12}| + |\sigma_{21}| + 2\mu\sigma_h \tag{4.13b}$$

$$\hat{\sigma}_3 \equiv |\sigma_{23}| + |\sigma_{32}| + 2\mu\sigma_h \tag{4.13c}$$

$$\hat{\sigma}_4 \equiv |\sigma_{13}| + |\sigma_{31}| + 2\mu\sigma_h \tag{4.13d}$$

where $\sigma_h \equiv (\sigma_{22} + \sigma_{33})/2$ is the in-plane hydrostatic stress in the *2-3* plane and μ is a coefficient representing the pressure dependence of the matrix flow strength. Note that μ is a fitting parameter in the current study. An analysis in Section 4.2.2.2 showed that $\mu \sim 0.2$ is appropriate for the CFRP laminates containing fully cured thermoset epoxy matrix. However, the value of μ in Dyneema® plies containing a softer thermoplastic polyurethane matrix is shown to be significantly lower at $\mu \sim 0.05$ (Attwood et al., 2014). Preliminary FE simulation trials showed that $\mu = 0.05$ is appropriate to predict the average pressure at compressive failure $\bar{p}_f$ of uncured material (A), whereas $\mu = 0.2$ is appropriate to predict the $\bar{p}_f$ of the partially cured material (B). These are the values of μ employed in further FE simulations, as shown in Table 4.1.

The viscoplastic flow potentials Φ_k in Eq. (4.11) are defined to be:

$$\Phi_1 \equiv |\sigma_{22} - \sigma_{33}| \tag{4.14a}$$

$$\Phi_2 \equiv |\sigma_{12}| + |\sigma_{21}| \tag{4.14b}$$

$$\Phi_3 \equiv |\sigma_{23}| + |\sigma_{32}| \tag{4.14c}$$

$$\Phi_4 \equiv |\sigma_{13}| + |\sigma_{31}| \tag{4.14d}$$

It is worth noting that the proposed over stresses $\hat{\sigma}_k$ in Eq. (4.14a) are selected such that $\hat{\sigma}_k = \Phi_k + 2\mu\sigma_h$.

Finally, the viscoplastic strain rate components are expressed according to Eq. (4.11). For instance, the viscoplastic direct strain rate $\dot{\varepsilon}^{pl}_{22}$ is expressed as:

$$\dot{\varepsilon}^{pl}_{22} = -\dot{\varepsilon}^{pl}_{33} = sgn\left(\sigma_{22} - \sigma_{33}\right)\dot{\varepsilon}_0 \left(\frac{\hat{\sigma}_1}{\sigma_0}\right)^{1/m} \tag{4.15}$$

and the viscoplastic shear strain rate $\dot{\varepsilon}^{pl}_{12}$ is expressed as:

$$\dot{\varepsilon}^{pl}_{12} = sgn\left(\sigma_{12}\right)\dot{\varepsilon}_0 \left(\frac{\hat{\sigma}_2}{\sigma_0}\right)^{1/m} \tag{4.16}$$

4.2.3 Failure Criterion for Each Composite Ply

As mentioned in Section 4.1.3, the tensile strength of dry carbon fibre tows and carbon fibre/epoxy plies has been shown to decrease with an increase in superimposed hydrostatic pressure (Hine et al., 2005, 1999; Parry and Wronski, 1985, 1986; Sigley et al., 1991; Zinoviev and Tsvetkov, 1998). To account for the pressure dependency of fibre tensile strength, the following tensile failure criterion is proposed for the carbon fibre UD plies used in the current study:

$$\sigma_{11} \leq S^+_L + \frac{\alpha}{2}(\sigma_{22} + \sigma_{33}) \tag{4.17}$$

where S^+_L is the ply tensile strength at zero $\sigma_h \equiv (\sigma_{22}+\sigma_{33})/2$ (i.e. the uniaxial tensile strength of a UD ply), and α is the coefficient that represents the pressure dependency of the fibre/ply tensile strength. The pressure dependence coefficient of ply tensile strength α should not be confused with the above pressure dependence coefficient of the matrix flow strength μ. Note that when $\alpha = 0$ the above tensile failure criterion collapses to the criterion ($\sigma_{11} \leq S^+_L$) proposed by Attwood et al. (2014).

A brief analysis using available data from the literature suggests that $\alpha \sim 2$ for the cured CFRP plies in the current system, as demonstrated below.

Hine et al. (1999) showed that the tensile strength of dry carbon fibre tows declines with an increase in superimposed hydrostatic pressure. Similarly, multiple research groups have conducted in-plane tensile tests on 0° plies of carbon fibre/epoxy, glass fibre/epoxy, and Kevlar® composites with

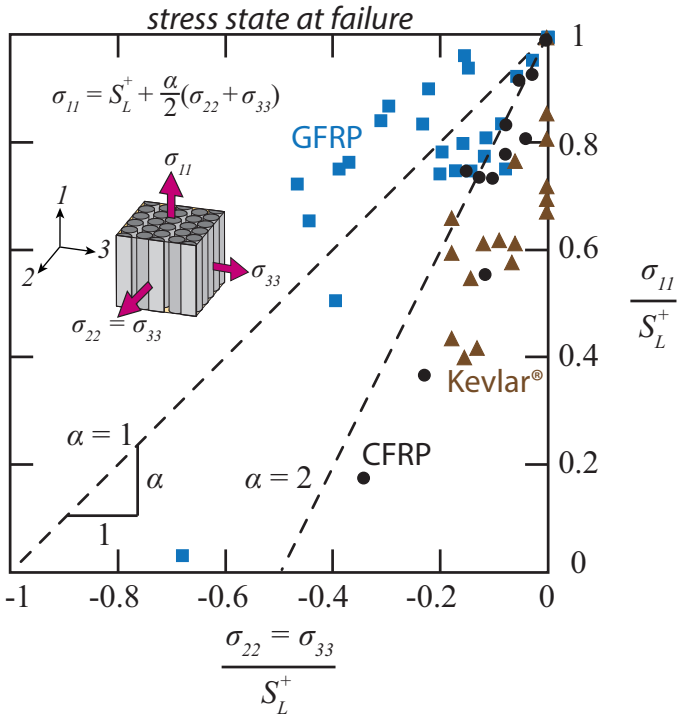

Figure 4.3: Plot of normalised stress components σ_{11}/S_L^+ and $\sigma_{22}/S_L^+ = \sigma_{33}/S_L^+$ at ply tensile failure of a UD composite ply subjected to in-plane tension with superimposed hydrostatic pressure. Data of CFRP were obtained from (Hine et al., 1999; Parry and Wronski, 1985). Data of GFRP were obtained from (Hine et al., 2005; Parry and Wronski, 1986; Sigley et al., 1991). Data of Kevlar® composites were obtained from (Zinoviev and Tsvetkov, 1998).

superimposed hydrostatic pressure. See (Hine et al., 1999; Parry and Wronski, 1985) for data on carbon fibre/epoxy composites; (Hine et al., 2005; Parry and Wronski, 1986; Sigley et al., 1991) for data on glass fibre/epoxy composites; and (Zinoviev and Tsvetkov, 1998) on Kevlar® composites. In general, they found that the tensile strength of 0° plies in these composites declined with increasing superimposed pressure. In these studies, 0° plies were first loaded to a constant hydrostatic pressure with a magnitude P in a triaxial pressure cell, followed by tensile loading in the *1*-direction parallel to the fibre. The stress state at ply tensile failure was $\sigma_{22} = \sigma_{33} = -P$ and $\sigma_{11} = -P + \sigma_a$, where σ_a is the applied tensile stress. Figure 4.3 presents these data in terms of the normalised stress components σ_{11}/S_L^+ and $\sigma_{22}/S_L^+ = \sigma_{33}/S_L^+$ at ply tensile failure.

This figure compares these data to the pressure dependent tensile failure criterion of 0° plies proposed in Eq. (4.17) and reveals that the pressure dependence coefficient α ranges from ~ 1 to ~ 2 in the different composite

systems, with $\alpha \sim 2$ for CFRP composites. Consequently, the current FE model assumes that $\alpha = 2$ in all the studied CFRP plies and the S_L^+ is determined based on ply tensile strength at atmospheric pressure (measured by Hexcel Composites (2013)). These values are summarised in Table 4.1.

4.3 Analytical Models for the Out-of-plane Compressive Strength

Further to the finite element simulation discussed above, additional insight was derived from analytical models. The analytical approach focused on: (i) the effect of specimen side length L on the average pressure at compressive failure $\bar{p}_f$ and (ii) the effect of out-of-plane strain rate $\dot{\varepsilon}_{33}^{tot}$ on the $\bar{p}_f$ and shear lag length λ. This study developed three analytical models to predict the average pressure at compressive failure $\bar{p}_f$ for laminates that deform in elastic, elastic-plastic, and elastic-viscoplastic manners. All these models were based on the proposed constitutive laws established in Section 4.2.2. The elastic analytical model in this section was based on laminate plate theory assuming no slip between the alternating plies. It is used as a benchmark to determine the upper limit of the compressive strength of the CFRP cross-ply laminates. The elastic-plastic analytical model was applied to laminate types (C) to (E) that have low rate sensitivity, while the elastic-viscoplastic analytical model was applied to rate sensitive laminate types (A) and (B). The material properties and specimen geometry parameters used in each of these models are summarised in Table 4.1. In this section, only the calculations of $\bar{p}_f$ are presented. A detailed derivation of the models, as well as the predictions of compression failure strain ε_f, can be found in Appendix C.

4.3.1 Elastic Laminate Plate Theory for the Out-of-plane Compressive Strength

Consider a pair of 0° and 90° plies (with specimen side length L) under out-of-plane compression in the z-direction, with each ply deforming in an elastic transverse isotropic manner. A schematic illustration is provided in Figure 4.4, with the 0° ply labelled A and the 90° ply labelled B. The current elastic laminate plate theory calculates the stress state at the centre

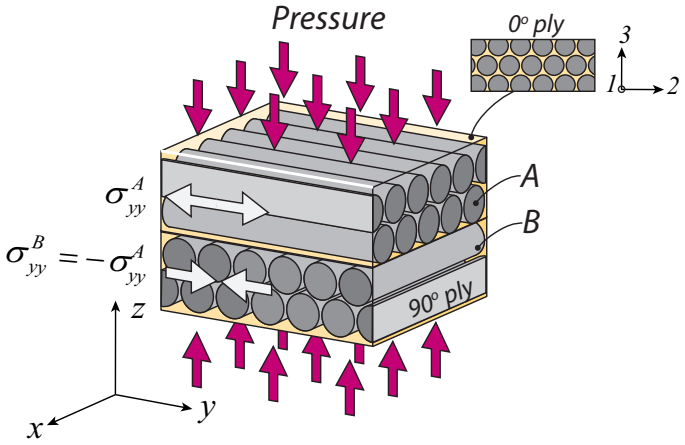

Figure 4.4: Schematic illustration of a pair of 0°/90° plies under out-of-plane compression.

$(x = y = 0)$ of a specimen where alternating plies are perfectly bonded to each other with no slip. Furthermore, this model serves as an upper limit on the compressive strength of a large specimen in which the edge effect of the specimen (i.e. shear lag effect) is negligible.

For the centre element where there is no slip, the elastic strain components ε^{el}_{ij} can be expressed in terms of σ_{ij}:

$$\begin{bmatrix} \varepsilon^{el}_{11} \\ \varepsilon^{el}_{22} \\ \varepsilon^{el}_{33} \end{bmatrix} = \begin{bmatrix} 1/E_{11} & -\nu_{12}/E_{11} & -\nu_{12}/E_{11} \\ -\nu_{12}/E_{11} & 1/E_{33} & -\nu_{23}/E_{33} \\ -\nu_{12}/E_{11} & -\nu_{23}/E_{33} & 1/E_{33} \end{bmatrix} \begin{bmatrix} \sigma_{11} \\ \sigma_{22} \\ \sigma_{33} \end{bmatrix} \tag{4.18}$$

In Figure 4.4, layer A is subjected to a tensile stress σ^A_{yy}, and layer B experiences a compressive stress $\sigma^B_{yy} = -\sigma^A_{yy}$ since there is no net force in the y-direction. In the local coordinate system, this force equilibrium causes $\sigma_{22} = -\sigma_{11}$.

The Poisson's ratio ν_{12} in Eq. (4.18) is negligible and can be assumed to be $\nu_{12} = 0$. For the out-of-plane compression of a cross-ply laminate, Eq. (4.18) can be written as:

$$\begin{bmatrix} \varepsilon_{11}^{el} \\ \varepsilon_{22}^{el} \\ \varepsilon_{33}^{el} \end{bmatrix} = \begin{bmatrix} 1/E_{11} & 0 & 0 \\ 0 & 1/E_{33} & -\nu_{23}/E_{33} \\ 0 & -\nu_{23}/E_{33} & 1/E_{33} \end{bmatrix} \begin{bmatrix} \sigma_{11} \\ -\sigma_{11} \\ \sigma_{33} \end{bmatrix} \tag{4.19}$$

In Figure 4.4, layer A and layer B are under equal straining in the x and y directions. In the local coordinate system, this strain compatibility causes $\varepsilon_{11}^{el} = \varepsilon_{22}^{el}$. The relationship between the ply tensile stress parallel to the fibre σ_{11} and the out-of-plane stress of a ply σ_{33} can be expressed as:

$$\sigma_{11} = \sigma_{33} \left(\frac{-\nu_{23} E_{11}}{E_{11} + E_{33}} \right) \tag{4.20}$$

As out-of-plane compression proceeds, σ_{11} and σ_{33} increase in magnitude. Compressive failure occurs when the ply tensile failure criterion in Eq. (4.17) is met; the ply tensile failure criterion can be rewritten as:

$$S_L^+ - \left(1 + \frac{\alpha}{2}\right) \sigma_{11} + \frac{\alpha}{2} \sigma_{33} = 0 \tag{4.21}$$

The compressive pressure $p \equiv -\sigma_{zz} \equiv -\sigma_{33}$ of the centre element at compressive failure can be determined by substituting σ_{11} from Eq. (4.20) into Eq. (4.17):

$$p = -\sigma_{33} = \frac{2S_L^+ \left(E_{11} + E_{33}\right)}{\left(2\nu_{23} + \alpha\nu_{23} + \alpha\right) E_{11} + \alpha E_{33}} \tag{4.22}$$

4.3.2 Elastic-plastic Analytical Model

If the above pair of 0° and 90° plies deforms elastically in the fibre direction ($\varepsilon_{11}^{pl} = 0$) and deforms in an elastic-plastic manner in the transverse directions due to the matrix yielding, then a plastic shear lag effect will occur. Thus, the local pressure $p \equiv -\sigma_{zz} \equiv -\sigma_{33}$ increases from the periphery of the specimen toward the centre and then remains at a maximum pressure after the shear lag length λ is reached, as shown in Figure 4.5. Within the shear lag zone, the stress states of the ply can be calculated by using the yielding criterion consisting of four facets that was established in Eq. (4.21). Consider a section of the specimen on the *2-3* plane of a ply, and define the coordinate

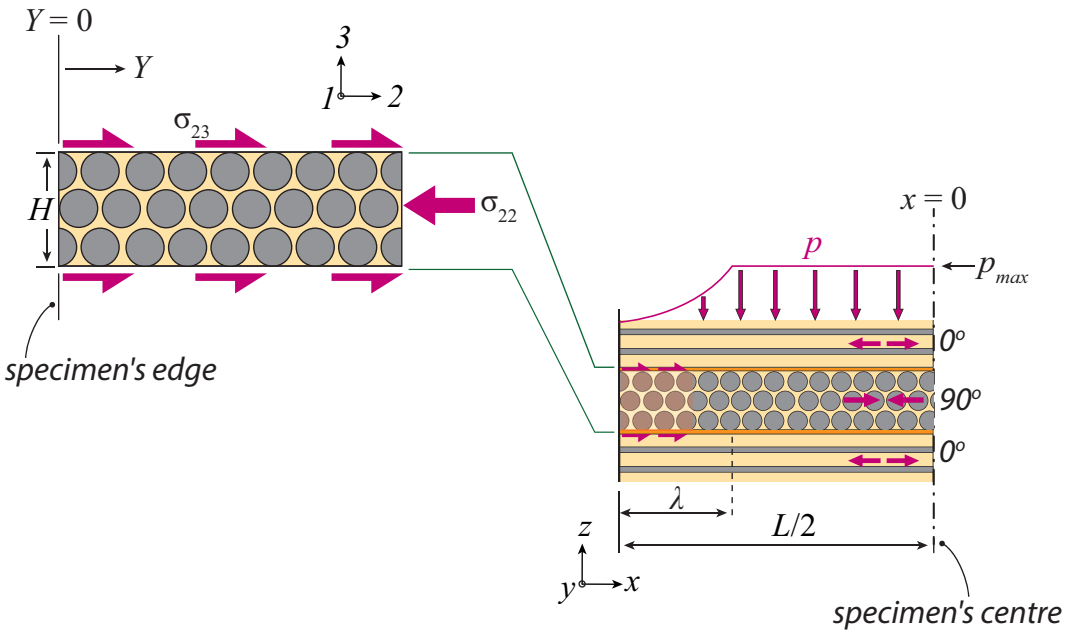

Figure 4.5: A free-body diagram of a section of the specimen on the *2-3* plane of a ply with the *1*-direction defined as parallel to the fibre, and the coordinate $Y = L/2 - x_2$ defined such that $Y = 0$ and $x_2 = L/2$ is the free edge of the specimen.

$Y = L/2 - x_2$ as shown in Figure 4.5 such that $Y = 0$ is the free edge of the specimen at $x_2 = L/2$ and $Y = L/2$ is at the centre of the specimen.

The normal stresses σ_{22} and σ_{33} within the core region of the layer can be determined by the yielding criterion f_1 previously given in Eq. (4.5). Given that the out-of-plane stress is $\sigma_{33} \leq 0$ and that $|\sigma_{33}| > |\sigma_{22}|$, the relationship between σ_{22} and σ_{33} in the core of a ply can be expressed as:

$$\sigma_{33} = \frac{2\tau_c - \sigma_{22}(\mu + 1)}{\mu - 1} \tag{4.23}$$

where τ_c with subscript c is the shear yield strength within the core region of a ply at zero $\sigma_h \equiv (\sigma_{22} + \sigma_{33})/2$. Similarly, the yielding criterion f_3 previously given in Eq. (4.5) determines the relationship among σ_{23}, σ_{22}, and σ_{33} at the interface:

$$\sigma_{23} = \tau_i - \frac{\mu}{2}(\sigma_{22} + \sigma_{33}) \tag{4.24}$$

where τ_i with subscript i is the interlaminar shear yield strength at zero $\sigma_h \equiv (\sigma_{22} + \sigma_{33})/2$. Recall that the matrix shear yield strength in the core layer τ_c can differ from that in the interface layer τ_i depending on the particular

laminate system and the selected manufacturing process. For materials (C) to (E), τ_c measured from $\pm 45^\circ$ tensile test differed from τ_i measured from short beam shear test, as set out in Table 4.1. Substituting σ_{33} in Eq. (4.23) into Eq. (4.24) gives:

$$\sigma_{23} = \frac{(1-\mu)\,\tau_i + \mu\tau_c - \mu\sigma_{22}}{1-\mu} \tag{4.25}$$

Assuming the stress is uniform throughout the thickness of the ply, equilibrium in the *2*-direction dictates that:

$$H\frac{d\sigma_{22}}{dY} = -2\sigma_{23} \tag{4.26}$$

where H is the height of the core layer. Recall that $\sigma_{22} = -\sigma_{11}$ due to force equilibrium. Substituting for σ_{23} from Eq. (4.25) and integrating using the boundary condition $\sigma_{22} = 0$ at $Y = 0$ yields:

$$\sigma_{11} = -\sigma_{22} = \left[\left(\frac{1-\mu}{\mu}\right)\tau_i + \tau_c\right]\left[exp\left(\frac{aY}{H}\right) - 1\right] \tag{4.27}$$

where $a \equiv 2\mu/(1-\mu)$. σ_{11} exponentially increases from the free edge ($Y = 0$) toward the centre. At the end of the shear lag zone ($Y = \lambda$), σ_{11} remains constant at a maximum value of σ_{11}^{max}. The size of the shear lag zone λ for a given σ_{11}^{max} is:

$$\lambda = \frac{H\,(1-\mu)}{2\mu} ln\left[1 + \frac{\sigma_{11}^{max}}{\left(\frac{1-\mu}{\mu}\right)\tau_i + \tau_c}\right] \tag{4.28}$$

The corresponding out-of-plane pressure $p \equiv -\sigma_{33}$ within the shear lag zone can be obtained by substituting for σ_{22} from Eq. (4.23) into Eq. (4.27):

$$p = \frac{(1+\mu)\left[\left(\frac{1-\mu}{\mu}\right)\tau_i + \tau_c\right]\left[exp\left(\frac{aY}{H}\right) - 1\right] + 2\tau_c}{1-\mu} \text{ for } (Y \leq \lambda) \tag{4.29}$$

while the out-of-plane pressure p remains constant at a maximum value of p_{max} outside of the shear lag zone; it can be determined from Eq. (4.23):

$$p_{max} = \frac{(1+\mu)\,\sigma_{11}^{max} + 2\tau_c}{1-\mu} \text{ for } (Y > \lambda) \tag{4.30}$$

Recall that Figure 4.5 illustrates that the pressure p increases from the

periphery of the specimen toward the centre in an exponential manner according to Eq. (4.29) and then remains at p_{max} according to Eq. (4.30) after the shear lag length λ is reached. It is worth noting that the sharp transition of p at the edge of the shear lag zone is a direct consequence from the proposed constitutive laws of a ply. Such a sharp transition of pressure profile was not observed in the experiments presented in Chapter 3. An asymmetric sigmoid function similar to that proposed by Fukuda and Chou (1981) may describe the pressure profile in a more realistic manner. However, the above sharp transition had little influence on the final calculation of the compressive load F and the average pressure $\bar{p}$ at indirect tension failure. Thus, for the sake of simplicity, the model in the current study assumes that the pressure profile behaves as illustrated in Figure 4.5.

As out-of-plane compression proceeds, σ_{11}^{max} and p_{max} at the centre of the specimen increase in magnitude. Indirect tension failure occurs when the ply tensile failure criterion in Eq. (4.17) is met; σ_{11}^{max} at failure is:

$$\sigma_{11}^{max} = \frac{2S_L^+ - \alpha p_{max}}{2 + \alpha} \tag{4.31}$$

The maximum pressure p_{max} at indirect tension failure p_f can be determined by substituting σ_{11}^{max} in Eq. (4.31) into Eq. (4.30):

$$p_f = \frac{(2 + \alpha)\,\tau_c + (1 + \mu)\,S_L^+}{1 - \mu + \alpha} \tag{4.32}$$

Similarly, the maximum in-plane tensile stress σ_{11}^{max} at indirect tension failure σ_{11}^f is:

$$\sigma_{11}^f = \frac{(2 + \alpha)\,\tau_c + (2 - 2\mu + \alpha - \alpha\mu)\,S_L^+}{(2 + \alpha)\,(1 - \mu + \alpha)} \tag{4.33}$$

Note that within the shear lag zone λ, the local pressure p and ply tensile stress σ_{11} are at a lower magnitude than p_f and σ_{11}^f, respectively. The critical shear lag length λ_c that is required for the pressure to build up to p_f and thus to cause indirect tension failure can be determined by substituting σ_{11}^f into Eq. (4.28):

$$\lambda_c = \frac{H\,(1 - \mu)}{2\mu} ln \left[1 + \frac{\sigma_{11}^f}{\left(\frac{1-\mu}{\mu}\right)\tau_i + \tau_c} \right] \tag{4.34}$$

For a square specimen with specimen side length L where the entire specimen is within the shear lag zone (i.e. $L/2 < \lambda_c$), the specimen would deform through shear yielding instead of failing by indirect tension. As a result, the total compressive load F and the average pressure at failure $\bar{p}_f$ both depend on the specimen size. The compressive load F can be determined by integrating the local pressure across the entire specimen:

$$F = 4 \int_0^{L/2} \int_0^{L/2} p dY dX \quad \text{for } (L/2 < \lambda_c) \text{ and} \tag{4.35}$$

$$F = 4 \int_0^{\lambda_c} \int_0^{\lambda_c} p dY dX + 4 (L - 2\lambda_c) \int_0^{\lambda_c} p dY + p_f (L - 2\lambda_c)^2 \quad \text{for } (L/2 \geq \lambda_c) \tag{4.36}$$

Finally, the average pressure at failure $\bar{p}_f$ is defined to be:

$$\bar{p}_f \equiv \frac{F}{L^2} \tag{4.37}$$

The current elastic-plastic analytical model provides some insight into the influence of matrix shear strength and specimen size on the average pressure at failure $\bar{p}_f$. Eq. (4.32) and Eq. (4.34) in the current model show that both the maximum pressure p_f and shear lag length λ_c at indirect tension failure are affected by the matrix shear strengths (τ_c and τ_i) but are independent of the specimen side length L. Increasing matrix shear strength would raise the p_f and decrease the λ_c, having the combined effect of increasing the average pressure at failure $\bar{p}_f$. For laminates with the same state of cure, both p_f and λ_c would remain constant regardless of the specimen side length L. However, as the specimen side length L increases, the proportion of the specimen that consists of the shear lag zone (with length λ_c) would decrease, having the effect of increasing average pressure at failure $\bar{p}_f$.

4.3.3 Elastic-viscoplastic Analytical Model

If the 0° and 90° plies deform in an elastic-viscoplastic manner, the stress components of a ply in the shear lag zone can be related to each other using the viscoplastic flow law described in Eq. (4.13a). Given that the out-of-plane

stress is $\sigma_{33} \leq 0$ and $|\sigma_{33}| > |\sigma_{22}|$, the relationship between σ_{22} and σ_{33} within the core region of the ply can be expressed as:

$$\hat{\sigma}_1^{(c)} = \sigma_{22}\,(\mu + 1) + \sigma_{33}\,(\mu - 1) \tag{4.38}$$

where $\hat{\sigma}_1^{(c)}$ with superscript c is the over stress $\hat{\sigma}_1$ in the core layer. Similarly, the relationship between, σ_{23}, σ_{22} and σ_{33} at the interface can be expressed as:

$$\hat{\sigma}_3^{(i)} = 2\sigma_{23} + \mu\sigma_{22} + \mu\sigma_{33} \tag{4.39}$$

where $\hat{\sigma}_3^{(i)}$ with superscript i is the over stress $\hat{\sigma}_3$ at the interface. $\hat{\sigma}_1^{(c)}$ and $\hat{\sigma}_3^{(i)}$ can be expressed in terms of the plastic strain rate by rearranging the power law in Eq. (4.11):

$$\hat{\sigma}_1^{(c)} = \sigma_0^{(c)} \left(\frac{\left| \dot{\varepsilon}_{33}^{pl} \right|}{\dot{\varepsilon}_0^{(c)}} \right)^{m_c} \tag{4.40}$$

$$\hat{\sigma}_3^{(i)} = \sigma_0^{(i)} \left(\frac{\left| \dot{\varepsilon}_{23}^{pl} \right|}{\dot{\varepsilon}_0^{(i)}} \right)^{m_i} \tag{4.41}$$

where σ_0, $\dot{\varepsilon}_0$, and m are the reference stress, reference strain rate, and rate sensitivity coefficient, respectively. Recall that the shear flow parameters σ_0, $\dot{\varepsilon}_0$, and m in materials (A) and (B) measured for the core layer (from the $\pm 45°$ tensile test) and the interface layers (from the short beam shear test) were equal, see Table 4.1. As a result, the following simplifications were made to model materials (A) and (B): $\sigma_0^{(c)} = \sigma_0^{(i)} = \sigma_0$, $\dot{\varepsilon}_0^{(c)} = \dot{\varepsilon}_0^{(i)} = \dot{\varepsilon}_0$, and $m_c = m_i = m$. The remainder of this analysis is based on these simplifications.

The normal stress σ_{33} can be expressed in terms of σ_{22} and the plastic strain rate $\dot{\varepsilon}_{33}^{pl}$ by substituting $\hat{\sigma}_1^{(c)}$ from Eq. (4.40) into Eq. (4.38):

$$\sigma_{33} = \frac{\sigma_0 \left(\frac{\left| \dot{\varepsilon}_{33}^{pl} \right|}{\dot{\varepsilon}_0} \right)^m - \sigma_{22}(\mu + 1)}{\mu - 1} \tag{4.42}$$

Similarly, shear stress σ_{23} at the interface can be expressed in terms of σ_{22}, σ_{33}, and $\dot{\varepsilon}_{23}^{pl}$ by substituting $\hat{\sigma}_3^{(i)}$ from Eq. (4.39) into Eq. (4.41):

$$\sigma_{23} = \frac{\sigma_0}{2}\left(\frac{\left|\dot{\varepsilon}_{23}^{pl}\right|}{\dot{\varepsilon}_0}\right)^m - \frac{\mu}{2}\left(\sigma_{22} + \sigma_{33}\right) \tag{4.43}$$

Substituting σ_{33} in Eq. (4.42) into Eq. (4.43) gives:

$$\sigma_{23} = \frac{\sigma_0}{2}\left(\frac{\left|\dot{\varepsilon}_{23}^{pl}\right|}{\dot{\varepsilon}_0}\right)^m + \frac{\mu\sigma_0}{2\left(1-\mu\right)}\left(\frac{\left|\dot{\varepsilon}_{33}^{pl}\right|}{\dot{\varepsilon}_0}\right)^m - \frac{\mu}{\left(1-\mu\right)}\sigma_{22} \tag{4.44}$$

As for the elastic-plastic model, consider a section of the specimen on the *2-3* plane of a ply, and define the coordinate $Y = L/2 - x_2$ as shown in Figure 4.5 such that $Y = 0$ is the free edge of the specimen at $x_2 = L/2$ and $Y = L/2$ is at the centre of the specimen. Equilibrium in the *2*-direction dictates that:

$$H\frac{d\sigma_{22}}{dY} = -2\sigma_{23} \tag{4.45}$$

where H is the height of the core layer. The above expression allows the calculation of $\sigma_{11} = -\sigma_{22}$ for a given location Y by substituting for σ_{23} from Eq. (4.44). However, this expression does not have an explicit solution and can only be solved numerically. The accurate solution was obtained from the FE simulation, but an approximate analytical solution is also provided below. It is first assumed that the material is under large deformation and the elastic strain rate is negligible compared to the plastic strain rate such that $\dot{\varepsilon}_{23}^{pl} \approx \dot{\varepsilon}_{23}^{tot}$ and $\dot{\varepsilon}_{33}^{pl} \approx \dot{\varepsilon}_{33}^{tot}$. It is then assumed that a uniform shear strain rate exists across the shear lag zone λ. Consequently, $\dot{\varepsilon}_{23}^{tot}$ can be estimated in terms of the applied out-of-plane strain rate $\dot{\varepsilon}_{33}^{tot}$ when considering incompressibility in the *2-3* plane (i.e. $\dot{\varepsilon}_{22}^{tot} = -\dot{\varepsilon}_{33}^{tot}$) as illustrated in Figure 4.6:

$$\dot{\varepsilon}_{23}^{tot} = \frac{d\dot{u}_2}{2dz} \approx \frac{\dot{\varepsilon}_{22}^{tot}\lambda}{2h} \approx \frac{-\dot{\varepsilon}_{33}^{tot}\lambda}{2h} \tag{4.46}$$

where λ is the shear lag length and h is the height of the interface layer.

Substituting $\dot{\varepsilon}_{23}^{tot}$ and $\dot{\varepsilon}_{33}^{tot}$ into Eq. (4.45) followed by substituting σ_{23} into Eq. (4.46) gives:

$$-H\frac{d\sigma_{22}}{dY} = \sigma_0\left(\frac{\left|\dot{\varepsilon}_{33}^{tot}\right|\lambda}{2\dot{\varepsilon}_0 h}\right)^m + \frac{\mu\sigma_0}{\left(1-\mu\right)}\left(\frac{\left|\dot{\varepsilon}_{33}^{tot}\right|}{\dot{\varepsilon}_0}\right)^m - \frac{2\mu}{\left(1-\mu\right)}\sigma_{22} \tag{4.47}$$

The above expression can be integrated to determine $\sigma_{11} = -\sigma_{22}$ for a given

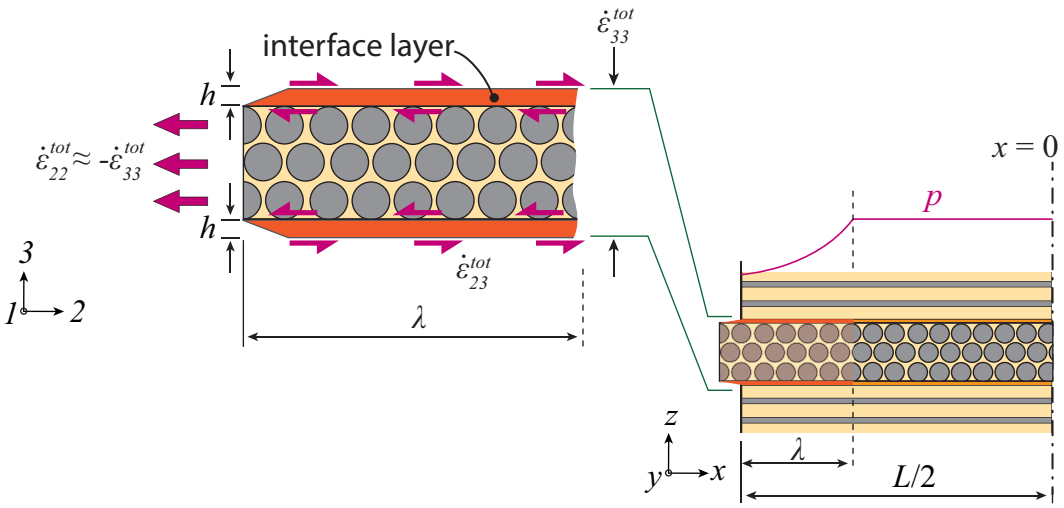

Figure 4.6: Schematic illustration of a section of the specimen on the *2-3* plane of a ply, with a close up view of the shear lag zone to emphasise the relationship between the strain rate components $\dot{\varepsilon}_{33}^{tot}$, $\dot{\varepsilon}_{22}^{tot}$, and $\dot{\varepsilon}_{23}^{tot}$ in this segment.

location Y using the boundary condition $\sigma_{22} = 0$ at $Y = 0$:

$$\sigma_{11} = -\sigma_{22} = \frac{\sigma_0}{2}\left[\left(\frac{1-\mu}{\mu}\right)\left(\frac{|\dot{\varepsilon}_{33}^{tot}|\,\lambda}{2\dot{\varepsilon}_0 h}\right)^m + \left(\frac{|\dot{\varepsilon}_{33}^{tot}|}{\dot{\varepsilon}_0}\right)^m\right]\left[exp\left(\frac{aY}{H}\right) - 1\right] \tag{4.48}$$

where $a \equiv 2\mu/(1-\mu)$. The size of the shear lag zone λ can be back-calculated by rearranging the above expression to determine the location ($Y = \lambda$) at which σ_{11} reaches a maximum value of σ_{11}^{max}:

$$\lambda = \frac{H\,(1-\mu)}{2\mu} ln\left[1 + \frac{\sigma_{11}^{max}}{\left(\frac{1-\mu}{\mu}\right)\frac{\sigma_0}{2}\left(\frac{|\dot{\varepsilon}_{33}^{tot}|\lambda}{2\dot{\varepsilon}_0 h}\right)^m + \frac{\sigma_0}{2}\left(\frac{|\dot{\varepsilon}_{33}^{tot}|}{\dot{\varepsilon}_0}\right)^m}\right] \tag{4.49}$$

The corresponding out-of-plane pressure $p \equiv -\sigma_{33}$ within the shear lag zone can be obtained by substituting for $\sigma_{11} = -\sigma_{22}$ from Eq. (4.48) into Eq. (4.42):

$$\begin{aligned} p \;=\; & \frac{\sigma_0}{2}\left[\left(\frac{1+\mu}{\mu}\right)\left(\frac{|\dot{\varepsilon}_{33}^{tot}|\,\lambda}{2\dot{\varepsilon}_0 h}\right)^m + \left(\frac{1+\mu}{1-\mu}\right)\left(\frac{|\dot{\varepsilon}_{33}^{tot}|}{\dot{\varepsilon}_0}\right)^m\right]\left[exp\left(\frac{aY}{H}\right) - 1\right] \\ & + \frac{\sigma_0}{1-\mu}\left(\frac{|\dot{\varepsilon}_{33}^{tot}|}{\dot{\varepsilon}_0}\right)^m \quad \text{for } (Y \le \lambda) \end{aligned} \tag{4.50}$$

while the out-of-plane pressure p remains constant at a maximum value of p_{max}

outside of the shear lag zone. This maximum pressure can be determined from Eq. (4.42):

$$p_{max} = \left(\frac{1+\mu}{1-\mu}\right)\sigma_{11}^{max} + \frac{\sigma_0}{1-\mu}\left(\frac{|\dot{\varepsilon}_{33}^{tot}|}{\dot{\varepsilon}_0}\right)^m \text{ for } (Y > \lambda) \tag{4.51}$$

As the out-of-plane compression test proceeds, σ_{11}^{max} and p_{max} at the centre of the specimen increase in magnitude. Indirect tension failure occurs when the stress state in the of centre of specimen reaches the ply tensile failure criterion in Eq. (4.17); for instance, σ_{11}^{max} at failure is:

$$\sigma_{11}^{max} = \frac{2S_L^+ - \alpha p_{max}}{2+\alpha} \tag{4.52}$$

The maximum pressure p_{max} at indirect tension failure p_f can be determined by substituting σ_{11}^{max} in Eq. (4.52) into Eq. (4.51):

$$p_f = \frac{\left(\frac{2+\alpha}{2}\right)\sigma_0\left(|\dot{\varepsilon}_{33}^{tot}|/\dot{\varepsilon}_0\right)^m + (1+\mu)\,S_L^+}{1-\mu+\alpha} \tag{4.53}$$

Similarly, the maximum in-plane tensile stress σ_{11}^{max} at indirect tension failure σ_{11}^f is:

$$\sigma_{11}^f = \frac{\left(\frac{2+\alpha}{2}\right)\sigma_0\left(|\dot{\varepsilon}_{33}^{tot}|/\dot{\varepsilon}_0\right)^m + (2-2\mu+\alpha-\alpha\mu)\,S_L^+}{(2+\alpha)(1-\mu+\alpha)} \tag{4.54}$$

Note that within the shear lag zone λ, the local pressure p and ply tensile stress σ_{11} are at a lower magnitude than p_f and σ_{11}^f, respectively. The critical shear lag length λ_c that is required for the pressure to build up to p_f and thus to cause indirect tension failure can be determined by substituting σ_{11}^f into Eq. (4.49):

$$\lambda_c = \frac{H(1-\mu)}{2\mu} ln\left[1 + \frac{\sigma_{11}^f}{\left(\frac{1-\mu}{\mu}\right)\frac{\sigma_0}{2}\left(\frac{|\dot{\varepsilon}_{33}^{tot}|\lambda_c}{2\dot{\varepsilon}_0 h}\right)^m + \frac{\sigma_0}{2}\left(\frac{|\dot{\varepsilon}_{33}^{tot}|}{\dot{\varepsilon}_0}\right)^m}\right] \tag{4.55}$$

Finally, the total compressive load F of the specimen can be determined by integrating the local pressure p across the entire specimen. The average pressure at failure $\bar{p}_f$ is defined to be $\bar{p}_f \equiv F/L^2$. The calculation methods of F and $\bar{p}_f$ in the current model are identical to those in the elastic-plastic analytical model, see Eq. (4.35) to Eq. (4.37) in Section 4.3.2.

The current elastic-viscoplastic analytical model provides some insight into the effect of applied strain rate $\dot{\varepsilon}_{33}^{tot}$ and specimen side length L on $\bar{p}_f$. Eq. (4.53) and Eq. (4.55) show that a higher out-of-plane strain rate $\dot{\varepsilon}_{33}^{tot}$ would result in an increase in p_f and a decrease in λ_c. Thus, the average pressure at failure $\bar{p}_f$ would increase as compressive strain rate $\dot{\varepsilon}_{33}^{tot}$ rises, for a given state of cure and specimen side length L. Eq. (4.53) and Eq. (4.55) also demonstrate that both p_f and λ_c are independent of the specimen side length L. For a given state of cure and applied strain rate $\dot{\varepsilon}_{33}^{tot}$, the maximum pressure p_f and the shear lag length λ_c would remain unchanged as the specimen side length L increases. However, the proportion of the specimen that consists of the shear lag zone (with length λ_c) would decrease, having the effect of increasing $\bar{p}_f$.

4.4 Accuracy of Predictions

4.4.1 Compressive Response

Figure 4.7 compares the compressive response (in terms of average pressure $\overline{p} = F/L^2$ versus compressive strain $-\varepsilon_{zz}$) calculated from the FE simulations to the measured experimental results. The stiffening response noted in the experiments was not observed in the FE simulations. Since the FE simulations are focused on deformation mechanics at the ply level, it stands to reason that they would not capture the stiffening response that is caused by fibre compaction at the sub-ply level (i.e. fibres come in contact with one another at large compressive strains). Acknowledging this limitation, the FE simulations perform well when predicting average pressure at failure $\overline{p}$. For instance, at $-\dot{\varepsilon}_{zz} = 8 \times 10^{-4} s^{-1}$, small specimens ($L \leq 5$ mm) of material (A) deformed through shear yielding instead of failing by indirect tension. The FE simulation showed a similar behaviour where the $\overline{p}$ reaches a plateau at $-\varepsilon_{zz} = 0.4$. At $L \geq 7$ mm, both the experimental and FE results of material (A) show failure at similar $\bar{p}_f$. For instance, $\bar{p}_f = 150$ MPa in the simulation and $\bar{p}_f = 175$ MPa in the experiment. As the state of cure of the laminates increases, the stiffening response becomes less pronounced and is no longer detectable for material (E). As a result, in material (E), both the failure pressure and failure strain calculated from the FE simulations are in agreement with the experimental data (i.e. $\bar{p}_f \sim 1250$ MPa and $-\varepsilon_f \sim 0.125$, respectively).

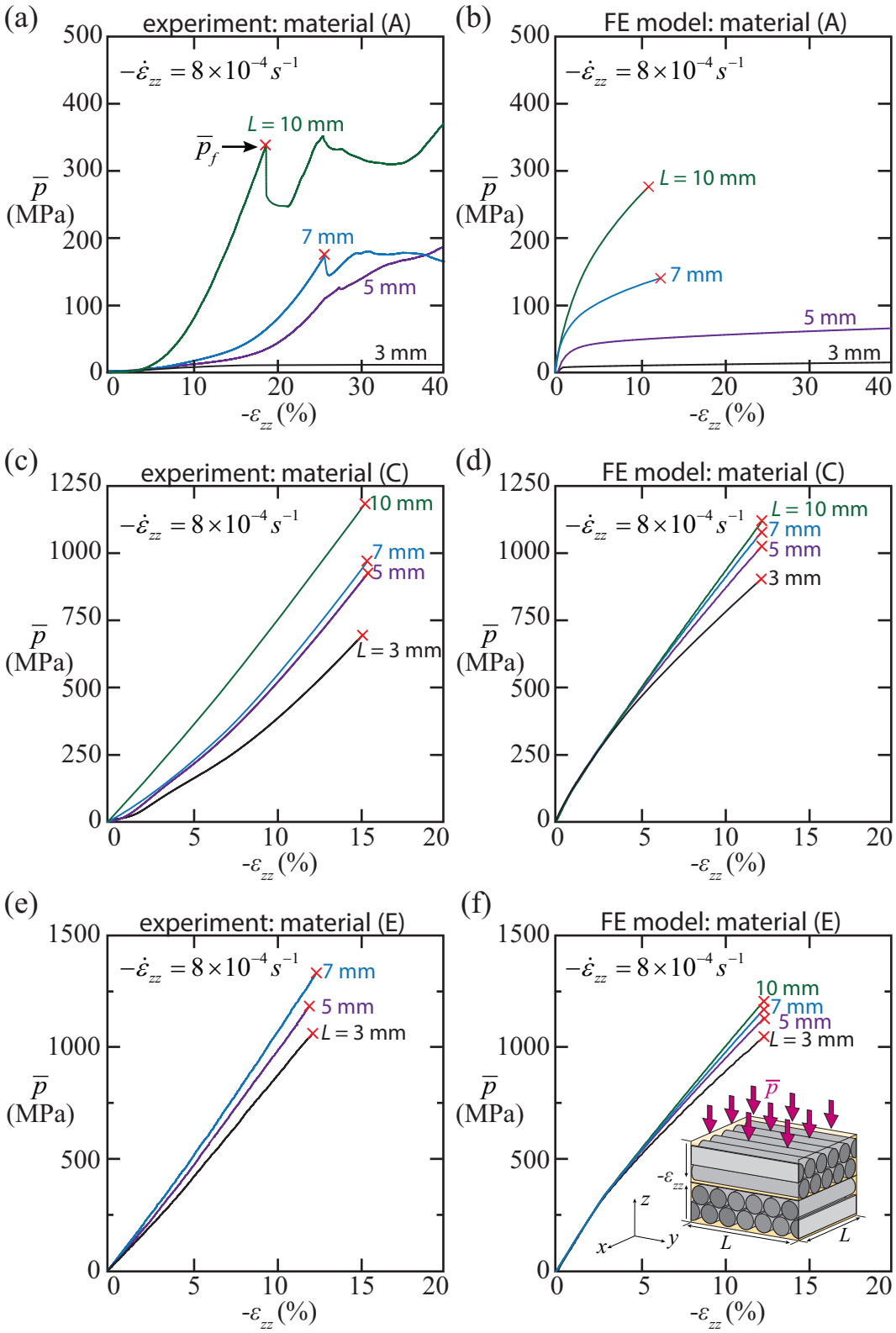

Figure 4.7: Plots of average pressure $\bar{p}$ as functions of compressive strain $-\varepsilon_{zz}$ of a-b) uncured material (A), c-d) partially cured material (C), and e-f) autoclaved material (E) at a strain rate of $-\dot{\varepsilon}_{zz} = 8 \times 10^{-4} s^{-1}$. Figures a, c, and e present the experimental data; and b, d, and f show the FE predictions.

4.4.2 Pressure Distribution during Out-of-plane Compression

In the experiments, materials (A), (B), and (E) with $L = 10$ mm were subjected to out-of-plane compression at a strain rate of $-\dot{\varepsilon}_{zz} = 8 \times 10^{-4} s^{-1}$ at three pressure levels: $p_{max} = 100$ MPa, 200 MPa, and 250 MPa. p_{max} is defined to be the maximum pressure at the centre ($x = y = 0$) of the specimen on the x-y plane. Figure 4.8 compares the pressure contours calculated from the FE simulations to those measured from the experiments at $p_{max} = 250$ MPa. The pressure profiles calculated from the FE simulations and those measured from the experiments are in good agreement.

Figure 4.9 compares the calculated and the measured p along the centre line ($y = 0$) of the specimens with $p_{max} = 100$ MPa, 200 MPa, and 250 MPa. Both the FE simulations and the experiments showed that p is at a minimum along the periphery of the specimens and builds up toward the centre of the specimens, denoting the existence of shear lag zones. After the pressure builds up and reaches the ends of the shear lag zones, pressure remains uniform at p_{max}. The lengths of the shear lag zones λ calculated from the FE simulations were also in agreement with the experimental data. Furthermore, the FE simulations captured the decrease in shear lag length λ as state of matrix cure increased from material (A) to material (E).

4.4.3 Compressive Strength versus Specimen Size

Figure 4.10 compares the predicted $\bar{p}_f$ from FE simulation and from the analytical models to the experimental results by plotting $\bar{p}_f$ as functions of specimen side length L at various compressive strain rates $\dot{\varepsilon}_{zz}$. The analytical solutions are in good agreement with the FE predictions, and both are consistent with the experimental data.

The predicted effect of specimen side length L on $\bar{p}_f$ was similar to the effect observed in the experiments. The strain rate dependency of $\bar{p}_f$ in material (A) was predicted using the elastic-viscoplastic FE models; they are in good agreement with the experimental data in the studied range of applied strain rates ($-\dot{\varepsilon}_{zz} = 8\times10^{-4}s^{-1}$, $8\times10^{-3}s^{-1}$, and $8\times10^{-2}s^{-1}$). In the case of material (B), the predicted strain rate dependency appears to have been overwhelmed by scattering of the observed experimental data. In materials (C) to (E),

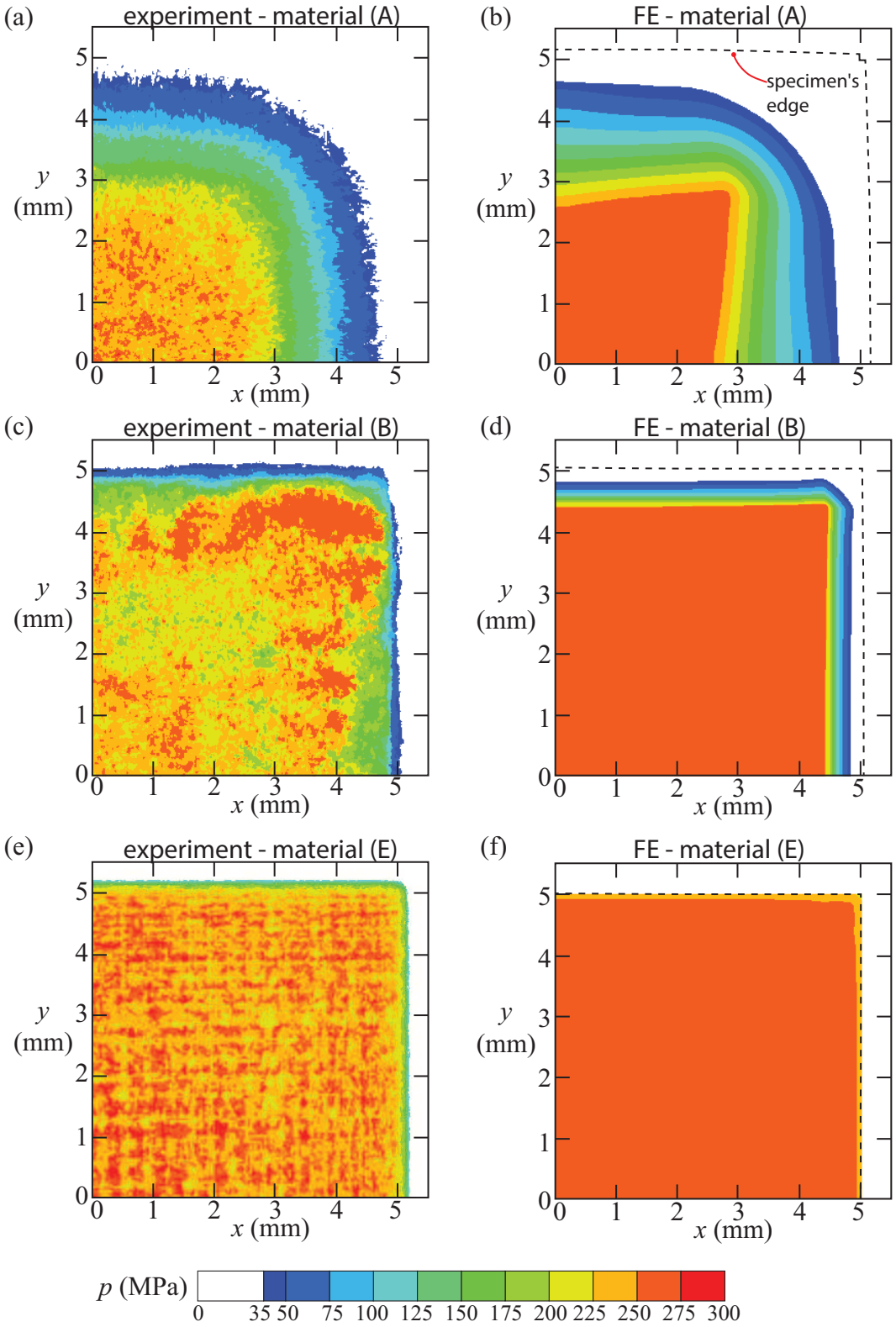

Figure 4.8: Out-of-plane pressure distributions measured from pressure sensitive films (a, c, and e) and the FE model (b, d, and f) of cross-ply laminates at different states of cure, all at a maximum pressure of $p_{max} = 250$ MPa (at $L = 10$ mm and $-\dot{\varepsilon}_{zz} = 8 \times 10^{-4} s^{-1}$). The dashed lines in figure b, d, and f represent the specimen's edge in the FE simulations.

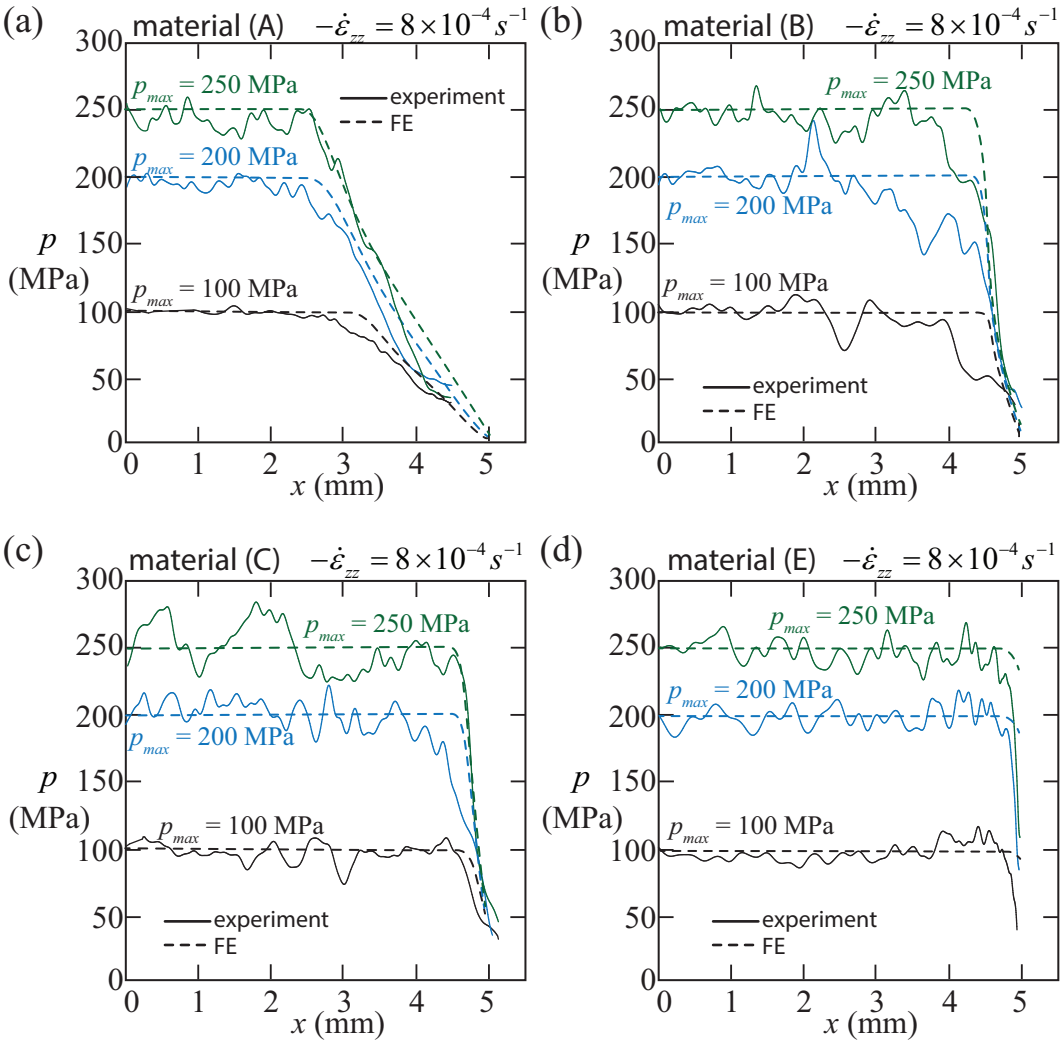

Figure 4.9: Plots of the pressure distribution along the centre line ($y = 0$) of a) material (A), b) material (B), c) material (C), and d) material (E) at different levels of p_{max} (at $L = 10$ mm and $-\dot{\varepsilon}_{zz} = 8 \times 10^{-4}s^{-1}$). Solid lines represent the data measured from pressure sensitive films and dashed lines represent the FE predictions.

the elastic-plastic models are also in good agreement with the experimentally measured $\bar{p}_f$. In addition, elastic FE predictions were presented in Figure 4.10e and compared against material (E), which is the material that has the highest measured $\bar{p}_f$. All the tested materials in the current study failed at a lower $\bar{p}_f$ than the elastic FE predictions, which establish the upper limit of the out-of-plane compressive strength of the current CFRP system.

Finally, Figure 3.4f compares the measured and FE predicted $\bar{p}_f$ (at test strain rates from $-\dot{\varepsilon}_{zz} = 8 \times 10^{-4} s^{-1}$ to $8 \times 10^{-2} s^{-1}$) versus the short beam shear strength of each material (tested at $\dot{\gamma} = 10^{-3} s^{-1}$) for a constant specimen size of $L = 7$ mm.

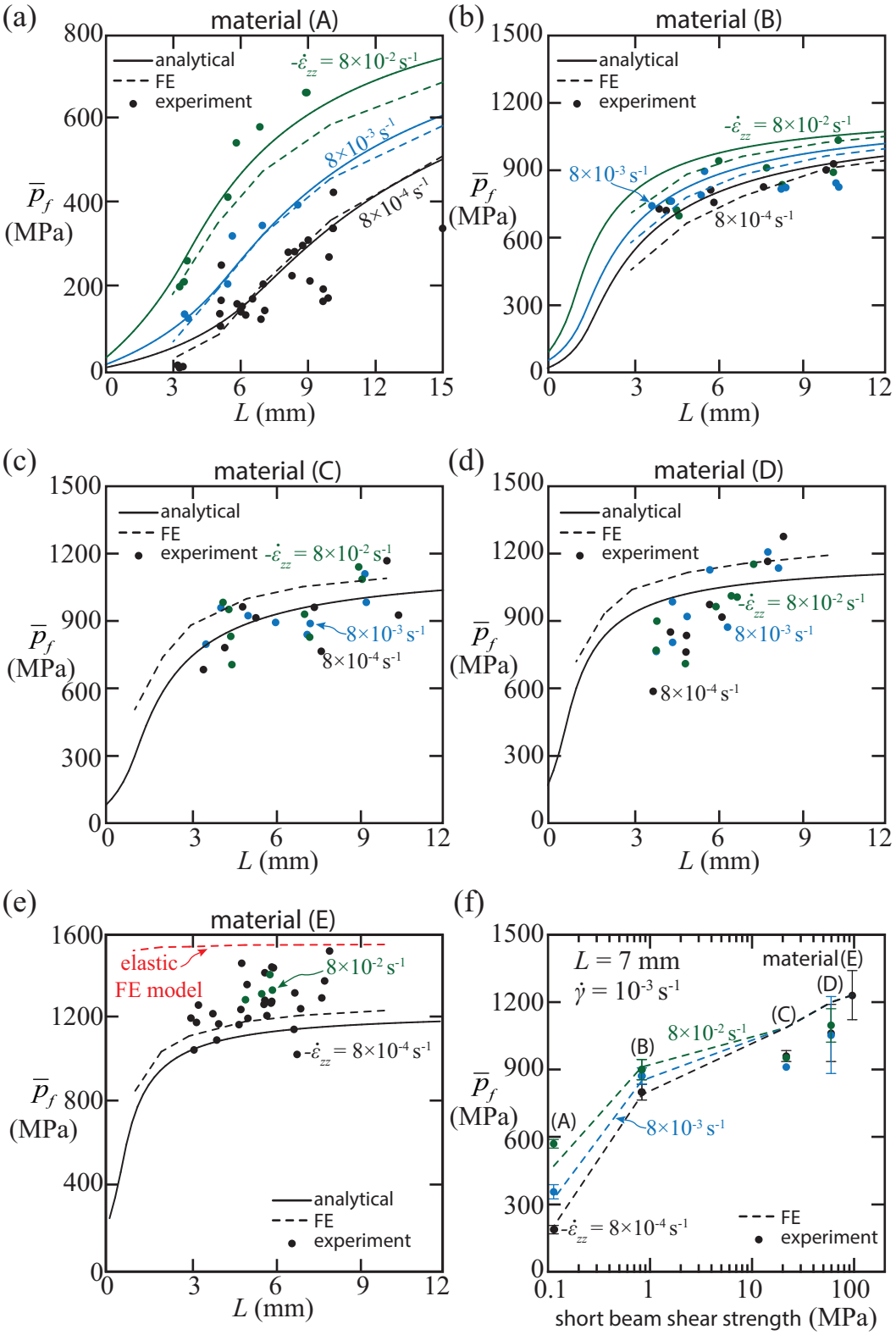

Figure 4.10: Plots of average pressure at failure $\bar{p}_f$ as functions of specimen side length L of a) material (A), b) material (B), c) material (C), d) material (D), and e) material (E) that were tested at various strain rates. f) Plot of average pressure at failure $\bar{p}_f$ at a constant $L = 7$ mm as a function of material short beam shear strength that was tested at a shear strain rate of $\dot{\gamma} = 10^{-3}s^{-1}$.

4.5 Conclusions

Experiments in Chapter 3 have revealed that, under uniaxial out-of-plane compression, CFRP cross-ply laminates generally fail by the indirect tension mechanism (except for uncured prepregs with small specimen size tested at a low applied strain rate, which deform by shear yielding). In this chapter, finite element (FE) simulations and analytical models were developed to predict the uniaxial out-of-plane compressive strength (expressed in terms of average pressure at failure $\bar{p}_f$) of CFRP cross-ply laminates.

The FE and analytical models in this study were adapted from the analysis given by Attwood et al. (2014) for Dyneema® cross-ply laminates that failed by indirect tension. Attwood et al. (2014) proposed that the composite plies deform in an elastic-plastic manner with a set of pressure dependent yield criteria. This study introduced modifications to account for the strain rate sensitivity of the matrix in some of the laminates and the pressure dependency of tensile failure strength in carbon fibre plies. Three types of constitutive laws were used to describe laminates that deform in elastic, elastic-plastic, and elastic-viscoplastic manners. The models revealed that out-of-plane pressure increases from the periphery of the specimen toward the centre in a shear lag manner and then remains at an elevated level in the centre (i.e. outside of the shear lag zone). Furthermore, the models indicated that increasing matrix shear strength raises the pressure required to cause indirect tension failure and decreases the size of the shear lag zone at failure, which has the combined effect of increasing the compressive strength (i.e. the average pressure at failure). Compressive strength also rises with increasing specimen size, as this reduces the proportion of the specimen that consists of the shear lag zone.

Overall, both the FE simulations and the analytical predictions were in good agreement with the experimental data. This confirms that CFRP cross-ply laminates under out-of-plane compression indeed fail by indirect tension. O'Masta et al. (2015a) recently revealed that indirect tension is the cause of impact damage of Dyneema® cross-ply laminates. A parallel study, presented in Chapter 5, demonstrated that CFRP laminates with low matrix shear strength also fail by indirect tension under ballistic loading. The analysis in the current chapter laid the groundwork for future predictive methods on the quasi-static and ballistic perforation of CFRP cross-ply laminates.

Chapter 5

The Effect of Matrix Shear Strength on the Perforation Behaviour of CFRP Beams under Quasi-static and Ballistic Loading

Summary

The preceding chapter revealed that the indirect tension mechanism can arise from quasi-static out-of-plane compression of carbon fibre/epoxy cross-ply laminates. This chapter investigates the dynamic failure mechanism as well as the role of matrix shear strength in the ballistic response of carbon fibre/epoxy cross-ply composite beams. CFRP [0°/90°] cross-ply laminates with six states of cure (matrix shear strength increasing from 0.1 MPa to 100 MPa) were prepared from as-received uncured prepregs, partially cured laminates, and autoclaved fully cured laminates. Composite beams with rectangular dimensions were manufactured and subjected to three types of tests: (i) a quasi-static indentation test with rigid back support, (ii) a quasi-static cropping test with a clearance c between the edge support and a flat indenter, and (iii) a ballistic impact test with a cuboid shaped projectile under a simply supported boundary condition. The failure mechanism in quasi-static tests

was found to be sensitive to the testing boundary condition but not to the matrix shear strength. Optical images recorded during and after quasi-static tests revealed that all composite beams failed by shear plugging (consisting of transverse matrix cracks, ply delamination, and fibre fracture) in the cropping tests, but failed by indirect tension (consisting of ply tensile failure in the fibre direction) in the back-supported indentation tests. In contrast, the dynamic failure mechanism was found to be sensitive to the matrix shear strength. Post-impact optical images revealed that CFRP beams with a high matrix shear strength (30 to 100 MPa) failed by a brittle shear plugging mode. As the matrix shear strength was reduced from 100 MPa to 22 MPa, penetration velocity improved two-fold. Once the matrix shear strength decreased below 22 MPa, the failure mode switched to indirect tension. For this failure regime, penetration velocity remained elevated and was independent of the matrix shear strength. Specimens with matrix shear strength of 22 MPa offer both acceptable penetration resistance and structural performance.

5.1 Introduction

Currently, carbon fibre reinforced plastic (CFRP) composites offer high stiffness and strength but have inferior ballistic performance compared to Dyneema® cross-ply laminates, which consist of matrix materials with low shear strength. This chapter explores whether the ballistic resistance of CFRP composites can be improved by altering the matrix shear strength.

Recent investigations have revealed that the high impact resistance of Dyneema® cross-ply composites (with thickness of 2 - 4 mm) could be attributed to a dynamic failure mechanism such as indirect tension (Attwood et al., 2014; Karthikeyan et al., 2013b; O'Masta et al., 2015a). Attwood et al. (2014) revealed that indirect tension failure can arise in Dyneema® cross-ply composites through uniaxial out-of-plane compression under quasi-static loading. Indirect tension is a result of anisotropic Poisson expansion in the unidirectional plies of Dyneema®. When alternating 0° and 90° plies are stacked together and subjected to out-of-plane compressive strain, the Poisson expansion of each ply in the direction transverse to the fibre is higher than that in the fibre direction. This expansion mismatch can in turn cause fibre tensile straining and failure will occur if the fibre tensile strength is reached. O'Masta et al. (2015a) revealed that the indirect tension mechanism is indeed present in the dynamic failure of Dyneema® cross-ply laminates. When Dyneema® cross-ply laminates are subjected to ballistic impact, a compressive stress can be generated underneath the projectile and can cause indirect tensile failure.

In contrast to Dyneema® cross-ply laminates, under ballistic loading, conventional CFRP composites with high matrix shear strength generally do not fail by indirect tension. When laminate thickness is above 2 mm, CFRP usually fails through a brittle shear plugging mechanism under ballistic impact tests. Cantwell and Morton (1989a,b, 1990) first identified this shear plugging mechanism through drop weight experiments on CFRP layers. These researchers revealed that when CFRP laminates are subjected to impact loading, a plug is formed underneath the projectile consisting of transverse matrix cracks, ply delamination, and fibre fracture. In this type of failure mechanism, the shear properties of the matrix as well as the fibre can play an important role in impact resistance. The difference in dynamic failure mechanism between CFRP and Dyneema® could be attributed to the choice

of matrix material. Whereas Dyneema® composites use a thermoplastic matrix with shear strength in the order of 1 - 10 MPa (Peijs et al., 1990a; Russell et al., 2013), commercially available CFRP consists of thermoset epoxy with shear strength in the order of 50 - 100 MPa (Berg et al., 1972; Chamis and Sinclair, 1977; Walrath and Adams, 1983).

Recent studies by de Ruijter et al. (2010); Karthikeyan et al. (2013b) have further demonstrated the significance of matrix properties to the failure mechanism of composite laminates and suggest the potential to improve impact resistance by modifying the composite's matrix properties. de Ruijter et al. (2010) demonstrated that there exists a regime of matrix modulus (0.01 - 1 GPa) in woven Twaron® aramid-based fibre composite where the impact resistance of the laminate is optimised. They proposed that the observed improvement is related to the change in friction coefficient between tows of fibre. Karthikeyan et al. (2013b) demonstrated that a reduction in matrix shear strength can improve the ballistic resistance of both Dyneema® and CFRP cross-ply plates. In particular, they tested CFRP cross-ply plates of as-received prepregs and autoclaved fully cured laminates. They observed a shear plugging mechanism in the autoclaved materials, but found progressive perforation (i.e. number of failed plies increases with impact velocity) in the prepregs; they noted that this failure mode involves tensile failure of the fibres, but they did not identify the mechanism to be one of indirect tension.

The above studies indicate that there remain several uncertainties in ballistic research and suggest the following questions: (i) Is the indirect tension mechanism responsible for the superior ballistic performance of Dyneema® composites compared to CFRP composites? (ii) What is the role of matrix shear strength in the dynamic failure mechanism and its effect on the impact resistance of fibre composites? (iii) Is it possible to suppress the commonly observed shear plugging mechanism or to activate the indirect tension mechanism in CFRP composites and thus enhance their impact resistance?

The objective of the current study is to provide a comprehensive experimental investigation to understand: (i) the effect of matrix cure on the failure mechanism and ballistic resistance of CFRP composites, (ii) the difference in quasi-static and dynamic response of CFRP composites, and (iii) the potential to improve the ballistic resistance of CFRP composites by suppressing the

commonly observed brittle shear plugging mechanism. To achieve these goals, the current study tests CFRP cross-ply composite beams at different states of cure achieved through partial curing and an autoclave process. Composite beams with rectangular dimensions were manufactured and then subjected to three types of tests: (i) a quasi-static indentation test with rigid back support, (ii) a quasi-static cropping test with a clearance c between the edge support and a flat indenter, and a (iii) ballistic impact test with a cuboid shaped projectile under a simply supported boundary condition. The use of composite beams rather than plates in each of the above tests allows for ease in identifying the potential failure mechanism.

5.2 Specimen Manufacture

Cross-ply laminates $[0°/90°]_{16}$ were constructed from Hexply® 8552/35%134/IM7 carbon fibre/epoxy prepregs (with a ply thickness of 0.131 mm). Six states of cure were produced, with the following labelling procedure employed throughout this study: (A) uncured, (B) partially cured at 100°C for 2 hours, (C) partially cured at 120°C for 2 hours, (D) partially cured at 120°C for 2 hours and 15 mins, (E) partially cured at 180°C for 24 hours, and (F) autoclaved fully cured specimens. The uncured laminates were first laid-up by hand. They were then cut using a band saw into rectangular beam dimensions with height of $H = 4$ mm (32 plies), breadth of $B = 11$ mm, length of $L = 300$ mm, and areal density of $\rho_A = 6.28$ kg/m^2. These uncured composite beams are referred to as material (A). Partially cured composites of types (B) to (E) were then prepared by placing the uncured beams in an air-oven using the above-mentioned cure cycles and were compressed in-situ at 0.1 MPa in the out-of-plane direction by spring-loaded platens (see detailed drawing in Appendix A). The fully cured specimens (F) were autoclaved following a procedure recommended by (Hexcel Composites, 2013). The matrix shear strength of the laminates was then measured through a short beam shear test at a quasi-static loading rate (for further detail, refer to Appendix B). Table 5.1 summarises the curing process and the matrix shear strength of laminates type (A) to (F). With the exception of the fully cured material (F), all laminates were stored at −15°C to avoid further curing and brought back to room temperature for 5 hours prior to testing.

Table 5.1: Curing process and matrix shear strength of CFRP beams.

Material	Curing method	Curing temperature	Curing duration	Applied pressure	Short beam shear strength τ (MPa)
A	uncured	room temperature	–	–	0.11 [a]
B	oven cured	100°C	2 hours	out-of-plane 0.1 MPa	0.82 [a]
C	oven cured	120°C	2 hours	out-of-plane 0.1 MPa	22 ± 1.9
D	oven cured	120°C	2 hours and 15 mins	out-of-plane 0.1 MPa	30. ± 1.3
E	oven cured	180°C	24 hours	out-of-plane 0.1 MPa	61 ± 3.7
F	autoclaved	180°C	2 hours	hydrostatic 0.7 MPa	99 ± 6.9

[a] Materials (A) and (B) are strain rate sensitive and their short beam shear test showed no shear failure. Therefore, the above short beam shear strengths τ represent the flow stresses at shear strain of 5% $\tau(\gamma = 5\%)$ and at a shear strain rate of $\dot{\gamma} = 10^{-3}s^{-1}$.

5.3 Test Methods

5.3.1 Quasi-static Indentation Test

CFRP composite beams with rectangular dimensions of height $H = 4$ mm (32 plies), breadth $B = 11$ mm, and length $L = 75$ mm were sectioned from cross-ply laminates $[0°/90°]_{16}$ (32 plies) with six states of cure. Specimens were subjected to an out-of-plane indentation test by placing them between a flat back support and a hardened steel indenter with a square bottom of $l_1 = l_2 = 12.5$ mm in the x-y plane, as illustrated in Figure 5.1a. A radius $R = 0.3$ mm was introduced to the indenter edges to reduce the stress concentration. Both the back support and the indenter were made from hardened silver steel (700 Vickers) and were lubricated with a low viscosity mineral oil. Materials (A) and (B) were tested using a screw-driven test machine with a 150 kN load cell, whereas materials (D) to (F) were tested using a servo hydraulic test machine with a 1 MN load cell. For consistency, all specimens were tested with the fibres of the top ply lying parallel to the x-direction in the figure. The indenter was then pressed into the middle of the specimens in the z-direction. Indentation tests were performed at a constant displacement rate of $\dot{u}_z = 4 \times 10^{-3}$ mm/s. The compressive load F was recorded by the machine load cell and the displacement between the steel plate and the indenter u_z was measured using a laser extensometer. During the indentation test, high-speed images were recorded from the side-view of the specimens using a Phantom® V1610 camera with an inter-frame time of 100 μs and an exposure time of 90 μs in order to identify the failure mechanism.

5.3.2 Quasi-static Cropping test

CFRP composite beams with same rectangular dimensions as mentioned above (i.e. $H = 4$ mm, $B = 11$ mm, and $L = 75$ mm) were examined through a cropping test at a quasi-static loading rate using a screw-driven test machine with a 150 kN load cell. Specimens were placed between a hardened steel indenter (with a square bottom of $l_1 = l_2 = 12.5$ mm in the x-y plane) and two back supports with 18.5 mm spacing, creating a clearance $c = 3$ mm (with $c/H = 0.75$) between the steel supports and the indenter (see Figure 5.1b). A radius $R = 0.3$ mm was introduced to the edges of the indenter and the steel support to reduce the stress concentration. Both the supports

and the indenter were made from hardened silver steel (700 Vickers) and were lubricated with a low viscosity mineral oil. Specimens were placed so that the fibres in the top ply were parallel to the x-direction in the figure and the indenter was then pressed into the middle of the specimens in the z-direction. The average shear strain of the specimen $\bar{\gamma}$ within the clearance c between the indenter and the back support was calculated based on the indenter displacement u_z: $\bar{\gamma} = u_z/c$. The cropping test was performed at an out-of-plane displacement rate of $\dot{u}_z = 3 \times 10^{-3}$ mm/s (associated with an average shear strain rate of $10^{-3}s^{-1}$). The compressive load F was recorded by the machine load cell and the displacement u_z between the steel plate and the indenter was measured using a laser extensometer. Side view optical images of the specimen were recorded during the cropping test using a PixeLINK® camera. For maximum resolution, only a 9×9 mm window of one side of the punched regions was filmed. The preliminary tests revealed that there exists a peak load accompanying damage initiation at a shear strain shortly below $\bar{\gamma} = 10\%$. Thus, additional interrupted tests were performed on specimens at each state of cure: the specimens were loaded to shear strain levels of $\bar{\gamma} = 10\%$ and $\bar{\gamma} = 40\%$, followed by unloading and optical examination.

5.3.3 Ballistic Impact Test

Initially, the experiment was designed such that CFRP plates were impacted by spherical steel projectiles under an edge-clamped boundary condition. The preliminary results are summarised in Appendix D. However, there were difficulties in identifying the failure mechanism through these tests. An improved ballistic test was designed, involving CFRP beams and cuboid shaped projectiles. The beam configuration allowed direct observation of the damaged areas and the cuboid shape assisted in identifying the location of the damage in relation to point of contact.

In the ballistic test, CFRP composite beams with rectangular dimensions of height $H = 4$ mm (32 plies), breadth $B = 11$ mm, and length $L = 300$ mm were subjected to ballistic impact by a cuboid shaped projectile under a simply supported boundary condition. In the ballistic tests, composite beams were adhered to a rigid steel foundation using double-sided adhesive tape so that they had a span length L_s of 250 mm (as illustrated in Figure 5.1c). Specimens were placed with the fibres of the top ply lying parallel to the x-direction in the figure. The centre of the specimens was then impacted

in the out-of-plane direction using a hardened steel cuboid shaped projectile with a square cross-section of $l_1 = l_2 = 12.5$ mm in the x-y plane, a length $l_3 = 9$ mm in the z-direction, and a mass of $m_p = 1.1 \times 10^{-2}$ kg. A radius $R = 0.3$ mm was introduced to the projectile edges to reduce the stress concentration. Projectiles were launched using a gas gun (utilising helium or nitrogen compressed gas) with an aluminium alloy barrel 4.5 m in length and with an inner cross-section of 13 mm $\times$ 13 mm (the same apparatus was described by Attwood et al. (2016)). The gas gun was capable of producing impact velocities of $v_0 = 25$ m/s to $v_0 = 550$ m/s. The impact velocity v_0 was measured using a set of laser gates placed near the gun barrel's exit. During the ballistic test, high-speed images were recorded from the side-view of the specimens using a Phantom® V1610 camera with an inter-frame time of 7.7 μs and an exposure time of 0.43 μs. Tested specimens were then examined through optical inspection to determine the level of damage (i.e. number of failed plies) and to identify the failure mechanisms.

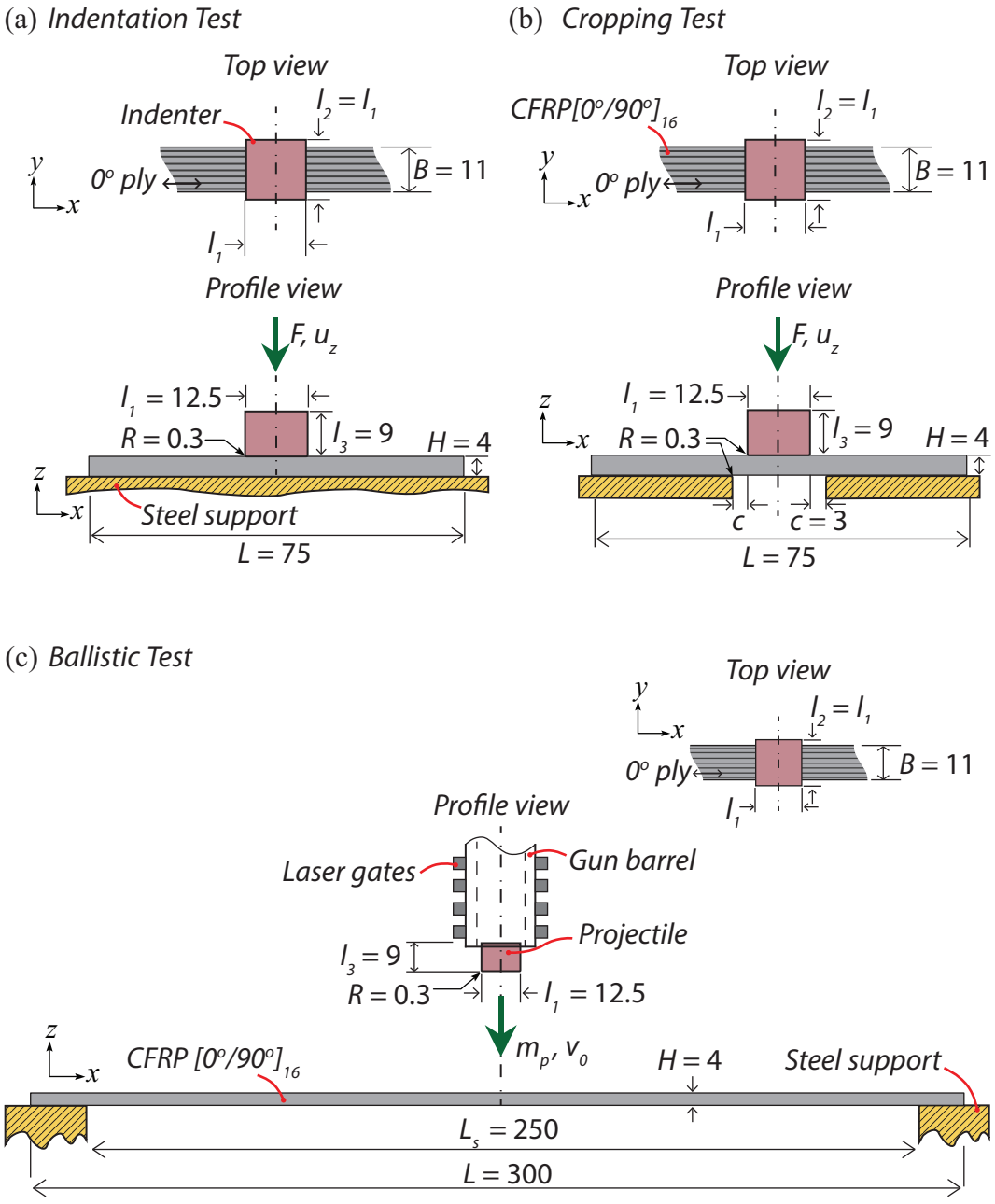

Figure 5.1: Schematic illustrations of the set-up used in the a) quasi-static indentation test, b) quasi-static cropping test, and c) ballistic test. All dimensions are in mm.

5.4 Results

5.4.1 Quasi-static Indentation Test

Quasi-static indentation tests were performed on CFRP composite beam types (A) to (F) and with matrix shear strength ranging from $\tau = 0.1$ to 100 MPa. Initial experiments showed that indented specimens failed in a catastrophic manner accompanied by acoustic emissions, similar to the indirect tensile failure observed in the uniaxial out-of-plane compression of these materials (presented in Chapter 3). Indirect tension is a failure mechanism that arises as a result of out-of-plane compressive pressure. Therefore, the indentation responses in this study are presented in terms of the average indentation pressure under the indenter $\bar{p}$ and the average out-of-plane compressive strain $\bar{\varepsilon}$ in the material directly beneath the projectile:

$$\bar{p} = \frac{F}{Bl_1} \tag{5.1}$$

$$\bar{\varepsilon} = \frac{u_z}{H} \tag{5.2}$$

Figure 5.2 shows the quasi-static indentation responses of materials (A) to (F) in terms of $\bar{p}$ versus $\bar{\varepsilon}$. The two observations noted below reveal the similarity of failure mechanism under quasi-static indentation and uniaxial out-of-plane compression.

(i) All specimens showed catastrophic failure at a critical average pressure of $\bar{p}_c$ at $\bar{\varepsilon} \sim 15$ - 20%. The critical average pressure $\bar{p}_c$ was comparable to the data obtained from the uniaxial out-of-plane compression test. Table 5.2 compares the failure pressure of each material obtained from the current indentation test to the average failure pressure $\bar{p}_f$ in uniaxial out-of-plane compression test, previously obtained and presented in Chapter 3. In general, the failure pressures are all in the order of 1 GPa and the ratio of $\bar{p}_c/\bar{p}_f$ is ~ 1. Such similarity in values implies that the indirect tension mechanism was responsible for the failure of the composite beams in the indentation experiment.

(ii) Furthermore, the average pressure at failure $\bar{p}_c$ increased with the state of matrix cure for all specimens. Material (A) showed indentation failure at $\bar{p}_c = 761$ MPa, with $\bar{p}_c$ increasing progressively along with the matrix shear strength of the material, and reaching $\bar{p}_c = 1252$ MPa in material (F). The effect of matrix shear strength on the indirect tension failure strength had also

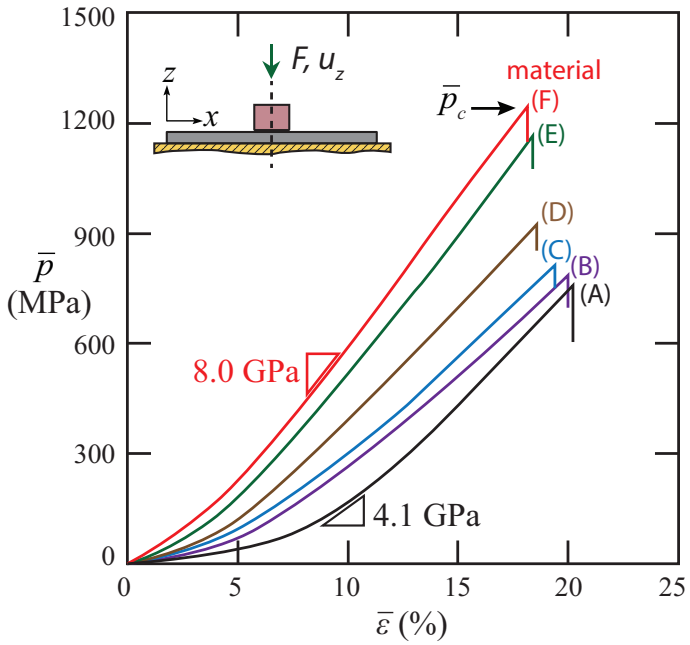

Figure 5.2: Static indentation responses of composite beams in terms of $\bar{p}$ versus $\bar{\varepsilon}$.

been observed in the uniaxial compression test of cross-ply laminates described in Chapter 3.

Figure 5.3 shows high-speed image sequences during the indentation test for the moments before and after the onset of failure (where $t = 0$ corresponding to the instant of failure). The results for materials (A) and (F) were selected to be shown here, as these represent the two extremes of matrix shear strength. The images demonstrate that the materials failed by a catastrophic explosion where ply tensile failure initiated directly underneath the indenter. Furthermore, the similarity of this indentation pressure measurement to that obtained from the out-of-plane compression test leads us to conclude that the composite beams failed by an indirect tension mechanism in the current indentation test.

5.4.2 Quasi-static Cropping Test

Figure 5.4 summarises the response of composite beams under the quasi-static cropping test in terms of the average shear stress $\bar{\tau}$ and average shear strain $\bar{\gamma}$ within the clearance c between the edge support and a flat punch. $\bar{\tau}$ and $\bar{\gamma}$ are defined as:

$$\bar{\tau} = \frac{F}{2BH} \tag{5.3}$$

$$\bar{\gamma} = \frac{u_z}{c} \tag{5.4}$$

Table 5.2: Comparison between failure pressures obtained from the indentation test versus those obtained from the out-of-plane compression test.

Material	Out-of-plane compression average failure pressure $\bar{p}_f$ (MPa) [a]	Indentation average failure pressure $\bar{p}_c$ (MPa)	Indentation apparent modulus at $\bar{\varepsilon} = 5\%$ (GPa)	Indentation apparent modulus at $\bar{\varepsilon} = 10\%$ (GPa)	Ratio between the two tests $\bar{p}_c/\bar{p}_f$
A	350	761	1.2	4.1	2.2
B	865	781	2.4	4.5	0.9
C	1243	812	4.5	5.6	0.7
D	1231	922	5.2	6.3	0.8
E	1215	1163	5.9	7.3	1.0
F	1350	1252	6.4	7.9	0.9

[a] out-of-plane compression test results were obtained from tests with specimen side length of $L \times L$ (with $L = 10$ mm) at a strain rate of $-\dot{\varepsilon}_{zz} = 8 \times 10^{-4} s^{-1}$.

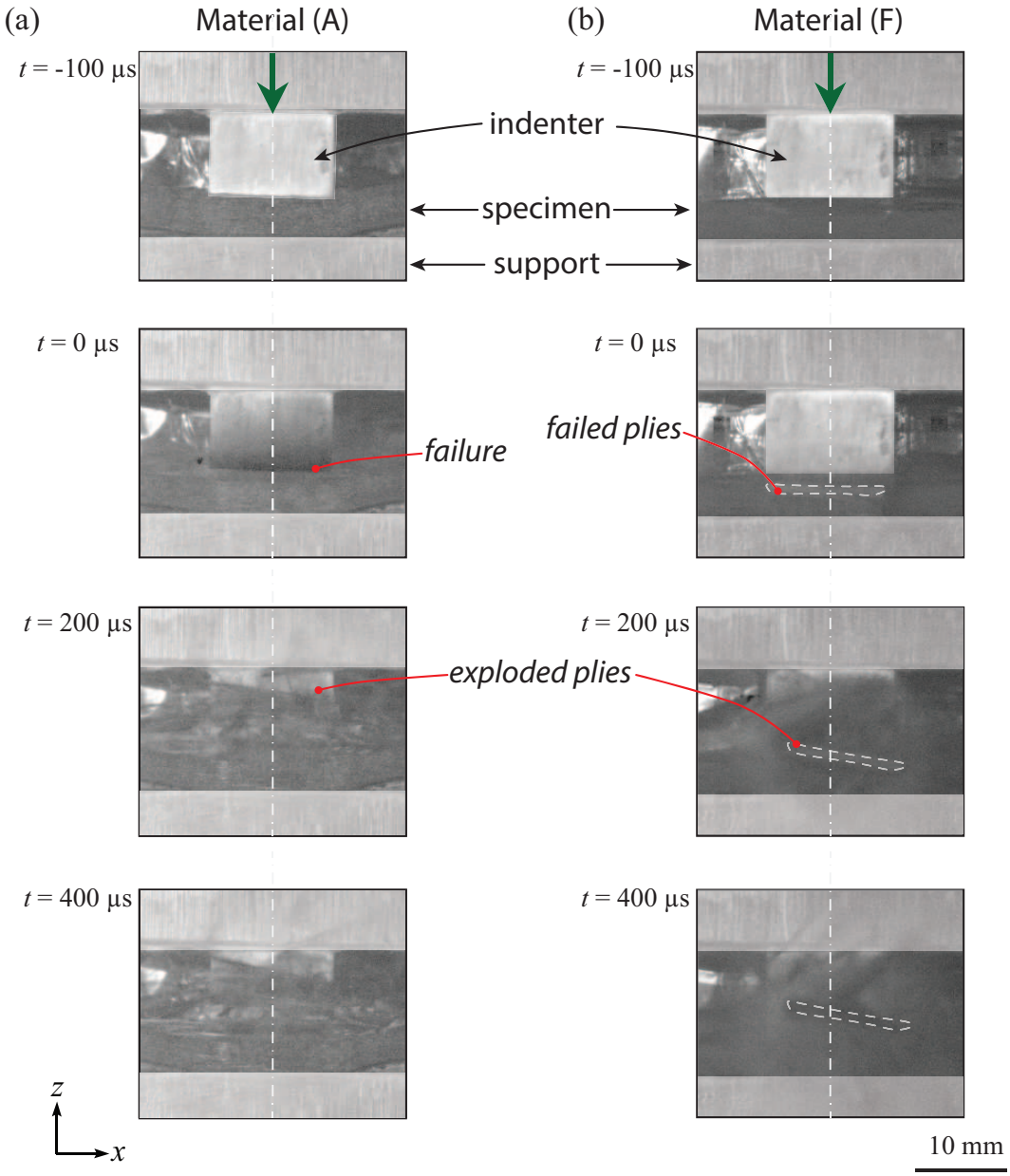

Figure 5.3: High-speed images of the failure in the quasi-static indentation test of a) material (A) and b) material (F). $t = 0$ corresponding to the instant of failure.

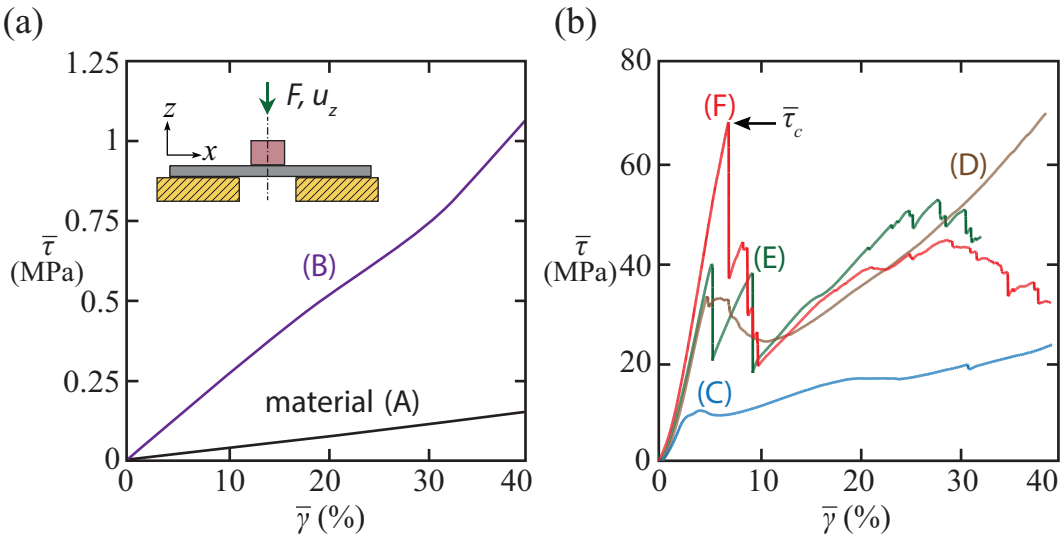

Figure 5.4: Quasi-static cropping test responses of a) materials (A) to (B) and b) materials (C) to (F) in terms of $\bar{\tau}$ versus $\bar{\gamma}$.

Recall that $B = 11$ mm, $H = 4$ mm, and $c = 3$ mm. Two types of response were observed. Materials (A) and (B) showed a ductile shear response without failure; the shear stress increased continuously throughout the test. Materials (C) to (F) showed initial peak stress $\bar{\tau}_c$ at $\bar{\gamma} \sim 10\%$ followed by a hardening response up to $\bar{\gamma} \sim 20\%$, and a sequence of loading drops at $\bar{\gamma} \sim 30$ - 40%.

Additional interrupted tests were performed on the selected materials (A), (C), and (F) through the process of loading the specimens to $\bar{\gamma} = 10\%$ and 40%, followed by unloading. During the interrupted tests, optical images of the specimens were recorded and are presented in Figure 5.5. Generally speaking, all specimens showed shear deformation in the cropping test. For material (A), shear deformation was observed within the region inside the clearance c between the edge support and the indenter at $\bar{\gamma} = 10\%$, and interfacial shear and delamination were observed at $\bar{\gamma} = 40\%$. For materials (C) and (F), damage was initiated underneath the edge of the indenter at $\bar{\gamma} = 10\%$, and shear cracks across the height of the specimen were observed at $\bar{\gamma} = 40\%$. Close up microscopy revealed that the damage in materials (C) and (F) was caused by fibre fracture in the top ply and the formation of transverse matrix cracks and ply delamination in the lower plies, see Figure 5.5d.

Table 5.3 summarises the measured shear strengths from the cropping test $\bar{\tau}_c$ and compares them against the matrix shear strength of the laminates measured from the short beam shear test τ (refer to Appendix B for the shear

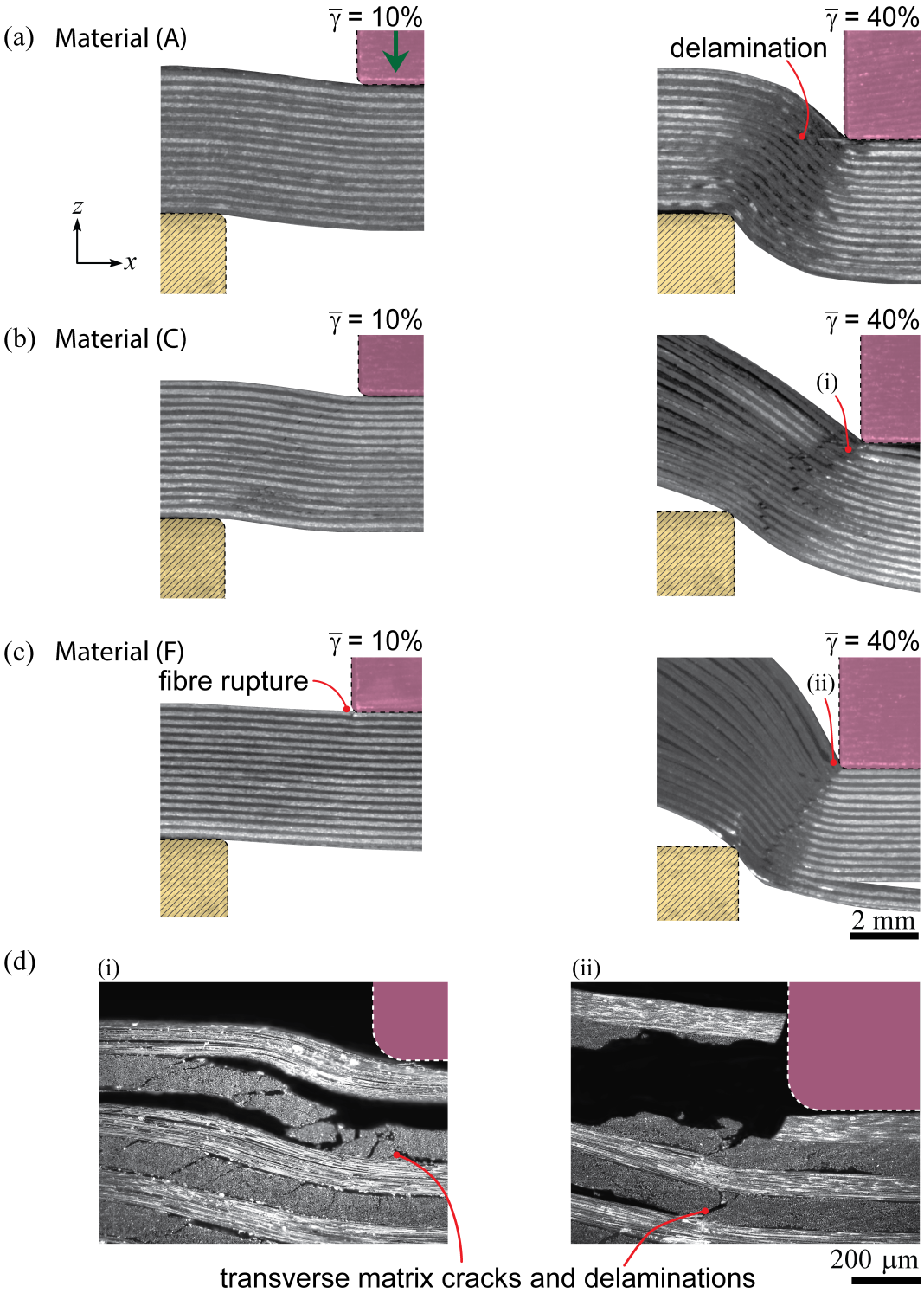

Figure 5.5: Optical images recorded during the interrupted cropping tests of a) material (A), b) material (C), and c) material (F) at $\gamma = 10\%$ and 40% (only a 9× 9 mm window of one side of the punched region was recorded). d) For materials (C) and (F), close up optical microscopy of the damaged areas is provided, labelled as (i) and (ii).

Table 5.3: Comparison between peak shear strengths obtained from the quasi-static indentation test versus those obtained from the short beam shear test.

Material	Short beam shear strength τ (MPa)	Cropping test average shear strength $\bar{\tau}_c$ (MPa)	Ratio between the two tests $\bar{\tau}_c/\tau$
A	0.11 [a]	0.05 [b]	0.45
B	0.82 [a]	0.4 [b]	0.49
C	22 ± 1.9	11	0.5
D	30. ± 1.3	32	1.1
E	61 ± 3.7	38	0.62
F	99 ± 6.9	67	0.67

[a] Materials (A) and (B) showed no failure in the short beam shear test. Therefore, the above short beam shear strengths τ represent the flow stresses at shear strain of 5% $\tau(\gamma = 5\%)$ and at a shear strain rate of $\dot{\gamma} = 10^{-3}s^{-1}$.
[b] Materials (A) and (B) showed no failure in the cropping test. Therefore, the above shear strengths are the average shear stress $\bar{\tau}_c$ at an average shear strain of 5% $\bar{\tau}_c(\bar{\gamma} = 5\%)$ and at an average shear strain rate of $10^{-3}s^{-1}$.

test specifications). The average shear strengths in the cropping test $\bar{\tau}_c$ are comparable to those obtained from the short beam shear test (the lower values of $\bar{\tau}_c$ could be attributed to the stress concentration caused by the indenter).

5.4.3 Ballistic Test

Ballistic tests were performed on the composite beams under a simply supported boundary condition and at impact velocities v_0 ranging from 45 m/s to 355 m/s. The fraction of cut plies f as a function of the projectile velocity v_0 is plotted in Figure 5.6. f is defined to be the ratio of the number of plies that show fibre failure to the total number of plies in the specimens (32 plies). Two critical velocities can be defined: v_{init} is the velocity at initiation of failure (i.e. $f \geq 0$), and v_p is the penetration velocity (i.e. $f = 1$). v_{init} is defined as the average between the lowest velocity resulting in damage to the target and

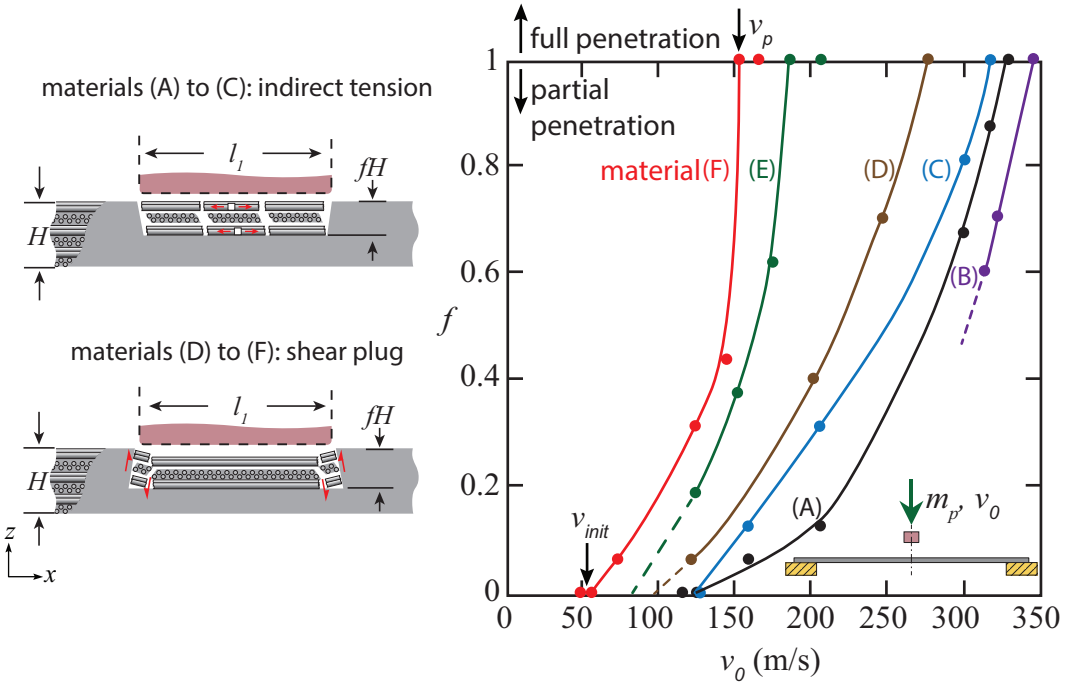

Figure 5.6: The ballistic cut fraction f in materials (A) to (F) are plotted as functions of the impact velocity v_0. Lines are drawn to help reveal trends.

the highest velocity that did not lead to damage of the target. v_p is defined as the average between the lowest velocity resulting in full penetration of the target and the highest velocity resulting in partial penetration of the target. The v_{init} of materials (A), (C), and (F) and the v_p of materials (A) to (F) are summarised in Table 5.4.

In general, both v_{init} and v_p increase as the state of matrix cure declines from material (F) to material (A). The effect of matrix shear strength on ballistic resistance becomes apparent in Figure 5.7, where v_{init} and v_p are plotted against the laminates' matrix shear strength τ in semi-log scale. There exist two regimes of ballistic behaviour, with a transition point at $\tau = 22$ MPa that corresponds to material (C). At the region where $\tau > 22$ MPa, specimens show lower ballistic resistance. For instance, the fully cured material (F) shows the weakest resistance against the projectile: $v_{init} = 64 \pm 9$ m/s and $v_p = 148 \pm 4$ m/s. Both v_{init} and v_p improve as matrix shear strength decreases up to $\tau = 22$ MPa and then remain constant. For example, the uncured material (A) shows a significantly higher ballistic resistance with $v_{init} = 142 \pm 16$ m/s and $v_p = 323 \pm 6$ m/s. This sudden change in the relationship between τ and v_p indicates a switch in failure mode at 22 MPa.

Table 5.4: Summary of the failure initiation velocity v_{init} and penetration velocity v_p of materials (A) to (F) in the ballistic test.

Material	Failure initiation velocity v_{init} (m/s)	Penetration velocity v_p (m/s)	v_{init}/v_p
A	141 ± 17	323 ± 6	0.44 ± 0.12
B	< 321	338 ± 12	–
C	143 ± 16	309 ± 8	0.46 ± 0.12
D	< 125	263 ± 15	–
E	< 124	181 ± 6	–
F	64 ± 8	148 ± 4	0.43 ± 0.13

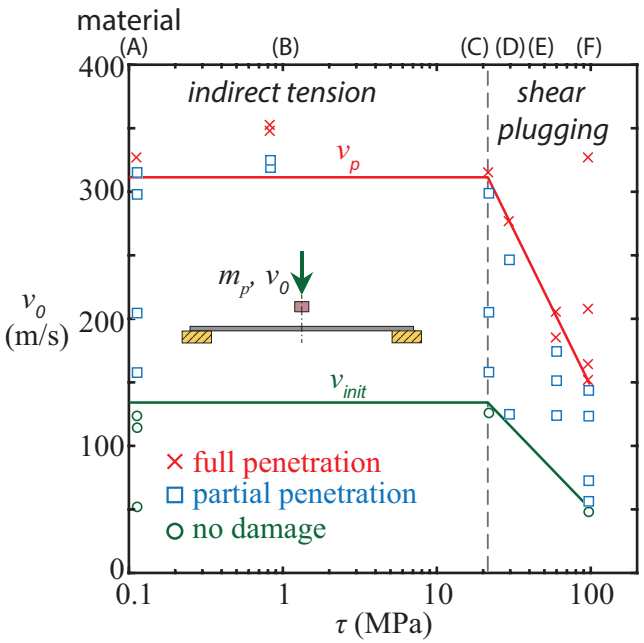

Figure 5.7: Failure initiation velocity v_{init} and penetration velocity v_p are plotted as functions of matrix shear strength τ. Lines are drawn to help reveal trends.

Figure 5.8c displays the post-test evidence that materials (A) and (C) failed by an indirect tension mode, materials (D) and (F) failed by a shear plugging mode. The top views of materials (A) and (C) reveal that fibre tensile failure occurred at multiple locations underneath the projectile (labelled (i) in Figure 5.8a) and was accompanied by two tensile cracks forming at the edge of contact, indicating that materials (A) to (C) failed by indirect tension (recall that a similar failure mechanism was observed in the out-of-plane compression experiment of CFRP cross-ply laminates reported Chapter 3). Furthermore, the profile view of material (A) shows Poisson expansion of the 90° plies extruded out from the edge of the specimen in the area beneath the projectile (labelled (ii) in Figure 5.8a). This reveals the existence of an out-of-plane compressive stress, which provides further evidence of indirect tension. For materials (D) to (F), fibre failure was not observed in the area underneath the projectile. Instead, the failure of these specimens was caused by transverse matrix cracks, ply delamination, and fibre fracture beneath the edge of contact (designated as location (iii) in Figure 5.8b). This mechanism is commonly observed in carbon/epoxy composites and is referred to as shear plugging.

Figure 5.9 shows a sequence of high-speed images in profile view of the composite beams impacted at velocities just above their failure initiation velocity v_{init}: $v_0 = 158$ m/s for materials (A) and (C), and $v_0 = 73$ m/s for material (F). Materials (A) and (C) failed by an indirect tension mechanism that is facilitated by ply tensile failure. In contrast, material (F) failed by a shear plugging mode where failure was localised underneath the edge of contact. Note that partially cured materials (D) and (E) generated large amounts of dust and debris immediately following impact due to the failure of the matrix materials. Although the high-speed images for these materials were not informative, post-test optical inspection revealed that they failed by a shear plugging mode. Furthermore, the high-speed images revealed the time at which fibre failure was first observed t_f (referred to here as failure time): $t_f = 10.4$ μs in material (A), $t_f = 11.6$ μs in material (C), and $t_f = 53.8$ μs in material (F).

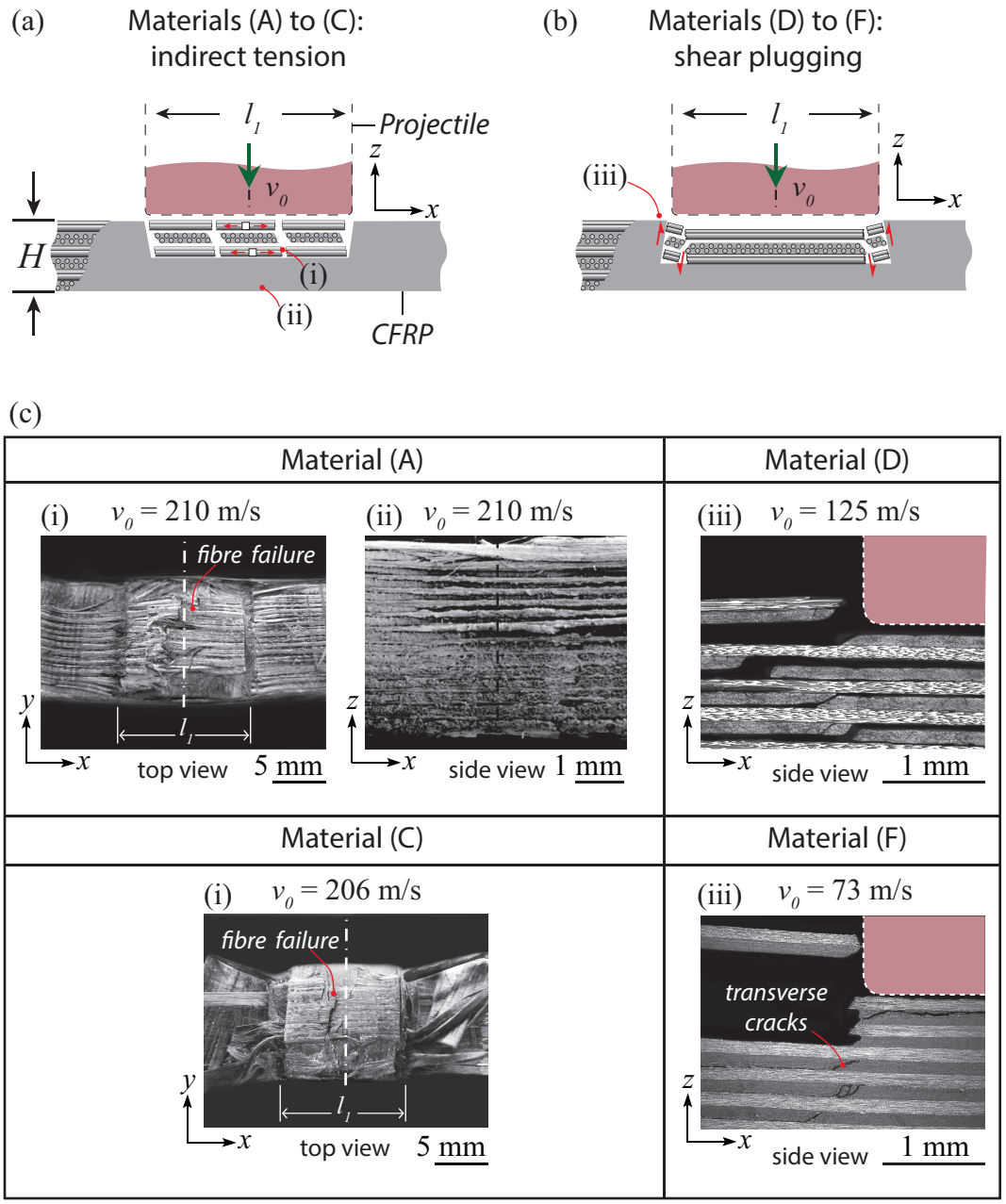

Figure 5.8: Schematic illustrations of the a) indirect tension and b) shear plugging mechanisms. c) The optical images showing the ballistic failure mechanism in materials (A), (C), (D), and (F).

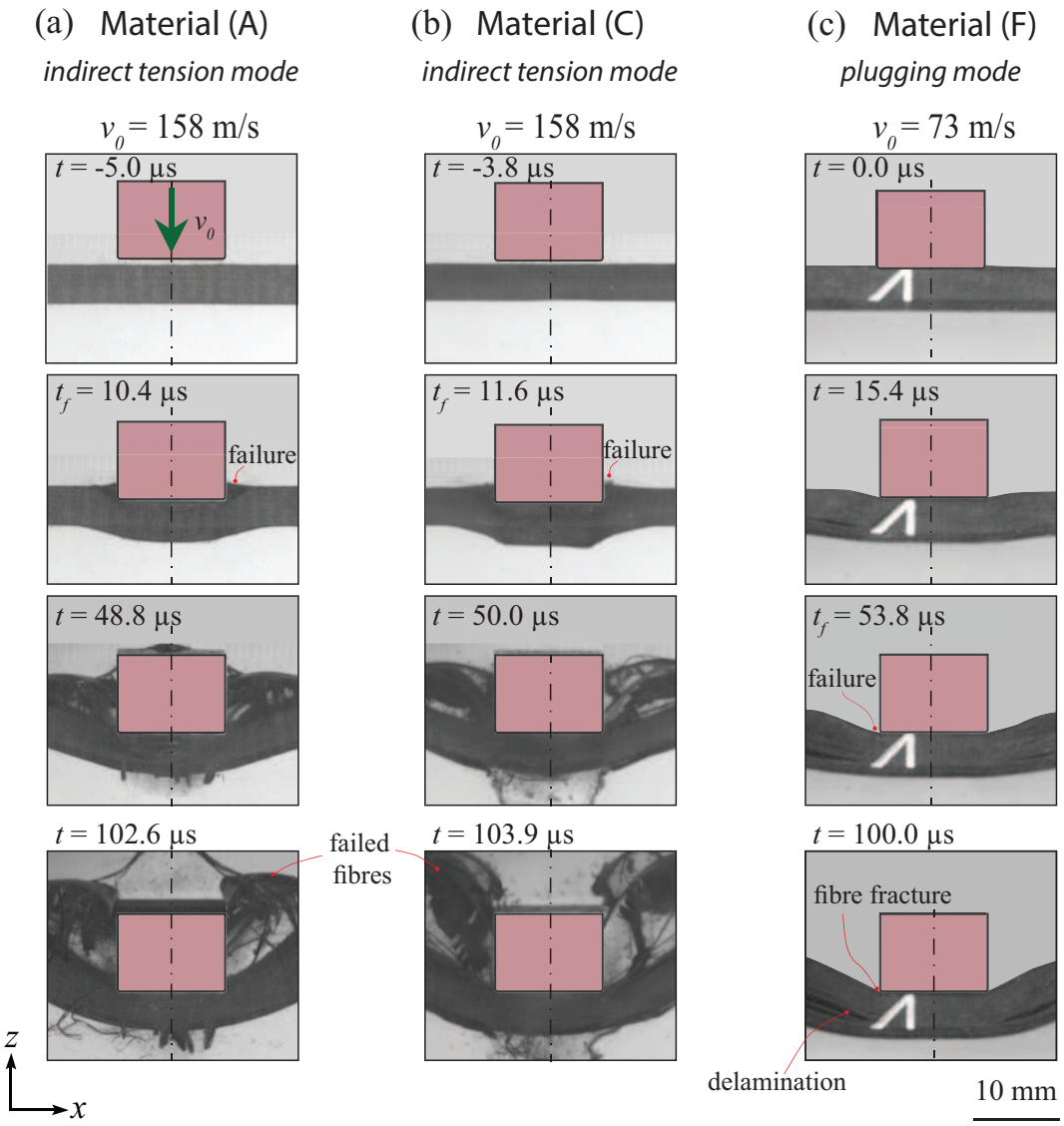

Figure 5.9: High-speed image sequences of a) material (A) b) material (C), and c) material (F) recorded during the ballistic test. Materials (A) and (C) failed by an indirect tension mechanism, whereas material (F) failed by a shear plugging mode. t = 0 corresponding to the instant of impact. t_f is defined to be the time when fibre failure is first observed.

5.5 Discussion

5.5.1 Failure Mechanisms in the Quasi-static Indentation and Cropping Tests

In the current study, shear plugging and indirect tension are the two competing mechanisms in the composite cross-ply beams. When a composite beam is supported on a rigid foundation in the indentation test, the out-of-plane shear deformation of the composite beam is prohibited and the shear plugging mechanism is thus suppressed. The materials that are sandwiched between the indenter and the back support are subjected to out-of-plane compression (see illustration in Figure 5.10a). As a result, the specimens failed by indirect tension at an average indentation pressure $\bar{p}_c$ ranging from 761 MPa to 1252 MPa (summarised in Table 5.2). It is worth noting that Attwood et al. (2016) have also conducted a similar back-supported indentation test with a flat indenter on Dyneema®cross-ply beams (with thickness $H = 12.4$ mm). Their results were in agreement with the overall failure mechanism observed in the current study, with one exception. Attwood et al. (2016) observed a 'saw-tooth' shaped pressure-displacement response. In contrast, the composite beams tested in the current study exhibited catastrophic failure where the fragments of the materials exploded away from the testing apparatus. This type of failure can be attributed to the lower thickness of the tested specimens (thickness $H = 4$ mm).

Conversely, when a composite beam is subjected to a cropping test, the opening of the back support permits out-of-plane shear deformation of the composite beams within clearance between the edge support and the flat indenter (see illustration in Figure 5.10b).

In the cropping test, the load required to cause shear failure F_{SP} can be estimated by:

$$F_{SP} = 2\tau HB \tag{5.5}$$

However, if the contact pressure underneath the indenter reaches the out-of-plane compressive strength of the material, the laminate would fail by indirect tension. In the cropping test, the load required to cause indirect tension failure F_{IT} can be estimated by:

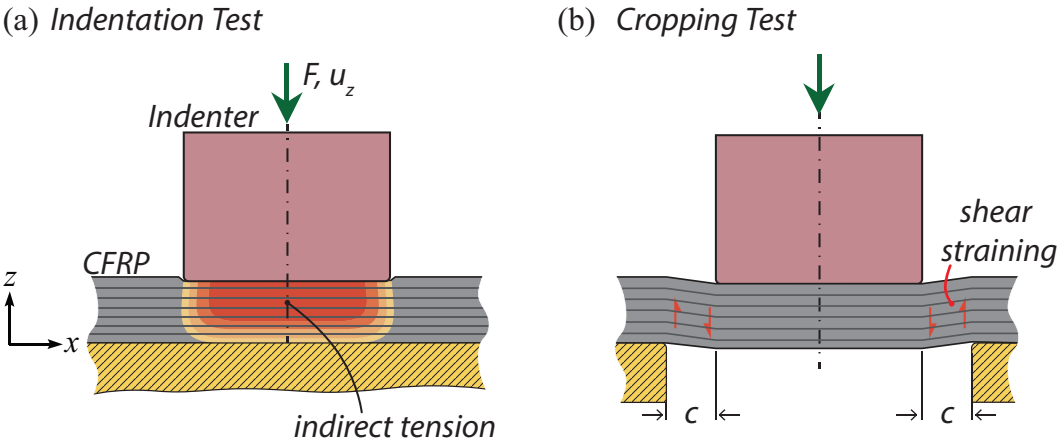

Figure 5.10: Schematic illustrations of the failure mechanism of a composite beam when subjected to a) the indentation test and b) the cropping test.

$$F_{IT} = \bar{p}_c l_1 B \tag{5.6}$$

The failure mechanism is determined by the ratio F_{SP}/F_{IT}:

$$\frac{F_{SP}}{F_{IT}} = \frac{2\tau H}{\bar{p}_c l_1} \tag{5.7}$$

The shear plugging mechanism occurs when $F_{SP}/F_{IT} < 1$ and the indirect tension mechanism occurs when $F_{SP}/F_{IT} > 1$. Thus, failure mechanism is sensitive to the material properties (i.e. $\tau/\bar{p}_c$) and the specimen geometry (i.e. $2H/l_1$). In the current study, $l_1 = 12.5$ mm, $H = 4$ mm, τ ranges from 0.11 MPa in material (A) to 99 MPa in material (F), and $\bar{p}_c$ ranges from 761 MPa in material (A) to 1252 MPa in material (F). Thus, the calculated ratio F_{SP}/F_{IT} ranges from 10^{-4} in material (A) to 0.06 in material (F). Both of these values are below 1, which explains the current study's findings that all specimens failed by shear plugging in the cropping test. However, if $2H/l_1$ were to increase from the current value of 0.73 to 20, the ratio F_{SP}/F_{IT} would then increase to range from 3×10^{-3} in material (A) to 1.6 in material (F). This suggests that the failure mechanism can potentially change from shear plugging to indirect tension as the state of matrix cure increases from material (A) to material (F).

5.5.2 Failure Mechanisms in the Ballistic Test

Materials (D) to (F) have a high matrix shear strength (30 to 100 MPa) and failed by a brittle shear plugging mode in the ballistic test. As the matrix

shear strength was reduced from 100 MPa to 22 MPa, both the initiation velocity v_{init} and the penetration velocity v_p improved two-fold. For matrix shear strength below 22 MPa, materials (A) to (C) failed by an indirect tension mechanism. In this failure regime, penetration velocity remained elevated and was independent of the matrix shear strength. The underlying reason for the change in failure mechanism as matrix shear strength decreases remains unclear. Furthermore, it is worth noting that the above trend for materials failing by the shear plugging mechanism is surprising. Whereas the ballistic test for these materials showed that penetration velocity increased as matrix shear strength decreased, the opposite trend was observed in the quasi-static cropping test (i.e. the indentation load required to cause shear plug formation increased proportionally to the matrix shear strength).

The effect of matrix properties on ballistic performance has also been observed by de Ruijter et al. (2010) through the ballistic testing of aramid composites with different grades of semi-flexible thermotropic liquid crystalline polyesters and poly(ester-amide)s matrices. They observed that the penetration velocity of these aramid laminates was independent of the matrix modulus within the range of 0.01 GPa to 1 GPa, whereas the penetration velocity decreased along with the matrix modulus in the range of 1 GPa to 10 GPa. They proposed that, at the high modulus level (i.e. 1 GPa to 10 GPa), the increase in friction among the fibres may result in a reduction in fibre mobility which can give rise to premature fibre breakage. Their results are in agreement with the findings of the current study.

5.5.3 Estimation of Penetration Velocity

The penetration velocity of composite beams can be estimated according to their particular failure mechanism. In the case of indirect tension, as observed in materials (A) to (C), failure can occur if the contact pressure underneath the projectile reaches the out-of-plane compressive strength of the material. The energy required to cause indirect tension failure E_{IT} can be estimated as:

$$E_{IT} = \int_0^H \bar{p}_c l_1 B dH = \bar{p}_c l_1 B H \tag{5.8}$$

where $\bar{p}_c$ is the failure pressure measured from the quasi-static indentation test. The penetration velocity of the indirect tensile failure mechanism v_{IT} can be estimated by equating E_{IT} with the kinetic energy of the projectile:

$$v_{IT} = \sqrt{\frac{2l_1 B\bar{p}_c H}{m_p}} \tag{5.9}$$

where m_p is the mass of the projectile (1.1×10^{-2} kg).

In the case of shear plugging, as observed in materials (D) to (F), failure can occur if the shear stress underneath edge of contact reaches the shear strength of the laminate. The energy required to cause shear plugging E_{SP} can be estimated as:

$$E_{SP} = \int_0^H 2\bar{\tau}_c BH dH = \bar{\tau}_c BH^2 \tag{5.10}$$

where $\bar{\tau}_c$ is the shear strength measured from the quasi-static cropping test. The penetration velocity that causes shear plugging v_{SP} can be estimated by equating E_{SP} with the kinetic energy of the projectile:

$$v_{SP} = \sqrt{\frac{2\bar{\tau}_c BH^2}{m_p}} \tag{5.11}$$

Figure 5.11a plots the measured penetration velocity v_p of materials (A) to (C) as well as the estimated v_{IT} in Eq. (5.9) as functions of $\bar{p}_c$. The predicted v_{IT} is in agreement with the data for materials (A) to (C), confirming that these materials indeed fail by the indirect tension mechanism. Figure 5.11b plots the measured penetration velocity v_p of materials (D) to (F) as well as the estimated v_{SP} in Eq. (5.11) as functions of $\bar{\tau}_c$. The predicted v_{SP} underestimated the penetration velocity v_p of materials (D) to (F). Part of this discrepancy could be attributed to the strain rate effect of the matrix shear strength. Hopkinson bar experiments on CFRP composites from the available literature have shown that matrix shear strength has a strain rate dependency and typically rises 50% to 100% as the strain rate increases from $10^{-3}s^{-1}$ to $10^3 s^{-1}$ (Gerlach et al., 2013; Guedes et al., 2005; Hosur et al., 2001; Hsiao et al., 1999; Koerber et al., 2010; Tsai, 2005). However, this rate dependency is not sufficient to account for the discrepancy between the predicted v_{SP} and the measured v_p for materials (D) to (F). Furthermore, the above prediction of v_{SP} suggests that the penetration velocity is proportional to the $\sqrt{\bar{\tau}_c}$. An opposite trend was observed for the v_p measured in the ballistic test of materials (D) to (F).

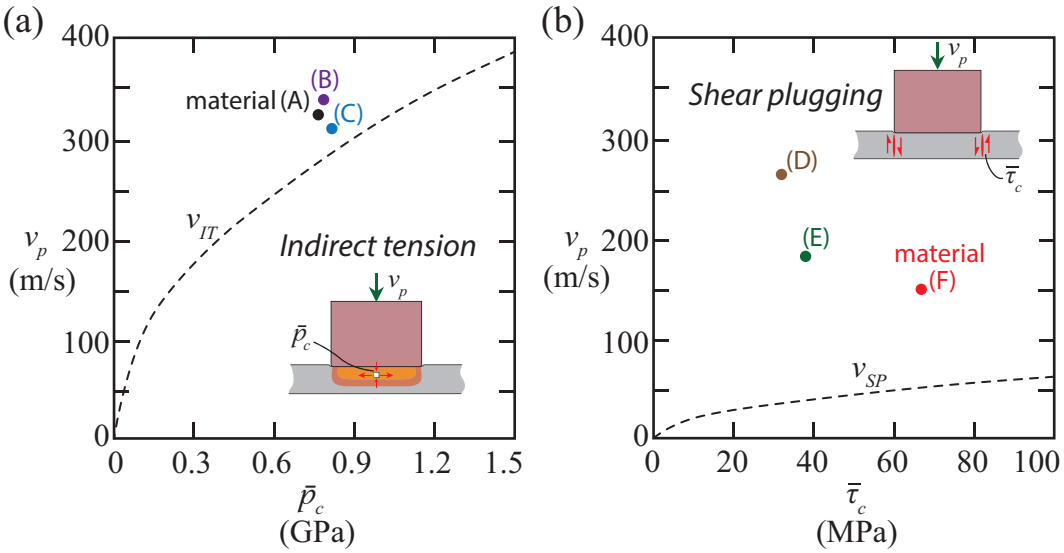

Figure 5.11: Plots of a) the predicted penetration velocity caused by indirect tension failure v_{IT} as a function of $\bar{p}_c$ and b) the predicted penetration velocity caused by shear plugging v_{SP} as a function of $\bar{\tau}_c$. Data for materials (A) and (F) were also presented in the figures.

Although the current analysis did not accurately predict the performance of materials that fail by shear plugging, it is clear that the change in perforation mechanism from a brittle shear plugging mode to indirect tension increases the penetration velocity v_p.

5.5.4 The Effect of Perforation Mechanism on the Failure Time

The above analysis demonstrated that the indirect tension failure observed in materials (A) to (C) is generated by the contact pressure p between the projectile and the composite laminate. O'Masta et al. (2015a) recently observed that Dyneema® cross-ply laminates also fail by the same indirect tension mechanism in an edge-clamped ballistic experiment. They proposed that the indirect tension mechanism of Dyneema® cross-ply laminates can be generated by the compressive pressure due to impact. They stated that, at the onset of impact, a compressive stress wave would travel through the thickness of the laminate from the projectile to the distal face at a speed of approximately $c_T \sim \sqrt{E_T/\rho}$, where E_T is the through-thickness tangent modulus and ρ is the density, with a peak pressure p scaling as $\rho c_T v_0$. When the wave front reaches the free boundary at the back face (at $t = H/c_T$ where H is the thickness of

the laminate), a zero-stress wave would then reflect back toward the projectile. The contact pressure at the top face is partially relieved when this wave arrives to the top (at $t = 2H/c_T$).

Recall that high-speed images revealed that laminates failing by indirect tension, such as materials (A) and (C), have lower failure times t_f ($\sim$ 10 μs) than material (F) ($\sim$ 54 μs), which failed by shear plugging, see Figure 5.9. t_f is defined to be the time when fibre fracture was first observed at an impact velocity just above v_{init}. Figure 5.12 presents these data by plotting a dimensionless parameter $n = t_f c_T/H$ as a function of the matrix shear strength τ of the laminates. n represents the number of transverse wave reflections before first failure occurs. In the figure, the transverse wave speeds $c_T^{(i)}$ and $c_T^{(ii)}$ were calculated based on the through-thickness tangent modulus of the composite beams measured from the quasi-static indentation tests at $\bar{\varepsilon} = 5\%$ and 10%, respectively (see Table 5.2). Figure 5.12 shows that laminates which failed by indirect tension, such as materials (A) and (C), have lower failure times t_f and the number of wave reflections before failure n can be as low as 2 to 5, in agreement with the premise from O'Masta et al. (2015a). In contrast, material (F), which failed by shear plugging, has a high failure time t_f and the number of wave reflections before failure n can be as high as 25 to 30.

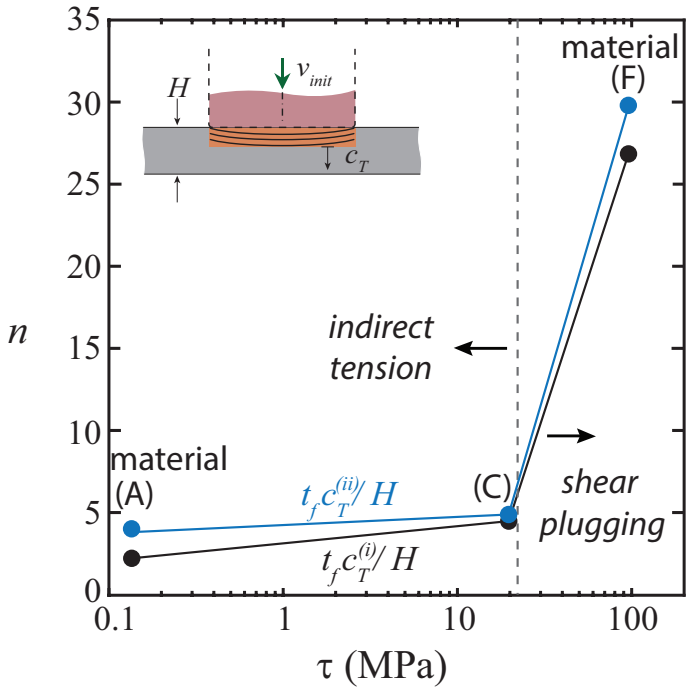

Figure 5.12: Plot of a dimensionless parameter $n = t_f c_T/H$ as a function of the matrix shear strength τ in the composite beams. $c_T^{(i)}$ and $c_T^{(ii)}$ were calculated based on the through-thickness tangent modulus of the composite beams measured from the quasi-static indentation tests at $\bar{\varepsilon} = 5\%$ and 10%, respectively.

5.6 Conclusions

The penetration resistance and failure mechanisms of $[0°/90°]_{16}$ CFRP composite beams with six different states of matrix cure (matrix shear strength τ ranging from 0.1 MPa to 100 MPa) were measured and compared through (i) a quasi-static indentation test with rigid back support, (ii) a quasi-static cropping test with a clearance c between the edge support and a flat indenter, and (iii) a ballistic impact test using a cuboid shaped projectile under a simply supported boundary condition.

Composite beams that were tested in quasi-static indentation with rigid back supports all exhibited an indirect tension failure mode that consisted of ply Poisson expansion in the direction transverse to the fibre and ply tensile failure in the fibre direction. Composite beams that were investigated in quasi-static cropping tests all showed a shear plugging mode that consisted of transverse matrix cracks, ply delamination, and fibre fracture beneath the edge of contact. In the ballistic impact tests, CFRP beams with a high matrix shear strength (30 to 100 MPa) failed by a brittle shear plugging mode. As the matrix shear strength was reduced from 100 MPa to 22 MPa, penetration velocity improved two-fold. Once the matrix shear strength decreased below 22 MPa, the failure mode switched to indirect tension. For this failure regime, penetration velocity remained elevated and was independent of the matrix shear strength. Specimens with matrix shear strength of 22 MPa offer both acceptable penetration resistance and structural performance.

The above findings suggest a solution to the shortcomings of CFRP laminates currently in use. At present, CFRP offers superior structural properties under quasi-static loading conditions but provides weaker impact resistance in dynamic environments compared to composites manufactured from flexible fibres such as Dyneema® and Kevlar®. The author attributes this weakness to a brittle shear plugging failure mode and demonstrate that impact resistance can be improved through the reduction of matrix cure. This creates the possibility of designing composite structural armour from CFRP laminates that can offer high impact resistance joined with strong structural performance.

Chapter 6

Perforation of Bilayer CFRP Beams under Quasi-static and Ballistic Loading

Summary

This chapter explores the possibility of improving the impact resistance of cured CFRP layers with high matrix shear strength by protecting them with uncured cross-ply laminates. Particular attention is paid to suppressing the commonly observed brittle shear plugging mechanism when cured CFRP layers are subjected to ballistic impact, as well as the comparison between quasi-static and ballistic failure mechanisms in the protected CFRP layer. CFRP cross-ply laminates were prepared under two states of cure: as-received uncured prepregs with matrix shear strength of 0.1 MPa and oven-cured layers with matrix shear strength of 61 MPa. Two types of bilayer composite beams were manufactured: (i) bilayer composite beams with the uncured layer on top of the cured layer, and (ii) bilayer composite beams with the cured layer on top of the uncured layer; each layer had half the thickness of the bilayer beams. The performance of the bilayer beams was compared against their monolithic precursors with the same thickness. All composite beams were then subjected to quasi-static indentation tests with rigid back support, quasi-static cropping tests, and ballistic impact tests with a cuboid shaped projectile under a simply supported boundary condition. In both quasi-static tests, the stacking configuration of the bilayer beams had no effect on the failure mechanism and the test

responses. Both types of bilayer beams failed by indirect tension (consisting of ply tensile failure in the fibre direction) in the back-supported indentation tests and failed by shear plugging (consisting of transverse matrix cracks, ply delamination, and fibre fracture) in the quasi-static cropping tests. In contrast, the bilayer beams showed a mixed mode failure in the ballistic impact test. The uncured layer was found to fail by indirect tension regardless of its stacking configuration, whereas the cured layer failed by shear plugging when it was placed at the front face and failed by a back face tensile mode when it was placed at the distal face. Overall, the impact resistance of the bilayer beams closely followed the rule of mixtures compared to their monolithic precursors. Compared to the monolithic cured CFRP beams, the ballistic penetration velocity of the bilayer beams showed a 43% improvement when the cured layer was at the distal face and showed a 64% improvement when the cured layer was at the front face.

6.1 Introduction

Conventional Carbon Fibre Reinforced Plastic (CFRP) laminates with a high strength epoxy matrix (with shear strength ranging from 50 MPa to 100 MPa) deliver inferior impact resistance compared to armour-grade composites such as UHMWPE fibre based Dyneema® laminates consisting of a soft theromplastic matrix (with shear strength in the order of 1 MPa to 10 MPa). Under ballistic loading, CFRP composites normally fail by a brittle shear plugging mode, whereas UHMWPE fibre composites fail by an indirect tension mode that is facilitated by ply tensile failure. This chapter explores the potential of improving the impact resistance of CFRP composites by suppressing the shear plugging mode through composite hybridisation.

Peijs and Venderbosch (1991); Peijs et al. (1990b) have demonstrated that it is possible to improve the ballistic limit (i.e. penetration velocity) of CFRP plates through a composite hybridisation technique. In their studies, the researchers conducted ballistic and Charpy impact tests on hybridised composite laminates that consisted of alternating layers of UHMWPE fibre composites and CFRP composites. They found that the penetration velocities of these hybridised composites were higher than those of monolithic CFRP with the same thickness. The penetration velocity increased along with the degree of hybridation (i.e. the total number of alternating layers for a given composite thickness). Other researchers have also investigated the impact resistance of various forms of fibre composite hybrids, such as glass fibre/carbon fibre hybrids (Enfedaque et al., 2010; Harris and Bunsell, 1975; Sevkat et al., 2009) and Kevlar® fibre/carbon fibre hybrids (Enfedaque et al., 2010; Park and Jang, 2001; Perry and Adams, 1975). Their results were in agreement with those observed by Peijs and Venderbosch (1991); Peijs et al. (1990b).

An investigation presented in Chapter 5 demonstrated that the penetration velocity of CFRP cross-ply beams can also be improved through the reduction of the matrix shear strength. CFRP beams with a high matrix shear strength fail by a brittle shear plugging mode. As the matrix shear strength is reduced from 100 MPa to 22 MPa, penetration velocity improves two-fold. Once the matrix shear strength decreases below 22 MPa, the failure mode switches to indirect tension and the CFRP laminates behave similarly to UHMWPE fibre composites. For this failure regime, penetration velocity remains elevated and

is independent of the matrix shear strength.

The findings from Chapter 5 suggest that CFRP laminates with low matrix shear strength can fulfill a similar role as UHMWPE fibre composites in the hybridisation technique described by Peijs and Venderbosch (1991); Peijs et al. (1990b). It is possible to develop a new form of CFRP hybrid composites with an improved ballistic limit by alternating layers of CFRP with low matrix shear strength and high matrix shear strength. As yet, no literature has investigated the impact response of this type of hybrid composite. Consequently, the current chapter seeks to determine whether this form of hybridisation can suppress the brittle shear plugging mode observed in conventional CFRP.

6.1.1 Scope of Study

In this chapter, the impact resistance and perforation mechanisms of bilayer CFRP composite beams (consisting of one layer with low matrix shear strength and one layer with high matrix shear strength) are compared to those of their monolithic precursors. Figure 6.1 illustrates the two types of bilayer composite beams investigated in this chapter: (i) bilayer composite beams with the uncured layer (with $\tau = 0.1$ MPa) on top of the cured layer (with $\tau = 61$ MPa), and (ii) bilayer composite beams with the cured layer on top of the uncured layer; each layer had half the thickness of the bilayer beams. The performance of the bilayer beams was compared against their monolithic precursors with the same thickness. Note that a composite beam configuration was selected for ease of identifying the failure mechanisms (such as shear plugging and indirect tension).

The composite beams were subjected to three types of tests: (i) a quasi-static indentation test with rigid back support, (ii) a quasi-static cropping test with a clearance c between the edge support and a flat indenter, and (iii) a ballistic test with a cuboid shaped projectile and a simply supported boundary condition. For ease of comparison, the dimensions of the composite beams and the test set-up in the current study were identical to those in Chapter 5. The perforation mechanisms and ballistic penetration velocities of these composite beams were then compared against one another.

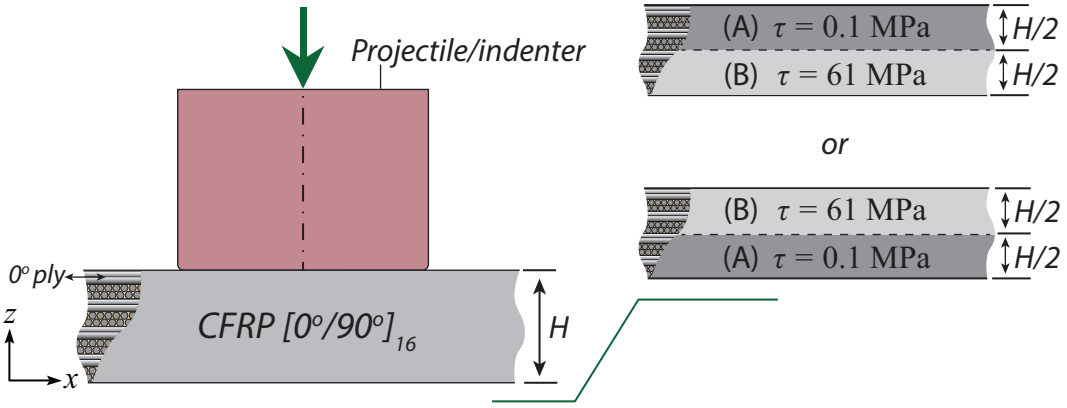

Figure 6.1: Schematic illustration of the stacking configuration of CFRP layers in the bilayer composite beams (A-on-B) and (B-on-A).

6.2 Specimen Manufacture

CFRP cross-ply laminates with thickness of 2 mm (corresponding to $[0°/90°]_8$) and 4 mm (corresponding to $[0°/90°]_{16}$) were made from Hexply® 8552/35%134/IM7 carbon fibre/epoxy prepregs (with a ply thickness of 0.131 mm). The uncured prepregs were first laid-up by hand. They were then cut into rectangular beams with uniform dimensions (height of 2 or 4 mm, breath $B = 11$ mm, and length $L = 300$ mm) using a band saw. Half of these beams were cured by being placed in an air-oven at 180°C for 24 hours while being compressed in-situ at 0.1 MPa in the through-thickness direction by spring-loaded platens (see detailed drawing in Appendix A). The uncured 4 mm thick beams were designated as monolithic material (A) and the cured 4 mm thick beams were designated as monolithic material (B). The 2 mm thick beams were then stacked to create bilayer composite beams in two configurations: bilayer (B-on-A), material A on top of material B; and bilayer (B-on-A), material B on top of material A. The total beam height was $H = 4$ mm. All four types of composite beams consisted of the same beam height of $H = 4$ mm (32 plies), a $[0°/90°]_{16}$ lay-up, and areal density of $\rho_A = 6.28$ kg/m^2. They were stored at -15°C to avoid further curing and brought back to room temperature for 5 hours prior to testing.

Table 6.1: Summary of curing process of the cross-ply laminate precursors used in the bilayer beams.

Material	Curing method	Curing temperature	Curing duration	Applied pressure	Short beam shear strength τ (MPa)
A	uncured	room temperature	–	–	0.1 MPa [a]
B	oven cured	180 $^\circ$C	24 hours	out-of-plane, 0.1 MPa	61 MPa

[a] Material (A) was strain rate sensitive and its short beam shear test showed no shear failure. The matrix shear strength reported here is the reference shear stress obtained at a shear strain of 5% $\tau(\gamma = 5\%)$ and at a shear strain rate of $\dot{\gamma} = 10^{-3}s^{-1}$.

6.3 Experimental Methods

The experiments in the current chapter use the same set-ups as in Chapter 5. Nevertheless, a brief summary is provided below.

6.3.1 Quasi-static Indentation Test

CFRP monolithic and bilayer beams with rectangular dimensions (height of $H = 4$ mm (32 plies), breath of $B = 11$ mm, and length of $L = 75$ mm) were subjected to out-of-plane indentation by being placed between a flat back support and a hardened steel indenter with a square bottom of $l_1 = l_2 = 12.5$ mm in the x-y plane, see Figure 6.2a. Specimens were tested using a screw-driven test machine with a 150 kN load cell (or a servo hydraulic machine with a 1 MN load cell for loads in excess of 150 kN) at an applied displacement rate of $\dot{u}_z = 4 \times 10^{-3}$ mm/s in the z-direction in the figure. The indentation load F was recorded by the machine load cell and the displacement u_z was measured using a laser extensometer. For consistency, specimens were tested such that fibres in the top ply were parallel to the x-direction.

6.3.2 Quasi-static Cropping Test

CFRP monolithic and bilayer beams with the same rectangular dimensions mentioned above (i.e. $H = 4$ mm, $B = 11$ mm, $L = 75$ mm) were examined through a cropping test using a screw-driven test machine with a 150 kN load cell. Specimens were placed between a hardened steel indenter (with a square bottom of $l_1 = l_2 = 12.5$ mm in the x-y plane) and two back supports with 18.5 mm spacing, creating a clearance $c = 3$ mm (with $c/H = 0.75$) between the edge support and the flat indenter, see Figure 6.2b. Specimens were placed such that fibres in the top ply were parallel to the x-direction in the figure. The average shear strain of the specimen $\bar{\gamma}$ within the clearance c was calculated from the indenter displacement u_z as: $\bar{\gamma} = u_z/c$. The cropping tests were performed at an out-of-plane displacement rate of $\dot{u}_z = 3 \times 10^{-3}$ mm/s (associated with an applied shear strain rate of $\dot{\gamma} = 10^{-3}s^{-1}$). Side views of the specimens were recorded during the cropping tests using a PixeLINK® camera.

6.3.3 Ballistic Impact Test

CFRP monolithic and bilayer beams with rectangular dimensions (height of $H = 4$ mm (32 plies), breath of $B = 12.5$ mm, and length of $L = 300$ mm) were subjected to ballistic impact using a cuboid shaped projectile under a simply supported boundary condition. The specimens were adhered to a rigid steel foundation using double-sided adhesive tape such that they had a span length of $L_s = 250$ mm, see Figure 6.2c. Specimens were placed such that fibres in the top ply were parallel to the x-direction in the figure. Specimens were then impacted in the z-direction using a hardened steel projectile with a square cross-section of $l_1 = l_2 = 12.5$ mm in the x-y plane, a depth of $l_3 = 9$ mm in the z-direction, and a projectile mass of $m_p = 1.1 \times 10^{-2}$ kg. Projectiles were launched using a gas gun with a 4.5 m long barrel having a square inner cross-section of 13 mm $\times$ 13 mm. The impact velocity v_0 was measured using a set of laser gates.

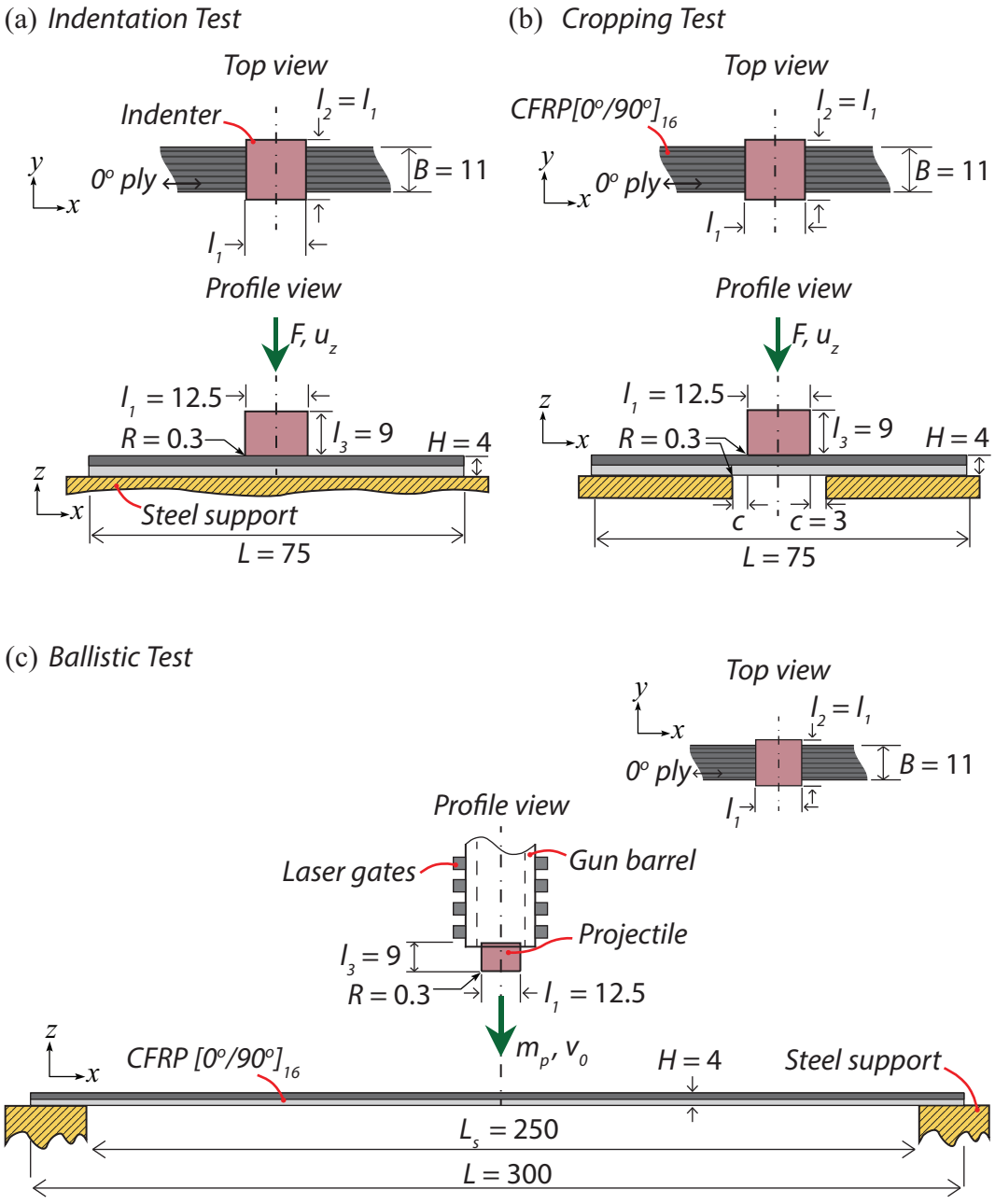

Figure 6.2: Schematic illustrations of the set-up used in the a) quasi-static indentation test, b) quasi-static cropping test, and c) ballistic test. All dimensions are in mm.

6.4 Results

6.4.1 Quasi-static Indentation Test

When the back-supported composite beams were subjected to indentation using a flat indenter, the material below the indenter experienced out-of-plane compression. The average indentation pressure $\bar{p}$ and the average compressive strain $\bar{\varepsilon}$ in the area underneath the indenter are expressed as:

$$\bar{p} = \frac{F}{Bl_1} \tag{6.1}$$

$$\bar{\varepsilon} = \frac{u_z}{H} \tag{6.2}$$

Figure 6.3 presents the indentation response of the two monolithic beams and the two bilayer beams in terms of $\bar{p}$ and $\bar{\varepsilon}$. All specimens showed catastrophic failure with acoustic emissions at peak values of average pressure $\bar{p}_c$. Among the four tested materials, monolithic material (A), bilayer composite beam (A-on-B), and bilayer composite beam (B-on-A) all failed at similar average pressures of $\bar{p}_c \sim 760$ MPa, whereas material (B) showed the highest average pressure at failure of $\bar{p}_c = 1260$ MPa. Post-test optical inspection revealed that all specimens showed catastrophic failure where plies exploded directly underneath the indenter (through fibre tensile failure). This failure mode resembles the indirect tension mechanism observed in the out-of-plane compression test of CFRP cross-ply laminates.

6.4.2 Quasi-static Cropping Test

When the composite beams were punched using a flat indenter through the opening of a back support with a clearance c between the edge support and the indenter, the material within the clearance was subjected to out-of-plane shear deformation. The average shear stress $\bar{\tau}$ and average shear strain $\bar{\gamma}$ are:

$$\bar{\tau} = \frac{F}{2BH} \tag{6.3}$$

$$\bar{\gamma} = \frac{u_z}{c} \tag{6.4}$$

Recall that $B = 11$ mm, $H = 4$ mm, and $c = 3$ mm. Figure 6.4 presents the cropping test responses of the composite beams in terms of $\bar{\tau}$ and $\bar{\gamma}$. Cropping tests in monolithic material (A) showed no failure. However, the scale of the

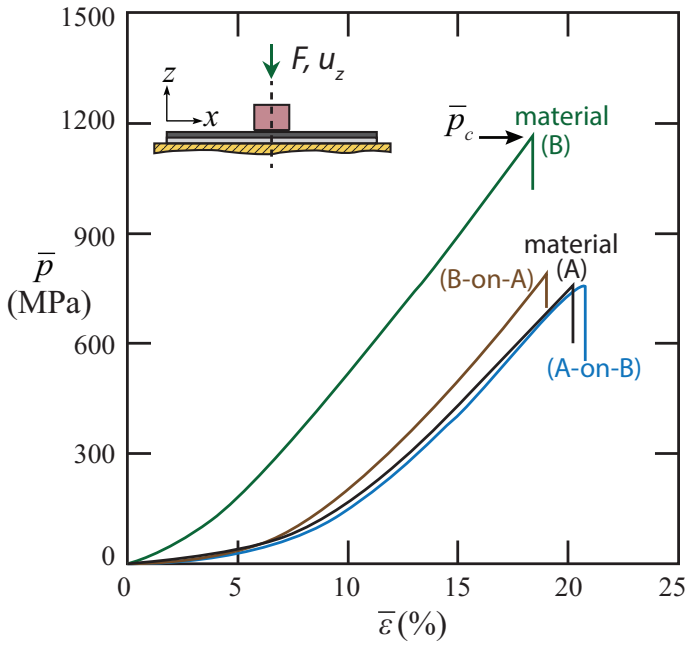

Figure 6.3: Static indentation responses of composite beams in terms of $\bar{p}$ versus $\bar{\varepsilon}$.

shear stress in material (A) was significantly lower than in the other specimens. In contrast, all other specimens showed initial peak values $\bar{\tau}_c$. Monolithic material (B) showed the highest peak strength with $\bar{\tau}_c = 38$ MPa at $\bar{\gamma} \sim 5\%$. Next, bilayer (A-on-B) had a peak strength of $\bar{\tau}_c = 20$ MPa at $\bar{\gamma} \sim 15\%$. Finally, bilayer (B-on-A) had a peak strength of $\bar{\tau}_c = 17$ MPa at $\bar{\gamma} \sim 18\%$. For the purpose of comparison, a reference shear stress of material (A) was taken for an intermediate $\bar{\gamma} = 5\%$: $\bar{\tau}(\bar{\gamma} = 5\%)$ is ~ 0.05 MPa. This reference shear stress was averaged with the peak strength of material (B), providing a mean value of 19 MPa for monolithic materials (A) and (B) in the quasi-static cropping test. This mean shear strength was superimposed on Figure 6.4b. Note that both of the bilayer composite beams showed similar responses and their peak shear stresses were within 10% of this mean shear strength.

Optical images recorded during the tests (at $\bar{\gamma} = 40\%$) and post-test micrographs revealed that the shear deformation in the uncured layer (A) was due to delamination at the interface between plies, whereas the shear damage in the cured layer (B) was facilitated by transverse matrix cracks, ply delamination, and fibre fracture (see Figure 6.5).

6.4.3 Ballistic Impact Test

Ballistic tests were performed on both the composite monolithic and bilayer

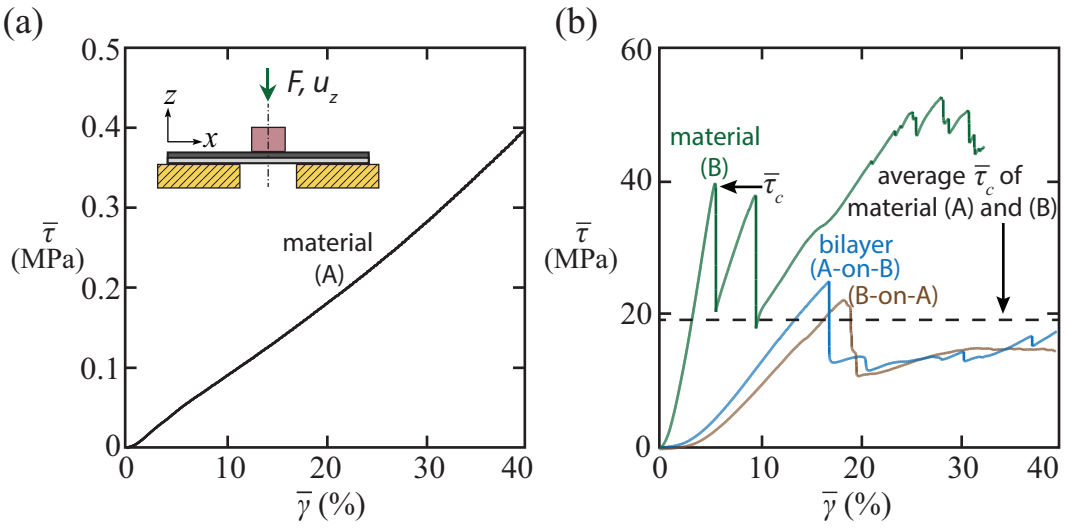

Figure 6.4: Static cropping test responses in terms of $\bar{\tau}$ versus $\bar{\gamma}$ for specimens of a) material (A) and b) material (B), bilayer (A-on-B), and bilayer (B-on-A).

beams under a simply supported boundary condition. Figure 6.6 shows the measured ballistic limit (i.e. penetration velocity v_p) of the composite beams. v_p is defined as the average of the lowest velocity to fully penetrate the target and the highest velocity to partially penetrate the target. Monolithic material (A) had the highest penetration velocity with $v_p = 323 \pm 6$ m/s, followed by bilayer (B-on-A) with $v_p = 296 \pm 20$ m/s, bilayer (A-on-B) with $v_p = 259 \pm 19$ m/s, and monolithic material (B) with $v_p = 181 \pm 6$ m/s.

Post-test optical analysis revealed the failure mechanisms of the monolithic and bilayer composite beams (refer to illustrations and microscopy evidence in Figure 6.7). The failure mechanisms of monolithic beams have been presented in Chapter 5; their results are presented here for the purpose of comparison. In brief, monolithic material (A) failed by an indirect tension mechanism, consisting of Poisson expansion of plies transverse to the fibre and fibre tensile failure in the area beneath the projectile. Monolithic material (B) failed by a shear plugging mechanism, consisting of transverse matrix cracks, ply delamination, and fibre fracture underneath the edge of the contact. In the case of the bilayer composites, the stacking configuration had no effect on the failure mechanism of the uncured layer (A), which failed by indirect tension in both configurations. However, the failure mechanism of the cured layer (B) was sensitive to the stacking configuration. When layer (B) was placed on top, it failed by the shear plugging mechanism. Whereas when layer (B) was placed at the bottom, it failed by a back face tensile mode.

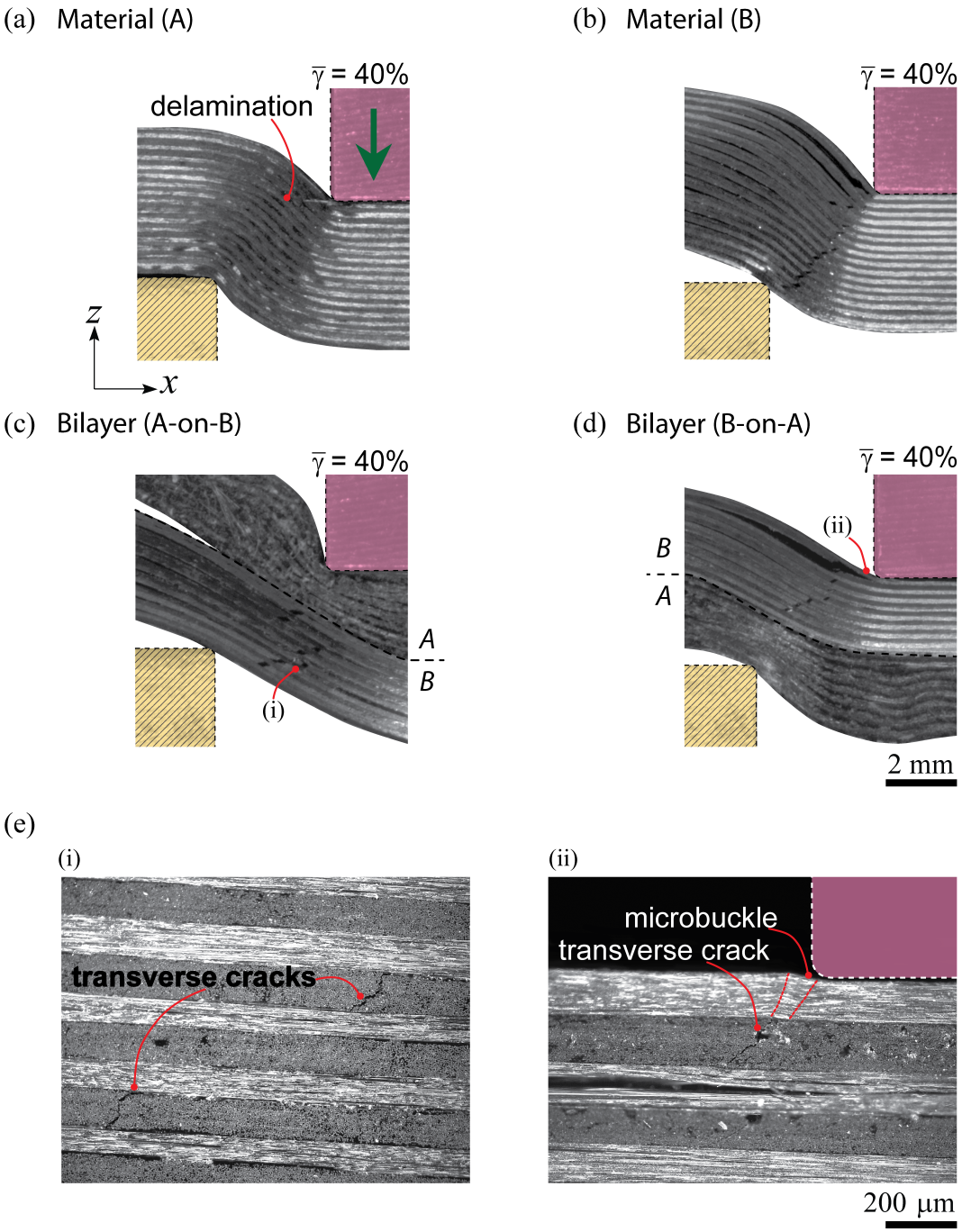

Figure 6.5: Optical images recorded during the interrupted cropping tests of a) monolithic material (A), b) monolithic material (B), c) bilayer (A-on-B), and d) bilayer (B-on-A) at $\bar{\gamma} = 40\%$ (only a 9× 9 mm window of one side of the punched region was recorded). For the bilayers (A-on-B) and (B-on-A), the damaged areas are labelled as (i) and (ii), respectively. e) Close up optical microscopy of the damaged areas, (i) and (ii).

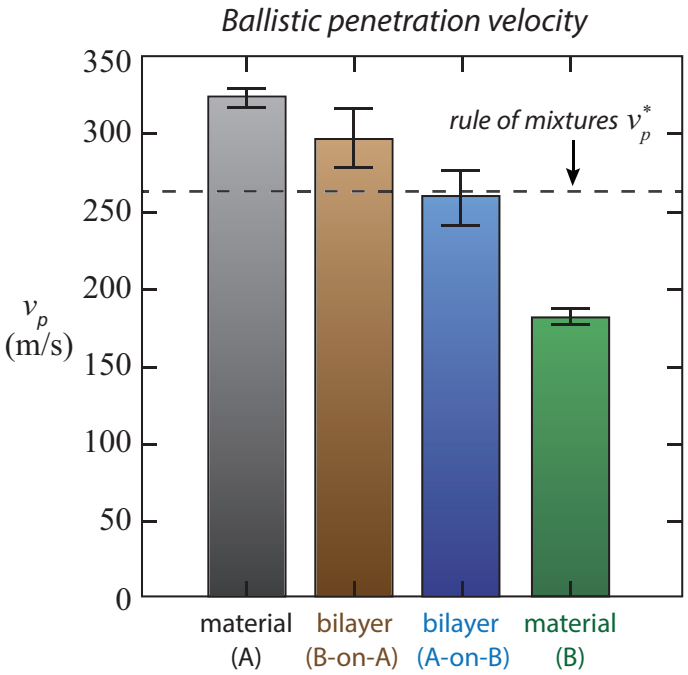

Figure 6.6: Summary of ballistic penetration velocity v_p in the monolithic and bilayer beams.

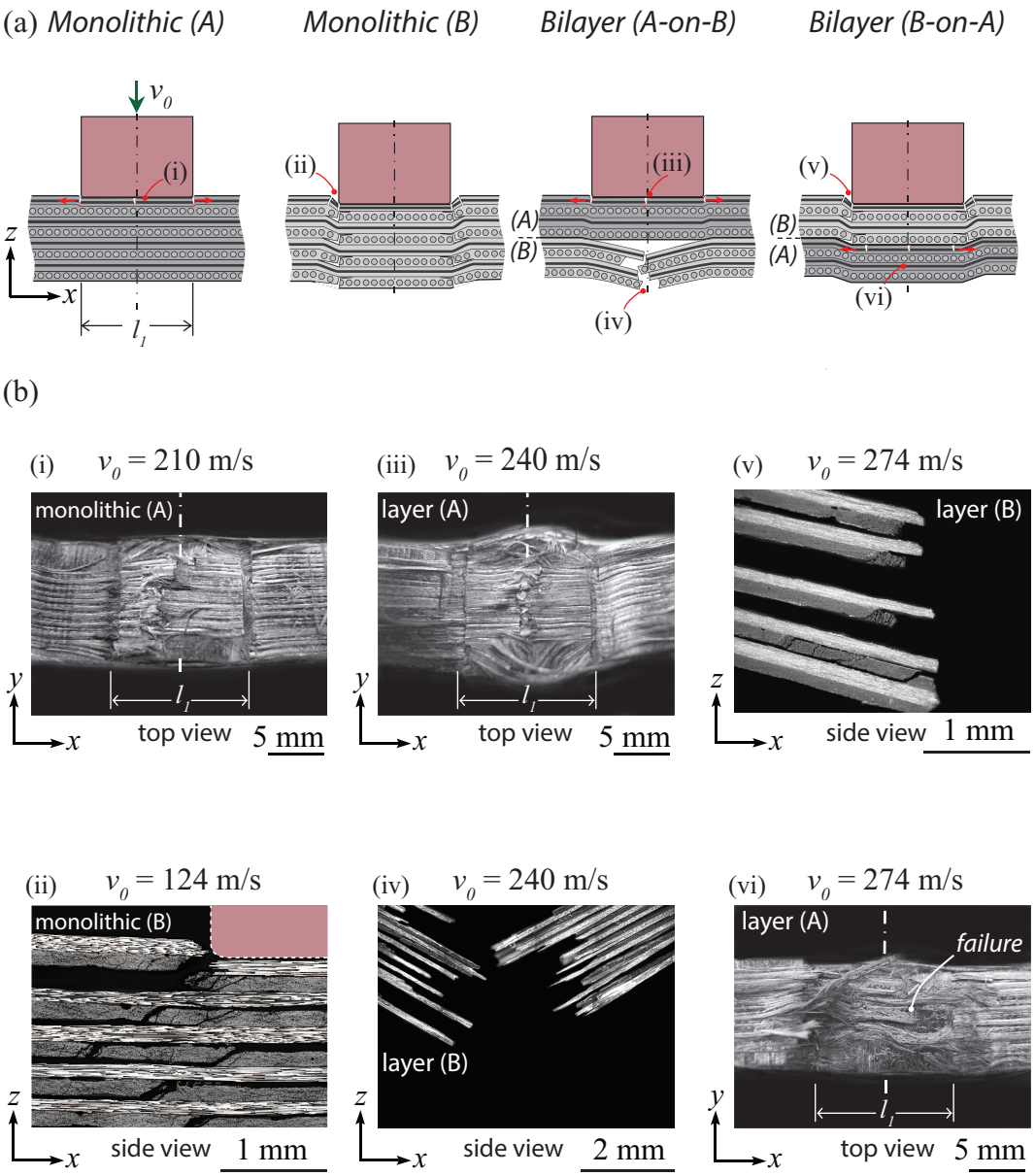

Figure 6.7: a) Schematic illustrations and b) optical microscopy images showing the ballistic failure modes in monolithic material (A), monolithic material (B), bilayer (A-on-B), and bilayer (B-on-A).

6.5 Discussion

6.5.1 Failure Mechanisms

Table 6.2 compares the observed failure modes of the bilayer composite beams to their composite precursors tested under quasi-static and dynamic loading. In the quasi-static indentation test, both the monolithic materials (A) and (B) failed by indirect tension. As a result, the failure mechanisms of the bilayer beams (A-on-B) and (B-on-A) also remained as indirect tension, similar to their composite precursors. In the quasi-static cropping test, both the monolithic materials (A) and (B) failed by a shear plugging mechanism; thus, the failure mechanisms of the bilayer beams both remained as shear plugging. In the ballistic test, however, monolithic material (A) failed by indirect tension and material (B) failed by shear plugging. The contrasting mechanisms of the composite precursors caused the bilayer beams to fail by a mixed mode. When layer (B) was placed on top, the two layers had little interaction and the failure mechanisms among the layers were 'decoupled', i.e. layer (B) failed by shear plugging and layer (A) failed by indirect tension. When layer (A) was placed on top, a rather surprising result was observed: layer (A) continued to fail by indirect tension, but layer (B) failed by a back face tensile mode instead of shear plugging. This change in failure mechanism in layer (B) could be attributed to: (i) the placement of layer (B) at the back face where in-plane tensile stress can be introduced through the bending deformation of the whole specimen or (ii) the soft matrix in layer (A) allowing it to conform to the projectile shape through plastic deformation and thus reducing the local shear stress underneath the projectile edge.

6.5.2 Penetration Velocity

In the ballistic test, monolithic material (A) failed by indirect tension and showed the highest penetration velocity at $v_p = 323 \pm 6$ m/s. In contrast, monolithic material (B) failed by a brittle shear plugging mode and showed the lowest penetration velocity at $v_p = 181 \pm 6$ m/s. Both of the bilayer composite beams experienced a mixed-mode failure where layer (A) failed by indirect tension and layer (B) failed by either shear plugging or back face tension. Their penetration velocities were in between those of the monolithic beams: $v_p = 259 \pm 19$ m/s in bilayer (A-on-B) and $v_p = 296 \pm 20$ m/s

Table 6.2: Summary of observed failure modes of composite beams in different tests.

Material	Uniaxial compression test [a]	Static indentation test	Static cropping test	Ballistic test
A	IT [b]	IT	SP [c]	IT
B	IT	IT	SP	SP
A-on-B	–	IT	SP	IT + BFT [d]
B-on-A	–	IT	SP	SP + IT

[a] Measured from a $[0°/90°]_8$ cross-ply specimen with a side length $L \times L$ (with $L = 10$ mm).
[b] IT - indirect tension mechanism
[c] SP - shear plugging mechanism
[d] BFT - back face tension

in bilayer (B-on-A). Bilayer (A-on-B) showed a 43% improvement and bilayer (B-on-A) showed a 64% improvement in penetration velocity compared to monolithic material (B). The measured v_p of the composite beams was compared to the predictions based on the rule of mixtures by plotting v_p as a function of the volume fraction of layer (A) $\hat{V}_A$, see Figure 6.8. Note that $\hat{V}_A = 1$ in monolithic material (A), $\hat{V}_A = 0$ in monolithic material (B), and $\hat{V}_A = 0.5$ in both of the bilayer beams. Assuming that the energy dissipation of each material is proportional to its thickness, the total kinetic energy dissipation ability of a hybrid beam W^* can be estimated as:

$$W^* = \frac{m_p \left(v_p^*\right)^2}{2} = \hat{V}_A \frac{m_p v_A^2}{2} + \left(1 - \hat{V}_A\right) \frac{m_p v_B^2}{2} \tag{6.5}$$

where m_p is the mass of the projectile and v_p^* is the penetration velocity of a hybrid material that obeys the rule of mixtures. v_p^* can be determined by:

$$v_p^* = \sqrt{\hat{V}_A v_A^2 + \left(1 - \hat{V}_A\right) v_B^2} \tag{6.6}$$

where v_A is the penetration velocity of a monolithic material (A), and v_B is the penetration velocity of a monolithic material (B).

Figure 6.8 shows that bilayer (A-on-B) is consistent with the rule of mixtures,

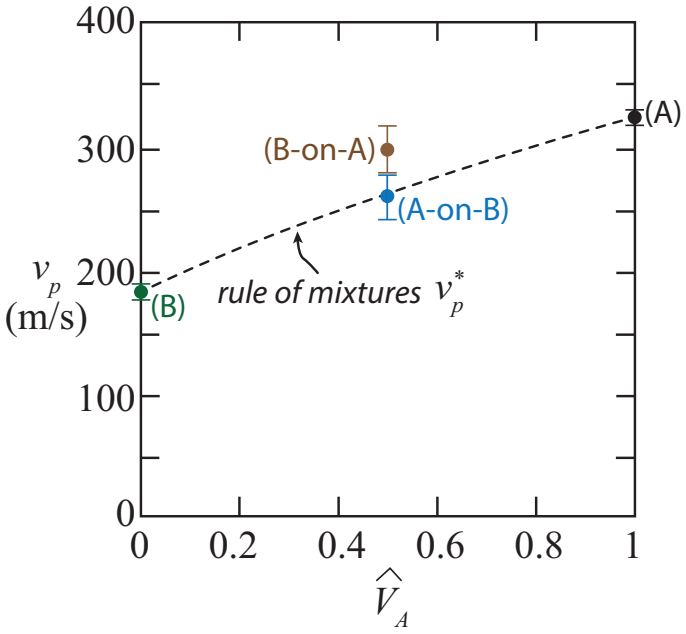

Figure 6.8: A plot of the penetration velocity v_p of the composite beams as a function of the volume fraction of layer (A) $\hat{V}_A$, showing both the measured penetration velocities and the predictions of the rule of mixtures.

but a small positive hybrid effect is observed in bilayer (B-on-A) (with penetration velocity 13% higher than predicted by the rule of mixtures). Recall that layer (A) failed by an indirect tension mechanism regardless of the stacking configuration. The slight improvement of bilayer (B-on-A) versus bilayer (A-on-B) indicates that more energy can be dissipated when the back face deflection of layer (A) is promoted. This observation is consistent with a finding given by Karthikeyan and Russell (2014), where the researchers demonstrated that when a thick laminate fails by an indirect tension mechanism, a small portion of the material at the back face can delaminate from the composite and then fail by membrane stretching. This portion of the material can dissipate ~ 6.5 times more energy than the rest of the composite.

6.6 Conclusions

This chapter investigated the impact resistance and perforation mechanisms of bilayer CFRP composite beams (consisting of one layer with low matrix shear strength and one layer with high matrix shear strength). Two types of bilayer composite beams were investigated in this chapter: (i) bilayer composite beams

with the uncured layer (with $\tau = 0.1$ MPa) on top of the cured layer (with $\tau = 61$ MPa), and (ii) bilayer composite beams with the cured layer on top of the uncured layer; each layer had half the thickness of the bilayer beam. The performance of the bilayer beams was compared against their monolithic precursors with the same thickness. The composite beams were subjected to three types of tests: (i) a quasi-static indentation test with rigid back support, (ii) a quasi-static cropping test with a clearance c between the edge support and a flat indenter, and (iii) a ballistic test with a cuboid shaped projectile and a simply supported boundary condition.

In the quasi-static indentation test, all four composite beams failed by the indirect tension mechanism facilitated by ply tensile failure in the area directly underneath the indenter. In the quasi-static cropping test, all four composite beams failed by the shear plugging mechanism, which consisted of transverse matrix cracks, ply delamination, and fibre fracture concentrated underneath the edges of the indenter. In the ballistic test, monolithic beams made of uncured prepregs failed by the indirect tension mechanism and showed the highest impact resistance in terms of ballistic penetration velocity. In contrast, monolithic beams made of cured laminates failed by a brittle shear plugging mode and had the lowest ballistic penetration velocity. The two bilayer composite beams experienced mixed-mode failure with the uncured prepregs failing by indirect tension regardless of the stacking configuration, whereas the cured layers failed by shear plugging when placed on top but showed a back face tensile mode when placed at the distal face. This demonstrated that it is possible to suppress the brittle shear plugging mode in cured CFRP laminates through the application of protective layers of uncured CFRP. It appears that the impact resistance of these bilayer composite beams closely follows the rule of mixtures based on the performance of their monolithic precursors. The bilayer composite beams demonstrated a significant improvement in ballistic limit (i.e. penetration velocity) when compared to monolithic cured CFRP beams: a 43% improvement when the cured layer was placed at the bottom, and a 64% improvement when the cured layer was placed on top.

Chapter 7

Perforation of Aluminium Alloy-CFRP Bilayer Plates under Quasi-static and Ballistic Loading

Summary

The current study explores the potential of protecting cured CFRP cross-ply plates against perforation by using a protective metal layer. In particular, can a protective metal layer suppress the commonly observed brittle shear plugging mechanism in conventional CFRP under ballistic loading? To address this, a protective aluminium alloy plate was placed in front of a CFRP plate. Monolithic CFRP plates were manufactured from autoclaved cross-ply $[0°/90°]_{16}$ laminates of Hexply® 8552/35%/134/IM7. Aluminium alloy-CFRP bilayers were manufactured by placing in turn two grades of aluminium alloy plates (AA1050A and AA6082-T6) in front of a CFRP layer. The composite plates were then subjected to quasi-static indentation and ballistic impact by a spherical indenter or projectile. Four types of tests were conducted: (i) quasi-static indentation test with rigid back support, (ii) quasi-static indentation test with an edge-clamped condition, (iii) ballistic test with rigid back support, and (iv) ballistic test with an edge-clamped condition.

The perforation mechanism of the CFRP layer depends on the testing

boundary condition (i.e. back-supported versus edge-clamped) but is affected neither by the presence of the metal layer nor by the choice of loading conditions (i.e. quasi-static versus ballistic). In the back-supported condition, the CFRP layers failed by an indirect tension mode that consists of tensile failure of plies in the material directly beneath the indenter or projectile. In the edge-clamped condition, the CFRP layers failed by a shear plugging mechanism. Although the metal layers were not able to suppress the shear plugging of the underlying CFRP layer under the edge-clamped condition, the contact area in the CFRP layer increased after the addition of the protective metal layer. This expansion in contact area increased the energy required to form a shear plug, hence improving the perforation resistance of the CFRP layer. On an equal areal density basis, the perforation resistance of the composite plates increased in the following order: monolithic CFRP, AA1050A-H6-CFRP bilayer, and AA6082-T6-CFRP bilayer.

7.1 Introduction

Under ballistic loading, conventional Carbon Fibre Reinforced Plastic (CFRP) laminates with high matrix shear strength fail by a brittle shear plugging mode, and consequently have inferior ballistic resistance compared to UHMWPE fibre based Dyneema® composites. The investigation presented in Chapter 5 revealed that the ballistic limit (i.e. penetration velocity) of CFRP can be improved by suppressing this shear plugging mode and activating an indirect tension mode that is facilitated by ply tensile failure. This had been achieved through the reduction of matrix shear strength. This chapter explores an alternative method of suppressing the shear plugging mode and enhancing penetration resistance in conventional CFRP, through the addition of a protective metal layer.

Many researchers have shown that the impact resistance of fibre composites, such as glass fibre reinforced plastic (GFRP) and aramid fibre composites, can be improved by bonding them with alternating metal layers into hybrid composites known as fibre metal laminates (Bieniaś et al., 2015; Jaroslaw et al., 2016; Lawcock et al., 1998; Song et al., 2010; Vlot and Krull, 1997; Yu et al., 2015). There are currently three types of fibre metal laminates: armaid fibre reinforced aluminium laminates (ARALL®), glass reinforced aluminium laminates (GLARE®), and carbon fibre reinforced aluminium laminates (CARAL). Pioneering work by Vlot (1993, 1996) showed that GLARE® composites offer higher impact resistance than both their monolithic composite precursors and monolithic aluminium alloys with the same thickness.

The general failure mechanism of the fibre metal laminates under impact loading is particularly complex as it involves both matrix and fibre failure in the composite layer, plastic deformation of the metal layer, and debonding at the metal-composite interface. Many researchers have reported that the metal-composite debonding occurs due to the weak adhesion and mismatch of stiffness between the metal and the composite layers (Atas, 2007; Bieniaś et al., 2015; Compston et al., 2001; Jaroslaw et al., 2016; Wu et al., 2007). To increase bond strength between the metal and composite layers, toughening methods such as chemical etching and introduction of micro-patterns on the metal surface have been explored by Kim et al. (2010); Ning et al. (2013); Yun et al. (2011). These studies showed that the failure mode in the adhesive

(i.e. cohesive failure or interfacial failure) can have a large influence on the overall bond strength. However, Pärnänen et al. (2015) revealed that these surface treatments do not resolve the debonding issue under impact loading. The weak bond between the metal and composite layers is an ongoing challenge in the manufacture of fibre metal laminates.

Currently, a relatively limited amount of literature is available regarding CARAL composites and their perforation mechanism is only beginning to be explored. A recent study by Bieniaś et al. (2015) investigated the damage mechanism of a composite sandwich consisting of a CFRP core and aluminium alloy face sheets, subjected to a low-velocity impact. They observed that the damage consisted of transverse matrix cracks and ply delamination in the CFRP layer, plastic deformation of the aluminium alloy layers, and debonding in the metal-CFRP interfaces. Furthermore, the presence of the metal layers reduced the matrix crack formation and delamination propagation within the CFRP layer compared to monolithic CFRP with the same thickness. However, this study did not extend to higher impact velocities involving fibre failure. This will be the focus of the current chapter.

7.1.1 Scope of Study

In this chapter, the protective effect of aluminium alloy layers on the impact resistance and perforation mechanism of a CFRP plate is investigated. Figure 7.1 illustrates the general problem in the current study. An aluminium alloy layer is placed in front of a CFRP cross-ply laminate, creating an aluminium alloy-CFRP bilayer plate. The bilayer plates are then subjected to quasi-static indentation and ballistic impact by a spherical indenter or projectile under different supporting boundary conditions. In total, four types of tests were conducted: (i) quasi-static indentation test with rigid back support, (ii) quasi-static indentation test with an edge-clamped condition, (iii) ballistic test with rigid back support, and (iv) ballistic test with an edge-clamped condition. To study the role of the metal layer's yield strength, two types of aluminium alloy layers were used in the fabrication of the bilayer plates: (i) AA1050A-H6 and (ii) AA6082-T6. The quasi-static and ballistic performance of these bilayer plates were then compared against each other and versus those obtained from the unprotected monolithic CFRP layers.

Note that this study used a simplified bilayer configuration with no adhesive between the aluminium alloy layer and the composite layer. This eliminates

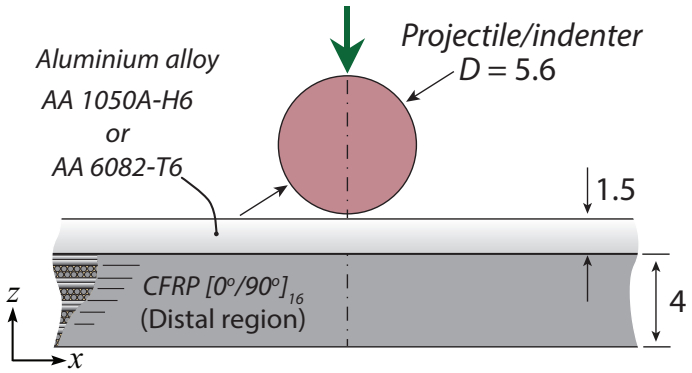

Figure 7.1: Schematic illustration of an aluminium alloy-CFRP bilayer struck by a spherical indenter/projectile. All dimensions are in mm.

the above-mentioned complexity of failure in the adhesive and allows a pressure indicating film to be placed between the aluminium alloy and the CFRP layers, in order to record the average pressure at the onset of damage in the indentation tests. Nevertheless, preliminary experiments were conducted on AA1050A-H6-CFRP bilayer plates with the aluminium alloy layer and the CFRP layer bonded together by a Redux 810® epoxy adhesive. Appendix E summarises the results of these tests and compares the ballistic performance under an edge-clamped condition of these bonded bilayer plates to that of bilayer plates without adhesive. It was observed that the adhesive had a limited effect on the ballistic resistance and had no influence on the failure mechanism of the CFRP layer.

7.2 Specimen Manufacture

Cross-ply laminates $[0°/90°]_{16}$ were made from Hexply® 8552/35%134/IM7 carbon fibre/epoxy prepregs (with a ply thickness of 0.131 mm). They were then cured in an autoclave environment following the procedure recommended by Hexcel Composites (2013). Three types of composite plates were manufactured using the above autoclave cured CFRP layer as the raw material: one type of monolithic CFRP plate, and two types of aluminium alloy-CFRP bilayer plates. Monolithic CFRP plates were made by cutting the cured CFRP laminates using a diamond saw into square dimensions of $w \times w$ (with a width of $w = 75$ mm, a thickness of 4 mm, and an areal density of 6.28 kg/m^2). The two aluminium alloy-CFRP bilayer plates were made by stacking aluminium alloy protective sheets, AA1050A-H6 (40 Vickers) or

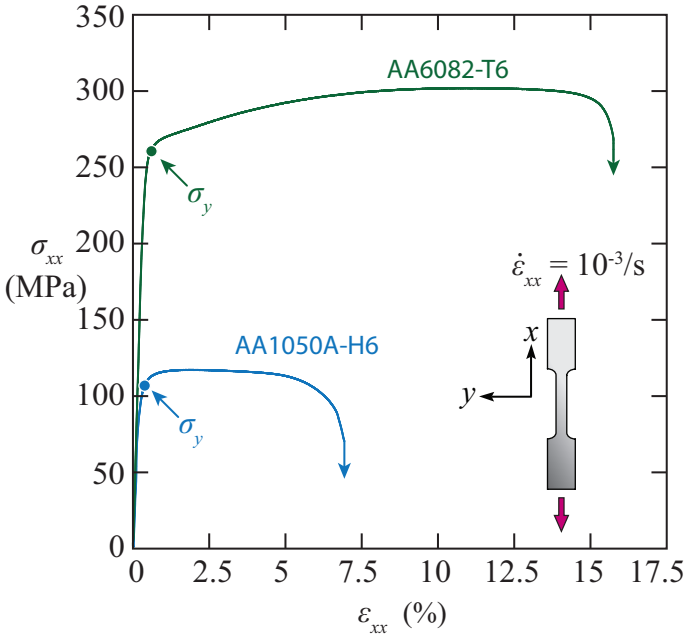

Figure 7.2: Uniaxial tensile curves of aluminium alloy AA1050A-H6 and AA6082-T6.

AA6082-T6 (120 Vickers), on top of the CFRP plates. The tensile properties of the aluminum alloy sheets were independently measured through uniaxial tensile tests using standard dog-bone shaped specimens with an applied strain rate of 10^{-3}/s. AA1050A-H6 showed a 0.2% offset yield strength σ_y of 107 MPa, an ultimate tensile strength (UTS) of 117 MPa, and elongation to failure of 7%. AA6082-T6 showed a σ_y of 262 MPa, a UTS of 303 MPa, and elongation to failure of 16%, as shown in Figure 7.2. In the current study, no adhesive was applied between the aluminium sheets and the CFRP plates; this eliminated the potential effects of adhesive bonding on the failure mechanism and thus simplified the analysis. The aluminium alloy sheets were cut in a guillotine machine into square dimensions of $w \times w$ (with a width of $w = 75$ mm, a thickness of $h = 1.5$ mm, and an areal density of 3.45 kg/m^2). The following labelling procedure is used throughout this study: (A) monolithic CFRP panels, (B) bilayer panels with an AA1050A-H6 sheet on top of CFRP, and (C) bilayer panels with an AA6082-T6 sheet on top of CFRP. Each monolithic plate (A) had a total thickness of $H = 4$ mm and an areal density ρ_A of 6.28 kg/m^2 while the bilayer plates (B) and (C) each had a total thickness of 5.5 mm and an areal density ρ_A of 9.73 kg/m^2; these parameters are summarised in Table 7.1.

Table 7.1: Summary of layer thickness and areal density of monolithic CFRP and the aluminium alloy-CFRP bilayer plates.

Material	Metal layer thickness h (mm)	CFRP layer thickness H (mm)	Total plate thickness $H + h$ (mm)	Total areal density ρ_A kg/m^2
A	–	4	4	6.28
B	1.5	4	5.5	9.73
C	1.5	4	5.5	9.73

7.3 Test Methods

7.3.1 Ballistic Tests

Composite plates with dimensions $w \times w$ (with a width of $w = 75$ mm) and total thickness of 4 mm for material (A) and 5.5 mm for bilayer plates (B) and (C) were subjected to ballistic impact by a ball bearing made of chrome steel with a diameter of $D = 5.6$ mm and a mass of $m_p = 7.2 \times 10^{-4}$ kg. In the case of bilayer plates, specimens were placed such that the projectile would hit the aluminium alloy protector first. The ballistic tests were performed under two boundary conditions: (i) edge-clamped and (ii) back-supported.

(i) Edge-clamped:

Under the edge-clamped condition, composite plates were frictionally clamped between two 12.7 mm thick steel plates using M6 bolts each with 8 Nm torque, as illustrated in Figure 7.3a. The front and back plates were previously surface-roughened through sand blasting. The front and backing plates each consisted of 12 equi-spaced holes (with hole diameter of 6 mm and pitch diameter of 90 mm) and a concentric opening window with a diameter of $D_s = 55$ mm that allowed for the back face deflection and perforation of the specimens. The backing plate was mounted to an outer frame allowing a projectile to impact the specimen normally through the centre of the opening.

(ii) Back-supported:

Under the back-supported condition, composite plates with the same specimen sizes were placed in front of a hardened silver steel (560 Vickers) backing plate with a thickness of 45 mm. The projectile would then impact normally and centrally from the z-direction in Figure 7.3b. To ensure that the specimens were fixed in place before the impact, they were adhered to the backing plate using double-sided adhesive tape.

In both boundary conditions, spherical projectiles were launched using a gas gun (with helium or nitrogen compressed gas) with a 4.5 m long aluminium barrel havin a bore diameter of 6 mm. In this set-up, the projectiles impacted the specimens normally and centrally. The impact velocity v_0 ranged from 30 m/s to 380 m/s, and was measured using a set of laser gates placed near the exit of the barrel.

During the ballistic test, high-speed images were taken using a Phantom® V1610 camera (with an inter-frame time of 16 μs and an exposure time of 0.43 μs) to record the rebound velocity v_r and to confirm the laser measurements of the impact velocity v_0.

7.3.2 Quasi-static Indentation Tests

Composite plates (A) to (C) were subjected to out-of-plane indentation by a hemispherical indenter made of hardened silver steel (700 Vickers) with a diameter of $D = 5.6$ mm under (i) an edge-clamped condition and (ii) a back-supported condition. With the exception of the indenter, the specimen dimensions and the test set-up of the current indentation test were identical to those in the ballistic test illustrated in Figure 7.3. The indentation tests applied a displacement rate $\dot{u}_z = 1.7 \times 10^{-2}$ mm/s in the out-of-plane direction and were performed using a screw-driven test machine with a 150 kN load cell. The indentation load F was recorded by the machine load cell and the displacement of the indenter u_z was measured using a laser extensometer.

For selected samples, the contact area of the CFRP layer (i.e. the contact area of the top face in the monolithic plates, and the contact area between the aluminium alloy layer and the CFRP in the bilayer plates) and the average contact pressure were measured during the interrupted indentation tests by placing pressure measurement films on top of the CFRP layer for

(a) *Edge-clamped condition*

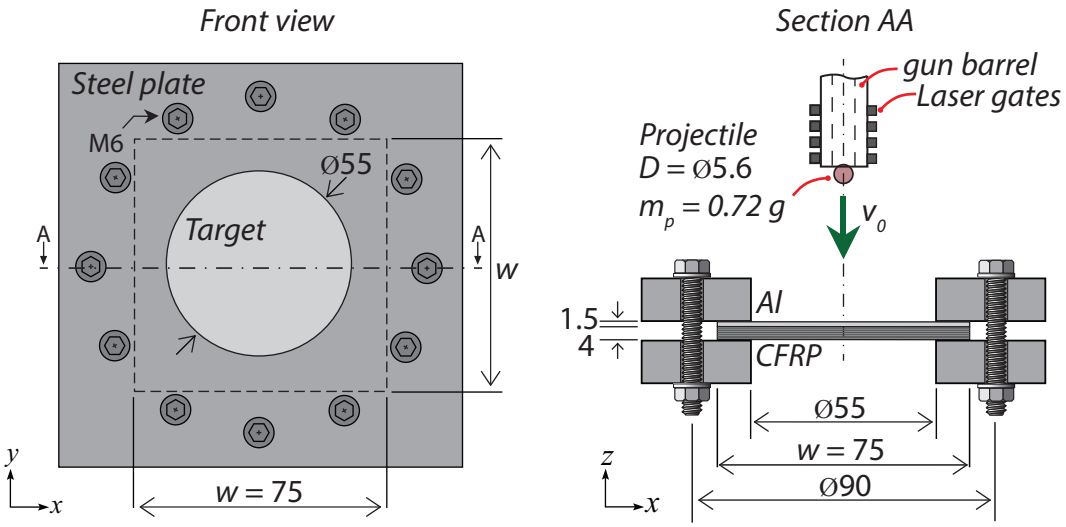

(b) *Back-supported condition*

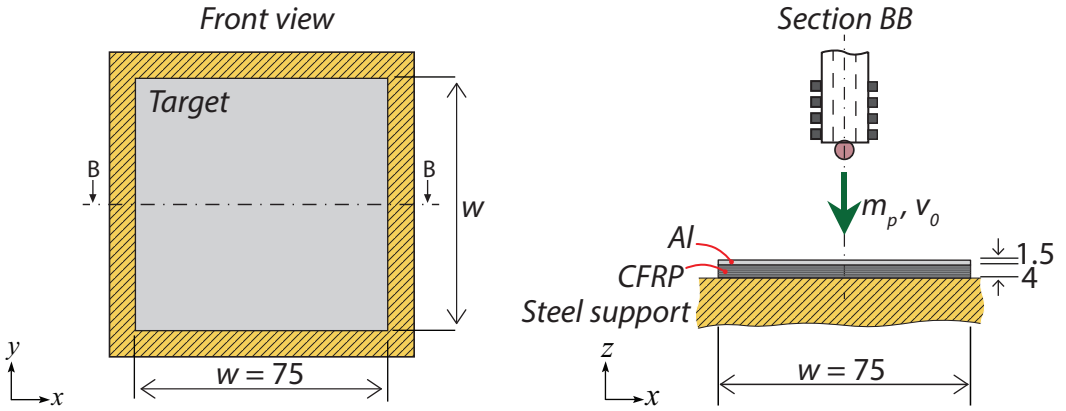

Figure 7.3: Schematic illustrations of a) edge-clamped and b) back-supported aluminium alloy-CFRP bilayer plates situated for impact by a spherical projectile. All dimensions are in mm.

each incremental displacement level. Three types of pressure measurement films with differing pressure ranges (Fuji Prescale® MS, HS, and HHS films) were purchased from Fujifilm Ltd. Each Fuji Prescale® film contains a colour-forming layer on top of a colour-developing layer. The colour-forming layer contains microcapsules with various sizes and wall strengths that are correlated with pressure. When pressure is applied, the microcapsules with various strengths would break at different pressures, creating a red coloured patch with varying intensity of colour depending on the local pressure. Calibrations had been conducted on the MS, HS, and HHS films by compressing them between two flat platens at incremental pressure levels, giving a calibrated pressure range of 35 MPa to 300 MPa.

In a preliminary test, a stack of MS, HS, and HHS Prescale® films was placed on top of a monolithic plate (A) that was indented under a back-supported condition at various indentation displacements u_z. The contact pressure distribution was recorded and it was similar to a Hertzian distribution, see Figure 7.4. However, the pressure required to cause first failure was in the range of 1 GPa, which greatly exceeds the pressure limit of commercially available Prescale® films (300 MPa). Since the pressure measurement films could not be used to record the full pressure distribution up to failure, they were instead employed to measure the contact radius a in order to calculate the average pressure $\bar{p} \equiv F/(2\pi a^2)$ in the subsequent interrupted tests. To minimise the influence of the pressure films on the indentation response, only one layer of MS film (with a thickness of ~ 90 μm) was placed on top of the CFRP layer (i.e. on top of the monolithic CFRP plate (A) or between the CFRP layer and the aluminium alloy layer of the bilayer plates (B) and (C), as illustrated in Figure 7.5a). The contact radius a in this study was estimated to be the radius at which the contact pressure exceeded the lower limit of the calibrated pressure range (i.e. 35 MPa). For high indentation displacements, the indenter penetrated both the pressure film and the CFRP layer and thus the contact radius was assumed to equal the indenter radius (i.e. $a = R$).

7.3.3 Post-test Characterisation

Tested specimens were sectioned across the impact zone using an abrasive cut-off wheel with a thickness of 0.8 mm. For consistency, all specimens were sectioned along the fibre direction in the top ply. Specimens were then mounted in epoxy, followed by surface polishing and optical microscopy.

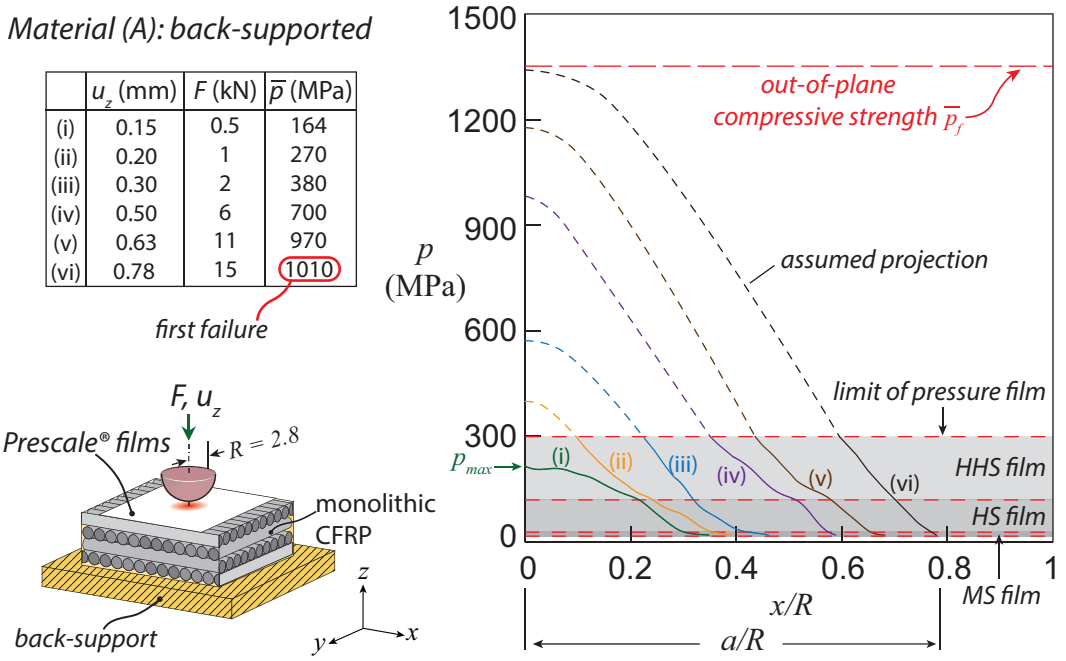

	u_z (mm)	F (kN)	$\bar{p}$ (MPa)
(i)	0.15	0.5	164
(ii)	0.20	1	270
(iii)	0.30	2	380
(iv)	0.50	6	700
(v)	0.63	11	970
(vi)	0.78	15	1010

Figure 7.4: Plot of the pressure distribution for the interrupted indentation test of material (A) under a back-supported condition.

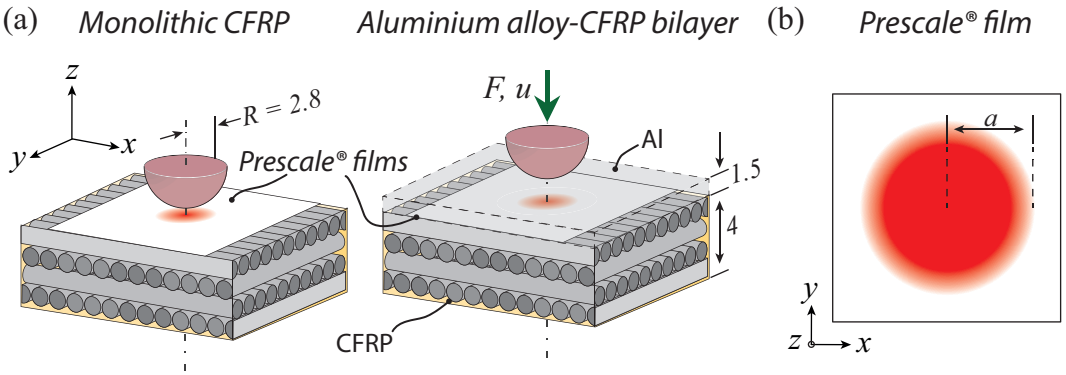

Figure 7.5: Schematic illustrations of the contact area measurement on the CFRP layer during interrupted indentation test. a) The placement of the Prescale® films during the interrupted test. b) Definition of the contact radius a.

7.4 Results

7.4.1 Failure Mechanisms

The failure mechanism of the CFRP layer depended on the testing boundary condition (i.e. back-supported versus edge-clamped) but was not affected by the presence of the metal layer nor the loading conditions (i.e. quasi-static versus ballistic). In the back-supported condition, the CFRP layers failed by an indirect tension mode consisting of tensile failure of plies in the material directly beneath and near the center line of the indenter/projectile. In the edge-clamped condition, the CFRP layers failed by a shear plugging mechanism consisting of matrix shear cracks, ply delamination, and fibre fracture beneath the edge of contact. Examples of the cross-sectional microscopy images of materials (A) and (C) are summarised in Figures 7.6 and 7.7, respectively.

7.4.2 Quasi-static Edge-clamped Indentation Response

7.4.2.1 Load-Displacement Response

The indentation response (in terms of load F versus displacement u_z) of the composite plates under an edge-clamped condition are presented in Figure 7.9a. All specimens exhibited an initial peak load F_i at u_z of $\sim$ 1-2 mm, labelled (i) in the figure. Among the three materials, monolithic CFRP (A) showed the lowest F_i at 3.7 kN. F_i increased when aluminium alloy layers were introduced, with $F_i = 6.4$ kN in bilayer plates (B) and $F_i = 7.2$ kN in bilayer plates (C). Post test inspection revealed that this initial peak load F_i was associated with matrix shear crack formation in the area beneath the edge of contact, while the fibres remained intact. After this initial peak load, the indentation load continued to increase up to a displacement of $u_z \sim 4$ mm, labelled (ii) in the figure. At this higher displacement, multiple spikes started to appear and the indentation load began to fall, indicating a series of failures in the underlying CFRP. Post test inspection revealed that these spikes were associated with fibre fracture beneath the edge of contact, and that the fractures would propagate to connect with the above-mentioned matrix shear cracks.

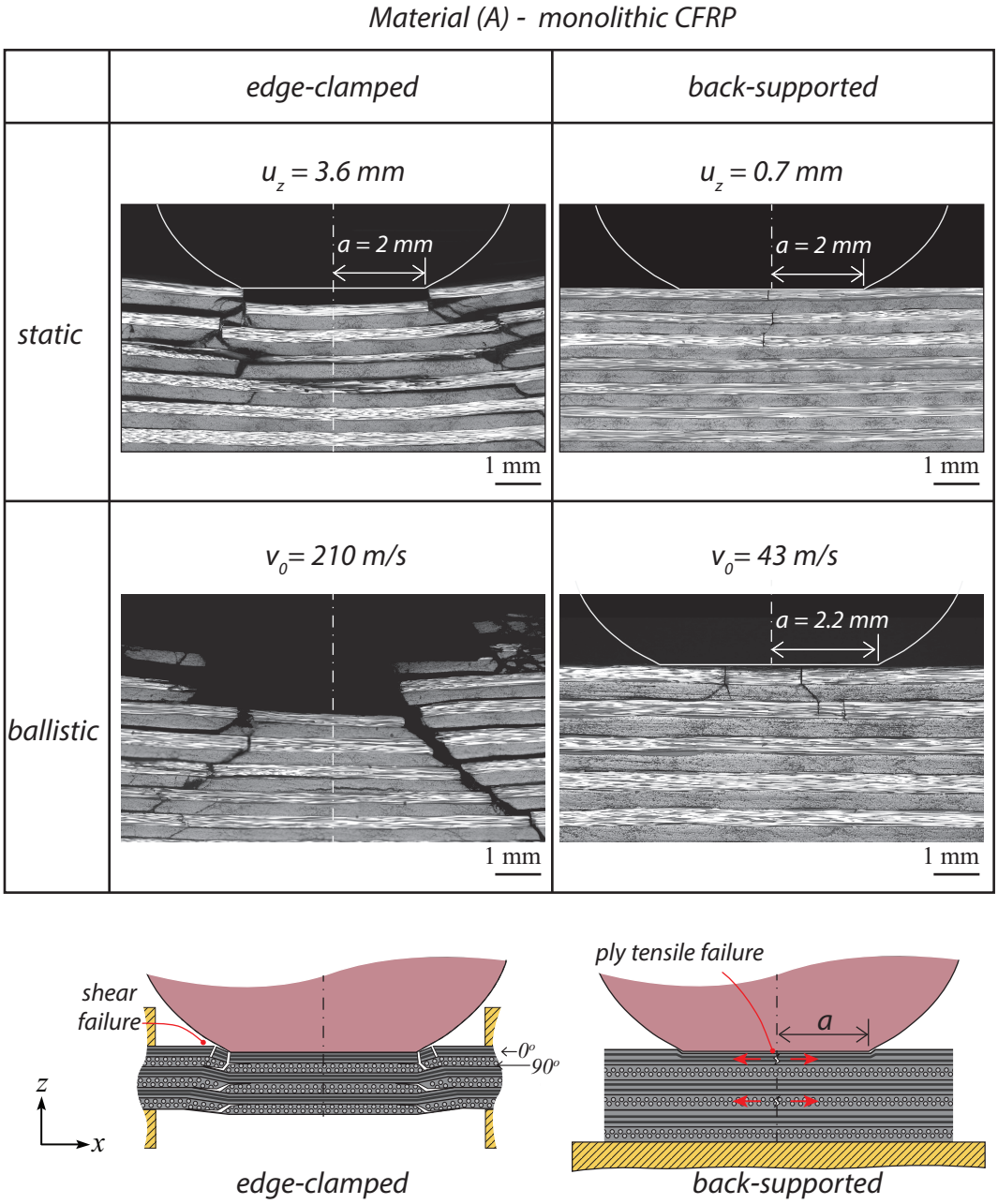

Figure 7.6: Cross-sectional microscopy images indicating that, regardless of the loading conditions, monolithic CFRP plate material (A) failed by shear plugging in the edge-clamped test and failed by indirect tension in the back-supported test.

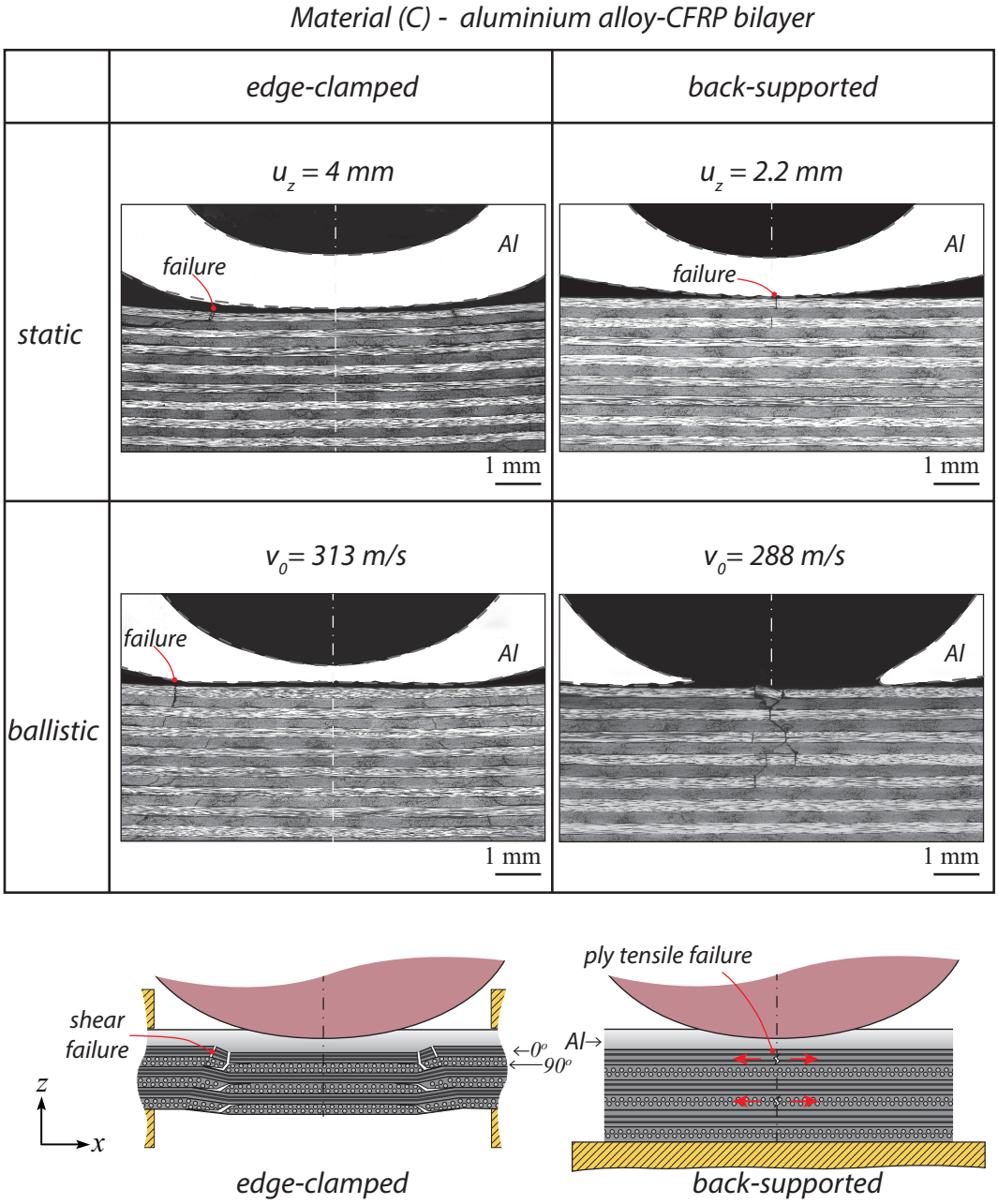

Figure 7.7: Cross-sectional microscopy images indicating that, regardless of the loading conditions, the CFRP layer in material (C) failed by shear plugging in the edge-clamped test and failed by indirect tension in the back-supported test.

7.4.2.2 Measurement of the Average Indentation Shear Stress in the CFRP Layer

Since damage initiation was triggered by the shear failure of the matrix in the CFRP layer underneath the edge of the contact, the indentation force F required to produce this shear failure can be estimated as:

$$F = 2\pi a \left(h\tau_{Al} + H\bar{\tau}\right) \tag{7.1}$$

where a is the contact radius, h is the height of the aluminum layer ($h = 1.5$ mm), H is the height of the CFRP layer ($H = 4$ mm), τ_{Al} is shear yield strength of the aluminium alloy layer (taken to be $\sigma_y/2$ of the aluminium alloy), and $\bar{\tau}$ is the average shear stress of the CFRP layer underneath the circumference of the contact area. $\bar{\tau}$ can be expressed as:

$$\bar{\tau} = \frac{F}{2\pi a H} - \frac{h\tau_{Al}}{H} \tag{7.2}$$

The contact radius a on the top face of the CFRP layer was measured during the interrupted indentation tests by placing a Prescale® film on top of the CFRP layer for each incremental displacement level (at least 17 levels for each material). The measurements of the contact radius are summarised in Figure 7.8b by plotting the ratios a/R (the radius of the indenter is $R = 2.8$ mm) as functions of displacement u_z.

Figure 7.9c shows the indentation responses of materials (A) to (C) by plotting the normalised average shear stresses $\bar{\tau}/\tau_y$ (where τ_y is defined to be the short beam shear strength of the CFRP layer, i.e. 99 MPa) as functions of the displacement u_z. Note that the damage initiation occurred at $\bar{\tau}/\tau_y \sim 1$ due to matrix shear failure (i.e. when the average shear stress reached the shear strength of the CFRP layer), refer to label (i) in the figure. As the displacement further increased to $u_z \sim 4$ mm, the normalised average shear stress of $\bar{\tau}/\tau_y$ exceeded unity and fibre fracture occurred underneath the edge of contact, refer to label (ii) in the figure.

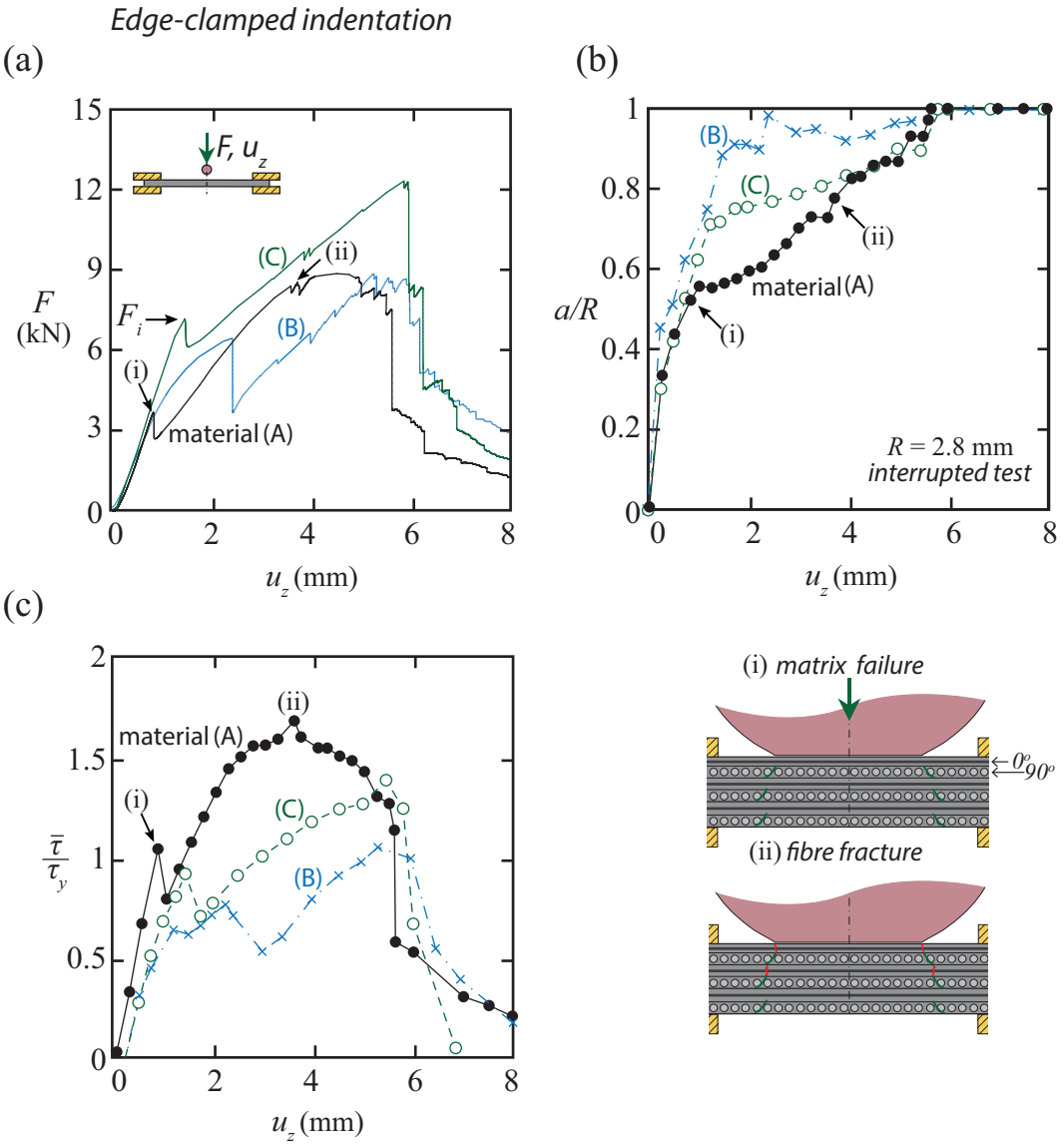

Figure 7.8: Static indentation responses of materials (A) to (C) under an edge-clamped condition in terms of a) load F versus displacement u_z, b) normalised contact radius a/R versus displacement u_z, and c) normalised average shear stress $\bar{\tau}/\tau_y$ versus displacement u_z. First failure, labelled as (i), is associated with matrix crack formation whereas the second failure, labelled as (ii), is associated with fibre fracture beneath the edge of contact.

7.4.3 Quasi-static Back-supported Indentation Response

7.4.3.1 Load-Displacement Response

The indentation response (in terms of load F versus displacement u_z) of the composite plates under a back-supported condition are presented in Figure 7.9b. Monolithic material (A) exhibited an initial peak load $F_i = 14.7$ kN at displacement $u_z \sim 0.8$ mm, labelled (i) in Figure 7.9a. In contrast, specimens types (B) and (C) showed yielding behaviours at similar displacement ($u_z \sim$ 1-2 mm) due to the plastic deformation of the aluminium alloy layers, delaying their peak loads F_i to occur at $u_z \sim 2.5$ mm. Their initial peak loads were higher than for material (A), with material (B) at $F_i = 22.2$ kN and material (C) at $F_i = 25.3$ kN. Post test inspection revealed that this initial peak load F_i was associated with fibre tensile failure at the top ply in the area directly beneath and near the centre line of the indenter.

7.4.3.2 Measurement of the Average Indentation Pressure on the CFRP Layer

For the specimens that were tested under a back-supported condition, there existed an out-of-plane pressure directly beneath the indenter. The average indentation pressure $\bar{p}$ underneath the indenter can be expressed as:

$$\bar{p} = \frac{F}{\pi a^2} \tag{7.3}$$

The contact radius a on the top face of the CFRP layer was measured using Prescale® films, and is summarised in Figure 7.9b. Figure 7.9c shows the indentation responses of materials (A) to (C) by plotting the normalised average pressure $\bar{p}/\bar{p}_f$ (where $\bar{p}_f = 1350$ MPa is defined to be the out-of-plane compressive strength of the CFRP layer) as functions of the displacement u_z. For specimens tested under a back-supported condition, damage occurred at $\bar{p}/\bar{p}_f \sim 1$ as a result of out-of-plane compressive failure, refer to label (i) in the figure. Since the out-of-plane compressive strength $\bar{p}_f$ of the CFRP layer was associated with an indirect tension mechanism (as mentioned in Chapter 3), it is concluded that the CFRP layer also failed by indirect tension when indented under a back-supported condition.

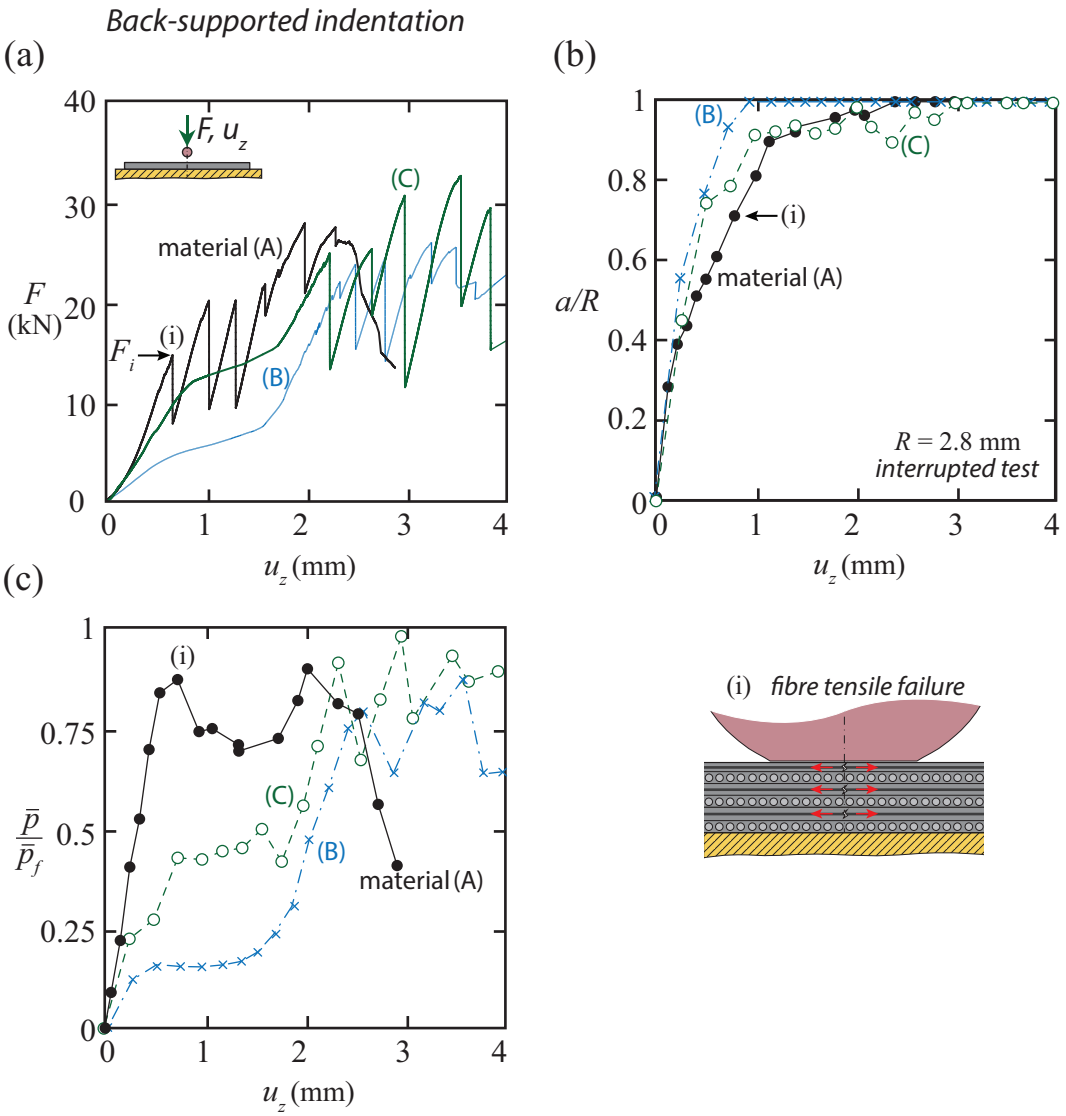

Figure 7.9: Static indentation responses of materials (A) to (C) under a back-supported condition in terms of a) load F versus displacement u_z, b) normalised contact radius a/R versus displacement u_z, and c) normalised average average pressure $\bar{p}/\bar{p}_f$ versus displacement u_z. First failure, labelled as (i), is associated with fibre tensile failure directly beneath the indenter.

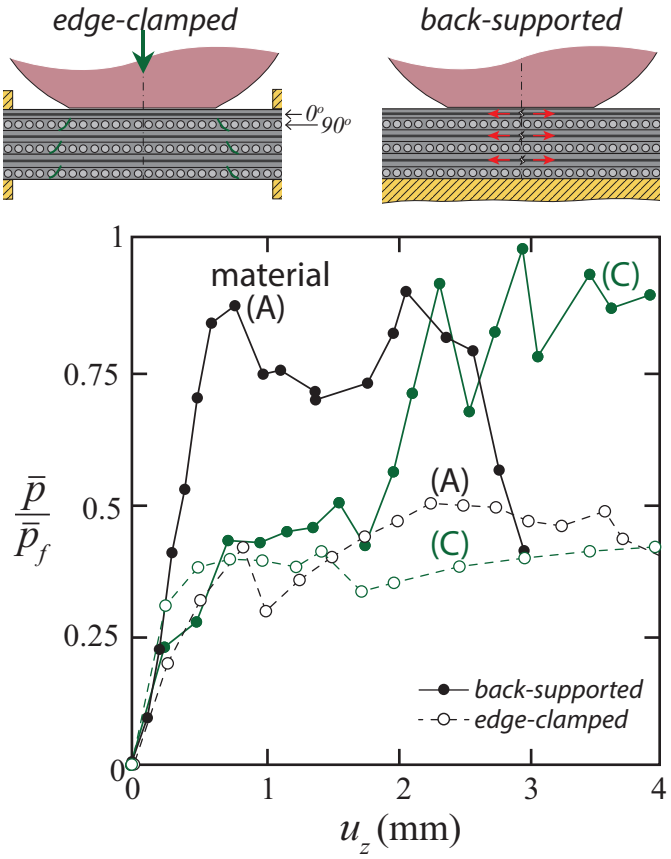

Figure 7.10: Static indentation load-displacement responses of materials (A) and (C) under edge-clamped and back-supported conditions in terms of normalised average pressure $\bar{p}/\bar{p}_f$ versus displacement u_z.

7.4.4 Effect of Boundary Condition on the Average Indentation Pressure

Figure 7.10 compares the average indentation pressure of composite plates under edge-clamped and back-supported conditions (data for material (B) are omitted for the sake of brevity). It is worth noting that the CFRP layer failed by an indirect tension mechanism under the back-supported condition, and thus the normalised average pressure $\bar{p}/\bar{p}_f$ was in the order of unity. In contrast, the CFRP layer failed by a shear plugging mechanism under the edge-clamped condition and average pressure $\bar{p}/\bar{p}_f$ was significantly lower.

7.4.5 Effect of the Metal Layer on the Indentation Cut Fraction

The level of damage in the CFRP layer can be represented by the fraction of plies that exhibited fibre failure f (referred to as cut fraction). Figure 7.11 compares the level of damage in the CFRP layer prior to and following the addition of a protective metal layer, by plotting f against the indentation load F. Under an edge-clamped condition, f is defined to be the fraction of plies where fibre tensile failure was observed. Under a back-supported condition, f is defined to be the fraction of plies where fibre shear cutting was observed. Figure 7.11 shows that the indentation loads required to cause the same degree of damage were consistently higher for CFRP protected by a metal layer. The resistance to damage increased in the following order: material (A), material (B), and material (C).

Measuring contact radius a in the interrupted tests revealed that when the CFRP layer is protected by a metal layer, the plastic deformation of the metal layer has the effect of spreading the indentation load over a larger area (i.e. to increase the contact radius a for a given indentation displacement u_z), relieving the pressure in the underlying CFRP. As a result, a larger indentation load F was required to achieve the same level of damage as for unprotected CFRP.

To illustrate this load spreading effect, the critical radius at which fibre failure was first observed a_c (defined to be the measured radius a at which fibre failure was first observed in the interrupted test) was recorded and the data are presented in Figure 7.12 by plotting the ratios a_c/R as functions of the shear yield strength of the aluminium alloy layer τ_{Al}. The presence of the metal layer lead to an increase of a_c/R in both edge-clamped and back-supported conditions. It is worth noting that the load spreading effect (indicated by the higher value of a_c/R) of the AA1050A-H6 layer (i.e. the aluminium alloy with the lower yield strength) was marginally higher than for the AA6082-T6 layer. However, the high yield strength of the AA6082-T6 layer offered additional indentation resistance. Consequently, the indentation force required to cause damage in material (C) was higher than in material (B).

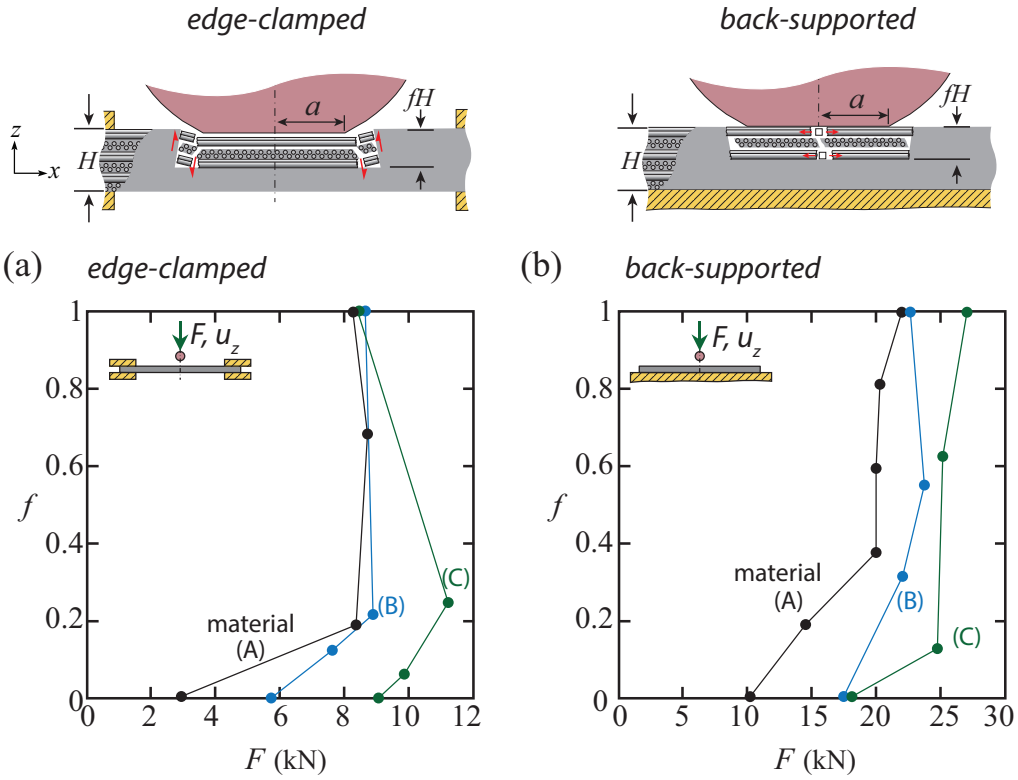

Figure 7.11: The indentation cut fraction f in materials (A) to (C) versus indentation load F under a) edge-clamped and b) back-supported conditions.

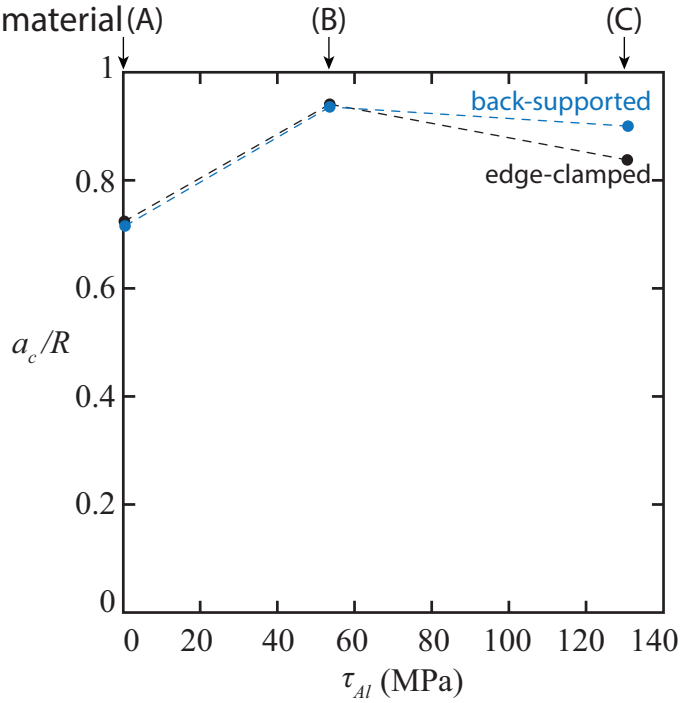

Figure 7.12: A plot of the ratios a_c/R as functions of the shear yield strength of the aluminium alloy layer τ_{Al}. a_c is defined to be the critical contact radius when fibre failure was first observed.

7.4.6 Ballistic Impact Response

The level of damage in the CFRP layer following ballistic impact, represented by the fraction of plies that exhibited fibre failure f, was plotted as a function of impact velocity v_0 in Figure 7.13. For all tests, the fraction of failed plies increased progressively with the impact velocity. Two critical velocities can be defined: v_{init} is the velocity at initiation of failure (defined to be the highest tested impact velocity at $f = 0$), and v_p is the penetration velocity (defined to be the lowest tested impact velocity at $f = 1$). Under both edge-clamped and back-supported boundary conditions, the ballistic resistance in terms of v_{init} and v_p improved in the following order: monolithic material (A), bilayer composite plates (B), and bilayer composite plates (C). The higher ballistic resistance of material (C) was especially pronounced under the edge-clamped condition, where v_p exceeded the launch velocity limit of the test set-up (380 m/s) and was estimated to be $v_p \sim 400$ m/s based on extrapolation from the data.

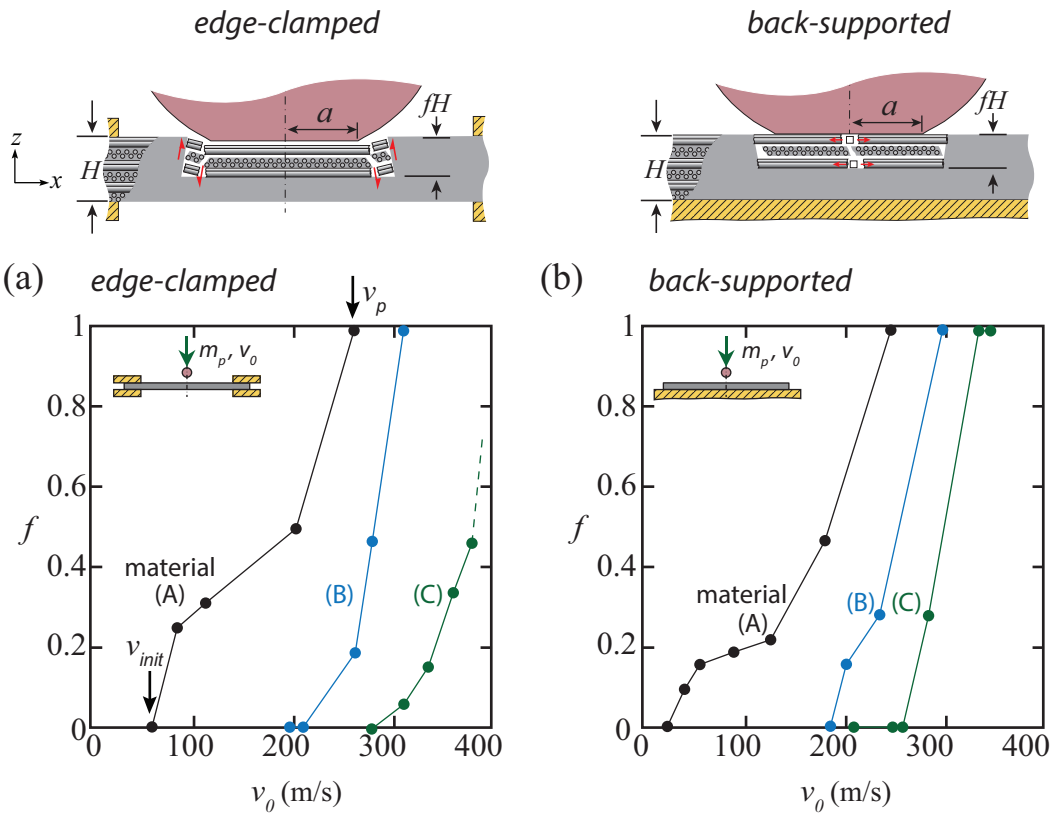

Figure 7.13: The ballistic cut fraction f in materials (A) to (C) plotted as functions of the impact velocity v_0 under a) edge-clamped and b) back-supported conditions.

7.5 Discussion

7.5.1 Failure Mechanisms

In both the quasi-static and the ballistic tests, the failure mechanisms of the CFRP layers in the monolithic and bilayer plates were sensitive to the testing boundary condition but were not affected by the presence of the metal layers.

In the edge-clamped condition, back face deflection of the CFRP layer was permitted. This caused the material beneath the edge of contact to undergo shear deformation. Transverse matrix cracks would form when the local shear stress reached the matrix shear strength of the CFRP. As the indentation force or impact velocity increased further, the matrix crack formation was followed by ply delamination and fibre fracture. Fibre fracture would propagate to connect with the above-mentioned matrix cracks. This failure mode is often referred to as the shear plugging mechanism, and is commonly observed in the impact failure of conventional CFRP (Cantwell and Morton, 1989a,b, 1990; Cristescu et al., 1975; Zhou, 1995). In the current study, the presence of the metal protection did not suppress this shear plugging mode in the CFRP layer under both quasi-static and ballistic loading. Measurements of the contact area during the interrupted quasi-static indentation test confirmed that first failure in the bilayer composite plates occured when the out-of-plane shear stress of the CFRP reached its matrix shear strength. However, the contact area measurement revealed that the plastic deformation of the metal layer had the effect of spreading the indentation load over a larger area. This increased the quasi-static indentation load required for shear plug formation. Analogously, this load spreading effect of the metal protection can also occur under ballistic loading, thus increasing the energy required for shear plug formation and enhancing the ballistic resistance.

In the back-supported condition, back face deflection was prohibited. This caused the material directly underneath the indenter or projectile to undergo out-of-plane compression. Chapter 3 has demonstrated that, under out-of-plane compression, CFRP cross-ply laminates can fail by an indirect tension mechanism facilitated by ply tensile failure. A similar failure mode was observed in this study, with fibre tensile failure occurring directly beneath the indenter/projectile where the pressure is at a maximum. Note that

this observed failure mode is in agreement with experimental results from Poe Jr. (1991), who also observed that fibre tensile failure occurred in the area directly underneath the indenter when a helical CFRP laminate was subjected to back-supported indentation. In the current study, the presence of the metal protection did not alter the failure mode of the underlying CFRP. Nevertheless, the above-mentioned load spreading effect was also observed in the back-supported tests and increased the indentation load as well as the energy required for fibre tensile failure.

7.5.2 A Comparision of the Quasi-static and Ballistic Responses

The above analysis indicates that the failure mechanisms of a CFRP layer are the same under both quasi-static and ballistic loading. The level of damage under different loading conditions can be compared by plotting the cut fraction of plies f in the CFRP layer as a function of energy dissipation W. The energy absorption W in the quasi-static experiments was calculated by integrating the indentation load F across the displacement u_z:

$$W = -\int_0^{u_0} F du_z \tag{7.4}$$

where u_0 is the maximum displacement before unloading in each interrupted test. The energy dissipation W in the ballistic tests was calculated from the different kinetic energies of the projectile before impact and after rebound:

$$W = \frac{m_p}{2}(v_0^2 - v_r^2) \tag{7.5}$$

where m_p is the projectile mass (7.2×10^{-4} kg), v_0 is the impact velocity, and v_r is the rebound velocity. Overall, the energy dissipation in the CFRP layer under quasi-static loading is comparable to the values from the ballistic test, see Figure 7.14. The disparity of the energy dissipation was larger in the edge-clamped condition; this can be attributed to the presence of stress wave propagation in the ballistic test as opposed to in the quasi-static test.

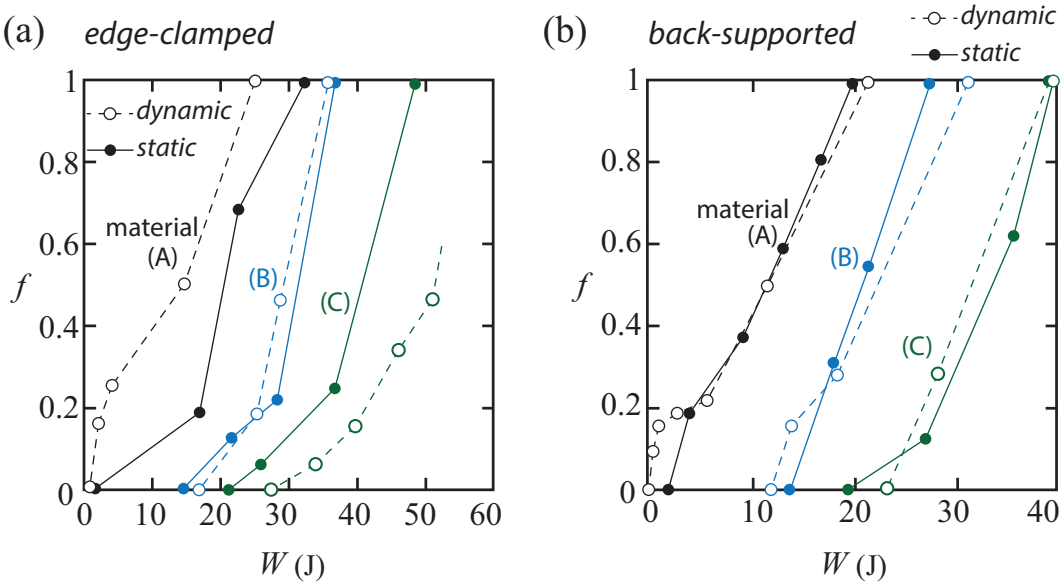

Figure 7.14: Cut fraction f in materials (A) to (C) from quasi-static and dynamic tests plotted as functions of the energy dissipation W under a) edge-clamped and b) back-supported conditions.

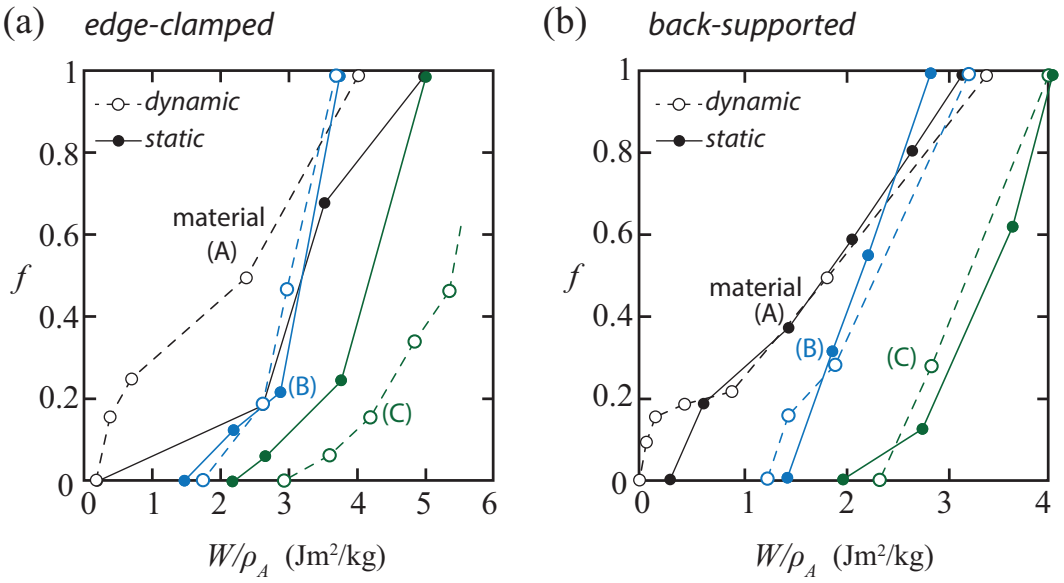

Figure 7.15: Cut fraction f in materials (A) to (C) from quasi-static and dynamic tests plotted as functions of the specific energy dissipation W/ρ_A under a) edge-clamped and b) back-supported conditions.

7.5.3 Effect of Metal Layer Protection on the Specific Energy Dissipation

The bilayer composite plates tested in this study have a higher areal density than that of the monolithic CFRP layer. To control for the effect of additional material on the energy absorption capability, the ratio of energy absorption to areal density for all the specimen types shall be compared Figure 7.15 plots the cut fraction of plies f in the CFRP layer as functions of specific energy absorption (defined to be W/ρ_A), where monolithic plates (A) have $\rho_A = 6.28$ kg/m^2 and bilayer plates (B) and (C) have $\rho_A = 9.73$ kg/m^2. Even in terms of specific energy dissipation, bilayer plates (C) and in most cases (B) have higher impact resistance than monolithic CFRP plates (A).

7.6 Conclusions

The current study explores the potential for protecting cured CFRP cross-ply plates against perforation by using a protective metal layer. In particular, it has been considered whether the presence of a protective metal layer can suppress the commonly observed brittle shear plugging mechanism in conventional CFRP under ballistic loading. For this purpose, two types of aluminium alloy-CFRP bilayers were manufactured: one layer of (i) AA1050A-T6 or (ii) AA6082-T6 was placed in front of a CFRP layer. The performance of bilayer plates was compared against that of monolithic CFRP plates without metal protection. The composite plates were then subjected to quasi-static indentation and ballistic impact by a spherical indenter or projectile under different supporting boundary conditions. In total, four types of tests were conducted: (i) quasi-static indentation test with rigid back support, (ii) quasi-static indentation test with an edge-clamped condition, (iii) ballistic test with rigid back support, and (iv) ballistic test with an edge-clamped condition.

In both quasi-static and ballistic tests, the perforation mechanism in the CFRP layers was sensitive to the testing boundary condition but was not affected by the presence of the metal layers. When the specimens were tested under the edge-clamped condition, back face deflection was permitted. This caused the CFRP layers to fail by shear plugging with transverse matrix cracks, ply delamination, and fibre fracture concentrated in the material underneath the

circumference of the contact area. In contrast, when the specimens were tested under the back-supported condition, back face deflection was prohibited and thus the material underneath the indenter/projectile was subjected to compression. As a result, the CFRP layers failed by an indirect tension mode consisting of ply tensile failure in the material directly underneath the indenter or the projectile, similar to the failure mode observed for CFRP cross-ply laminates when subjected to uniaxial out-of-plane compression.

The presence of the metal layer did not alter the failure mechanism in the underlying CFRP layer, but did provide a beneficial load spreading effect. This effect expanded the indentation and impact contact areas, which increased the load and energy required to initiate failure. As a result, under both edge-clamped and back-supported conditions, the quasi-static strength and impact resistance of the CFRP layers increased when they were protected by metal layers. A greater benefit was derived from metal layers with higher yield strength. The impact resistance (in terms of absorbed energy per areal density) measured from all the tests generally increased in the following order: monolithic CFRP, AA1050A-H6-CFRP bilayer, and AA6082-T6-CFRP bilayer. These data suggest that the use of metal layers with higher yield strength can potentially suppress shear plugging in the CFRP laminates altogether.

Chapter 8

Conclusions and Future Work

8.1 Conclusions

The investigations in this thesis led to the following conclusions.

(i) Under quasi-static out-of-plane compression and indentation, indirect tension can arise in CFRP cross-ply laminates due to the anisotropy in Poisson expansion within the plane of each ply. This indicates that the indirect tension mechanism is not unique to Dyneema® cross-ply laminates, in which the mechanism was first reported. For this failure mode, the material's resistance to failure depends more on the tensile strength of the ply than on the shear strength of the matrix. This has been analysed by finite element simulations and analytical models, and the influence of strain rate and specimen size on the compressive strength has been explored.

(ii) Under quasi-static out-of-plane punch loading, CFRP cross-ply laminates fail by shear plugging. For this failure mode, the material's resistance to failure largely depends on the matrix shear strength, and this is supported by a simple analytical model.

(iii) Under ballistic loading, CFRP cross-ply laminates with a high matrix shear strength fail by a brittle shear plugging mode. For this failure regime, the ballistic resistance (i.e. penetration velocity) can be enhanced by the reduction of matrix shear strength. Once the matrix shear strength decreases below 22 MPa, the failure mode switches from shear plugging to indirect tension. For this failure regime, the penetration velocity remains elevated and is independent of matrix shear strength.

(iv) A CFRP bilayer composite has been developed through lamination of both a low and a high matrix shear strength layer in order to suppress shear plugging under ballistic loading. When the layer with high matrix shear strength is placed at the distal face (protected by the layer with low matrix shear strength), its perforation mechanism switches from shear plugging to a back face tensile mode.

(v) The ballistic resistance of these bilayer composites closely follows the rule of mixtures. Depending on the stacking configuration, the bilayer composites can provide a 43% to 64% improvement compared to monolithic CFRP with high matrix shear strength.

(vi) The ballistic resistance of CFRP laminates with high matrix shear strength can be improved through protection by placing a metal layer at the front face. The presence of a protective metal layer provides a load spreading effect that increases the contact area of the underlying CFRP layer, and thus increases the energy required to initiate shear plugging.

(vii) The impact resistance of the protected CFRP rises with the yield strength of the metal layers, implying that there remains potential to suppress shear plugging (or to activate indirect tension) in the CFRP layer if a sufficiently hard protective layer is employed.

Overall, it was found that the impact resistance of conventional structural composites such as CFRP cross-ply laminates can be enhanced by activating the indirect tension mechanism. In the future, the challenge will be to develop methods of promoting indirect tension under ballistic loading without diminishing the structural performance of the fibre composite (e.g. without reducing the matrix shear strength).

8.2 Suggestions for Future Work

To develop a fulsome understanding of the impact mechanics of fibre composites, some avenues for future research are suggested below.

8.2.1 Numerical Methods to Predict the Ballistic Limit of Cross-ply Laminates Failing by Indirect Tension

Chapter 4 and an investigation by Attwood et al. (2014) have developed numerical models of the indirect tension mechanism of cross-ply laminates under uniaxial out-of-plane compression. However, no literature is available on utilising numerical methods to predict the ballistic limit (i.e. penetration velocity) of laminates that fail by indirect tension. Such analysis could also provide insight into the underlying cause of the switch in perforation mechanism (from shear plugging to indirect tension) observed for CFRP cross-ply laminates as their matrix shear strength decreases. The challenge involved in simulating dynamic loading conditions is the necessity of accounting for the propagation of stress waves as well as the inertia of the target, with consideration given to the target's geometry and the boundary conditions of the problem. Consequently, the whole composite structure must be simulated and the problem cannot be simplified by enforcing periodic boundary conditions on a small unit cell of material.

8.2.2 The Effect of Matrix Shear Strength on the Impact Tolerance of Cross-ply Laminates

Chapter 5 demonstrated that the impact resistance of CFRP cross-ply laminates can be improved by a reduction in matrix shear strength. This investigation can be extended to assess the effect of matrix shear strength on impact tolerance (i.e. the ability to provide structural performance after impact damage has occurred). For instance, CFRP with various matrix shear strengths can first be impacted by a projectile at a velocity that can cause internal damage and then be subjected to an in-plane compression test to determine the remaining structural performance of the material. Typically, the in-plane compressive strength of an undamaged composite increases along

with increasing matrix shear strength. In contrast, this thesis has shown that impact resistance is lower for CFRP laminates with high matrix shear strength. Therefore, it is expected that the post-impact compressive strength will rise up to an optimal shear strength level, after which it will fall due to the declining impact resistance.

8.2.3 The Effect of the Metal Layer's Yield Strength on the Ballistic Resistance of Metal-CFRP Bilayers

Chapter 7 demonstrated that the presence of a protective metal layer provides a load spreading effect that increases the energy required to initiate shear plugging in the underlying CFRP layer. The experiments also showed that the impact resistance of the protected CFRP rises with the yield strength of the metal layers (AA6082-T6 with yield strength of $\sigma_y \sim 262$ MPa versus AA1050A-H6 with $\sigma_y \sim 107$ MPa), implying that there remains potential to suppress shear plugging (or to activate indirect tension) in the CFRP layer if a sufficiently hard protective layer is used. Considering that indirect tension in CFRP cross-ply laminates under out-of-plane compression occurs at a pressure of ~ 1 GPa, the yield strength of the metal layer may need to be in the same order of magnitude to activate indirect tension. Possible candidates include: a high strength aluminium alloy AA7075-T6 ($\sigma_y \sim 450$ MPa), titanium alloy Ti-6Al-4V ($\sigma_y \sim 900$ MPa), Nanovate^{TM} nanocrytalline nickel-based alloy ($\sigma_y \sim 1100$ MPa), and tool steel AISI H13 ($\sigma_y \sim 1600$ MPa).

References

Abrate, S., 1991. Impact on laminated composite materials. Applied Mechanics Reviews 44 (4), 155–190.

Airbus, 2011. The A350 XWB "MSN1" forward fuselage takes shape. http://www.airbus.com/newsevents/news-events-single/detail/the-first-a350-xwb-forward-fuselage-takes-shape/.

Argon, A. S., Andrews, R. D., Godrick, J. A., Whitney, W., 1968. Plastic deformation bands in glassy polystyrene. Journal of Applied Plysics 39, 1899–1906.

ASTM Standard, 2013a. ASTM D2344/D2344M–13 Standard test method for short-beam strength of polymer matrix composite materials and their laminates. ASTM International, West Conshohocken, PA.

ASTM Standard, 2013b. ASTM D3518/D3518M–13 Standard test method for in-plane shear response of polymer matrix composite materials by tensile test of a $\pm 45^{\circ}$ laminate. ASTM International, West Conshohocken, PA.

Atas, C., 2007. An experimental investigation on the impact response of fiberglass/aluminum composites. Journal of Reinforced Plastics And Composites 26 (14), 1479–1491.

Attwood, J. P., 2015. Static and dynamic properties of polyethylene fibre composites. Ph.D. Thesis, University of Cambridge.

Attwood, J. P., Fleck, N. A., Wadley, H. N. G., Deshpande, V. S., 2015. The compressive response of ultra-high molecular weight polyethylene fibres and composites. International Journal of Solids and Structures 71 (1), 141–155.

Attwood, J. P., Khaderi, S. N., Karthikeyan, K., Fleck, N. A., O'Masta, M. R., Deshpande, V. S., Wadley, H. N. G., 2014. The out-of-plane compressive response of Dyneema composites. Journal of the Mechanics and Physics of Solids 70, 200–226.

Attwood, J. P., Russel, B. P., Wadley, H. N. G., Deshpande, V. S., 2016. Mechanisms of the penetration of ultra-high molecular weight polyethylene composite beams. International Journal of Impact Engineering 93, 153–165.

Beaumont, P. W. R., Riewald, P. G., Zweben, C., 1975. Methods for improving the impact resistance of composite materials. In: Foreign Object Impact Damage to Composites, ASTM STP 568, American Society for Testing and Materials. pp. 134–158.

Berg, C. A., Tirosh, J., Israeli, M., 1972. Analysis of short beam bending of fiber reinforced composites. In: Composite Materials: Testing and Design (Second Conference),. STP27748S, H. Corten, Ed., ASTM International, West Conshohocken, PA, pp. 206–218.

Bibo, G. A., Hogg, P. J., 1996. The role of reinforcement architecture on impact damage mechanisms and post-impact compression behaviour. Journal of Material Science 31 (5), 1115–1137.

Bieniaś, J., Jakubczak, P., Surowska, B., Dragan, K., 2015. Low-energy impact behaviour and damage characterization of carbon fibre reinforced polymer and aluminium hybrid laminates. Archives of Civil and Mechanical Engineering 15 (4), 925–932.

Boll, D. J., Bascom, W. D., Weidner, J. C., Murri, W. J., 1986. A microscopy study of impact damage of epoxy-matrix carbon-fibre composites. Journal of Material Science 21 (8), 2667–2677.

Cai, Z., Gutowski, T., 1992. The 3-D deformation-behavior of a lubricated fiber bundle. Journal of Composite Materials 26 (8), 1207–1237.

Cain, J., Gaviola, M., 2015. Investigation into the material properties and penetration resistant behavior of UHMWPE composites using a novel test methodology and correlation with ballistic performance. In: Proc SAMPE. Baltimore, MD.

Cantwell, W. J., Morton, J., 1989a. Comparison of the low and high velocity impact response of CFRP. Composites 20 (6), 545–551.

Cantwell, W. J., Morton, J., 1989b. Geometrical effects in the low velocity impact response of CFRP. Composite Structures 12 (1), 39–59.

Cantwell, W. J., Morton, J., 1990. Impact perforation of carbon fibre reinforced plastic. Composites Science and Technology 38 (2), 119–141.

Cantwell, W. J., Morton, J., 1991. The impact resistance of composite materials - a review. Composites 22 (5), 347–362.

Caprino, G., Spataro, G., Del Luongo, S., 2004. Low-velocity impact behaviour of fibreglass-aluminium laminates. Composites Part A: Applied Science and Manufacturing 35 (5), 605–616.

Chamis, C. C., Sinclair, J. H., 1977. 10° off-axis test for shear properties in fiber composites. Experimental Mechanics 17 (9), 339–346.

Chang, F.-K., Choi, H. Y., Jeng, S.-T., 1990. Study on impact damage in laminated composites. Mechanics of Materials 10 (1-2), 83–95.

Cheeseman, B. A., Bogetti, T. A., 2003. Ballistic impact into fabric and compliant composite laminates. Composite Structures 61 (1-2), 161–173.

Choi, H. Y., Chang, F.-K., 1992. A model for predicting damage in graphite/epoxy laminated composites resulting from low-velocity point impact. Journal of Composite Materials 26 (14), 2134–2169.

Choi, H. Y., Downs, R. J., Chang, F.-K., 1991a. A new approach toward understanding damage mechanisms and mechanics of laminated composites due to low-velocity impact: part I-experiments. Journal of Composite Materials 25 (8), 992–1011.

Choi, H. Y., Wu, H.-Y. T., Chang, F.-K., 1991b. A new approach toward understanding damage mechanisms and mechanics of laminated composites due to low-velocity impact: part II-analysis. Journal of Composite Materials 25 (8), 1012–1038.

Collings, T. A., 1974. Transverse compressive behaviour of unidirectional carbon fibre reinforced plastics. Composites 5 (3), 108–116.

Compston, P., Cantwell, W, J., Jones, C., Jones, N., 2001. Impact perforation resistance and fracture mechanisms of a thermoplastic based fiber-metal laminate. Journal of Material Science Letters 20 (7), 597–599.

Cristescu, N., Malvern, L. E., Sierakowski, R. L., 1975. Failure mechanisms in composite plates impacted by blunt-ended penetrators. In: Foreign object impact damage to composites. ASTM International, West Conshohocken, PA, pp. 159–172.

Cunniff, P. M., 1992. An analysis of the system effects in woven fabrics under ballistic impact. Textile Research Journal 62 (9), 495–509.

Cunniff, P. M., 1999. Dimensionless parameters for optimization of textile-based body armor systems. In: Proceedings 18th International Symposium of Ballistic. San Antonio, TX, pp. 1303–1310.

Daniel, I. M., LaBedz, R. H., Liber, T., 1981. New method for testing composites at very high strain rates. Experimental Mechanics 21 (2), 71–77.

de Ruijter, C. S., van der Zwaag, S., R. Stolze, R., Dingemans, T. J., 2010. Liquid crystalline matrix polymers for aramid ballistic composites. Polymer Composites 31 (4), 612–619.

Dransfield, K., Baillie, C., Mai, Y. W., 1994. Improving the delamination resistance of CFRP by stitching - a review. Composites Science and Technology 50 (3), 305–317.

Enfedaque, A., Molina-Aldareguia, J. M., Gálvez, F., González, C., LLorca, J., 2010. Effect of glass fiber hybridization on the behavior under impact of woven carbon fiber/epoxy laminates. Journal of Composite Materials 44 (25), 3051–3068.

Freeman, S. M., 1982. Characterization of lamina and interlaminar damage in graphite/epoxy composites by the deply technique. In: Daniel, I. (Ed.), Composite Materials: Testing and Design (6th Conference), STP28473S. West Conshohocken, PA, pp. 50–62.

Fukuda, H., Chou, T.-W., 1981. An advanced shear-lag model applicable to discontinuous fiber composites. Journal of Composite Materials 15 (1), 79–91.

Gama, B. A., Gillespie Jr., J. W., 2008. Punch shear based penetration model of ballistic impact of thick-section composites. Composite Structures 86 (4), 356–369.

Gama, B. A., Gillespie Jr., J. W., 2011. Finite element modeling of impact, damage evolution and penetration of thick-section composites. International Journal of Impact Engineering 38 (4), 181–197.

Gates, T. S., Sun, C. T., 1991. Elastic/viscoplastic constitutive model for fiber reinforced thermoplastic composites. AIAA Journal 29 (3), 457–463.

Gerlach, R., Siviour, C. R., Wiegand, J., Petrinic, N., 2013. The strain rate dependent material behavior of S-GFRP extracted from GLARE. Mechanics of Advanced Materials and Structures 20 (7), 505–514.

Goldsmith, W., Dharan, C. K. H., Chang, H., 1995. Quasi-static and ballistic perforation of carbon-fiber laminates. International Journal of Solids and Structures 32 (1), 89–103.

González, C., LLorca, J., 2007. Mechanical behavior of unidirectional fiber-reinforced polymers under transverse compression: Microscopic mechanisms and modeling. Composites Science and Technology 67 (13), 2795–2806.

González, E. V., Maimí, P., Sainz de Aja, J. R., Crus, P., Camanho, P., 2014. Effects of interply hybridization on the damage resistance and tolerance of composite laminates. Composite Structures 108, 319–331.

Greenhalgh, E. S., 2009. Defects and damage and their role in the failure of polymer composites. In: Failure analysis and fractography of polymer composites. Woodhead Publishing Limited and CRC Press LLC.

Guedes, R. M., Vaz, M. A., Ferreira, F. J., Morais, J. L., 2005. Response of CFRP laminates under high strain rate compression until failure. Science and Engineering of Composite Materials 12 (1-2), 145–151.

Guild, F. J., Hogg, P. J., Prichard, J. C., 1993. A model for the reduction in compression strength of continuous fibre composites after impact damage. Composites 24 (4), 333–339.

Gutowski, T. G., Cai, Z., Bauer, S., Boucher, D., Kingery, J., Wineman, S., 1987. Consolidation experiments for laminate composites. Journal of Composite Materials 21 (7), 650–669.

Gutowski, T. G., Dillon, G., 1992. The elastic-deformation of lubricated carbon-fiber bundles - comparison of theory and experiments. Journal of Composite Materials 26 (16), 2330–2347.

Harris, B., Bunsell, A., 1975. Impact properties of glass fibre/carbon fibre hybrid composites. Composites 6 (5), 197–201.

Henriksson, A., 1990. Transverse compressive behaviour of carbon-epoxy laminates and its influence on contact laws. M.S. Thesis, The Aeronautical Research Institute of Sweden (FFA).

Hexcel Composites, March 2007. Hexply M9.1F/M9.6F product data. Hexcel Composites. Publication FTU 143b.

Hexcel Composites, February 2013. Hexply 8552 epoxy matrix (180°C/356°F curing matrix), product data. Hexcel Composites. Publication FTA 072e.

Hine, P. J., Duckett, R. A., Kaddour, A. S., Hinton, M. J., Wells, G. M., 2005. The effect of hydrostatic pressure on the mechanical properties of glass fibre/epoxy unidirectional composites. Composites Part A: Applied Science and Manufacturing 36 (2), 279–289.

Hine, P. J., Duckett, R. A., van Schepdael, L. J. J. M., Hamoen, J. R., van den Oever, M. J. A., van den Berg, R. W., 1999. The effect of high pressure on the failure of unidirectional carbon fibre/epoxy composites. In: Hogg, P. (Ed.), 5th conference on deformaiton and fracture of composites. London, UK, pp. 251–259.

Hirschbuehler, K. R., 1987. A comparison of several mechanical tests used to evaluate the toughness of composites. In: Johnston, N. (Ed.), Toughened Composites. ASTM International, West Conshohocken, PA, pp. 61–73.

Hoo Fatt, M. S., Lin, C., Revilock Jr., D. M., Hopkins, D. A., 2003. Ballistic impact of GLARE^{TM} fiber-metal laminates. Composite Structures 61 (1-2), 73–88.

Hosur, M. V., Alexander, J., Vaidya, U. K., Jeelani, S., 2001. High strain rate compression response of carbon/epoxy laminate composites. Composite Structures 52 (3-4), 405–417.

Hou, J. P., Petrinic, N., Ruiz, C., 2001. A delamination criterion for laminated composites under low-velocity impact. Composites Science and Technology 61 (14), 2069–2074.

Hou, J. P., Petrinic, N., Ruiz, C., Hallett, S. R., 2000. Prediction of impact damage in composite plates. Composites Science and Technology 60 (2), 273–281.

Hsiao, H. M., Daniel, I. M., Cordes, R. D., 1999. Strain rate effects on the transverse compressive and shear behavior of unidirectional composites. Journal of Composite Materials 33 (17), 1620–1642.

Hsieh, C. Y., Mount, B. Z., Jang, B. Z., Zee, R. H., 1990. Response of polymer composites to high and low velocity impact. In: 22nd International SAMPLE Technical Conference. Amercian Society for Testing and Materials, Boston, MA., pp. 14–327.

Hubert, P., Poursartip, A., 2001. A method for the direct measurement of the fibre bed compaction curve of composite prepregs. Composites Part A: Applied Science and Manufacturing 32 (2), 179–187.

Hull, D., 1981. Fibres and matrices. In: An Introduction to Composite Materials. Cambridge University Press, pp. 9–35.

Iremonger, M., Went, A. C., 1996. Ballistic impact of fibre composite armours by fragment-simulating projectiles. Composites Part A: Applied Science and Manufacturing 27 (7), 575–581.

Jang, B. Z., Chen, L. C., Wang, C. Z., Lin, H. T., Zee, R. H., 1989. Impact resistance and energy absorption mechanisms in hybrid composites. Composites Science and Technology 34 (4), 305–335.

Jaroslaw, B., Barbara, S., Patryk, J., 2016. The comparison of low-velocity impact resistance of aluminum/carbon and glass fiber metal laminates. Polymer Composites 37 (4), 1056–1063.

Jessel, B., 2013. BMW to double carbon fiber production. http://www.brianjesselbmwjournal.com/2013/11/bmw-to-double-carbon-fiber-production/.

Ji, X., Wang, C., Francis, B. A. P., Chia, E. A. M., Zheng, L., 2015. Mechanical and interfacial properties characterisation of single carbon fibres for composite applications. Experimental Mechanics 55 (6), 1057–1065.

Jørgensen, O., 1994. Indentation failure in cross ply laminates, comparison between observations and 3D field solutions. Journal of Composite Materials 28 (18), 1803–1824.

Jørgensen, O., Giannakopoulos, A. E., Suresh, S., 1998. Spherical indentation of composite laminates with controlled gradients in elastic anisotropy. International Journal of Solids and Structures 35 (36), 5097–5113.

Jørgensen, O., Horsewell, A., 1997. On the indentation failure of carbon-epoxy cross-ply laminates, and its suppression by elasto-plastic interleaves. Acta Materialia 45 (8), 3431–3444.

Joshi, S. P., Sun, C. T., 1985. Impact induced fracture in a laminated composite. Journal of Composite Materials 19 (1), 51–66.

Karthikeyan, K., Russell, B. P., 2014. Polyethylene ballistic laminates: Failure mechanics and interface effect. Materials and Design 63, 115–125.

Karthikeyan, K., Russell, B. P., Deshpande, V. S., Fleck, A., 2012. Multi-hit armour characterisation of metal-composite bi-layers. Journal of Mechanics of Materials and Structures 7, 721–734.

Karthikeyan, K., Russell, B. P., Fleck, N. A., O'Masta, M., Wadley, H. N. G., Deshpande, V. S., 2013a. The soft impact response of composite laminate beams. International Journal of Impact Engineering 60, 24–36.

Karthikeyan, K., Russell, B. P., Fleck, N. A., Wadley, H. N. G., Deshpande, V. S., 2013b. The effect of shear strength on the ballistic response of laminated composite plates. European Journal of Mechanics - A/Solids 42, 35–53.

Kavesh, S., Prevorsek, D. C., 1995. Ultra high strength, high modulus polyethylene spectra fibers and composites. International Journal of Polymeric Materials and Polymeric Biomaterials 30 (1-2), 15–56.

Kim, W.-S., Yun, I. H., Lee, J.-J., Jung, H.-T., 2010. Evaluation of mechanical interlock effect on adhesion strength of polymer-metal interfaces using micro-patterned surface topography. International Journal of Adhesion and Adhesives 30 (6), 408–417.

Koerber, H., Xavier, J., Camanho, P. P., 2010. High strain rate characterisation of unidirectional carbon-epoxy IM7-8552 in transverse compression and in-plane shear using digital image correlation. Mechanics of Materials 42 (11), 1004–1019.

Lawcock, G. D., Ye, L., Mai, Y. W., Sun, C. T., 1998. Effects of fibre/matrix adhesion on carbon-fibre-reinforced metal laminates-II. impact behaviour. Composites Science and Technology 57 (12), 1621–1628.

Lee, B. L., Walsh, T. F., Won, S. T., Patts, H. M., Song, J. W., Mayer, A. H., 2001. Penetration failure mechanisms of armor-grade fiber composites under impact. Journal of Composite Materials 35 (18), 1605–1633.

Lee, S.-W. R., Sun, C. T., 1993. A quasi-static penetration model for composite laminates. Journal of Composite Materials 27 (3), 251–271.

Lim, C. T., Shim, V. P. W., Ng, Y. H., 2003. Finite-element modeling of the ballistic impact of fabric armor. International Journal of Impact Engineering 28 (1), 13–31.

Lim, C. T., Tan, V. B. C., Cheong, C. H., 2002. Perforation of high-strength double-ply fabric system by varying shaped projectiles. International Journal of Impact Engineering 27 (6), 577–591.

Liu, Y. Liaw, B., 2010. Effects of constituents and lay-up configuration on drop-weight tests of fiber-metal laminates. Applied Composite Materials 17 (1), 43–62.

Liu, D., 1988. Impact-induced delamination-a view of bending stiffness mismatching. Journal of Composite Materials 22 (7), 674–692.

Liu, D., Malvern, L. E., 1987. Matrix cracking in impacted glass/epoxy plates. Journal of Composite Materials 21 (7), 594–609.

Liu, S., Kutlu, Z., Chang, F.-K., 1993. Matrix cracking and delamination in laminated composite beams subjected to a transverse concentrated line load. Journal of Composite Materials 27 (5), 436–470.

Majeed, M. A., Yigit, A. S., Christoforou, A. P., 2012. Elastoplastic contact/impact of rigidly supported composites. Composites Part B: Engineering 43 (3), 1244–1251.

Mallick, P. K., Broutman, L. J., 1977. Static and impact properties of laminated hybrid composites. Journal of Testing and Evaluation 5 (3), 190–200.

Marlett, K., 2011. Hexcel 8552 IM7 unidirectional prepreg 190 & gsm 35% RC qualification material property data report. National Institute for Aviation Research, Wichita State University, CAM–RP–2009–015.

Mines, R. A. W., Roach, A. M., Jones, N., 1999. High velocity perforation behavior of polymer composite laminates. International Journal of Impact Engineering 22 (6), 561–588.

Mouritz, A. P., 2007. Review of z-pinned composite laminates. Composites Part A: Applied Science and Manufacturing 38 (12), 2383–2397.

Ning, H., Li, Y., Hu, N., 2013. Improvement of interlaminar mechanical properties of CARALL based on nanofiller interface reinforcement and other fabrication techniques. In: 13th International Conference on Fracture. Vol. 5. Beijing, China, pp. 3465–3475.

O'Masta, M. R., 2014. Mechanisms of dynamic deformation and failure in ultra-high molecular weight polyethylene fiber-polymer matrix composites. Ph.D. Thesis, University of Virginia.

O'Masta, M. R., Crayton, D. H., Deshpande, V. S., Wadley, H. N. G., 2015a. Mechanisms of penetration in polyethylene reinforced cross-ply laminates. International Journal of Impact Engineering 86, 249–264.

O'Masta, M. R., Crayton, D. H., Deshpande, V. S., Wadley, H. N. G., 2016. Indentation of polyethylene laminates by a flat-bottomed cylindrical punch. Composites Part A: Applied Science and Manufacturing 80, 138–147.

O'Masta, M. R., Deshpande, V. S., Wadley, H. N. G., 2015b. Defect controlled transverse compressive strength of polyethylene fiber laminates. International Journal of Solids and Structures 52 (1), 130–149.

Oya, N., Hamada, H., 1998. Axial compressive behaviour of reinforcing fibres and interphase in glass/epoxy composite materials. Journal of Materials Science 33 (13), 3407–3417.

Pae, K. D., Phee, K. Y., 1995. Effect of hydrostatic pressure on the compressive behaviour of thick laminates 45° and 90° undirectional graphite–fibre/epoxy matrix composites. Composites Science and Technology 53 (3), 281–287.

Park, R., Jang, J., 2001. Impact behavior of aramid fiber/glass fiber hybrid composite: evaluation of four-layer hybrid composites. Journal of Materials Science 36 (9), 2359–2367.

Pärnänen, T., Kanerva, M., Sarlin, E., Saarela, O., 2015. Debonding and impact damage in stainless steel fibre metal laminates prior to metal fracture. Composite Structures 119, 777–786.

Parry, T. V., Wronski, A. S., 1985. The effect of hydrostatic pressure on the tensile properties of pultruded CFRP. Journal of Materials Science 20 (6), 2141–2147.

Parry, T. V., Wronski, A. S., 1986. The tensile properties of pultruded GRP tested under superposed hydrostatic pressure. Journal of Materials Science 21 (12), 4451–4455.

Parry, T. V., Wronski, A. S., 1990. The effect of hydrostatic pressure on transverse strength of glass and carbon fibre–epoxy composites. Journal of Material Science 25 (7), 3162–3166.

Peijs, A. A. J. M., Catsman, P., Govaert, L. E., Lemstra, P. J., 1990a. Hybrid composites based on polyethylene and carbon fibres part 2: influence of composition and adhesion level of polyethylene fibres on mechanical properties. Composites 21 (6), 513–521.

Peijs, A. A. J. M., Venderbosch, R. W., 1991. Hybrid composites based on polyethylene and carbon fibres part iv influence of hybrid design on impact strength. Journal of Materials Science Letters 10 (19), 1122–1124.

Peijs, A. A. J. M., Venderbosch, R. W., Lemstra, P. J., 1990b. Hybrid composites based on polyethylene and carbon fibres part 3: Impact resistant structural composites through damage management. Composites 21 (6), 522–530.

Peirce, D., Shih, C., Needleman, A., 1984. A tangent modulus method for rate dependent solids. Computers & Structures 18 (5), 875–887.

Perry, J. L., Adams, D. F., 1975. Charpy impact experiments on graphite/epoxy hybrid composites. Composites 6 (4), 166–172.

Phoenix, S. L., Porwal, P. K., 2003. A new membrane model for the ballistic impact response and V_{50} performance of multi-ply fibrous systems. International Journal of Solids and Structures 40 (24), 6723–6765.

Poe Jr., C. C., 1991. Simulated impact damage in a thick graphite/epoxy laminate using spherical indenters. Journal of Reinforced Plastic and Composites 10 (3), 293–307.

Rabinowitz, S., Ward, I. M., Parry, J. S. C., 1970. The effect of hydrostatic pressure on the shear yield behaviour of polymers. Journal of Materials Science 5 (1), 29–39.

Richardson, M. O. W., Wisheart, M. J., 1996. Review of low-velocity impact properties of composite materials. Composites Part A: Applied Science and Manufacturing 27 (12), 1123–1131.

Robinson, P., Davies, G. A. O., 1992. Impactor mass and specimen geometry effects in low velocity impact of laminated composites. International Journal of Impact Engineering 12 (2), 189–207.

Russell, B. P., Karthikeyan, K., Deshpande, V. S., Fleck, N. A., 2013. The high strain rate response of ultra high molecular-weight polyethylene: From fibre to laminate. International Journal of Impact Engineering 60, 1–9.

Sadighi, M., Alderliesten, R. C., Benedictus, R., 2012. Impact resistance of fiber-metal laminates: A review. International Journal of Impact Engineering 49, 77–90.

Sayer, M., Bektaş, N. B., Sayman, O., 2010. An experimental investigation on the impact behavior of hybrid composite plates. Composite Structures 92 (5), 1256–1262.

Scott, B., Cheeseman, B., 2008. The mechanics of projectile arrest for compliant cross plied unidirectional laminates. In: Proceedings of the 24th international symposium on ballistics. Vol. 2. DESTech Publications, Inc., New Orleans, LA, pp. 992–1002.

Scott, B. R., 1999. The penetration of compliant laminates by compact projectiles. In: Proceedings of the 18th International Symposium on Ballistics. Vol. 1. San Antonio, TX, pp. 1184–1191.

Scott, B. R., 2011. Unusual transverse compression response of non-woven ballistic laminates. In: Proceedings of the 26th International Symposium on Ballistics. Vol. 1-2. Miami, FL, pp. 12066–12067.

Sevkat, E., Liaw, B., Delale, F., Raju, B. B., 2009. Drop-weight impact of plain-woven hybrid glass-graphite/toughened epoxy composites. Composites Part A: Applied Science and Manufacturing 40 (8), 1090–1110.

Shinohara, A. H., Sato, T., Saito, F., Tomioka, T., Arai, Y., 1993. A novel method for measuring direct compressive properties of carbon fibres using a micro-mechanical compression tester. Journal of Materials Science 28 (24), 6611–6616.

Shivakumar, K., Elber, W., Illg, W., 1985. Prediction of low velocity impact damage in thin circular laminates. AIAA Journal 23 (3), 442–449.

Shyr, T.-W., Pan, Y. H., 2003. Impact resistance and damage characteristics of composite laminates. Composite Structures 62 (2), 193–203.

Sigley, R. H., Wronski, A. S., Parry, T. V., 1991. Tensile failure of pultruded glass-polyester composites under superimposed hydrostatic pressure. Composites Science and Technology 41 (4), 395–409.

Silverstein, M. S., Breuer, O., 1993. Mechanical properties and failure of etched UHMW-PE fibres. Journal of Materials Science 28 (15), 4153–4158.

Singletary, J., 2000. Transverse compression of PPTA fibers. Mechanics of Composite Materials 36 (4), 319–326.

Singletary, J., Davis, H., Ramasubramanian, M. K., Knoff, W., Toney, M., 2000. The transverse compression of PPTA fibers. part i single fiber transverse compression testing. Journal of Materials Science 35 (3), 573–581.

Sinmazçelik, T., Avcu, E., Bora, M. Ö., Çoban, O., 2011. A review: fibre metal laminates, background, bonding types and applied test methods. Materials & Design 32 (7), 3671–3685.

Sjoblom, P. O., Hartness, J. T., Cordell, T. M., 1988. On low-velocity impact testing of composite materials. Journal of Composite Materials 22 (1), 30–52.

Sjögren, A., Krasnikov, A., Varna, J., 2001. Experimental determination of elastic properties of impact damage in carbon fibre/epoxy laminates. Composites Part A: Applied Science and Manufacturing 32 (9), 1237–1242.

Song, S. H., Byun, Y. S., Song, W. J., Kim, J., Kang, B. S., 2010. Experimental and numerical investigation on impact performance of carbon reinforced aluminum laminates. Journal of Materials Science and Technology 26 (4), 327–332.

Soutis, C., Turkmen, D., 1997. Moisture and temperature effects of the compressive failure of CFRP unidirectional laminates. Journal of Composite Materials 31 (8), 832–849.

Srivastava, A., Majumdar, A., Butola, B. S., 2012. Improving the impact resistance of textile structures by using shear thickening fluids: a review. Critical Reviews in Solid State and Materials Sciences 37 (2), 115–129.

Staab, G. H., Gilat, A., 1995. High strain rate response of angle-ply glass/epoxy laminates. Journal of Composite Materials 29 (10), 1308–1320.

Suemasu, H., Kerth, S., Maier, M., 1992. Indentation of spherical head indentors on transversely isrotropic composite plates. Journal of Composite Materials 28 (17), 1723–1739.

Sun, C. T., Chen, J. L., 1989. A simple flow rule for characterizing non-linear behavior of fiber composites. Journal of Composite Materials 23 (10), 1009–1020.

Swolfs, Y., Gorbatikh, L., Verpoest, I., 2014. Fibre hybridisation in polymer composites: a review. Composites Part A: Applied Science and Manufacturing 67, 181–200.

Tabiei, A., Nilakantan, G., 2008. Ballistic impact of dry woven fabric composites: a review. Applied Mechanics Reviews 61 (1), 1–13.

Takeda, N., Sierakowski, R. L., Malvern, L. E., 1981. Wave propagation experiments on ballistically impacted composite laminates. Journal of Composite Materials 15 (2), 157–174.

Takeda, N., Sierakowski, R. L., Malvern, L. E., 1982a. Microscopic observations of cross sections of impacted composite laminates. Journal of Composites, Technology and Research 4 (2), 40–44.

Takeda, N., Sierakowski, R. L., Ross, C. A., Malvern, L. E., 1982b. Delamination-crack propagation in ballistically impacted glass/epoxy composite laminates. Experimental Mechanics 22 (1), 19–25.

Textile World, 2009. Life-saving fabrics. http://www.textileworld.com/textile-world/nonwovens-technical-textiles/2009/06/life-saving-fabrics/.

Tsai, J-L. Sun, C. T., 2005. Strain rate effect on in-plane shear strength of unidirectional polymeric composites. Composites Science and Technology 65 (13), 1941–1947.

Vlot, A., 1991. Low-velocity impact loading on fibre reinforced aluminium laminates (ARALL) and otheraircraft sheet materials. Ph.D. Thesis, Delft University of Technology.

Vlot, A., 1993. Impact properties of fibre metal laminates. Composites Engineering 3 (10), 911–927.

Vlot, A., 1996. Impact loading on fibre metal laminates. International Journal of Impact Engineering 18 (3), 291–307.

Vlot, A., Krull, M., 1997. Impact damage resistance of various fibre metal laminates. Journal de Physique IV Colloque 7 (C3), 1046–1050.

Walker, J. D., 2001. Ballistic limit of fabrics with resin. In: 19th International Symposium of Ballistics. Amercian Society for Testing and Materials, Interlaken, Switzerland, pp. 1409–1414.

Walrath, D. E., Adams, D. F., 1983. The losipescu shear test as applied to composite materials. Experimental Mechanics 23 (1), 105–110.

Ward, I. M., 1971. Review: The yield behaviour of polymers. Journal of Materials Science 6 (11), 1397–1417.

Weeks, C. A., Sun, C. T., 1998. Modeling non-linear rate-dependent behavior in fiber-reinforced composites. Composites Science and Technology 58 (3-4), 603–611.

Williams, J. G., Rhodes, M. D., 1982. The effect of resin on the impact damage tolerance of graphite/epoxy laminates. In: Daniel, I. M. (Ed.), Composite Materials: Testing and Design, (6th Conference). ASTM International, West Conshohocken, PA, pp. 450–480.

Woodward, R. L., Egglestone, G. T., Baxter, B. J., Challis, K., 1994. Resistance to penetration and compression of fiber-reinforced composite-materials. Composites Engineering 4 (3), 329–341.

Written, E., Kraus, T., Kuhnel, M., 2015. Composites market report 2015. Report, AVK - Industrievereinigung Verstarkte Kunststoffe e.V. and and Carbon Composites e.V.

Wu, E., Shyu, K., 1993. Response of composite laminates to contact loads and relationship to low-velocity impact. Journal of Composite Materials 27 (15), 1443–1464.

Wu, G., Yang, J. M., Hahn, H. T., 2007. The impact properties and damage tolerance and of bi-directionally reinforced fiber metal laminates. Journal of Materials Science 42 (3), 948–957.

Wu, H. Y., Springer, G. S., 1988. Measurements of matrix cracking and delamination caused by impact on composite plates. Journal of Composite Materials 22 (6), 518–532.

Yu, G. C., Wu, L. Z., Ma, L., Xiong, J., 2015. Low velocity impact of carbon fiber aluminum laminates. Composite Structures 119, 757–766.

Yun, I. H., Kim, W.-S., Kim, K.-H., Jung, J.-M., Lee, J.-J., Jung, H.-T., 2011. Highly enhanced interfacial adhesion properties of steel-polymer composites by dotshaped surface patterning. Journal of Applied Physics 109 (7), 074302.

Zhou, G., 1995. Damage mechanisms in composite laminates impacted by a flat-ended impactor. Composite Science and Technology 54 (3), 267–273.

Zhou, G., 1996. Static bahaviour and damage of thick composite laminates. Composite Structures 36 (1-2), 13–22.

Zinoviev, P. A., Tsvetkov, S. V., 1998. Mechanical properties of unidirectional organic–fiber–reinforced plastics under hydrostatic pressure. Composites Science and Technology 58 (1), 31–39.

Appendix A

Summary of the Partial Curing Process

In this thesis, CFRP laminates were tested with various states of cure. This appendix discusses the methodology used to manufacture the partially cured specimens in order to achieve reproducible states of matrix cure. A lab-designed oven curing process was employed such that the laminates were partially cured in an air-oven and then rapidly cooled to avoid further curing. Compared to the standard autoclave method, this oven curing procedure allows for easier control of the curing duration and better handling because the laminates are rapidly cooled from their elevated temperatures.

Figure A.1 illustrates a custom-made spring-loaded set-up for the partial curing process of a CFRP panel with dimensions $L \times L \times H$ (with panel side length of $L = 150$ mm and height of $H = 2$ - 4 mm). Before curing, all the components in the set-up (except the heat exchanging plates and the CFRP) were preheated in an air oven. A thermocouple was placed on the bottom aluminium platen to monitor the temperature. The CFRP panel was first sandwiched between two heat exchanging plates (with releasing films on the top and bottom surfaces of the CFRP) and then placed between the two aluminium platens with 12 equispaced M8 holes (clearance holes in the top platen and threaded holes in the bottom platen). The two platens and the whole fixture were fastened together with compression springs, spacers, and washers. Each compression spring had a free length of 49 mm, a spring constant of $k = 12$ N/mm, and a compressive load F range of 0 - 300 N. Each spring was then compressed to a

spacer height $h = 33$ mm, resulting in a total clamping force of $F = 2280$ N and an average pressure of 0.1 MPa exerted onto the CFRP.

After fastening, the whole fixture was placed into an air oven to cure the CFRP at various temperatures (100°C to 180°C) and durations (2 hours to 24 hours). The distance between the two platens was measured before and after each curing process; the change in distance was observed to be negligible, indicating that clamping pressure remained constant throughout the process. After curing, the heat exchanging plates and the sandwiched CFRP panel were rapidly cooled to −15°C and then separated once the CFRP stiffened. Finally, laminates were cut to test dimensions using either a sharp knife, an abrasive cutting wheel, or a water jet, depending on the state of cure and the complexity of the specimen geometries. The laminates were stored at −15°C to avoid further curing.

For the tests described in Chapters 5 and 6, long composite beams had to be prepared with dimensions of length $L = 300$ mm, breadth $B = 11$ mm, and height $H = 2$ or 4 mm. For these specimens, the length of the composite beams exceeded the width of the spring-loaded platens. Therefore, a modification was made to the above fixture, see Figure A.2. An additional pair of aluminium platens with six positive and negative channels was made. Six composite beams were first cut to test dimensions using a band saw, then wrapped with releasing films and placed inside the channels of the aluminum platens. The channeled platens were sandwiched in the above spring-loaded fixture with eight compression springs compressed to $h = 27$ mm, a total clamping force of $F = 2112$ N, and an average pressure of 0.1 MPa.

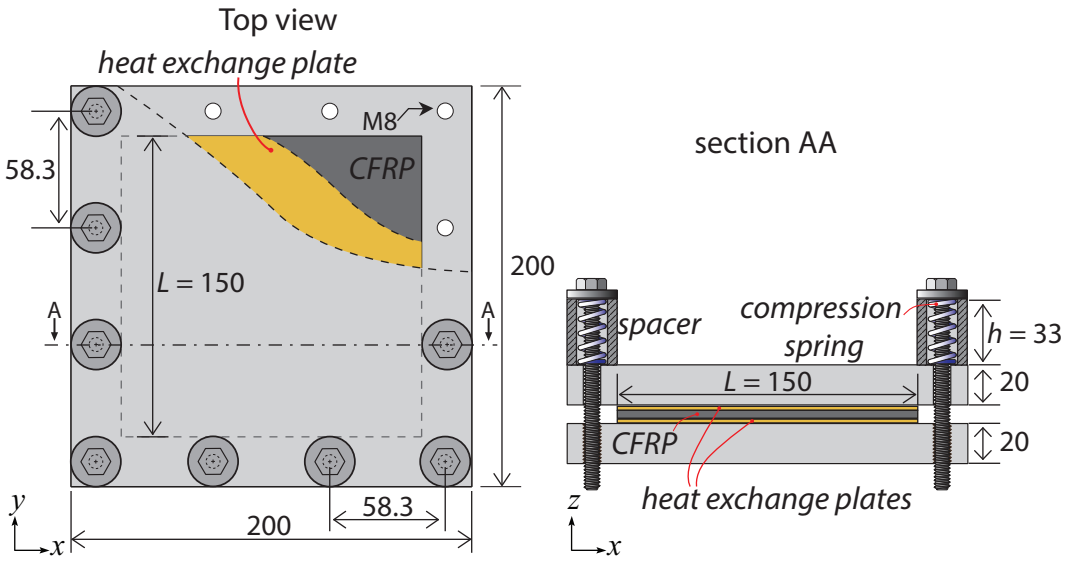

Figure A.1: Schematic illustrations of the spring-loaded set-up of the partial curing process for a CFRP plate. All dimensions are in mm.

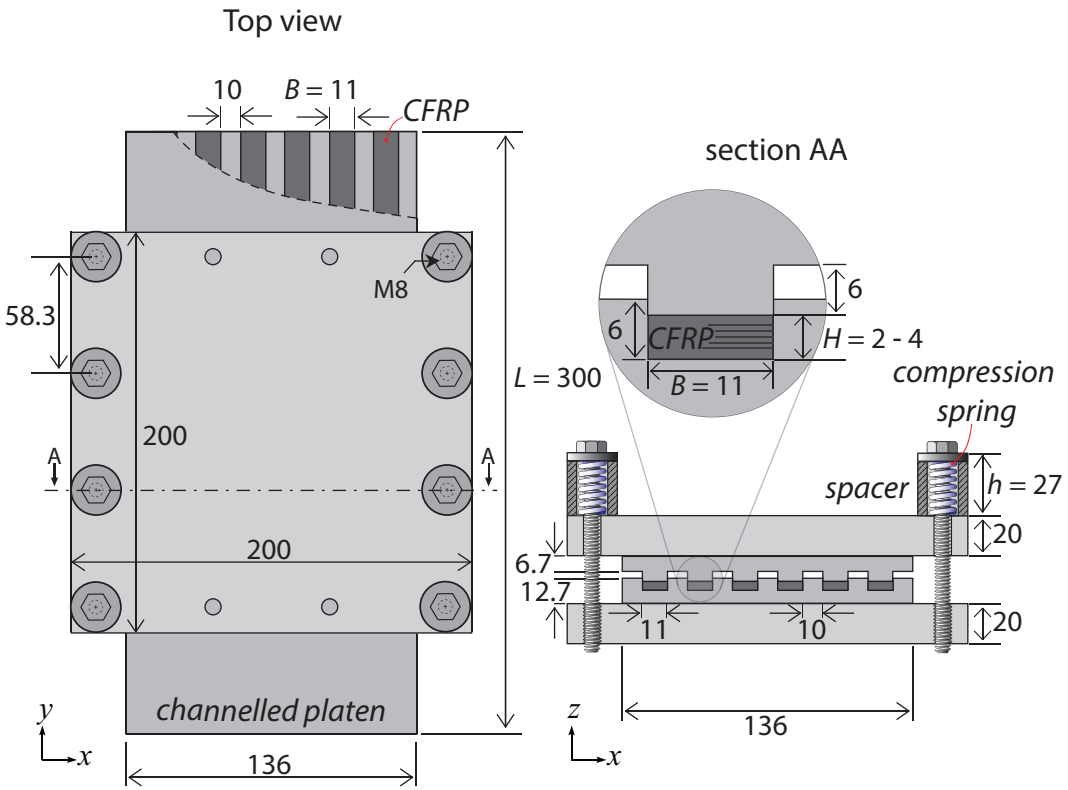

Figure A.2: Schematic illustrations of the spring-loaded set-up of the partial curing process for CFRP composite beams. All dimensions are in mm.

Appendix B

Measurements of Matrix Shear Strength of CFRP Laminates

The cross-ply laminates [0°/90°] described in Appendix A were made from carbon fibre/epoxy prepregs provided by Hexcel Ltd.: Hexply® 8552/35%/134/IM7 and Hexply® M9/35%/134/IM7 (both with ply thickness of 0.131 mm). In total, eight types of composite plates with the same dimensions were tested in this study and are defined in Table B.1. The uncured 8552/IM7 laminates (A) were laid-up by hand. Partially cured 8552/IM7 laminates (B) to (F) were prepared in an air oven using the procedure described in Appendix A. The fully cured 8552/IM7 laminates (G) and M9/IM7 laminates (H) were autoclaved following a procedure recommended by Hexcel Ltd., see (Hexcel Composites, 2007, 2013). With the exception of the fully cured materials (G) and (H), all laminates were stored at −15°C to avoid further curing and brought back to room temperature for 5 hours prior to testing.

The matrix shear responses of the above eight CFRP laminates were examined using two ASTM-recommended shear test methods, see (ASTM Standard, 2013a,b). A ±45° tensile test was used to measure the in-plane shear strength and a short beam shear test was used to measure the out-of-plane interlaminar shear strength at various shear strain rates.

Table B.1: Summary of curing processes of CFRP cross-ply laminates used in the shear tests.

Material	Prepreg Type	Curing method	Curing temperature	Curing time	Applied pressure
A	8552/IM7	uncured	room temperature	–	–
B	8552/IM7	partially cured	100 ° C	2 hr	out-of-plane 0.1 MPa
C	8552/IM7	partially cured	110 ° C	2 hr	out-of-plane 0.1 MPa
D	8552/IM7	partially cured	120 ° C	2 hr	out-of-plane 0.1 MPa
E	8552/IM7	partially cured	120 ° C	2 hr 15 min	out-of-plane 0.1 MPa
F	8552/IM7	partially cured	180 ° C	24 hr	out-of-plane 0.1 MPa
G	8552/IM7	autoclaved	180 ° C	2 hr	hydrostatic 0.7 MPa
H	M9/IM7	autoclaved	120 ° C	2 hr	hydrostatic 0.7 MPa

B.1 $\pm 45^\circ$ Tensile Test

Dog-bone tensile specimens with a $[\pm 45^\circ]_{4s}$ lay-up, a thickness of $t = 2$ mm (16 plies), and a width of $w = 10$ mm within the gauge length were manufactured from materials (A) to (H) mentioned in Table B.1. The specimens were cut using a water jet into the geometry specified in Figure B.1a. The tensile test was performed using a screw-driven test machine. The tensile load F was mostly recorded by a 100 kN load cell, with the exception of soft material (A) where a 1 kN load cell was used. The tensile displacements within the gauge of the specimen were measured by a laser extensometer. The $\pm 45^\circ$ tensile test was performed at applied displacement rates ranging from $u_x = 1.7 \times 10^{-2}$ mm/s to 6.1 mm/s, associated with an axial strain rate of $\dot{\varepsilon}_{xx} = 5 \times 10^{-5}\ s^{-1}$ to $0.13\ s^{-1}$.

The in-plane shear stress τ within each ply can be expressed as:

$$\tau = \frac{\sigma_{xx}}{2} = \frac{F}{2wt} \tag{B.1}$$

The in-plane shear strain γ can be expressed as:

$$\gamma = \varepsilon_{xx} - \varepsilon_{yy} \approx 2\varepsilon_{xx} \tag{B.2}$$

where ε_{xx} is the axial tensile strain. Figure B.2 shows some examples of the in-plane shear stress-strain response from materials (A) to (H) at a reference shear strain rate of $\dot{\gamma}_0 = 1 \times 10^{-3} s^{-1}$. In general, all materials showed shear yielding at shear strain γ less than 2% and a plateauing region was observed at $\gamma \sim 5\%$. ASTM standard D3518 recommends defining the in-plane shear yield strength τ_y as the flow stress τ at $\gamma = 5\%$. As a result, Figures B.3a to B.3d plot the measured $\tau_y \equiv \tau(\gamma = 5\%)$ as functions of shear strain rate $\dot{\gamma}$ in log-log scale. For comparison purposes, trend lines of τ at $\gamma = 2.5\%$, 5%, and 10% as functions of shear strain rate $\dot{\gamma}$ are also presented in the figure. Materials (A) to (C) showed various degrees of strain rate sensitivity while materials (D) to (H) were strain rate insensitive. The strain rate sensitivity of the shear flow stress τ in materials (A) to (C) can be characterised by a viscoplastic power law:

$$\frac{\tau}{\tau_0} = \left(\frac{\dot{\gamma}}{\dot{\gamma}_0}\right)^m \tag{B.3}$$

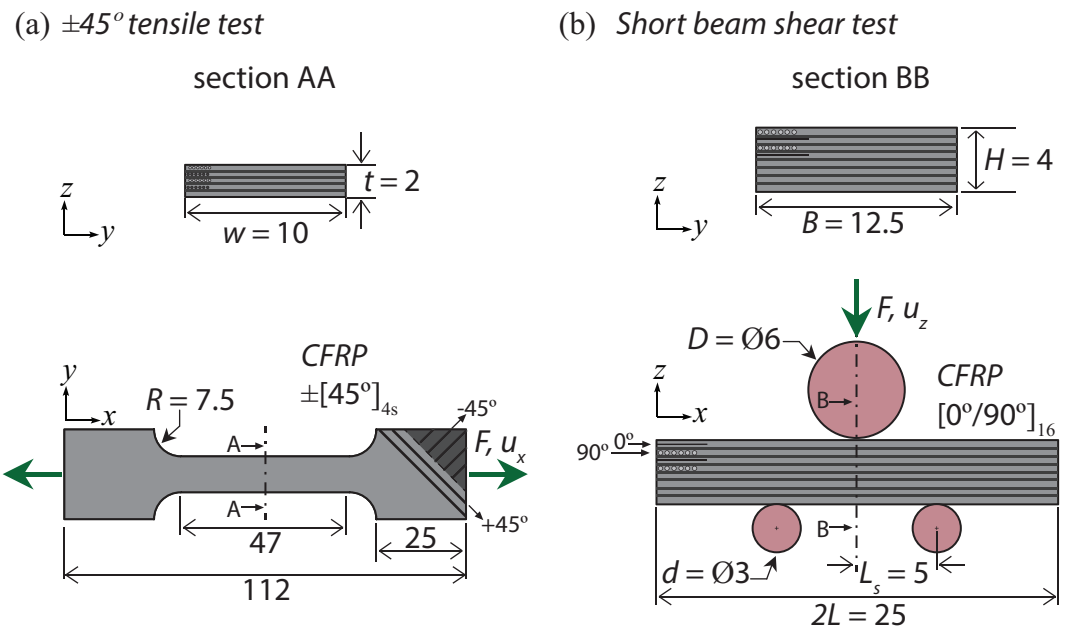

Figure B.1: Schematic illustrations of a) a ±45° tensile test dog-bone specimen and b) a short beam shear test specimen. All dimensions are in mm.

where $\dot{\gamma}_0$ is the reference strain rate, τ_0 is the reference shear stress, and m is the strain rate sensitivity coefficient (where $m > 0$). τ_0 is defined to be the flow stress $\tau(\gamma = 5\%)$ at a given reference strain rate $\dot{\gamma}_0 = 1 \times 10^{-3} s^{-1}$. The viscoplastic parameters (τ_0, $\dot{\gamma}_0$, and m) in materials (A) to (C), and the in-plane shear yield strength τ_c (the subscript c refers to core of a ply) in materials (D) to (H), are summarised in Table B.2. τ_c is defined to be the reference stress $\tau(\gamma = 5\%)$ measured from the ±45° tensile test. Finally, Figure B.3d shows that the matrix shear strength τ at a given applied strain rate $\dot{\gamma} = 1 \times 10^{-3} s^{-1}$ increases from $\tau = 0.1$ MPa to 100 MPa as the curing temperature increases from room temperature to $T = 180$°C.

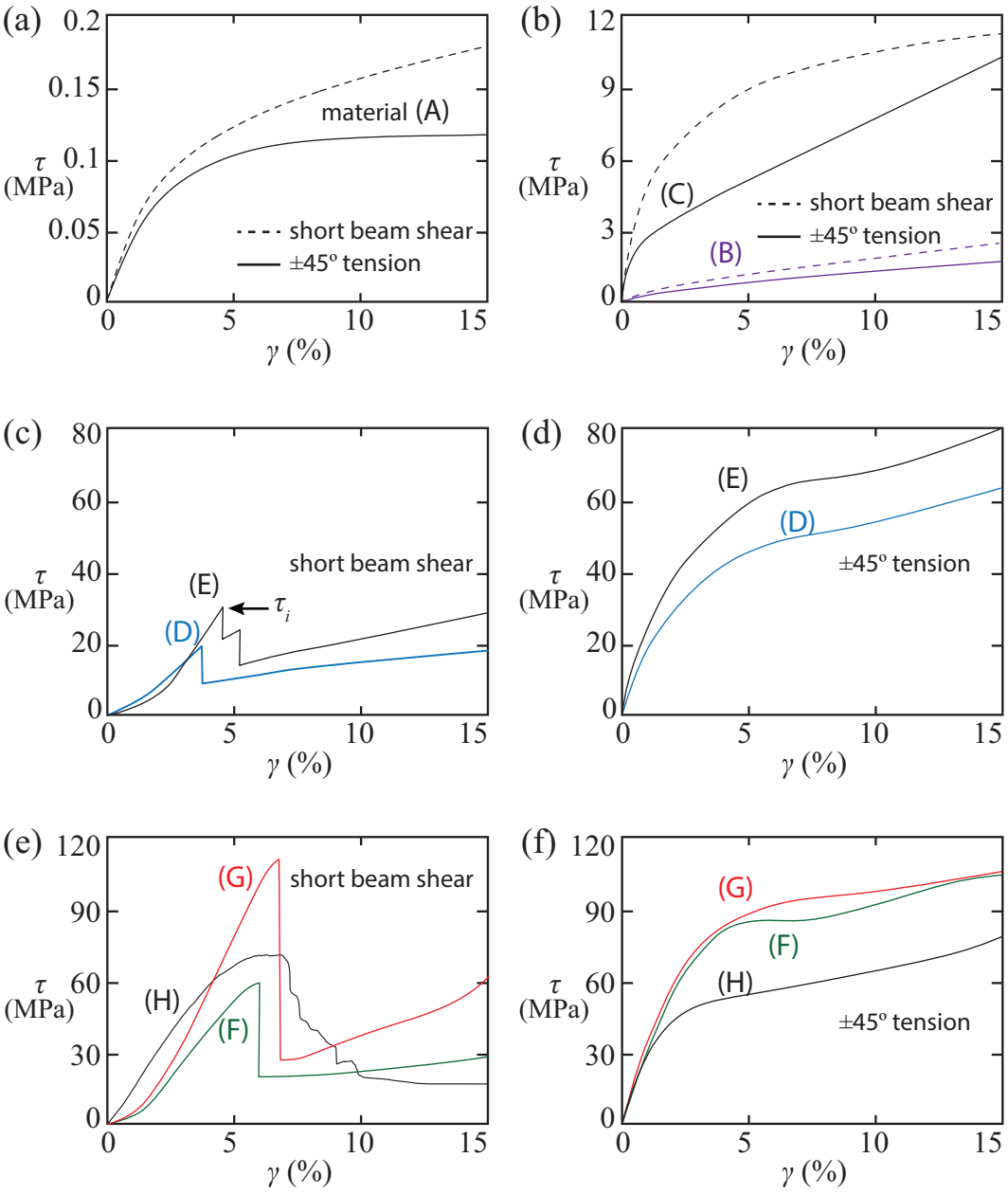

Figure B.2: Shear stress-strain curves of materials (A) to (H) at a shear strain rate of $\dot{\gamma}_0 = 1 \times 10^{-3} s^{-1}$. a) data of materials (A), b) data of materials (B) and (C), c) short beam shear test data of materials (D) and (E), d) ±45° tensile test data of material (D) and (E), e) short beam shear test data of materials (F) to (H), and f) ±45° tensile test data of material (F) to (H).

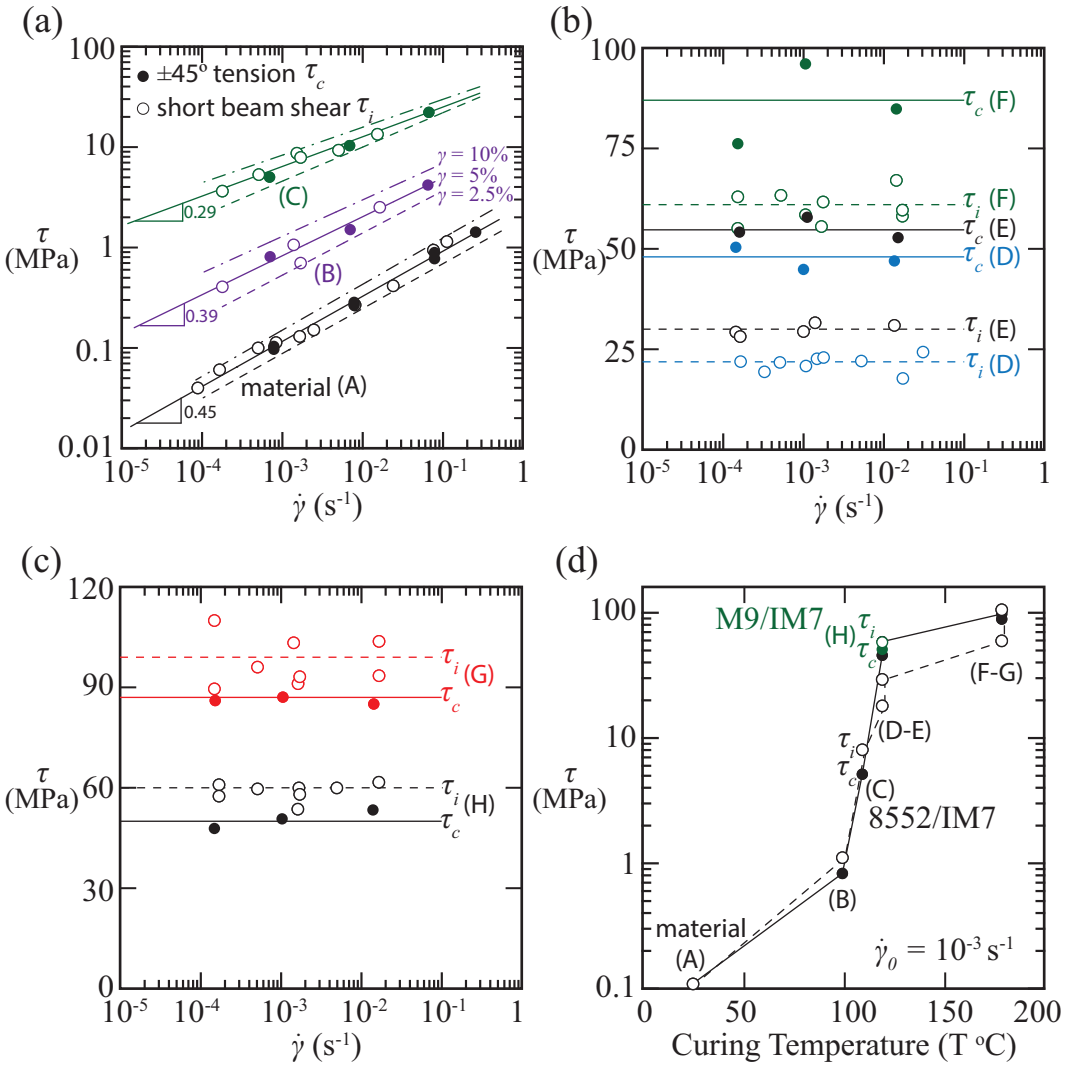

Figure B.3: a-c) Plots of matrix shear strength as functions of shear strain rate $\dot{\gamma}$. Data points ● and ○ represent the τ_c measured in the ±45° tensile tests and τ_i measured in the short beam shear tests, respectively. d) Plot of measured τ_c and τ_i at $\dot{\gamma}_0 = 1 \times 10^{-3} s^{-1}$ as functions of curing temperature.

B.2 Short Beam Shear Test

Rectangular composite beams with $[0°/90°]_{16}$ lay-up and dimensions of beam height $H = 4$ mm (32 plies), breadth $B = 12$ mm, and length $2L = 25$ mm were manufactured from the materials (A) to (H). The composite beams were then tested in a three-point bending set-up following ASTM standard D2344, as illustrated in Figure B.1b. The three-point bending test involved a screw-driven test machine and the set-up consisted of one top roller with a diameter of $D = 6$ mm and two bottom rollers with diameters of $D = 3$ mm, separated by a span length of $L_s = 5$ mm (defined to be the centre-to-centre distance between the top and bottom rollers in the x-direction in the figure). Specimens were placed such that fibres in the top ply were parallel to x-direction in the figure. The short beam shear test was performed by driving the top roller downward in the z-direction at displacement rates ranging from 5×10^{-3} mm/s to 5 mm/s. The deflection of the composite beams δ during the test was measured using a laser extensometer. During the short beam shear test, the specimens were subjected to out-of-plane shear. The maximum shear stress τ was located at the centre of the beam in the x-z plane of the figure, and can be expressed as:

$$\tau = \frac{3F}{4BH} \tag{B.4}$$

The out-of-plane shear strain γ can be expressed as:

$$\gamma = \frac{\delta}{L_s} \tag{B.5}$$

Figure B.2 provides some examples of the short beam shear stress-strain responses of materials (A) to (H) at a shear strain rate of $\dot{\gamma}_0 = 1 \times 10^{-3} s^{-1}$. Materials (A) to (C) showed interlaminar shear yielding while materials (D) to (H) showed interlaminar shear failure at $\gamma \sim 5\%$. Figures B.3a to B.3d plot the measured short beam shear strength as functions of shear strain rate $\dot{\gamma}$ in log-log scale. Short beam shear strength is defined to be $\tau(\gamma = 5\%)$ in materials (A) to (C) and to be the peak shear stress in materials (D) to (H). Similar to the results of the $\pm 45°$ tensile test, materials (A) to (C) showed strain rate sensitivity while materials (D) to (H) were strain rate insensitive. Furthermore, the viscoplastic parameters (τ_0, $\dot{\gamma}_0$, and m) of materials (A) to

Table B.2: Summary of the shear test results measured from the CFRP laminates.

Material	Reference strain rate $\dot{\gamma}_0(s^{-1})$	Reference shear stress τ_0 (MPa)	Strain rate sensitivity coefficient m	τ_c in $\pm 45^\circ$ tensile test (MPa)	τ_i in short beam shear test (MPa)
A	10^{-3}	0.11	0.45	–	–
B	10^{-3}	0.82	0.39	–	–
C	10^{-3}	6.5	0.29	–	–
D	–	–	–	48 ± 2.3	22 ± 1.9
E	–	–	–	55 ± 2.2	30. ± 1.3
F	–	–	–	87 ± 8.2	61 ± 3.7
G	–	–	–	87 ± 0.85	99 ± 6.9
H	–	–	–	50. ± 2.3	60. ± 2.4

(C) measured from short beam shear test were the same as in the $\pm 45^\circ$ tensile test. In contrast, materials (D) to (H) showed different shear strengths in the short beam shear test versus the $\pm 45^\circ$ tensile test. The short beam shear strengths τ_i (the subscript i refers to interfacial shear) of materials (D) to (H) are summarised in Table B.2, separately from the results of the $\pm 45^\circ$ tensile test.

Appendix C

Analytical Models of the Stress State at the Centre of a Cross-ply Laminate under Out-of-Plane Compression

Consider a cross-ply [0°/90°] laminate with specimen side length L at least twice as large as the shear lag length λ. Under out-of-plane compression, the local pressure p increases from the periphery of the specimen toward the centre and then remains constant and elevated in the centre (i.e. outside of the shear lag zone). Away from the periphery, at the centre of the specimen, slipping is prohibited and each ply can deform normally in an elastic, elastic-plastic, or elastic-viscoplastic manner. This appendix analyses the stress state (and strain) at the centre of a cross-ply laminate under out-of-plane compression and provides analytical solutions for elastic, elastic-plastic, and elastic-viscoplastic deformations. Please refer to the schematic illustration in Figure C.1 of the global coordinate system with labels x, y, and z, and the local coordinate system with labels *1*, *2*, and *3*.

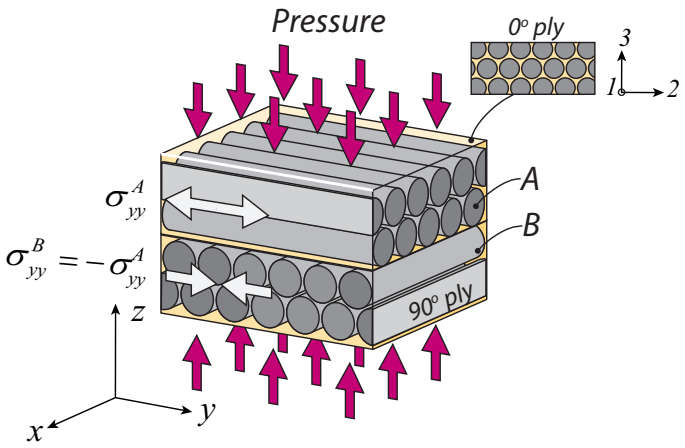

Figure C.1: Schematic illustration of a pair of 0°/90° plies under out-of-plane compression and its defined global and local coordinate systems.

C.1 Elastic Laminate Plate Theory

Consider a pair of 0° and 90° plies under out-of-plane compression in the z-direction in Figure C.1 and where each ply is deforming in an elastic transverse isotropic manner. The elastic strain components ε_{ij}^{el} can be expressed in terms of σ_{ij}:

$$\begin{bmatrix} \varepsilon_{11}^{el} \\ \varepsilon_{22}^{el} \\ \varepsilon_{33}^{el} \end{bmatrix} = \begin{bmatrix} 1/E_{11} & -\nu_{12}/E_{11} & -\nu_{12}/E_{11} \\ -\nu_{12}/E_{11} & 1/E_{33} & -\nu_{23}/E_{33} \\ -\nu_{12}/E_{11} & -\nu_{23}/E_{33} & 1/E_{33} \end{bmatrix} \begin{bmatrix} \sigma_{11} \\ \sigma_{22} \\ \sigma_{33} \end{bmatrix} \tag{C.1}$$

In Figure C.1, layer A is subjected to a tensile stress σ_{yy}^{A} and layer B experiences a compressive stress $\sigma_{yy}^{B} = -\sigma_{yy}^{A}$, since there is no net force in the y-direction. In the local coordinate system, this force equilibrium causes $\sigma_{22} = -\sigma_{11}$. The Poisson's ratio ν_{12} in Eq. (C.1) is negligible and can be assumed to be $\nu_{12} = 0$. For out-of-plane compression, Eq. (C.1) can be written as:

$$\begin{bmatrix} \varepsilon_{11}^{el} \\ \varepsilon_{22}^{el} \\ \varepsilon_{33}^{el} \end{bmatrix} = \begin{bmatrix} 1/E_{11} & 0 & 0 \\ 0 & 1/E_{33} & -\nu_{23}/E_{33} \\ 0 & -\nu_{23}/E_{33} & 1/E_{33} \end{bmatrix} \begin{bmatrix} \sigma_{11} \\ -\sigma_{11} \\ \sigma_{33} \end{bmatrix} \tag{C.2}$$

Also, layers A and B are under equal straining in the x- and y-directions. In the local coordinate system, this strain compatibility causes $\varepsilon_{11}^{el} = \varepsilon_{22}^{el}$. The relationship between ply tensile stress parallel to the fibre σ_{11} and the out-of-plane stress of a ply σ_{33} can be expressed as:

$$\sigma_{11} = \sigma_{33}\left(\frac{-\nu_{23}E_{11}}{E_{11}+E_{33}}\right) \tag{C.3}$$

Thus, the relationship between ε_{33}^{el} and σ_{33} is calculated by substituting Eq. (C.3) into Eq. (C.2):

$$\varepsilon_{33}^{el} = \sigma_{33}\left[\frac{(\nu_{23}-1)\,E_{11}-E_{33}}{E_{33}\,(E_{11}+E_{33})}\right] \tag{C.4}$$

As the out-of-plane compression proceeds, ε_{33}^{el}, σ_{11}, and σ_{33} increase in magnitude, and compressive failure occurs when the ply tensile failure criterion is met; the proposed pressure dependent ply tensile failure criterion from Chapter 4 can be rewritten as:

$$S_L^+ - \left(1+\frac{\alpha}{2}\right)\sigma_{11} + \frac{\alpha}{2}\sigma_{33} = 0 \tag{C.5}$$

where S_L^+ is the ply tensile strength at atmospheric pressure, and α is a pressure dependent term for the ply failure criterion. The out-of-plane strain at failure ε_f can be calculated by substituting σ_{11} in Eq. (C.3) and σ_{33} in Eq. (C.4) into Eq. (C.5):

$$\varepsilon_f = -S_L^+\frac{E_{11}+E_{33}-E_{11}\nu_{23}^2}{\left(1+\frac{\alpha}{2}\right)\nu_{23}E_{11}E_{33}+\frac{\alpha}{2}E_{11}\,(E_{11}+E_{33})} \tag{C.6}$$

C.2 Elastic-plastic Model

If the above plies deform elastically in the fibre direction (i.e. $\varepsilon_{11}^{pl} = 0$) but deform in an elastic-plastic manner in the *2*- and *3*-directions in Figure C.1, the total strain components inside each ply are:

$$\varepsilon_{11}^{tot} = \varepsilon_{11}^{el} \tag{C.7a}$$

$$\varepsilon_{22}^{tot} = \varepsilon_{22}^{el} + \varepsilon_{22}^{pl} \tag{C.7b}$$

$$\varepsilon_{33}^{tot} = \varepsilon_{33}^{el} + \varepsilon_{33}^{pl} \tag{C.7c}$$

The elastic strain components are identical to those expressed in Eq. (C.2) in the above elastic model. Given the strain compatibility in the *1-2* plane in the local coordinate system (i.e. $\varepsilon_{11}^{tot} = \varepsilon_{11}^{el} = \varepsilon_{22}^{tot}$) and the plastic incompressibility in the *2-3* plane (i.e. $\varepsilon_{33}^{pl} = -\varepsilon_{22}^{pl}$), the out-of-plane plastic strain ε_{33}^{pl} can be expressed as:

$$\varepsilon_{33}^{pl} = -\varepsilon_{11}^{el} + \varepsilon_{22}^{el} = -\left(\frac{E_{11} + E_{33}}{E_{11}E_{33}}\right)\sigma_{11} - \left(\frac{\nu_{23}}{E_{33}}\right)\sigma_{33} \tag{C.8}$$

Similarly, the out-of-plane total strain ε_{33}^{tot} can be expressed as:

$$\varepsilon_{33}^{tot} = \varepsilon_{33}^{el} + \varepsilon_{33}^{pl} = \left(\frac{\nu_{23}E_{11} - E_{11} - E_{33}}{E_{11}E_{33}}\right)\sigma_{11} + \left(\frac{1 - \nu_{23}}{E_{33}}\right)\sigma_{33} \tag{C.9}$$

The relationship between σ_{11} and σ_{33} is governed by the yielding criterion; the proposed pressure dependent ply yielding criterion in the *2-3* plane of a ply used in Chapter 4 can be rewritten as:

$$\tau_c = \frac{|\sigma_{22} - \sigma_{33}|}{2} + \mu\sigma_h \tag{C.10}$$

where τ_c is the shear strength of the core material in the *2-3* plane of a ply when $\sigma_h \equiv (\sigma_{22} + \sigma_{33})/2$ is equal to zero, and μ is a pressure dependent term for the yielding criterion. Given that out-of-plane stress is $\sigma_{33} \leq 0$, $|\sigma_{33}| > |\sigma_{22}|$, and force equilibrium $\sigma_{22} = -\sigma_{11}$, the relationship between σ_{11} and σ_{33} can be expressed as:

$$\sigma_{11} = \frac{\sigma_{33}(\mu - 1) - 2\tau_c}{\mu + 1} \tag{C.11}$$

The compressive stress at the onset of yielding σ_{33}^{Y} is determined by substituting σ_{11} in Eq. (C.8) into Eq. (C.11) and setting $\varepsilon_{33}^{pl} = 0$:

$$\sigma_{33}^{Y} = -\frac{2\tau_c}{1 - \mu}\left[1 + \frac{\nu_{23}}{\left(1 + \frac{E_{11}}{E_{33}}\right)\left(\frac{1-\mu}{1+\mu}\right) - \nu_{23}}\right] \tag{C.12}$$

Before σ_{33}^{Y} is reached, the laminate behaves in a linear elastic manner and the stress-strain relationship is identical to the above elastic model. After

σ_{33}^{Y} is reached, the laminate deforms in an elastic-plastic manner and the relationship between ε_{33}^{tot} and σ_{33} is determined by substituting σ_{11} in Eq. (C.9) into Eq. (C.11):

$$\begin{aligned}\varepsilon_{33}^{tot} &= \sigma_{33}\left[\frac{\mu-1}{\mu+1}\left(\frac{\nu_{23}E_{11}-E_{11}-E_{33}}{E_{11}E_{33}}\right)+\frac{1-\nu_{23}}{E_{33}}\right]- \\ &\quad \frac{2\tau_c}{\mu+1}\left(\frac{\nu_{23}E_{11}-E_{11}-E_{33}}{E_{11}E_{33}}\right)\end{aligned} \tag{C.13}$$

As the compression test proceeds, ε_{33}^{tot}, σ_{11}, and σ_{33} increase in magnitude, and failure occurs when the failure criterion in Eq. (C.5) is met. The out-of-plane strain at failure ε_f can be calculated by substituting σ_{11} in Eq. (C.5) into Eq. (C.11), followed by removing σ_{33} in Eq. (C.13):

$$\begin{aligned}\varepsilon_f &= -\left[S_L^{+}+\frac{2\tau_c}{\mu+1}\left(1+\frac{\alpha}{2}\right)\right]\frac{2\left(1-\nu_{23}\right)E_{11}+\left(1-\mu\right)E_{33}}{\left(\alpha-\mu+1\right)E_{11}E_{33}}- \\ &\quad \frac{2\tau_c\left(\nu_{23}E_{11}-E_{11}-E_{33}\right)}{\left(\mu+1\right)E_{11}E_{33}}\end{aligned} \tag{C.14}$$

C.3 Elastic-viscoplastic Model

If the above plies deform elastically in the fibre direction ($\varepsilon_{11}^{pl}=0$) but deform in an elastic-viscoplastic manner in the *2*- and *3*-directions in Figure C.1, the out-of-plane strains ε_{33}^{el}, ε_{33}^{pl}, and ε_{33}^{tot} can be expressed as (similar to the elastic-plastic model):

$$\varepsilon_{33}^{el}=\frac{\nu_{23}\sigma_{11}+\sigma_{33}}{E_{33}} \tag{C.15a}$$

$$\varepsilon_{33}^{pl}=-\varepsilon_{11}^{el}+\varepsilon_{22}^{el}=-\left(\frac{E_{11}+E_{33}}{E_{11}E_{33}}\right)\sigma_{11}-\left(\frac{\nu_{23}}{E_{33}}\right)\sigma_{33} \tag{C.15b}$$

$$\varepsilon_{33}^{tot}=\varepsilon_{33}^{el}+\varepsilon_{33}^{pl}=\left(\frac{\nu_{23}E_{11}-E_{11}-E_{33}}{E_{11}E_{33}}\right)\sigma_{11}+\left(\frac{1-\nu_{23}}{E_{33}}\right)\sigma_{33} \tag{C.15c}$$

$\dot{\varepsilon}_{33}^{el}$, $\dot{\varepsilon}_{33}^{pl}$ and $\dot{\varepsilon}_{33}^{tot}$ can be expressed by taking the rate derivative of the above:

$$\dot{\varepsilon}_{33}^{el} = \frac{\nu_{23}\dot{\sigma}_{11} + \dot{\sigma}_{33}}{E_{33}} \tag{C.16a}$$

$$\dot{\varepsilon}_{33}^{pl} = -\left(\frac{E_{11} + E_{33}}{E_{11}E_{33}}\right)\dot{\sigma}_{11} - \left(\frac{\nu_{23}}{E_{33}}\right)\dot{\sigma}_{33} \tag{C.16b}$$

$$\dot{\varepsilon}_{33}^{tot} = \left(\frac{\nu_{23}E_{11} - E_{11} - E_{33}}{E_{11}E_{33}}\right)\dot{\sigma}_{11} + \left(\frac{1 - \nu_{23}}{E_{33}}\right)\dot{\sigma}_{33} \tag{C.16c}$$

At the centre of the specimen, where slipping between plies is prohibited, $\dot{\varepsilon}_{33}^{pl}$ is also governed by the proposed flow law. The proposed viscoplastic power law in the *2-3* plane of a ply used in Chapter 4 can be rewritten as:

$$\dot{\varepsilon}_{33}^{pl} = sgn\left(\sigma_{33} - \sigma_{22}\right)\dot{\varepsilon}_0\left(\frac{|\sigma_{22} - \sigma_{33}| + \mu\left(\sigma_{22} + \sigma_{33}\right)}{\sigma_0}\right)^{1/m} \tag{C.17}$$

where $\dot{\varepsilon}_0$ is the reference strain rate, σ_0 is the reference flow stress at $\dot{\varepsilon}_0$, and m is the strain rate sensitivity (where $m > 0$). Note that $\dot{\varepsilon}_{33}^{pl}$ in Eq. (C.17) can only be solved numerically. However, an analytical solution can be derived by assuming $m = 1$ (i.e. a viscoelastic behaviour), as follows. Given that out-of-plane stress is $\sigma_{33} \leq 0$, $|\sigma_{33}| > |\sigma_{22}|$, and force equilibrium $\sigma_{22} = -\sigma_{11}$, $\dot{\varepsilon}_{33}^{pl}$ in Eq. (C.17) can be expressed as:

$$\dot{\varepsilon}_{33}^{pl} = \frac{\dot{\varepsilon}_0}{\sigma_0}\left(1 + \mu\right)\sigma_{11} + \frac{\dot{\varepsilon}_0}{\sigma_0}\left(1 - \mu\right)\sigma_{33} \tag{C.18}$$

The total out-of-plane strain rate $\dot{\varepsilon}_{33}^{tot}$ can be determined by adding the elastic strain $\dot{\varepsilon}_{33}^{el}$ in Eq. (C.16a) to Eq. (C.18):

$$\dot{\varepsilon}_{33}^{tot} = \frac{\nu_{23}}{E_{33}}\dot{\sigma}_{11} + \frac{1}{E_{33}}\dot{\sigma}_{33} + \frac{\dot{\varepsilon}_0}{\sigma_0}\left(1 + \mu\right)\sigma_{11} + \frac{\dot{\varepsilon}_0}{\sigma_0}\left(1 - \mu\right)\sigma_{33} \tag{C.19}$$

The out-of-plane stress σ_{33} at a given time and at a constant total strain rate (i.e. $\varepsilon_{33}^{tot}\left(t\right) = \dot{\varepsilon}_{33}^{tot}t$) can be expressed as a first order differential equation by first eliminating σ_{11} in Eq. (C.19) using of Eq. (C.15c) and writing ε_{33}^{tot} as $\dot{\varepsilon}_{33}^{tot}t$, followed by eliminating $\dot{\sigma}_{11}$ using Eq. (C.16c):

$$\mathrm{T}\dot{\sigma}_{33} + \sigma_{33} = at + b \tag{C.20a}$$

$$a = \frac{(\mu + 1) E_{11} E_{33} \dot{\varepsilon}_{33}^{tot}}{2 (1 - \nu_{23}) E_{11} + (1 - \mu) E_{33}} \tag{C.20b}$$

$$b = \frac{\sigma_0 (E_{11} + E_{33}) \dot{\varepsilon}_{33}^{tot}}{\dot{\varepsilon}_0 [2 (1 - \nu_{23}) E_{11} + (1 - \mu) E_{33}]} \tag{C.20c}$$

$$\mathrm{T} = \frac{\sigma_0 ({\nu_{23}}^2 E_{11} - E_{11} - E_{33})}{\dot{\varepsilon}_0 [2 (\nu_{23} - 1) E_{11} + (\mu - 1) E_{33}] E_{33}} \tag{C.20d}$$

$\sigma_{33}(t)$ can be expressed by integrating Eq. (C.20a) using the initial condition $\sigma_{33}(0) = 0$:

$$\sigma_{33}(t) = at + (b - a\mathrm{T}) \left(1 - e^{-t/\mathrm{T}}\right) \tag{C.21}$$

As the compression test proceeds, $\varepsilon_{33}^{tot}(t)$, $\sigma_{11}(t)$, and $\sigma_{33}(t)$ increase in magnitude. The in-plane stress $\sigma_{11}(t)$ is related to $\sigma_{33}(t)$ by rearranging Eq. (C.15c):

$$\sigma_{11}(t) = \frac{\sigma_{33}(t) (\nu_{23} - 1) E_{11} + E_{11} E_{33} \dot{\varepsilon}_{33}^{tot} t}{\nu_{23} E_{11} - E_{11} - E_{33}} \tag{C.22}$$

Ply failure occurs when the failure criterion in Eq. (C.5) is met.

C.4 Compressive Response at Specimen Centre

The remainder of this analysis investigates the effects of elastic properties (such as E_{33} and ν_{23}), matrix shear strength, and applied strain rate on the out-of-plane compressive response at the centre of a cross-ply laminate based on the above models. All the calculations below share the following input parameters: $E_{11} = 164$ GPa, $E_{33} = 5$ - 10 GPa, $\nu_{23} = 0.3$ - 0.5, $S_L^+ = 2724$ MPa, and $\alpha = 2$. For the elastic-plastic model, μ is set at 0.05, and τ_c is set to range from 0 to 100 MPa. For the elastic-viscoplastic model, μ is set at 0.05, $\dot{\varepsilon}_0$ is set at $5 \times 10^{-4} s^{-1}$, σ_0 is set at 0.2 MPa, $-\dot{\varepsilon}_{33}^{tot}$ is set to range from $8 \times 10^{-4} s^{-1}$ to $8 s^{-1}$, and m is assumed to be 1.

C.4.1 Effect of Out-of-Plane Elastic Modulus

Figure C.2a plots the compressive responses for laminates with elastic modulus $E_{33} = 5$ GPa and 10 GPa for a constant value of $\nu_{23} = 0.3$ (τ_c in the elastic-plastic model is set at 10 MPa and $-\dot{\varepsilon}_{33}^{tot}$ in the elastic-viscoplastic model is set at $8 \times 10^{-4} s^{-1}$). In all the models, the increase in E_{33} causes a decrease in the failure strain ε_f, while the compressive peak strength σ_{33}^{max} is unaffected.

C.4.2 Effect of Poisson's Ratio

Figure C.2b plots the compressive responses for laminates with $\nu_{23} = 0.3$ and 0.5 for a constant value of $E_{33} = 10$ GPa (τ_c in the elastic-plastic model is set at 10 MPa and $-\dot{\varepsilon}_{33}^{tot}$ in the elastic-viscoplastic model is set at $8 \times 10^{-4} s^{-1}$). With the exception of the elastic model, the increase in ν_{23} causes a decrease in ε_f, while σ_{33}^{max} is unaffected.

C.4.3 Effect of Matrix Shear Strength in the Elastic-plastic Model

Figure C.2c plots the compressive responses for an elastic-plastic laminate with $\nu_{23} = 0.4$, $E_{33} = 10$ GPa, and $\tau_c = 0$ MPa, 50 MPa, and 100 MPa. The increase in τ_c causes an increase in σ_{33}^{max}, while ε_f is unaffected.

C.4.4 Effect of Strain Rate in the Elastic-viscoplastic Model

Figure C.2d plots the compressive response for an elastic-viscoplastic laminate with $\nu_{23} = 0.4$, $E_{33} = 10$ GPa, and an applied strain rate $-\dot{\varepsilon}_{33}^{tot}$ increasing from $8 \times 10^{-4} s^{-1}$ to $8 s^{-1}$. The increase in applied strain rate causes an increase in σ_{33}^{max}, while ε_f is largely unaffected.

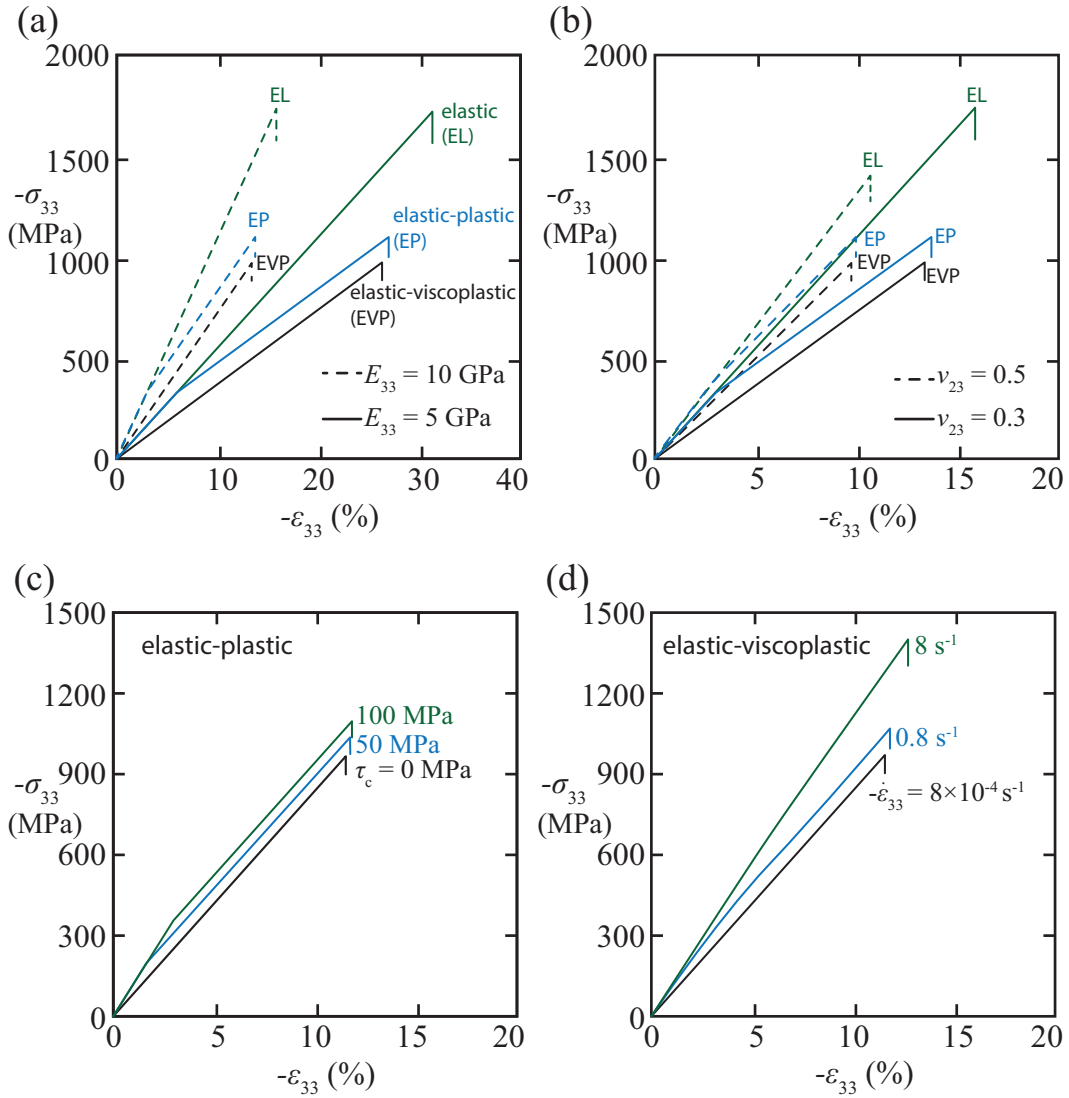

Figure C.2: Plots of out-of-plane compressive responses at the centre of a cross-ply laminate based on the elastic, elastic-plastic, and elastic-viscoplastic calculations showing: a) the effect of E_{33}, b) the effect of ν_{23}, c) the effect of τ_c in elastic-plastic response, and d) the effect of stain rate in elastic-viscoplastic response.

Appendix D

Preliminary Experiment: Effect of Matrix Shear Strength on the Ballistic Response of CFRP Plates

Prior to the ballistic test of CFRP beams described in Chapter 5, a set of preliminary experiments was conducted to investigate the effect of matrix shear strength on the dynamic failure mechanism and ballistic impact resistance of carbon fibre/epoxy cross-ply composite plates. CFRP cross-ply composite plates with matrix shear strength ranging from 0.1 to 100 MPa were impacted by spherical projectiles under an edge-clamped boundary condition. CT-scan images of specimens revealed that composite plates failed by a shear plugging mode when the matrix shear strength was above 22 MPa. When the matrix shear strength was below 22 MPa, the composites showed ply tensile failure beneath the contact. It was initially unclear whether this failure mode was indirect tension, which motivated the design of the experiment described in Chapter 5. Nevertheless, a summary is given below.

D.1 Materials Manufacturing and Properties

Cross-ply laminates $[0°/90°]_{16}$ were made from Hexply® 8552/35%/134/IM7 and Hexply® M9/35%/134/IM7 carbon fibre/epoxy prepregs (both with ply

thickness of 0.131 mm). In total, seven types of composite plates with the same dimensions were tested. The composites made from 8552/IM7 prepregs are labelled as materials (A) to (F). The composites made from M9/IM7 prepregs are labelled as material (G). Note that materials (B) to (E) were prepared in an air oven using the procedure described in Appendix A. The fully cured 8552/IM7 laminates (F) and M9/IM7 laminates (G) were autoclaved following a procedure recommended by Hexcel Ltd. (Hexcel Composites, 2007, 2013). Table B.1 summarises the curing process specifications and the matrix shear strength of materials (A) to (G), measured from the short beam shear test in Appendix B. With the exception of the fully cured materials (F) and (G), all laminates were stored at -15 $^{\circ}$C to avoid further curing and brought back to room temperature for 5 hours prior to testing.

Table D.1: Summary of curing process of cross-ply laminates for the preliminary ballistic test.

Material	Composite Type	Curing specification	Applied pressure in the curing process	Short beam shear strength τ (MPa)
A	8552/IM7	room temperature (uncured)	N/A	0.13 [a]
B	8552/IM7	oven cured 100 ° C 2 hours	out-of-plane 0.1 MPa	0.78 [a]
C	8552/IM7	oven cured 110 ° C 2 hours	out-of-plane 0.1 MPa	5.7 [a]
D	8552/IM7	oven cured 120 ° C 2 hours	out-of-plane 0.1 MPa	18
E	8552/IM7	oven cured 180 ° C 24 hours	out-of-plane 0.1 MPa	50
F	8552/IM7	autoclaved 180 ° C 2 hours	hydrostatic 0.7 MPa	95
G	M9/IM7	autoclaved 120 ° C 2 hours	hydrostatic 0.7 MPa	50

[a] Materials (A) to (C) are strain rate sensitive and their short beam shear tests show no shear failure. The matrix shear strengths reported here are the reference shear stresses obtained at shear strain of 5% $\tau(\gamma = 5\%)$ and at shear strain rate of $\dot{\gamma} = 10^{-3}s^{-1}$.

D.2 Ballistic Impact Test

Figure D.1 illustrates the experimental set-up (the same set-up was used in Karthikeyan et al. (2013b)). CFRP $[0°/90°]_{16}$ plates with dimensions $w \times w \times H$ (with width $w = 150$ mm and thickness $H = 4$ mm) were subjected to impact by a chrome steel ball with a diameter of $D = 12.7$ mm and a mass $m_p = 8.3 \times 10^{-3}$ kg under an edge-clamped boundary condition, fastened by nine M6 bolts each with 8 Nm torque. The projectile was launched through a gas gun with a 4.5 m long barrel having a bore diameter of 13 mm. Impact velocity v_0 ranged from 25 m/s to 555 m/s, and was measured using a set of laser gates. Tested specimens were then examined via X-ray computed tomography (CT-scanning) using the same method discussed by Karthikeyan et al. (2013b), followed by cross-sectional imaging.

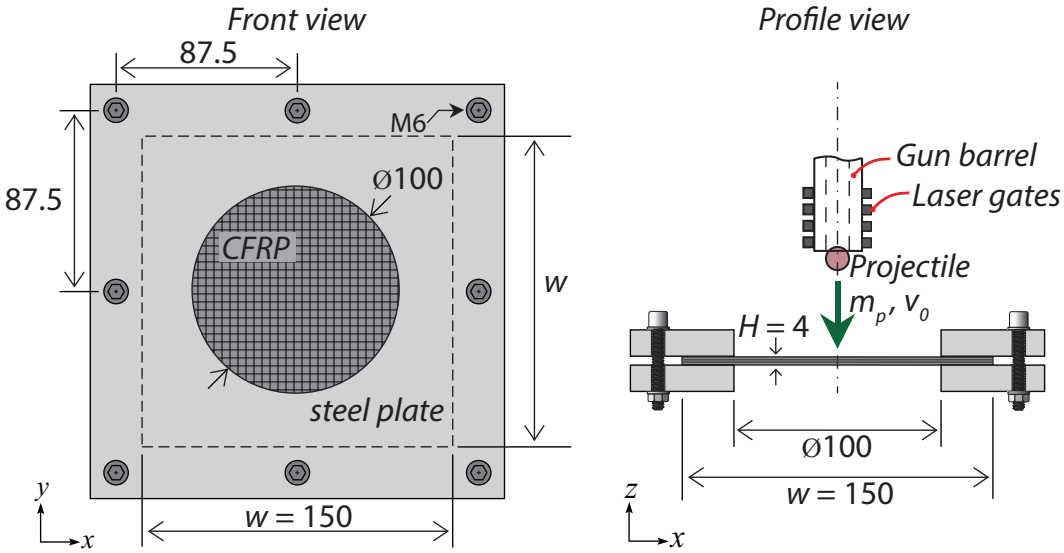

Figure D.1: Schematic illustrations of an edge-clamped CFRP $[0°/90°]_{16}$ plate situated for impact by a spherical projectile.

D.3 Results

Figures D.2 and D.3 show examples of post-impact CT-scan images and cross-sectional optical images of materials (A) to (D) and materials (E) to (G), respectively. CT-scan images of materials (A) and (F) have been previously analysed by Karthikeyan et al. (2013b), and are presented here for the sake of comparison. It is clear from the figure that two different perforation mechanisms have been observed. Materials (E) to (G) failed by a shear plugging mode (consisting of transverse matrix cracks, ply delamination, and fibre fracture beneath the edge of contact). In contrast, materials (A) to (D) failed by a tensile mode (with fibre failure located beneath the projectile near the centre line). It was initially unclear whether this was an instance of the indirect tension mechanism.

Figure D.4 plots the measured ballistic penetration velocity v_p (defined as the average of the lowest velocity to fully penetrate the target and the highest impact velocity to partially penetrate the target) as a function of the matrix shear strength τ of each laminate. It appears that there exist two regimes of ballistic behaviour with the transition occurring at $\tau = 22$ MPa, i.e. material (D). At $\tau > 22$ MPa, v_p increases from $\sim$ 100 m/s to $\sim$ 300 m/s as τ decreases. Once τ falls below 22 MPa, v_p remains elevated at $\sim$ 300 m/s and is insensitive to matrix shear strength. Note that this relationship of v_p versus τ is remarkably similar to that observed in Figure 5.7 in Chapter 5. In conjunction with the evidence provided in Chapter 5, it is concluded that materials (A) to (D), with $\tau < 22$ MPa, in this preliminary ballistic test failed by the same indirect tension mechanism.

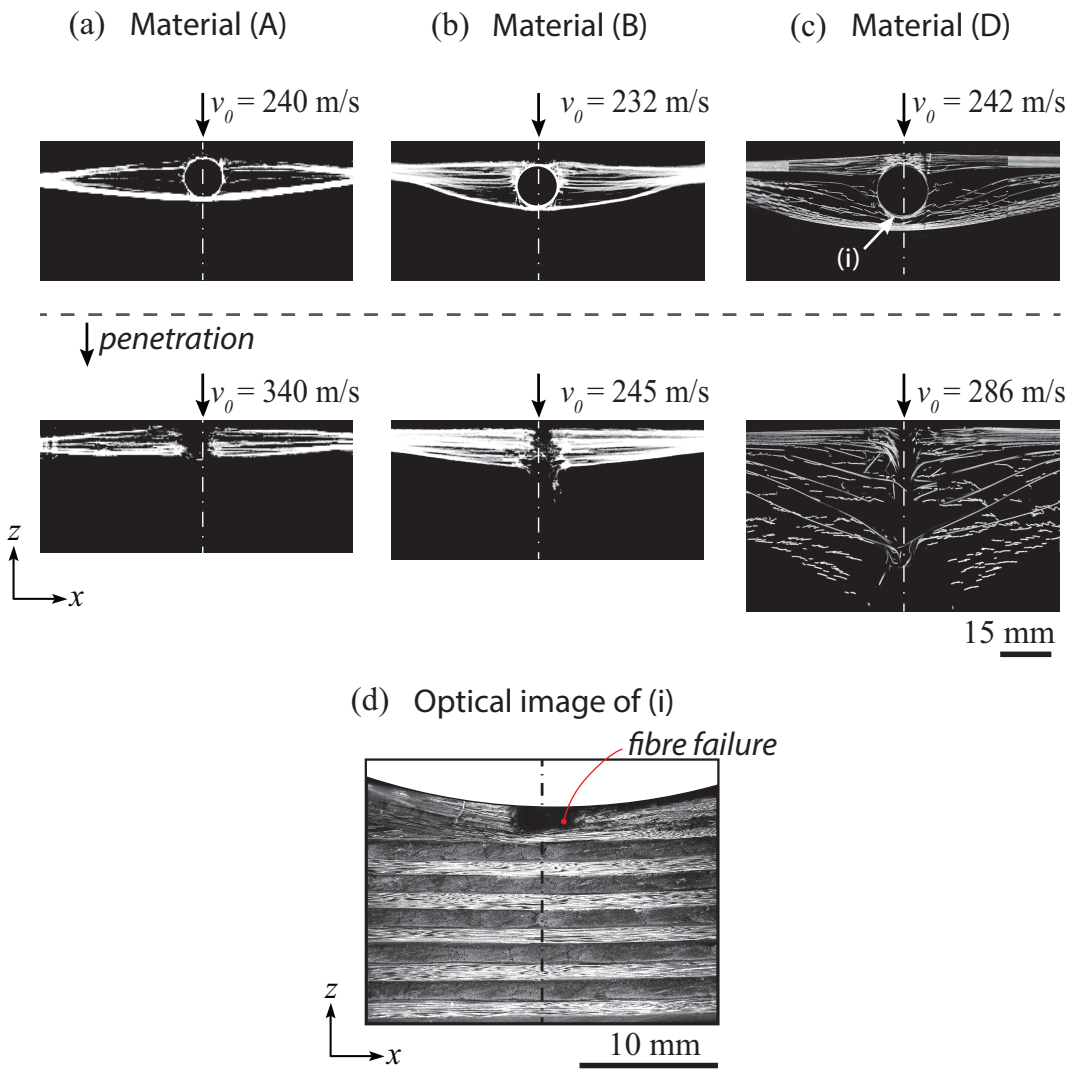

Figure D.2: CT images of the cross-section of composite plates made of a) material (A), b) material (B), and c) material (D), all impacted by a 8.3×10^{-3} kg steel ball at selected impact velocities v_0 below and above the penetration velocity v_p. d) An optical image of the damaged area in material (D), labelled as (i). CT-scan images of material (A) were adapted from Karthikeyan et al. (2013b).

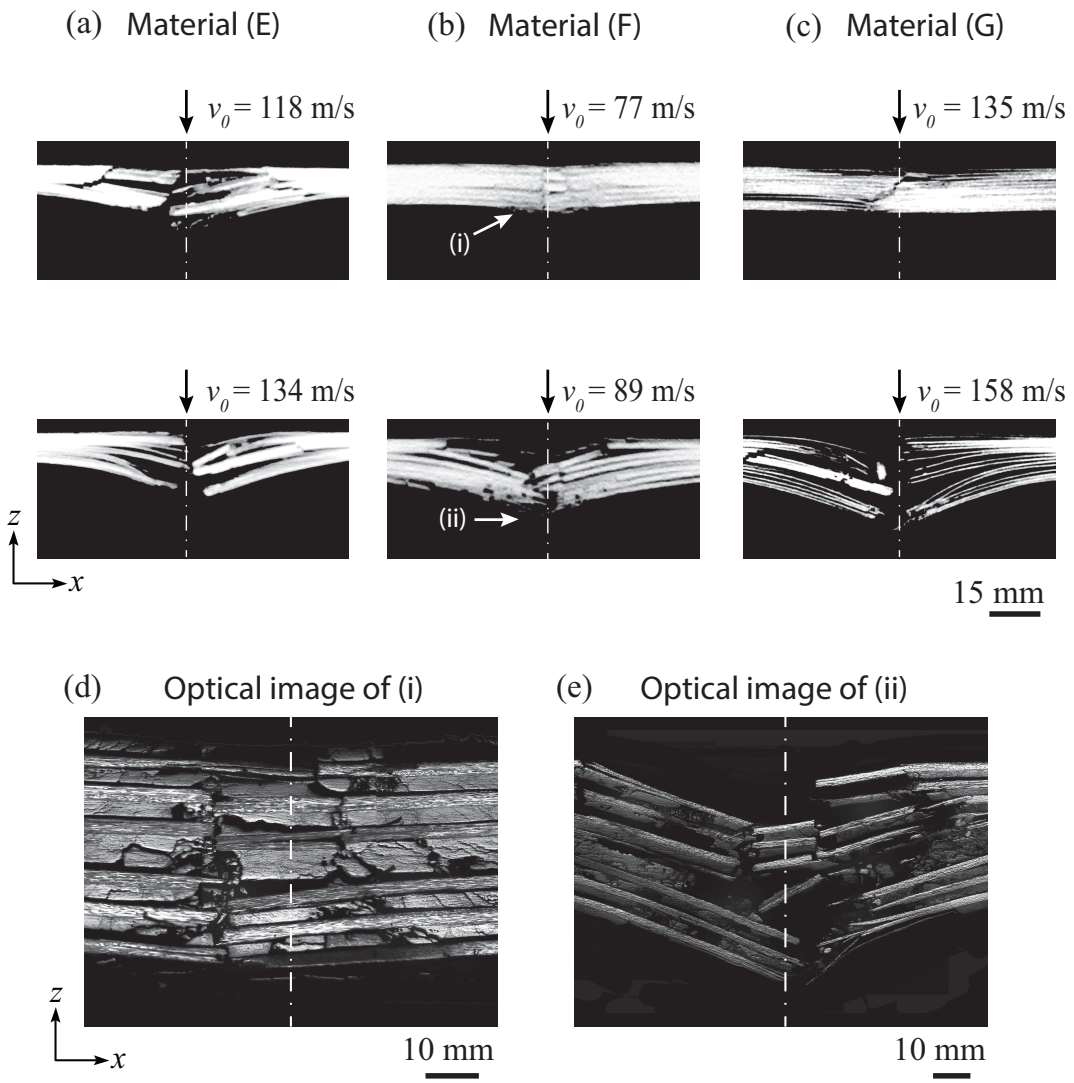

Figure D.3: CT images of the cross-section of composite plates made of a) material (E), b) material (F) and c) material (G), all impacted by a 8.3×10^{-3} kg steel ball at selected impact velocities v_0. d-e) Optical images of the damaged areas in material (F), labelled as (i) and (ii). CT-scan images of material (F) were adapted from Karthikeyan et al. (2013b).

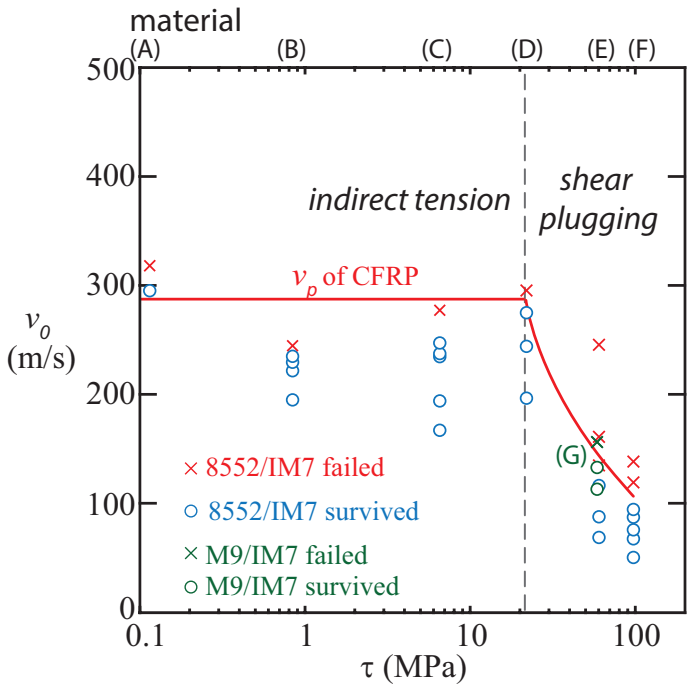

Figure D.4: Plot of measured ballistic penetration velocity v_p as a function of the matrix shear strength τ in materials (A) to (G). Each data point represents an individual test. A solid line is drawn to help reveal the trend.

Appendix E

Preliminary Experiment: Effect of Adhesive on the Ballistic Response of an AA1050A-H6-CFRP Bilayer Plate

Chapter 7 investigated the failure mechanism and the perforation resistance of an AA1050A-H6-CFRP bilayer plate impacted by a 7.2×10^{-4} kg steel ball under an edge-clamped boundary condition (referred to as material (B) in the chapter). Please refer to Chapter 7 for the specimen dimensions and ballistic set-up. In the chapter, the bilayer plates were constructed without adhesive between the metal layer and the CFRP layer. This appendix summarises a set of preliminary experiments conducted on similar AA1050A-H6-CFRP bilayer plates where the aluminium alloy layer and the CFRP layer were bonded together with a Redux® 810 epoxy adhesive (using the same procedure described in Karthikeyan et al. (2012)). In brief, the adhesive was applied between the metal and the composite layers, the layers were then bonded under a pressure of 22 kPa for 5 hours at room temperature, and the bilayer plates were allowed to cure for a further 120 hours at room temperature to attain the fully cured state.

Figure E.1a compares the impact response of the bilayer plates with and

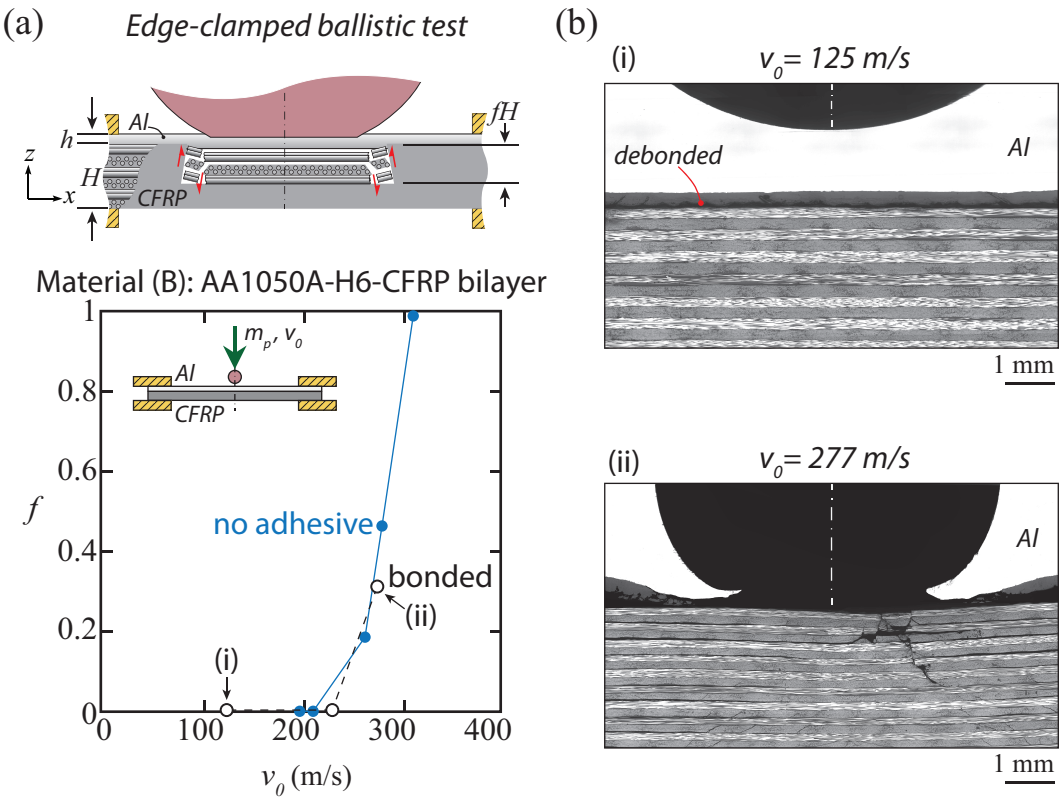

Figure E.1: Summary of the ballistic response of AA1050A-H6-CFRP bilayer plates with and without adhesive. a) The ballistic cut fraction f plotted as functions of the impact velocity v_0. b) Cross-sectional micrographs of the bonded test specimen prior to damage initiation in the CFRP layer (i) and following damage (ii).

without adhesive by plotting the ballistic cut fraction f (defined to be the fraction of plies that exhibited fibre failure) as functions of impact velocity v_0. Cross-sectional micrographs of the bonded bilayer plates revealed that metal-CFRP debonding occurred at a low impact velocity before any damage in the CFRP layer was observed, refer to (i) in Figure E.1b. Accordingly, the adhesive had a limited effect on the impact resistance of the bilayer plates, as can be seen by the similarity in the trend lines of materials with and without adhesive in Figure E.1a. The adhesive had no influence on the failure mechanism of the CFRP layer and the CFRP layer failed by a shear plugging mode consisting of matrix shear crack formation and fibre fracture beneath the edge of contact, refer to (ii) in Figure E.1b.